This is to certify that the

dissertation entitled

The Effect of Interface and Arrangement of Inclusions on Local Stress Fields and Fracture of Model Composites

presented by

Ahmed Al-Ostaz

has been accepted towards fulfillment
of the requirements for

Ph.D. degree in Mechanics

Irvona M. Jasiuk
Major professor

Date May 3, 1996

THE EFFECT OF INTERFACE AND ARRANGEMENT OF INCLUSIONS ON LOCAL STRESS FIELDS AND FRACTURE OF MODEL COMPOSITES

By

Ahmed Al-Ostaz

A DISSERTATION

Submitted to
Michigan State University
in partial fulfillment of the requirements
for the degree of

DOCTOR OF PHILOSOPHY

Department of Materials Science and Mechanics

1996

ABSTRACT

THE EFFECT OF INTERFACE AND ARRANGEMENT OF INCLUSIONS ON LOCAL STRESS FIELDS AND FRACTURE OF MODEL COMPOSITES

By

Ahmed Al-Ostaz

We consider a model composite material consisting of a thin epoxy plate (matrix) reinforced with circular copper disks (inclusions) and subjected to either a uniaxial tension or to thermal strains. At each inclusion-matrix interface there is an interfacial layer, the interphase, which has uniform properties. Inclusions are arranged in the matrix at random but with the restriction that they are not allowed to overlap and there is a minimum separation distance between them. For a comparison we also consider two periodic arrangements: square and triangular. We study elastic fields of such a composite both experimentally using a photoelasticity method and numerically with a finite element method. For a more basic understanding of this problem we consider a single inclusion and several inclusions solutions, too.

We also investigate crack initiation and propagation in both elastic-brittle (epoxy) and ductile (aluminum) sheets, each containing randomly distributed holes and subjected to a uniaxial tension. In this study, which includes both numerical and experimental results, we find that the crack paths in sheets containing holes are not unique and thus a stochastic fracture analysis is needed. This study also sets a basis for a fracture analysis of more complex material systems involving two phase composite materials with randomly arranged inclusions.

Finally, we study a problem involving an elastic circular inclusion embedded in a half-plane and subjected to transformation strains. The inclusion-matrix interface is either perfectly bonded or is allowed to slip, while the straight edge of the half-plane is either fixed or is allowed to move freely in the horizontal direction (frictionless). We compare our results with a recently obtained solution of an inclusion in a half-plane with a traction-free edge (Lee *et al.*, 1992) and show that the boundary conditions have a significant effect on stress fields.

This work is dedicated to the memory of my mother

and to my father

ACKNOWLEDGMENT

From the beginning of my graduate education to the conclusion of my research, and from conception to completeness, this dissertation has required not only my own devotion but also that of an experienced and patient advisor. Thus, I would like to express my sincere appreciation and deep gratitude to my thesis adviser Professor Iwona Jasiuk for her careful guidance, innovative suggestions, keen interest and constant encouragement throughout the course of this research.

I am also sincerely thankful to other members of my thesis committee, Professors: Gary Cloud, Martin Ostoja-Starzewski, Michael Thorpe and Lawrence Drzal for their cooperation and valuable suggestions. Indeed it was a pleasure to work with them.

Special thanks and appreciation are due to my father, the memory of my mother, my wife, my brothers and sisters for their patience, understanding and encouragement which helped me in the completion of this study.

I would further like to express my thanks to all my friends and colleagues, who helped me in different phases during this research.

Finally, I would like to acknowledge the financial support from the National Science Foundation Grant No. MSS 9402285 and the Research Excellence Fund from the State of Michigan.

TABLE OF CONTENTS

LIST OF TABLES

LIST OF FIGURES

Fig 2.3d The joint effect of the coating stiffness E^c (E^c/E^m) and the coating Poisson's ratio ν^c on $\sigma_{\theta\theta}{}^m/\sigma_o$ at $r = a+t$ and $\theta = \pi/2$.

Fig. 2.4a Contour plot of σ_{eff}/σ_o around a single inclusion of radius a with coating 2 of thickness $t = a/4$.

Fig. 2.4b σ_{eff}/σ_o of a single copper inclusion embedded in an epoxy matrix with different coating interfaces and subjected to an axial stress of *0.4 ksi* in the vertical direction.

Fig. 2.5 Isochromatic fringe patterns in an epoxy matrix around a circular perfectlly bonded copper inclusion for an applied stress of *1.75 ksi.*

Fig. 2.6 Isochromatic fringe patterns in an epoxy matrix around a circular coated inclusion with coating 1 for an applied stress of *1 ksi.*

Fig. 2.7 Isochromatic fringe patterns in an epoxy matrix around a circular coated inclusion with coating 2 for an applied stress of *1 ksi.*

Fig. 2.8 The influence of the coating stiffness E^c on σ_{eff}/σ_o in the matrix, the coating and the inclusion at $r = a+t$.

Fig. 2.9-a Isochromatic fringe patterns in an epoxy matrix with randomly distributed and perfectly bonded copper inclusions for an applied stress of $\sigma_0 = 492.3\ psi$ in the horizontal direction when the volume fraction $f = 23\%$.

Fig. 2.9-b Isochromatic fringe patterns in an epoxy matrix with randomly distributed copper inclusions with a weak interface bonding for an applied stress of $\sigma_0 = 492.3\ psi$ in the horizontal direction when the volume fraction $f = 23\%$.

Fig. 2.9-c Isochromatic fringe patterns in an epoxy matrix with randomly distributed copper inclusion coated with coating 2 ($E^c = 30\ ksi$) for an applied stress of $\sigma_0 = 492.3\ psi$ in the horizontal direction when $f = 23\%$.

Fig. 2.9-d Isochromatic fringe patterns in an epoxy matrix with randomly distributed copper inclusion coated with coating 1 ($E^c = 1\ ksi$) for an applied stress of $\sigma_0 = 492.3\ psi$ in the horizontal direction when $f = 23\%$.

Fig. 2.10a σ_{eff}/σ_o in a model composite with volume fraction $f = 23\%$ of randomly distributed and coated inclusions with coating 1 ($E^c = 1$ *ksi*) obtained by FEM.

Fig. 2.10b σ_{eff}/σ_o in a model composite with volume fraction $f = 23\%$ of randomly distributed and coated inclusions with coating 2 ($E^c = 30$ *ksi*) obtained by FEM.

Fig. 2.10c σ_{eff}/σ_o in a model composite with volume fraction $f = 23\%$ of randomly distributed and coated inclusions with coating 3 ($E^c = 120$ *ksi*) obtained by FEM.

Fig. 2.10d σ_{eff}/σ_o in a model composite with volume fraction $f = 23\%$ of randomly distributed and coated inclusions with coating 4 ($E^c = 450$ *ksi*) obtained by FEM.

Fig. 2.10e σ_{eff}/σ_o in a model composite with volume fraction $f = 23\%$ of randomly distributed and coated inclusions with coating 5 ($E^c = 9000$ *ksi*) obtained by FEM.

Fig. 2.10f σ_{eff}/σ_o in a model composite with volume fraction $f = 23\%$ of randomly distributed and coated inclusions with coating 6 ($E^c = 90{,}000$ *ksi*) obtained by FEM.

Fig. 2.11 The influence of the coating stiffness E^c on σ_{eff}/σ_o of the matrix, the coating and the inclusion for coated and randomly distributed inclusions case.

Fig. 2.12a-f $(\sigma_1 - \sigma_2)/\sigma_o$ in a model composite with volume fraction f = .23 of randomly distributed and coated inclusions obtained by FEM for various coating materials.

Fig.2.13 Influence of the coating stiffness E^c on $(\sigma_1 - \sigma_2)/\sigma_o$ of the matrix, the coating and the inclusion for randomly distributed coated inclusions case.

Fig. 2.14 Comparison between analytical (Kouris, 1991) and our numerical (FEM) results of σ_{eff}/σ_o around two inclusions separated by d=a.

Fig. 2.15 Effect of the inclination angle θ on the maximum shear stress $(\sigma_1 - \sigma_2)/\sigma_o$ in the matrix for a two-inclusions solution.

Fig. 2.16 Effect of inclination angle θ on the maximum shear stress $(\sigma_1 - \sigma_2)/\sigma_o$ in the coating for a two-inclusions solution.

Fig. 2.17 Effect of inclination angle θ on the maximum shear stress $(\sigma_1 - \sigma_2)/\sigma_o$ in the

Fig. 3.6 Effect of temperature on the deformation of coating 1.

Fig. 3.7 Effect of temperature on the deformation of coating 2.

Fig. 3.8 Calibration of the epoxy matrix for photoelasticity measurements using a four-point-loading beam.

Fig. 3.9 The joint effect of the non-dimensionalized Young's modulus of the coating E^c with respect to the Young's modulus of the matrix E^m (E^c/E^m) and the non-dimensionalized thickness t with respect to the inclusion radius a (t/a) on $\sigma_{rr}^m/\Delta T$ *(psi/°C)* at $r = a + t$ *when* $\nu^c = 0.36$ and $\alpha^c = \alpha^m$.

Fig. 3.10 The joint effect of the non-dimensionalized Young's modulus of the coating E^c with respect to the Young's modulus of the matrix E^m (E^c/E^m) and the coefficient of thermal expansion of the coating α^c on $\sigma_{rr}^m/\Delta T$ *(psi/°C)* at $r = a + t$ *when* $\nu^c = 0.36$ and $t/a = 0.25$.

Fig. 3.11. The joint effect of the Young's modulus of the coating E^c and the non-dimen-

sionalized coefficient of thermal expansion of the coating α^c with respect to the coefficient of thermal expansion of the matrix α^m on $\sigma_{rr}^m/\Delta T$ *(psi/°C)* at $r = a + t$ *when* $\nu^c = 0.36$ and $t/a = 0.25$.

Fig. 3.12 The joint effect of the non-dimensionalized Young's modulus of the coating E^c with respect to the Young's modulus of the matrix E^m (E^c/E^m) and the Poisson's ratio of the coating ν^c on $\sigma_{rr}^m/\Delta T$ *(psi/°C)* at $r = a + t$ *when* $\nu^c = 0.36$ and $t/a = 0.25$.

Fig. 3.13 The effect of the elastic modulus of the coating E^c on the effective stresses $\sigma_{eff}/\Delta T$ *(psi/°C)* in the matrix, coating and inclusion when $\alpha^c = \alpha^m$, $\nu^c = \nu^m$ and $t = 0.25$ *a.*

Fig. 3.14 The effect of the coefficient of thermal expansion of the coating α^c on the effective stresses $\sigma_{eff}/\Delta T$ *(psi/°C)* in the matrix, coating and inclusion when $E^c = E^m$, $\nu^c = \nu^m$ and $t = .25$ *a.*

Fig. 3.15 The distribution of $(\sigma_1 - \sigma_2)/\Delta T$ *(psi/°C)* in the matrix, coating and inclusion

along the radial direction for the case of a constant $t = 0.25a$, $\alpha^c = \alpha^m$ and $\nu^c = \nu^m$.

Fig. 3.16a. Isochromatic fringe patterns around a cast-in-place copper inclusion in an epoxy matrix for two curing conditions: i) post curing, and ii) standard curing.

Fig. 3.16b. The effect of curing conditions on experimental and numerical results for $(\sigma_1 - \sigma_2)/\Delta T$ *(psi/°C)* stress distribution in the matrix along the radial direction.

Fig. 3.17a. The contours of $(\sigma_1 - \sigma_2)/\Delta T$ *(psi/°C)* in the epoxy matrix around a perfectly bonded single copper inclusion as obtained i) experimentally, ii) analytically, and iii) numerically.

Fig. 3.17b. Isochromatic fringe pattern obtained by photoelasticity for an epoxy matrix with coated single inclusion using i) coating 1, ii) coating 2, or (iii) no coating case.

Fig. 3.18 Effect of separation distance d on the effective stress in the matrix $\sigma^m_{eff}/\Delta T$ *(psi/°C)* for a coating thickness $t = 0.25a$, a thermal coefficient of expansion of the coating $\alpha^c = \alpha^m = 64x10^{-6}/°C$ and a Poisson's ratio of the coating $\nu^c = \nu^m = 0.36$.

Fig. 3.19 Effect of separation distance d on the effective stress in the coating $\sigma^c_{eff}/\Delta T$ *(psi/°C)* for a coating thickness $t = 0.25a$, a thermal coefficient of expansion of the coating $\alpha^c = \alpha^m = 64x10^{-6}$ /°C and a Poisson's ratio of the coating $\nu^c = \nu^m = 0.36$.

Fig. 3.20 Effect of separation distance d on the effective stress in the inclusion $\sigma^i_{eff}/\Delta T$ *(psi/°C)* for a coating thickness $t = 0.25a$, a thermal coefficient of expansion of the coating $\alpha^c = \alpha^m = 64x10^{-6}$ /°C and a Poisson's ratio of the coating $\nu^c = \nu^m = 0.36$.

Fig. 3.21 Effect of separation distance d on the effective stress in the matrix $\sigma_{eff}/\Delta T$ *(psi/°C)* for a coating thickness $t = 0.25a$, a thermal coefficient of expansion of the coating $\alpha^c = 219x10^{-6}$ /°C and a Poisson's ratio of the coating $\nu^c = \nu^m = 0.36$.

Fig. 3.22 Effect of separation distance d on the effective stress in the matrix $\sigma_{eff}/\Delta T$ *(psi/°C)* for a coating thickness $t=.25a$, an elastic Young's modulus of the coating $E^c=E^m$, and a Poisson's ratio of the coating $\nu^c = \nu^m = 0.36$.

Fig. 3.23 Isochromatic fringe pattern obtained by photoelasticity for an epoxy matrix with two perfectly bonded copper inclusions separated by different separation distances *(a/D)*

Fig. 3.24 Effect of separation distance between two perfectly bonded copper inclusions in an epoxy matrix on $(\sigma_1 - \sigma_2)/\Delta T$ *(psi/°C)* experimentally and numerically.

Fig. 3.25 Effect of the mismatch in elastic Young's modulus between the inclusions and the matrix in a two-phase material on $\sigma_{rr}^m/(2G\varepsilon^*)$ for $\nu^c = \nu^m = 0.36$ using Kouris' solution (1991).

Fig. 3.26 Effect of elastic Young's modulus of the coating E^c on radial stress in the matrix $\sigma_{rr}^m/\Delta T$ *(psi/°C)* for $\nu^c = \nu^m = 0.36$ and $t = 0.25a$ using a finite element method.

Fig. 3.27 Isochromatic fringe pattern obtained by photoelasticity for an epoxy matrix with a 14% volume fraction cast-in-place and randomly arranged copper inclusions.

Fig. 3.28 Isochromatic fringe pattern obtained by photoelasticity for an epoxy matrix with a 17% volume fraction cast-in-place and randomly arranged copper inclusions.

Fig. 3.29 Isochromatic fringe pattern obtained by photoelasticity for an epoxy matrix with a 20% volume fraction cast-in-place copper inclusions arranged in a periodic arrangement.

Fig. 3.30 $\sigma_1 - \sigma_2$ in a model composite with volume fraction $f = 14\%$ of randomly distributed and perfectly bonded copper inclusions obtained by FEM for a uniform tempera-

Fig. 3.36 The effect of coefficient of thermal expansion of the coating (α^c) on the maximum $(\sigma_1 - \sigma_2)/\Delta T$ *(psi/°C)* for the case of $t = 0.25a$, $\nu^c = \nu^m = 0.36$.

Fig. 3.37 $\sigma_{eff}/\Delta T$ *(psi/°C)* in a model composite with volume fraction $f = 23\%$ of randomly arranged coated copper copper inclusions with elastic modulus of the coating $E^c = 1ksi$, thermal coefficient of expansion of the coating $\alpha^c = 64x10^{-6}$ /°C as obtained by FEM for a uniform temperature loading of ΔT =-1°C using linear analysis.

Fig. 3.38 $\sigma_{eff}/\Delta T$ *(psi/°C)* in a model composite with volume fraction $f = 23\%$ of randomly arranged coated copper inclusions with elastic modulus of the coating $E^c = 30$ *ksi*, thermal coefficient of expansion of the coating $\alpha^c = 64x10^{-6}$ /°C as obtained by FEM for a uniform temperature loading of ΔT =-1°C using linear analysis.

Fig. 3.39 $\sigma_{eff}/\Delta T$ *(psi/°C)* in a model composite with volume fraction $f = 23\%$ of randomly arranged coated copper inclusions with elastic modulus of the coating $E^c = 120$ *ksi*, thermal coefficient of expansion of the coating $\alpha^c = 64x10^{-6}$ /°C as obtained by FEM for a uniform temperature loading of ΔT =-1°C using linear analysis.

Fig. 3.40 $\sigma_{eff}/\Delta T$ *(psi/°C)* in a model composite with volume fraction f = 23% of randomly arranged coated copper inclusions with elastic modulus of the coating $E^c = E^m$ = *450 ksi,* thermal coefficient of expansion of the coating $\alpha^c = 64x10^{-6}$ */°C* as obtained by FEM for a uniform temperature loading of ΔT =-1°C using linear analysis.

Fig. 3.41 $\sigma_{eff}/\Delta T$ *(psi/°C)* in a model composite with volume fraction f = 23% of randomly arranged coated copper inclusions with elastic modulus of the coating E^c=*9000 ksi,* thermal coefficient of expansion of the coating $\alpha^c = 64x10^{-6}$ */°C* as obtained by FEM for a uniform temperature loading of ΔT =-1°C using linear analysis.

Fig. 3.42 $\sigma_{eff}/\Delta T$ *(psi/°C)* in a model composite with volume fraction f = 23% of randomly arranged coated copper inclusions with elastic modulus of the coating $E^c = E^m$ = *450 ksi,* thermal coefficient of expansion of the coating $\alpha^c = 16.7x10^{-6}$ */°C* as obtained by FEM for a uniform temperature loading of ΔT =-1°C using linear analysis.

Fig. 3.43 $\sigma_{eff}/\Delta T$ *(psi/°C)* in a model composite with volume fraction f = 23% of randomly arranged coated copper inclusions with elastic modulus of the coating $E^c = E^m$ = *450 ksi,* thermal coefficient of expansion of the coating $\alpha^c = 40.35x10^{-6}$ */°C* as obtained

by FEM for a uniform temperature loading of ΔT=-1°C using linear analysis.

Fig. 3.44 $\sigma_{eff}/\Delta T$ *(psi/°C)* in a model composite with volume fraction f = 23% of randomly arranged coated copper inclusions with elastic modulus of the coating $E^c = E^m$ = *450 ksi,* thermal coefficient of expansion of the coating $\alpha^c = 219x10^{-6}/°C$ as obtained by FEM for a uniform temperature loading of ΔT=-1°C using linear analysis.

Fig. 3.45. Isochromatic fringe pattern obtained by photoelasticity around a single cast-in-place copper inclusion subjected to a continuous increase in temperature.

Fig. 3.46. Comparison between experimental and numerical results of maximum $\sigma_1 - \sigma_2$ in an epoxy matrix around a cast-in-place copper inclusion subjected to thermal heating ΔT=-50 °C.

Figure 4.1 Analytical stress contours of $(\sigma_1 - \sigma_2)/\sigma_0$ around an isolated hole for an applied uniaxial tensile loading in the vertical direction.

Figure 4.2 Finite element contours of a) $(\sigma_1 - \sigma_2)/\sigma_0$ and b) $(max(\sigma_1, \sigma_2))/\sigma_o$ around an isolated hole for an applied uniaxial tensile loading in the vertical direction.

Fig. 4.3 Isochromatic fringe pattern obtained by photoelasticity for an epoxy matrix with a holes and subjected to a uniaxial tensile loading of 1 ksi.

Fig. 4.4 Isochromatic fringe pattern obtained by photoelasticity for an epoxy matrix with a 23% volume fraction holes at the middle portion of the specimen and subjected to a uniaxial tensile loading of 492.5 psi in the vertical direction.

Fig. 4.5 Isochromatic fringe pattern obtained by photoelasticity for an epoxy matrix with a 31% volume fraction holes at the middle portion of the specimen and subjected to a uniaxial transverse loading of 492.5 psi in the vertical direction.

Fig. 4.6 Stress contours of $(\sigma_1 - \sigma_2)/\sigma_0$ in an elastic sheet perforated with holes of volume fraction 23% and subjected to a uniaxial tensile loading in the vertical direction.

Fig. 4.7 Stress contours of $(\sigma_1 - \sigma_2)/\sigma_0$ in an elastic sheet perforated with holes of volume fraction 31% and subjected to a uniaxial tensile loading in the vertical direction.

Fig. 4.8 Stress contours of $(max(\sigma_1, \sigma_2))/\sigma_o$ in an elastic sheet with two holes aligned at a) $\theta_{inc} = 0$, b) $\theta_{inc} = \pi/2$, and c) $\theta_{inc} = \pi/4$ for an applied uniaxial tensile loading in the vertical direction.

Fig. 4.9 Effect of inclination angle θ_{inc} on the maximum principal stress $(max(\sigma_1, \sigma_2))/\sigma_o$ in an elastic sheet with two holes separated by a constant distance $d = a$.

Fig 4.10 Effect of separation distance between two holes inclined at $\theta_{inc} = 0$ or $\theta_{inc} = \pi/2$ on the maximum principal stress $(max(\sigma_1, \sigma_2))/\sigma_o$ in an elastic sheet.

Fig 4.11 Effect of number of holes in a row inclined at $\theta_{inc} = 0$ or $\theta_{inc} = \pi/2$ with a separation distance of $d = a$ between each two holes on the maximum principal stress in an elastic sheet.

Fig. 4.12 Crack propagation between two isolated holes using a) adaptive meshing technique b) a relatively crude mesh.

Fig. 4.13 Crack initiation and propagation in an epoxy sheet, with randomly distributed holes of volume fraction f = 31%, subjected to a uniaxial displacement in the vertical direction (experimentally).

Fig. 4.14 Crack initiation and propagation in an epoxy sheet with randomly distributed holes of volume fraction (f = 23%), subjected to a uniaxial displacement loading (experimentally), for two different samples.

Fig. 4.15 Crack initiation and propagation in an epoxy sheet, with randomly distributed holes, subjected to a uniaxial tensile loading using the elastic strain energy fracture criterion with a mesh size = 0.4a around the holes (selected 12 steps) as obtained by a finite element method.

Fig. 4.16 The final crack pattern obtained numerically by finite element method using (a) the maximum principal stress criterion with a mesh size of *0.4a* around the holes, (b) the maximum principal stress fracture criterion with a mesh size of 0.2*a* around the holes, and (c) the elastic strain energy fracture criterion with a mesh size of *0.4a* around the holes for a brittle elastic material with volume fraction f = 23%.

Fig. 4.17 The final crack pattern obtained numerically by finite element method using (a) the maximum principal stress criterion with a mesh size of.*4a* around the holes, (b) the maximum principal stress fracture criterion with a mesh size of.*2a* around the holes, and (c) the elastic strain energy fracture criterion with a mesh size of.*4a* around the holes for a brittle elastic material with volume fraction f = 31%

Fig. 4.18 (a-g) The final crack pattern in a brittle elastic material with holes of volume fraction f = 23% obtained numerically using finite difference method for different mesh sizes.

Fig. 4.19 Final crack pattern in an epoxy sheet with randomly distributed holes, subjected to a uniaxial displacement loading, obtained experimentally from two samples with the

Fig. 4.25a. Crack initiation and propagation in an epoxy sheet with randomly distributed coated inclusions subjected to a uniaxial displacement loading (experimentally)

Fig. 4.25b Crack branching in an epoxy sheet with randomly distributed coated inclusions.

Fig 4.26 Stress contours of $(\sigma_1 - \sigma_2)/\sigma_o$ of a partially cracked specimens subjected to a uniaxial tensile loading in the vertical direction using photoelasticity.

Fig 4.27 Stress contours of $(max(\sigma_1, \sigma_2))/\sigma_o$ of a partially cracked specimen subjected to a uniaxial tensile loading in the vertical direction using FEM.

Fig 4.28 Stress contours of $(\sigma_1 - \sigma_2)/\sigma_o$ of an elastic material perforated with holes of f = 31% and subjected to a uniaxial tensile loading in the vertical direction which shows a localization of stresses.

Fig 4.29 A typical stress strain curve of an epoxy sheet with perforated holes for a) seven different specimens of the same geometric arrangement with f = 23%, b) a comparison between elastic response of two sheets having two volume fractions of holes for the same locations of holes centers.

Fig. 4.30 (a-b) Crack initiation and propagation in an aluminum sheet, with randomly distributed holes of volume fraction (f=23%), subjected to a uniaxial displacement loading

(experimentally) for two selected samples.

Fig. 4.31 Final crack pattern in an aluminum sheet, with randomly distributed holes, subjected to a uniaxial displacement loading obtained experimentally from two samples with the same hole arrangement with volume fraction f= 23%.

Fig. 4.32 Schematic plot of the final crack pattern in an aluminum sheet, with randomly distributed holes and subjected to a uniaxial displacement loading, obtained experimentally from seven samples with the same hole arrangement with volume fraction f= 23%.

Fig. 4.33 (a-b) Crack initiation and propagation in an aluminum sheet, with randomly distributed holes of volume fraction f= 31% and subjected to a uniaxial displacement loading (experimentally), for two selected samples.

Fig. 4.34 Final crack pattern in an aluminum sheet, with randomly distributed holes, subjected to a uniaxial displacement loading obtained experimentally from two samples with the same hole arrangement with volume fraction f = 31%.

Fig. 4.35 Schematic plot of the final crack pattern in an aluminum sheet, with randomly distributed holes and subjected to a uniaxial displacement loading, obtained experimentally from seven samples with the same hole arrangement with volume fraction f = 31%.

Fig. 4.36 Strain energy density stress contours using finite element around randomly dis-

tributed holes of volume fraction a) f=23% b) f=31% in an aluminum sheet at the initiation of cracking (when $\varepsilon_{zz} \approx -0.25$.

Fig. 4.37 σ_{eff}/σ_y stress contours using finite element around randomly distributed holes of volume fraction a) f = 23% and b) f = 31% in an aluminum sheet at the initiation of cracking (when $\varepsilon_{zz} \approx -0.25$ where σ_y is the yield stress of the aluminum.

Fig. 4.38 Final crack pattern obtained numerically by finite element method using the minimum strain criterion with a mesh size of *0.4a* around the holes for a) f = 23% and b) f = 31%.

Fig 4.39 A typical stress strain curve of an aluminum sheet with holes a) for five different specimens of the same geometric arrangement with f = 23% and b) a comparison between elastic response of two sheets having two volume fractions of holes for the same geometric arrangement.

Fig. 5.1 A circular inclusion in a half-plane.

Fig. 5.2 The hoop stress $\sigma_{\theta\theta} = \sigma_{yy}$ in the matrix at point M versus the inclusion radius *a* when

$$\varepsilon_{xx}^* = \varepsilon_{yy}^* = \varepsilon_{zz}^* \text{ and } \Gamma = 100.$$

Fig. 5.3 The hoop stress $\sigma_{\theta\theta} = \sigma_{yy}$ in the matrix at point N versus the inclusion radius a when

$$\varepsilon_{xx}^* = \varepsilon_{yy}^* = \varepsilon_{zz}^* \text{ and } \Gamma = 100.$$

Fig. 5.4 The hoop stress $\sigma_{\theta\theta} = \sigma_{yy}$ in the matrix at point P versus the inclusion radius a when

$$\varepsilon_{xx}^* = \varepsilon_{yy}^* = \varepsilon_{zz}^* \text{ and } \Gamma = 100.$$

Fig. 5.5 The radial stress $\sigma_{rr} = \sigma_{xx}$ in the matrix at point M versus the inclusion radius a when

$$\varepsilon_{xx}^* = \varepsilon_{yy}^* = \varepsilon_{zz}^* \text{ and } \Gamma = 100.$$

Fig. 5.6 The radial stress $\sigma_{rr} = \sigma_{xx}$ in the matrix at point N versus the inclusion radius a when

$$\varepsilon_{xx}^* = \varepsilon_{yy}^* = \varepsilon_{zz}^* \text{ and } \Gamma = 100.$$

Fig. 5.7 The radial stress $\sigma_{rr} = \sigma_{xx}$ in the matrix at point P versus the inclusion radius a when

$$\varepsilon_{xx}^* = \varepsilon_{yy}^* = \varepsilon_{zz}^* \text{ and } \Gamma = 100.$$

Fig. 5.8 The effective stress σ_{eff} in the matrix at point M versus the inclusion radius a when

$$\varepsilon_{xx}^* = \varepsilon_{yy}^* = \varepsilon_{zz}^* \text{ and } \Gamma = 100.$$

Fig. 5.9 The effective stress σ_{eff} in the matrix at point N versus the inclusion radius a when

$$\varepsilon_{xx}^* = \varepsilon_{yy}^* = \varepsilon_{zz}^* \text{ and } \Gamma = 100.$$

Fig. 5.10 The hoop stress $\sigma_{\theta\theta} = \sigma_{yy}$ in the matrix at point N versus Γ when $\nu = \bar{\nu} = 0.3$,

$$\varepsilon_{xx}^* = \varepsilon_{yy}^* = \varepsilon_{zz}^*, \text{ and } a = 0.8.$$

Fig. 5.11 The radial stress $\sigma_{rr} = \sigma_{xx}$ in the matrix at point N versus the shear moduli ratio Γ

$$\text{when } \varepsilon_{xx}^* = \varepsilon_{yy}^* = \varepsilon_{zz}^*, \nu = \bar{\nu} = 0.3, \text{ and } a = 0.8.$$

Fig. 5.12 The stress σ_{yy} in the matrix and in the inclusion along the x-axis when

$$\varepsilon_{xx}^* = \varepsilon_{yy}^* = \varepsilon_{zz}^*, \nu = \bar{\nu} = 0.3, \Gamma = 100, \text{ and } a = 0.6.$$

Fig. 5.13 The stress $\sigma_{r\theta}$ along the matrix-inclusion interface versus the angle θ when

$\varepsilon_{xx}^* = \varepsilon_{yy}^* = \varepsilon_{zz}^*$, $\nu = \bar{\nu} = 0.3$, $\Gamma = 100$, and $a = 0.6$.

Fig. 5.14 The jump in the tangential displacement $2G[u_\theta]$ along the matrix-inclusion interface

versus the angle θ when $\varepsilon_{xx}^* = \varepsilon_{yy}^* = \varepsilon_{zz}^*$, $\nu = \bar{\nu} = 0.3$, $\Gamma = 100$, and $a = 0.6$.

Fig. 5.15 The stress $\sigma_{r\theta}$ along the matrix-inclusion interface versus the angle θ when

$\varepsilon_{xx}^* = 2\varepsilon_{yy}^* = \varepsilon_{zz}^*$, $\nu = \bar{\nu} = 0.3$, $\Gamma = 100$, and $a = 0.8$.

Fig. 5.16 The stress $\sigma_{r\theta}$ along the matrix-inclusion interface versus the angle θ when

$2\varepsilon_{xx}^* = \varepsilon_{yy}^* = \varepsilon_{zz}^*$, $\nu = \bar{\nu} = 0.3$, $\Gamma = 100$, and $a = 0.8$.

CHAPTER 1

INTRODUCTION

Finding local stress fields in matrix-inclusion composite materials is very important since the presence of inclusions may give rise to stress concentrations in the composite which in turn may result in an initiation of cracking and/or plasticity. The magnitude of these stresses depends on many factors which include the material constants of constituents, the shape and relative size of inclusions, the boundary conditions at the inclusion-matrix interfaces, the geometric arrangement of inclusions and the proximity to the surface. Physically, inclusions may represent reinforcing bars in a concrete slab or fibers in a composite material, for example.

Inclusion problems have been addressed by many researchers, but most of the solutions involved a single perfectly bonded inclusion embedded in an infinite material (Eshelby, 1957; Mura, 1987).

The geometric distribution of fibers in a composite material is often approximated by assuming a periodic arrangement of inclusions. This simplifies considerably this complicated problem and enables one to solve it either numerically or analytically for the local fields by considering a unit cell (e.g., Zhang, 1988; Zhu and Achenbach, 1991). However, since the fiber distribution in composite materials is usually non-uniform, this approach may not capture the true behavior of composites. Such an approximation may be adequate to describe the effective elastic response of a composite but will not serve as a good model for a study of local stress fields and crack initiation and propagation in composites with randomly arranged inclusions because fracture is a highly localized phenomenon

influenced by the local geometric and material disorder (e.g. Basista and Krajcinovic, 1991; Brockenbrough *et al.* 1991; Ostoja-Starzewski *et al.* 1994; Pyrz and Bochenek, 1995). The unit cell is not sufficient to investigate the random distribution of fibers and, rather, it is important to redefine the representative volume element (RVE) so that it contains enough fibers and cracks to represent the microstructure (here scale effects will enter, see e.g., Bazant *et al.* 1990). The issue of elasticity and fracture has been addressed to some extent in Ostoja-Starzewski *et al.* (1994), for example, where the out-of-plane elasticity of a unidirectional fiber reinforced composite was considered. That research points out that the arrangement of inclusions has a small influence on the effective elastic moduli of the pre-damage state, but the random arrangement of inclusions, as compared with a periodic one, has a weakening effect on the moduli in the damage stage and on the overall strength. The magnitude of these effects, however, depends on the combination of elastic constants and the mismatch in strain-to-failure ratio. Similar observations about the reduced strength and the fracture strain of a material with randomly distributed holes have been made by Becker and Smelser (1994), Magnusen *et al.* (1988), and others.

The issues of the influence of random arrangement of fibers on the effective properties and local fields were addressed by several researchers. For example, the papers involving a spring network model include Day *et al.* (1992) and Snyder *et al.* (1992) where the effective elastic moduli of a material with randomly arranged holes and inclusions, respectively, were studied. The finite element studies include Brokenbrough *et al.* (1991) where the elasto-plastic stress-strain curves were computed and the effect of random versus periodic arrangement was addressed. Effective elastic moduli of composites with randomly arranged and rigid inclusions were investigated numerically (by using a spring network or

a finite element method) and analytically by Davis *et al.* (1994) and Chen *et al.* (1995). The local elastic fields of randomly arranged inclusions were studied by Ghosh and Mukhopadhyay (1993) and Zhang and Katsube (1995) by using a new finite element method in which an n-sided polygonal network was formed and each polygon contained a single inclusion and served as an element. The analytical solution for a material with several inclusions was given by Gong and Meguid (1993). Also, the recent works of Honein *et al.* (1994) and Bird and Steele (1993) dealt with a solution of a multiple inclusions problem. The more basic studies focusing on inclusion interactions involved a solution of two neighboring inclusions with either perfectly bonded or slipping interfaces (Kouris and Tsuchida, 1991 and Kouris, 1993) and a multiple inclusion case of particular geometry (Kouris, 1995).

The study of fracture, including crack initiation and propagation, of materials with multiple holes or inclusions is a very complex problem which requires, in principle, a numerical solution. Numerical approaches, which can be used to simulate the crack propagation through a material, include spring networks, finite elements, and boundary element methods.

In the spring network approach, a fine mesh model of the matrix-inclusion composite forms a basis for computer simulations. A specimen or an RVE is subjected to kinematic boundary conditions (e.g. Ostoja-Starzewski *et al.* 1994; Pyrz and Bochenek, 1994). The increase in load is simulated by raising the applied strain by small increments. In every run a relaxation method or a conjugate gradient method, for example, is used to solve for the equilibrium of a lattice and then the search for bonds in either matrix or inclusions, which exceed the local fracture criterion, is carried out. If the fracture condition is met,

the given bond is removed from the lattice, thus representing a crack increment. The increase in loading is usually conducted by first unloading the entire lattice and then reloading it. These steps are repeated until a crack is formed through a specimen.

The use of finite elements to simulate fracture requires either removing finite elements or disconnecting them. This may include remeshing which involves a considerable numerical effort.

The boundary element method has an advantage in that it involves considerably less remeshing as only the line of crack needs to be remeshed. However, since this method employs Green's function it can cover a limited scope of problems.

The recent paper which is most closely related to the present study is by Becker and Smelser (1994) and deals with the elasto-plastic response and fracture of a thin aluminum sheet with 40 randomly arranged holes under a uniaxial tension. They use a finite element method and simulate local fracture by the element removal at a critical thickness strain. They find that both the load bearing capacity and the fracture strain of a sheet with randomly arranged holes are significantly reduced as compared with a sheet with a periodic array of holes.

Similar studies, also involving ductile fracture, are due to Xu and Needleman (1991) who simulated ductile failure with two size scales of randomly distributed voids in an elastic-viscoplastic material. Ohno and Hutchinson (1984) proposed a model for an elasto-plastic solid with voids in a disk-shaped cluster to study the plastic flow localization caused by a non-uniform void distribution. The effect of void distribution on the void linkage and plastic flow during fracture was studied experimentally by Magnusen *et al.* (1988) and analytically by Needleman and Kushner (1990). They found that the influence

of random versus periodic arrangement of holes on the effective response was small for the elastic range but large in the plastic range and the materials with random arrays of holes were less ductile. The fracture behavior was found to be a function of the minimum void spacing, void size, and strain hardening.

The combined finite element or boundary element and spring network approaches were also considered. For example, Balanger *et al.* (1994, 1995) proposed a large-scale fracture analysis which combined a boundary element method used for remote regions and a lattice network for the area surrounding a crack, which, by using adaptive meshing guided by a fuzzy logic scheme, can move with the crack tip. Schlangen (1993) and Schlangen and van Mier (1992) used a finite element method to model remote regions and a lattice network with beam elements in the areas where the crack propagates.

Fracture of brittle heterogeneous materials was discussed in Herrmann et al. (1989) and Herrmann and Roux (1990), for example. A similar approach was used by Schlangen and van Mier (1992) and Schlangen (1993) who employed a triangular lattice spring network to simulate cracking of a concrete. Recently Schlangen and Garboczi (1995) proposed a new method to simulate cracking of brittle materials using a lattice with a small scale random geometry to avoid crack mesh dependence in homogeneous media. Jagoda and Bennison (1993) presented a comparison between the fracture results using a random spring network and a random finite element mesh. Similar studies included the works of Jirasek and Bazant (1994/1995) and Bazant *et al.* (1990) who represented concrete as a collection of particles which have elastic but only axial interactions as in a truss (Zubelewicz and Bazant, 1987). The matrix layers between the particles were described by a strain softening behavior. Crack initiation and localization was simulated and size

effects were addressed. Related works are due to Pyrz and his coworkers, who also used a Voronoi-type of truss and studied the effects of inclusion arrangement in a transverse plane of a unidirectional composite material on the strength of a material and related it to the second order statistics of microstructure (Pyrz, 1994; Pyrz and Bochenek, 1994, 1995; Axelsen and Pyrz, 1995).

Recently, a new method, called the Element Free Galerkin (EFG) method, has been employed by Belytschko *et al.* (1994, 1995) to study crack propagation in materials with holes. This method needs a description of geometry and a set of nodes, but as the name implies does not require elements. When simulating crack propagation by using this method the region in front of the crack tip requires an increased number of nodes. This method can easily model crack growth in an arbitrary direction.

An important factor in simulating crack propagation is the choice of a proper crack criterion. Some of the cracking criteria are: the maximum circumferential stress (Erdogan and Sih, 1963), the minimum elastic strain energy density (Sih, 1974), the maximum principal stress (e.g. Ugural and Fenster, 1995), the maximum energy release rate (Griffith, 1921; Hussain *et al.*, 1974), the quadratic failure theories (Theocaris, 1995), and other. The choice of a criterion depends on the type of material.

Whereas crack propagation in ductile matrial is slow, crack propagation in brittle material is often fast and usually associated with an unpredictable scatter. Thus a probabilistic model will be a good method to understand the fracture behavior of such material. This area of study was the focus of many researchers in the last few years. Kunin (1994) adressed a stochastic prediction of a slow crack growth in a brittle material. Chudnovsky and Kunin (1987) studied the probability of a brittle crack formation in an elastic solid

with a fluctuating strength. Their study was applied on first mode cracking of a notched specimen. Their evaluation of specific fracture energy showed a large scatter of the predicted crack paths. Jeulin (1994) presented a statistical model to study the crack propagation in a heterogeneous medium. He proposed a probabilistic model for mode I crack propagation in brittle materials with random distribution of fracture energy which enabled him to calculate the probability of fracture involving the crack nucleation and propagation. Many other reasearchers studied and proposed different probabilistic models for the crack propagation in brittle materials, e.g. Lin and Yang (1983), Moet *et al.* (1992) and Breysse *et al.*, (1994). To our knowledge there is no stochastic model in literature which can be used directly for our case of study which involves both material and geometric disorders.

Another important and complicating factor which influences the composite response is the matrix-inclusion interface. The interface is often represented as a thin layer or coating around the fiber, called *interphase* (Drzal, 1983). For reviews see e.g. Kerans *et al.* (1989), Wright (1990), and Hughes (1991). The interphase may be due to a chemical reaction, diffusion, or other complex processes which occur during manufacturing.

The effect of interphase on the local fields and effective properties of composites has been the subject of study in the last decade. For example, Hashin (1991), Benveniste and Miloh (1986), Pukanszky and Voros (1993), Benveniste *et al.* (1989), and many others studied the effective elastic properties of composites with coated inclusions. The effective properties of composite materials subjected to thermal strain were studied by Hashin (1990), Takao and Taya (1985), Taya *et al.* (1990), Mikata and Taya (1985), Hatta and Taya (1986), Pagano and Tandon (1988), Arnold and Wilt (1993), and others.

Experimentally local stress fields due to a cast-in place inclusion or inclusions in peri-

odic arrangement in composites under thermal loading were studied by Javornicky (1970), Marloff and Daniel (1969), Daniel and Durelli (1962), Herrera and Drzal (1992), and others. The temperature dependence of some cured epoxy resin systems was studied by Gupta *et al.* (1985).

According to our knowledge, the joint effect of geometric arrangement of inclusions and inclusion-matrix interface on local stress fields and damage initiation in composite materials under various loading has not been yet explored in detail.

Another geometric effect in composite materials is the proximity of inclusions to the surface. In structural applications inclusions often are present near a surface, which is not necessarily traction-free and the bonding at the inclusion-matrix interface is not always perfect. Thus, it is of interest to investigate the effects of other boundary conditions, at both the matrix surface and the inclusion's interface, on the stress fields. In the context of plane elasticity the problems of a circular hole or a perfectly bonded inclusion in a half-plane with a traction free surface were considered by Jeffery (1920), Mindlin (1948), Saleme (1958), Shioya (1967), and Richardson (1969), among others. The case involving a sliding circular inclusion in an infinite plane was first considered by Muskhelishvili (1953), while the problem of a sliding inclusion in a half-space with a traction-free edge was solved by Lee *et al.* (1992).

In this dissertation we study the local stress fields in a transverse plane of unidirectional fiber-reinforced composites (Fig. 1.1). We also consider a problem of an inclusion with either perfectly bonded or slipping interface embedded in a half plane in which surface is either fixed or is allowed to move freely in the horizontal direction (frictionless surface)

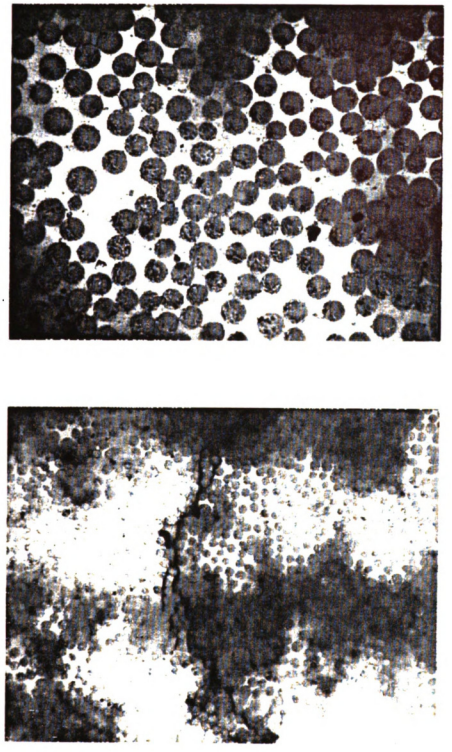

Fig. 1.1 Random geometric distribution of glass fibers in an epoxy matrix.

OBJECTIVES

The main objectives of this research are:

1. To study experimentally, numerically, and theoretically the joint effect of random arrangement of inclusions and interface on the local stress field in a model composite material subjected to a uniaxial loading.

2. To investigate experimentally, numerically, and analytically the joint effect of random arrangement and coating on thermal stresses of a composite with cast-in-place inclusions.

3. To predict the crack initiation and propagation in a composite with coated and randomly arranged inclusions under a transverse uniaxial loading on the basis of experimental and numerical observations with the emphasis on damage initiation and propagation in an elastic brittle (epoxy) or elasto-plastic (aluminum) sheet with randomly distributed holes.

4. To study the joint effect of the matrix-inclusion interface and boundary conditions at the surface of a half-plane for a single inclusion case embedded near a surface.

METHODOLOGY OF THE RESEARCH

To achieve these objectives the following tasks were conducted:

Task 1. The study of the effect of interface and random arrangement of inclusions on the local elastic stresses in model composite materials subjected to a mechanical loading (a

uniaxial tension).

Task 2. The study of the effect of interface and random arrangement of inclusions on the thermal stresses in a model composite material.

Task 3. Investigation of damage in composite materials: study of the effect of interface and fiber arrangement on the damage in composite materials with an emphasis on damage initiation and propagation of elastic-brittle and elasto-plastic sheets with randomly distributed holes.

Task 4. The study of the effect of interface and boundary conditions at the surface of a half-plane on stress concentration when a single elastic circular inclusion is embedded near the surface.

Tasks 1, 2 and 3 were solved experimentally and numerically. Analytical solution was implemented for simpler cases. Task 4 was solved analytically.

CHAPTER 2

TASK1: THE INFLUENCE OF INTERFACE AND RANDOM ARRANGEMENT OF INCLUSIONS ON LOCAL STRESSES IN COMPOSITE MATERIALS

In this phase of study we focus on the influence of the geometric arrangement of inclusions and the matrix-inclusion interface on the local elastic fields. We conduct this analysis by considering a plane elasticity problem involving a model composite material.

More specifically, we investigate the stresses in a model composite made of an epoxy sheet reinforced with circular copper inclusions. At each matrix-inclusion interface there is an interfacial layer, which we refer to as an interphase or a coating. Experimentally, we consider two different interphases, which are more compliant than the matrix, by using two commercially available adhesives, and denote them as coatings 1 and 2, and a third coating having the same properties as the matrix. Material properties of the composite's constituents used in experiments are given in Table 2.1. Numerically we use six types of coatings ranging from very compliant to relatively stiff ones. The properties of these coatings are given in Table 2.2.

Inclusions are arranged randomly in the matrix but with a restriction that they are not allowed to overlap and that there is a minimum distance between them. For a comparison we also include composites with triangular and square periodic arrangements. We subject

Table 2.1 Mechanical properties of materials used in the experimental analysis.

Material	ν	E (ksi)
coating 1	.4	1
coating 2	.4	30
matrix	.36	450
inclusions	.34	17,400

Table 2.2 Mechanical properties of coatings used in the numerical analysis.

	E^c (ksi)	ν^c	Description
coating 1	1	0.36	very compliant
coating 2	30	0.36	compliant
coating 3	120	0.36	optimum (Carman *et al.*, 1992)
coating 4	450	0.36	$E^c=E^m$
coating 5	9000	0.36	stiff $E^c=(E^m + E^i)/2$
coating 6	90000	0.36	very stiff

these composites to a mechanical loading, the uniaxial tension, and analyze the local stress fields experimentally by using the photoelasticity method and numerically via the finite element method. We also consider a single coated inclusion problem, which we study analytically, numerically and experimentally, as well as other simple geometries.

THE SINGLE INCLUSION SOLUTION

A fundamental problem in micromechanics is one involving a single inclusion in an infinite matrix. The famous result dealing with a single inclusion is due to Eshelby (1957) who found that the stress field in an ellipsoidal and perfectly bonded inclusion, subjected to either a uniform transformation strain or a uniform remote loading, is constant. The solution of a single inclusion is applicable for the dilute case in which inclusions are far enough from each other so they don't interact, but it also gives a basic understanding of the stress fields in composite materials in general.

Thus, we first briefly consider a single coated inclusion solution and discuss the influence of several parameters on the local stress fields. In the analysis we assume that all the components of the composite are linearly elastic and isotropic. We denote the Young's modulus and the Poisson's ratio of the constituents by E and ν, and use the superscripts i, c, and m to denote the inclusion, coating (interphase), and matrix, respectively. The geometry involves a large plate containing a small circular inclusion of radius a with the interphase of thickness t (Fig. 2.1). Thus we have an elasticity problem of a plane stress type. The applied loading is a remote uniaxial tension. In the analysis it is convenient to

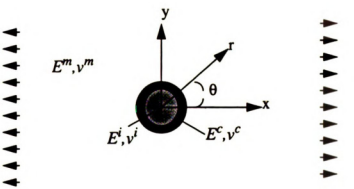

Fig. 2.1 A single coated inclusion embedded in an infinite matrix.

employ the polar coordinate system(r, θ). We assume perfect bonding conditions between the inclusion-coating ($r = a$) and the coating-matrix ($r = a + t$) interfaces, which imply continuity of tractions and displacements. Thus at $r = a$

$$\begin{aligned} \sigma_{rr}^{i} &= \sigma_{rr}^{c} \qquad \sigma_{r\theta}^{i} = \sigma_{r\theta}^{c} \\ u_{r}^{i} &= u_{r}^{c} \qquad u_{\theta}^{i} = u_{\theta}^{c} \end{aligned} \tag{2.1}$$

and at $r = a + t$

$$\begin{aligned} \sigma_{rr}^{m} &= \sigma_{rr}^{c} \qquad \sigma_{r\theta}^{m} = \sigma_{r\theta}^{c} \\ u_{r}^{m} &= u_{r}^{c} \qquad u_{\theta}^{m} = u_{\theta}^{c} \end{aligned} \tag{2.2}$$

where σ_{kl} and u_{k} $(k, l = r, \theta)$ are stresses and displacements, respectively.

For the applied uniaxial tension $\sigma_{xx} = \sigma_{o}$ at infinity, the remote boundary conditions in polar coordinates are (e.g. Timoshenko and Goodier, 1953)

$$\sigma_{rr}^{m} = \frac{\sigma_{o}}{2}(1 + \cos 2\theta) \tag{2.3}$$

$$\sigma_{r\theta}^{m} = -\frac{\sigma_{o}}{2}\sin 2\theta \tag{2.4}$$

Then, our plane elasticity problem can be solved by using the following Airy stress functions Φ

$$\Phi^{m} = \frac{\sigma_{o}}{4}\left(r^{2} - r^{2}\cos 2\theta + Aa^{2}\log r + \frac{Ba^{4}\cos 2\theta}{r^{2}} + Ca^{2}\cos 2\theta\right) \tag{2.5}$$

$$\Phi^{i} = \frac{\sigma_{o}}{4}(Dr^{2} + Fr^{2}\cos 2\theta + Gr^{4}\cos 2\theta) \tag{2.6}$$

$$\Phi^{c} = \frac{\sigma_{o}}{4}\left(Hr^{2} + J\log r + L\frac{\cos 2\theta}{r^{2}} + M\cos 2\theta + Nr^{2}\cos 2\theta + Qr^{4}\cos 2\theta\right) \tag{2.7}$$

The problem involves twelve unknown constants: *A, B, C, D, F, G, H, J, L, M, N, Q*, which are evaluated by solving twelve equations given by the boundary conditions (2.1)-(2.2).

Note that σ_{rr} and u_r each give two equations. The boundary conditions (2.3)-(2.4) are automatically satisfied by Φ^m given in eqn. (2.5). The results of a parametric study are shown in Figs. 2.3a-d and Tables 2.3-4.

If the initiation of plasticity were of interest then it would be convenient to use an equivalent or effective stress σ_{eff}, based on the Huber-Mises yield criterion (e.g. Mendelson,1968), and defined as

$$\sigma_{eff} = \frac{1}{\sqrt{2}}[(\sigma_{rr}-\sigma_{\theta\theta})^2+(\sigma_{zz}-\sigma_{\theta\theta})^2+(\sigma_{rr}-\sigma_{zz})^2+6(\sigma_{r\theta}^2+\sigma_{\theta z}^2+\sigma_{rz}^2)]^{1/2} \quad (2.8)$$

where for a plane stress case, considered in this paper, $\sigma_{zz} = \sigma_{\theta z} = \sigma_{rz} = 0$.

THE MULTI-INCLUSION SOLUTION

When more than one inclusion is present in the material the problem of finding local stresses becomes very complex due to the inclusions' interactions. The analytical solution for a problem of multiple coated inclusions is possible, in principle, by using the approach of Gong and Meguid (1993) or Honein *et al.* (1994), for example, but it would be computationally very involved. Alternately, the numerical means, such as finite element, boundary element, and finite difference methods; or experimental means, such as optical methods, can be used. In this dissertation, for simplicity, we use the finite element program ANSYS 5.1 (1995) and the photoelasticity method (e.g. Dally and Rilley, 1991) to calculate the elastic fields in a composite with randomly arranged inclusions. For a comparison we consider composites with square and triangular periodic arrangements of inclusions, too. Also, we use these two methods to find the solutions for a single inclusion

problem and compare them with the analytical solution in order to check the accuracy of our experimental and numerical approaches.

The Experimental Approach

The experimental set-up involved epoxy plates, with dimensions of 3.2x13.0x0.125 inches, containing 31 randomly distributed non-overlapping coated circular copper inclusions (Fig. 2.2), which are 0.25 inches in diameter (volume fraction of inclusions is approximately 23% in the middle portion of the specimen). To create a non-uniform arrangement of inclusions the random numbers, indicating the centers of inclusions, were generated by a computer according to a planar Poisson's distribution. We imposed restrictions that the coated inclusions didn't overlap, were located at least one diameter away from the edge of the specimen, and there was a minimum clear distance $0.1a$ between any two inclusions (a is the inclusion radius). Inclusions were introduced in the following way. First, the epoxy plates were cut to the desired dimensions. Then, the epoxy plates were placed one at a time between two steel plates and holes were drilled at a slow speed to reduce residual stresses and to minimize microcracks. The holes were drilled according to the random distribution as described above and they were of the size equal the combined size of inclusions and the coatings. To remove any remaining residual stresses due to machining, the specimens were heated to $260^{o}F$ (which is beyond the glass transition temperature), were held at this temperature for two hours and then cooled at the rate of $5^{o}F/hr$ to $150^{o}F$, and finally cooled in 7 hours to a room temperature. To simulate dif

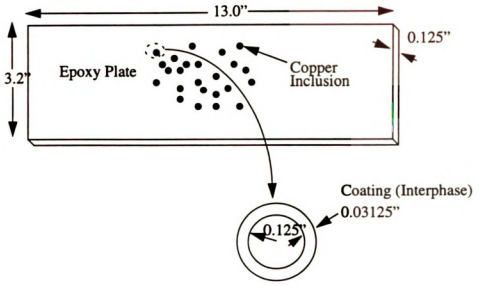

Fig. 2.2 Schematic plot of a model composite specimen used in experimental and numerical studies.

ferent interphases the inclusions were coated with two different adhesive materials. Mechanical properties of these materials are shown in Table 2.1. After the preparation of samples the photoelasticity method was used to find the stress distributions in these birefringent composite plates. A more detailed description of experimental set-up and materials used is given in the Appendix.

Photoelastic measurements.

Photoelasticity is an experimental stress analysis method which takes advantage of the property of double refraction exhibited by certain isotropic transparent materials when subjected to stress or strain. This optical phenomenon manifests itself in the form of interference fringes or alternate dark and light bands when the material is viewed in a field of polarized monochromatic light. These fringes, referred to as isochromatics are ordered according to the number of darkness-brightness cycles that occur at any given point as the load is increased from zero to its final value.

To obtain stresses with this method of analysis, typically, a model is fabricated from a transparent plastic known to possess the required photoelastic properties. The model is machined to be geometrically similar to the prototype. and loaded also similarly to the prototype loading.

In the case of inserts a somewhat different procedure is required. The photoelastic material is cast around the insert, and, if desired, allowed to bond to the insert. If a shrinkage load is desired, advantage is taken of the curing shrinkage of the matrix (this includes a large proportion of ordinary thermal shrinkage). Mechanical loading may be superposed on the

shrinkage load, or special precautions may be taken to avoid any shrinkage loading and then stresses due to mechanical loading are obtained separately.

1. TWO-DIMENSIONAL TESTS.

In two-dimensional problems the loaded model is examined in a field of polarized light. The fringe pattern gives the stress distribution and direct visual observation can ordinarily be used to locate regions of high and low stresses.

Essentially, two patterns can be obtained. If the polariscope is set to produce the maximum darkness in the background outside the model (dark field), then the fringes are ordered n = 0,1,2,3,... If the polariscope is arranged to produce the maximum light in the field outside the model (light field), then the fringes have the values of the intermediate orders n=1/2, 1 1/2, 2 1/2, 3 1/2, ...etc. By the simple process of counting the fringes and multiplying their order by a calibration constant, the maximum shear stress distribution can be determined throughout the body of the model. The model stress distribution can then be converted by the use of appropriate scaling laws to the stress distribution in the prototype.

The relation between fringe numbers and the maximum shear stress is given by:

$$\sigma_1 - \sigma_2 = 2\tau_{max} = nf_\sigma/h \tag{2.9}$$

where

n = fringe order

h = model thickness

τ_{max} = maximum in-plane shear stress

σ_1, σ_2 = in-plane principal stresses

f_σ = material fringe coefficient

When the applied stress is uniaxial, one of the principal stresses at the boundary is zero and the other can be determined directly from the photoelastic data. At the interior points of the model an additional information is required for determining each of the principal stresses. The evaluation of them becomes appreciably more complicated. A number of methods are available, however, to solve the two-dimensional problem completely.

2. THREE-DIMENSIONAL TESTS.

For the photoelasticity solution of a three-dimensional problem a somewhat more involved technique is necessary, since the observation of the loaded model in a field of polarized light does not result in a fringe pattern which can readily be interpreted. To overcome this difficulty, a stress pattern is "locked - in" or "frozen" in the model, and thin slices are removed from the model wherever the stress distribution is required. By viewing the slices in polarized light, a fringe pattern is obtained which corresponds to the stress distribution in the three-dimensional model at the time of stress freezing.

In this phase of study we consider the model composite in a form of a thin plate in order to simplify the experimental analysis. By having the plane stress case we reduce the free edge effects, i.e. the disturbance of stresses near the traction free surface due to a relaxation of stresses there, and in this case, we can see the photoelastic fringes more easily. Alternately, we could simulate directly the plane strain case by using a fringe freezing

technique.

In order to calibrate the epoxy matrix material for the fringe value f_σ different levels of loading were applied to either specimens involving thin sheets with a hole or to a four-point-loaded beam. The average value of number of fringes was used to determine the material fringe value f_σ. For our case f_σ was found to be 53 lb/in/fringe at room temperature.

The Finite Element Solution

In this study we used a commercially available finite elements package ANSYS 5.1 (1995). We utilized quadrilateral plane elements, such that each element was defined by eight nodes having two degrees of freedom: translations in the nodal x and y directions, with the element edge size of $.25a$. We simulated in this analysis the exact geometry of the experimental specimens (described in the previous section) with the following boundary conditions: traction-free conditions at two side edges and an applied uniaxial tension at the third edge with a fixed displacement condition at the remaining edge. Numerically, we used six different coatings (Table 2.2) and we considered seven different configurations of inclusions arranged randomly but with no overlap and a minimum distance of $0.1a$ between them. Other studied geometric configurations included square and triangular periodic arrangements, and two, three and four inclusion cases.

RESULTS AND DISCUSSION

The Single Inclusion Case

In the parametric study of a single coated inclusion solution we illustrate the influence of three parameters characterizing the coating (interphase): the Young's modulus E^c, the Poisson's ratio ν^c, and the thickness t, on the stress fields in the matrix. The composite system is a thin epoxy plate with copper inclusions with the properties given in Table 2.1.

Figs. 2.3a-b illustrate the joint effect of the non-dimensionalized Young's modulus of the coating E^c with respect to the Young's modulus of the matrix E^m (E^c/E^m) and the non-dimensionalized thickness t with respect to the inclusion radius a (t/a) on σ^m_{rr} at $\theta = 0$ and $\sigma^m_{\theta\theta}$ at $\theta = \pi/2$ respectively, at $r = a + t$ when $\nu^c = 0.36$. Observe that both the thickness t and the Young's modulus of the coating E^c contribute to the stress fields. The effect of the Young's modulus of the coating E^c on the stresses in the matrix is more pronounced when the coating is verycompliant, i.e. E^c/E^m is small, and is highly influenced by the thickness. Thus, we only plot the results in the range $0 \le E^c/E^m \le 1$. It is interesting to observe that this effect of E^c is larger on $\sigma^m_{\theta\theta}$ at $\theta = \pi/2$ when the thickness is very small while the opposite behavior is true for σ^m_{rr} at $\theta = 0$.

The effect of the Poisson's ratio of the coating material is very small in comparison to the influence of the other two parameters as shown in Figs. 2.3 c-d. This effect increases somewhat as the thickness increases, as illustrated in Fig. 2.3c, which gives $\sigma^m_{\theta\theta}$ at $\theta = \pi/2$ and $r = a + t$, when the coating 2 is used (see Table 2.1). Also, note the much

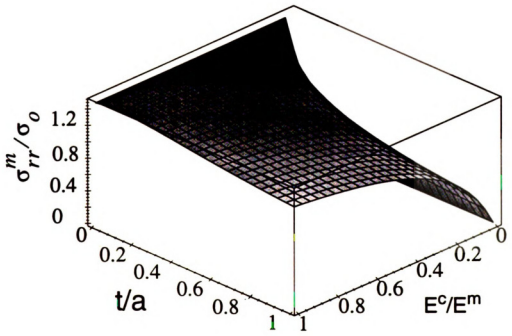

Fig. 2.3a The joint effect of the coating stiffness E^c (E^c/E^m) and coating thickness t (t/a) on σ_{rr}^{m}/σ_o at $r = a+t$ and $\theta = 0$.

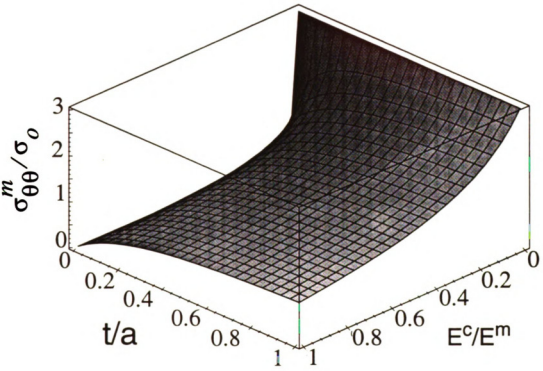

Fig. 2.3b The joint effect of the coating stiffness E^c (E^c/E^m) and coating thickness t (t/a) on $\sigma_{\theta\theta}{}^{m}/\sigma_o$ at $r = a+t$ and $\theta = \pi/2$.

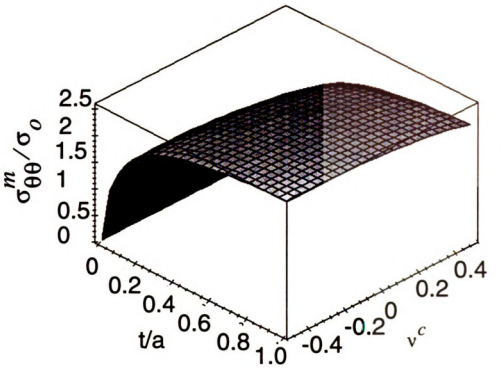

Fig. 2.3c The joint effect of coating thickness t (t/a) and Poisson's ratio ν^c on $\sigma_{\theta\theta}{}^m/\sigma_o$ at $r = a+t$ and $\theta = \pi/2$.

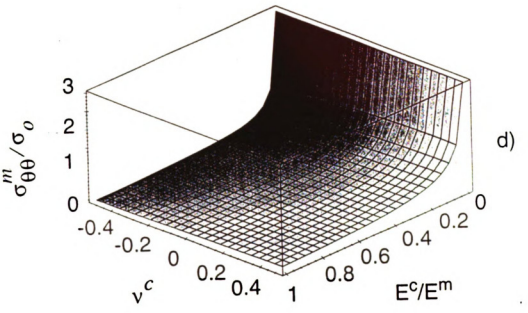

Fig 2.3d The joint effect of the coating stiffness E^c (E^c/E^m) and the coating Poisson's ratio ν^c on $\sigma_{\theta\theta}{}^m/\sigma_o$ at $r = a+t$ and $\theta = \pi/2$.

larger influence of the thickness on $\sigma_{\theta\theta}^{m}$ in comparison to ν^{c} for this case. Fig. 2.3d presents the joint effect of the Poisson's ratio ν^{c} and E^{c}/E^{m} for the same stress component and location. Again, the influence of ν^{c} is negligible in comparison to the influence of E^{c}. Thus, in the finite element calculations we assume a common value of $\nu^{c} = 0.36$ for all the coating types considerd.

In order to check the accuracy of both our photoelastic results and finite element outputs, we compared the contours of σ_{eff} obtained analytically (Fig. 2.4a), and numerically (Fig. 2.4b) and experimentally (the photoelastic fringe patterns are illustrated in Figs. 2.5-2.7). These results, given in Table 2.3, show a good agreement between our numerical, experimental, and analytical solutions.

Note, that in the case of perfect bonding, experimentally, the fringes start forming at the inclusion-matrix interface along the line of action of the applied load and then they propagate to the other side of the inclusion (Fig. 2.5). The opposite behavior is observed in cases of an inclusion with a compliant coating (Fig. 2.6-2.7) or a hole, where fringes start forming in a plane perpendicular to the line of action of the applied load and eventually migrate to the line of action of the applied load.

Fig. 2.8 illustrates the maximum effective stress in the matrix, inclusion, and the coating as a function of E^{c}/E^{m} for the single inclusion case (dilute concentration). Note that for the case of a compliant coating the maximum stress is in a plane perpendicular to the applied loading ($\theta = 0$), while for the case of $E^{c}/E^{m} \geq 1$ the maximum stress is located

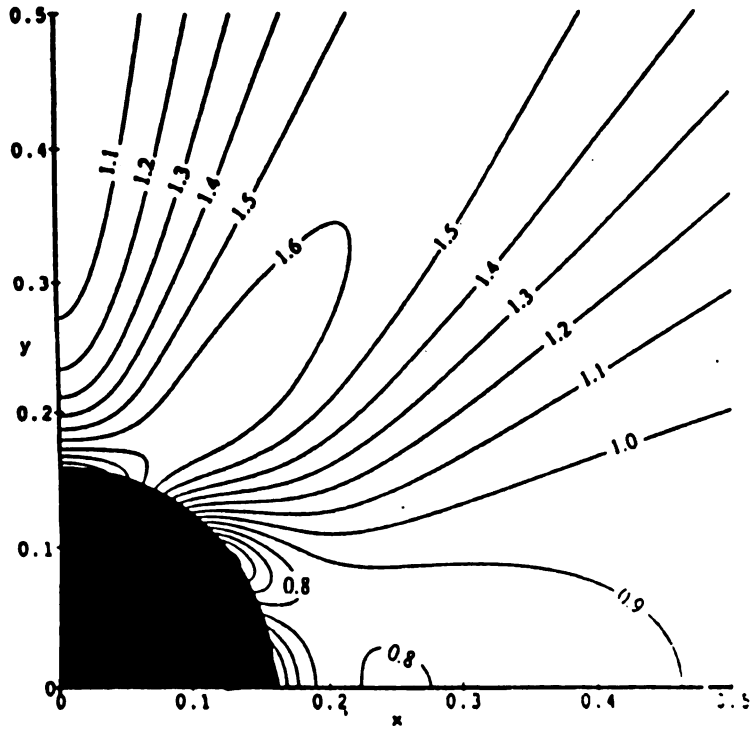

Fig. 2.4a Contour plot of σ_{eff}/σ_o around a single inclusion of radius a with coating 2 of thickness $t = a/4$.

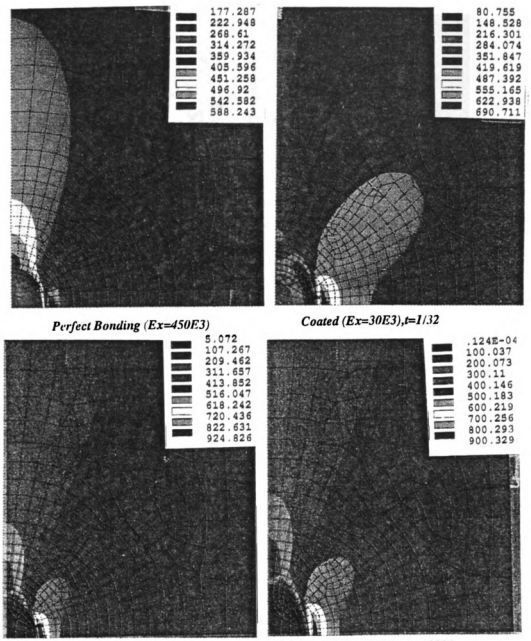

Fig. 2.4b σ_{eff}/σ_o of a single copper inclusion embedded in an epoxy matrix with different coating interfaces and subjected to an axial stress of *0.4 ksi* in the vertical direction.

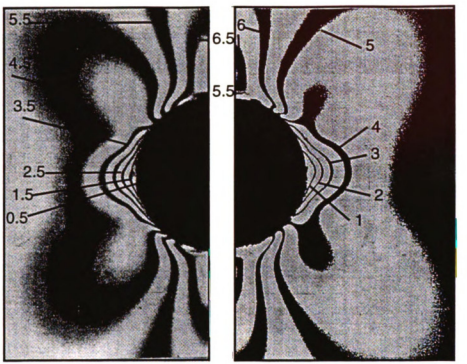

a) Light Field b) Dark Field

Fig. 2.5 Isochromatic fringe patterns in an epoxy matrix around a circular perfectly bonded copper inclusion for an applied uniaxial stress of 1.75 ksi in the vertical direction.

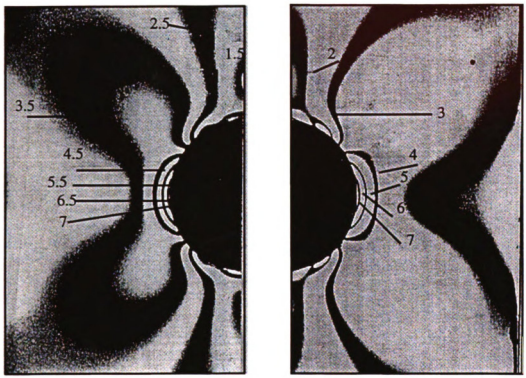

a) Light Field b) Dark Field

Fig. 2.6 Isochromatic fringe patterns in an epoxy matrix around a circular coated inclusion of coating 1 for an applied uniaxial stress of 1 ksi in the vertical direction.

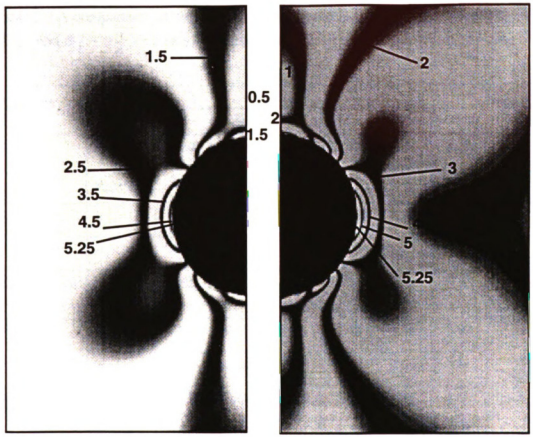

a) Light Field b) Dark Field

Fig. 2.7 Isochromatic fringe patterns in an epoxy matrix around a circular coated inclusion of coating 2 for an applied uniaxial stress of 1 ksi in the vertical direction.

Table 2.3 A comparison between experimental, numerical and analytical results for σ_{eff} and $\sigma_1 - \sigma_2$ for a single inclusion case and a unit uniaxial applied load.

Analysis Type		E^c (ksi)						Material
		1	30	120	450	9,000	90,000	
FEM	σ_{eff}	2.68	1.98	1.28	1.38	1.37	1.38	Matrix
	$\sigma_1 - \sigma_2$	2.62	1.93	1.19	1.33	1.32	1.35	
Analytical	σ_{eff}	2.96	2.17	1.33	1.40	1.40	1.40	
	$\sigma_1 - \sigma_2$	2.96	2.25	1.45	1.35	1.35	1.35	
Experimental	$\sigma_1 - \sigma_2$	2.85	2.12	N.A.	1.34	N.A.	N.A.	
FEM	σ_{eff}	0.034	0.63	1.13	1.40	1.55	3.92	Coating
	$\sigma_1 - \sigma_2$	0.026	0.50	0.99	1.39	1.50	3.81	
Analytical	σ_{eff}	0.033	0.62	1.13	1.40	1.55	4.64	
	$\sigma_1 - \sigma_2$	0.025	0.50	0.96	1.32	1.61	4.81	
FEM	σ_{eff}	0.040	0.76	1.31	1.47	1.65	1.44	Inclusion
	$\sigma_1 - \sigma_2$	0.037	0.69	1.46	1.46	1.62	1.69	
Analytical	σ_{eff}	0.043	0.78	1.35	1.49	1.69	1.52	
	$\sigma_1 - \sigma_2$	0.047	0.84	1.422	1.50	1.66	1.67	

N.A. Experimental results are not available.

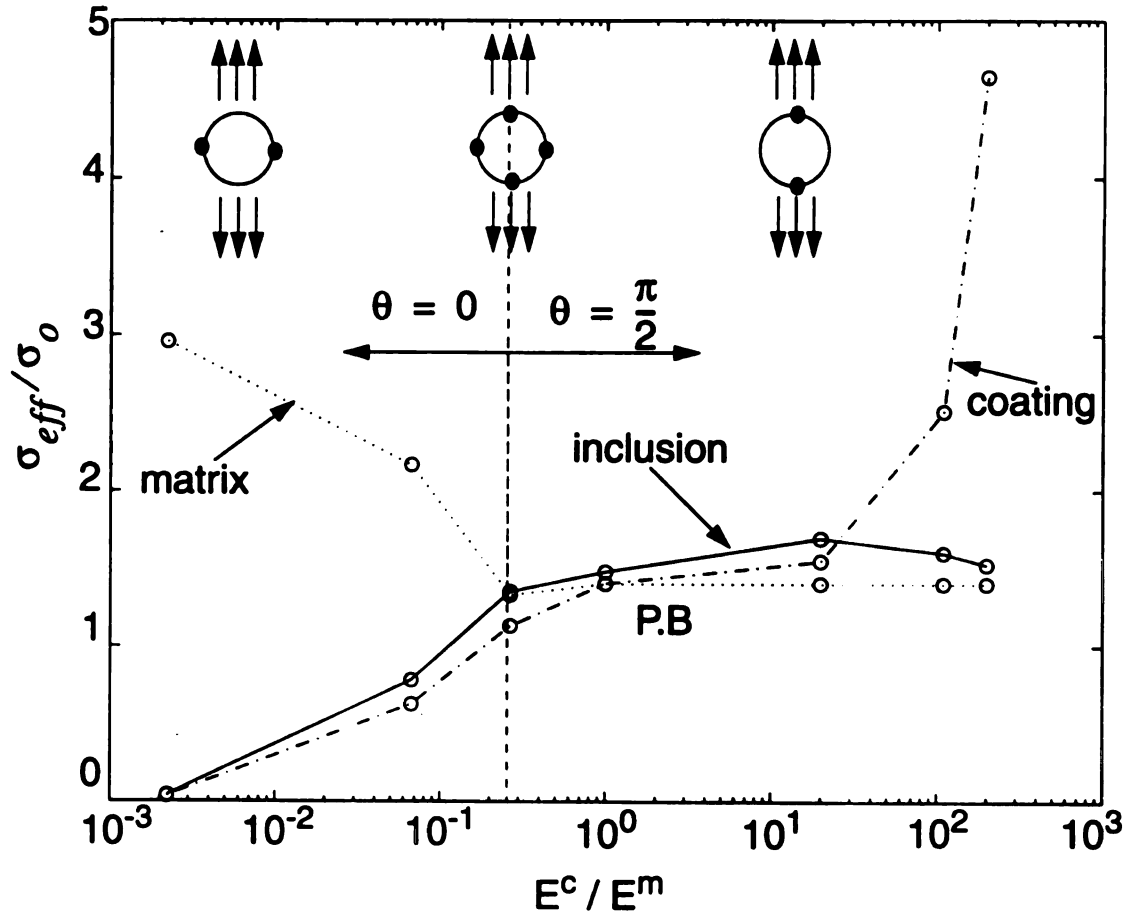

Fig. 2.8 The influence of the coating stiffness E^c on σ_{eff}/σ_o in the matrix, the coating and the inclusion at $r = a+t$.

along the line of action of the applied load ($\theta = \pi/2$). Carman *et al.* (1992) observed that when the hoop stress at $\theta = 0$ and at $\theta = \pi/2$ is equal, then the stress in the matrix is minimum. They refer to this case as the optimum one with respect to stresses. In the case of a compliant coating the maximum stress is located in the matrix, and the inclusion and coating carry almost no load, even though the inclusion is much stiffer. As the value of E^c increases both the coating and the inclusion start carrying the load. In the case of a stiff coating the maximum stress in the composite is located in the coating. Note that when $E^c/E^m > 1$ and the inclusion is stiff the stress field in the matrix remains almost unchanged, as seen in Fig. 2.8

These results are also given in Table 2.4 which summarizes the magnitudes and locations of the maximum stress σ_{eff} and $\sigma_1 - \sigma_2$ in different constituents of the model composite (matrix, coating and inclusion) with a single coated inclusion when $t = 0.25a$. Note that the location of the maximum stress is not necessarily at one of the interfaces. In the matrix the maximum stress is at the coating-matrix interface for a compliant coating, but as the coating stiffness increases, the locations of the maximum stress in the matrix move further away from the interface.

The Multi-inclusion Case

A similar behavior, in terms of the fringe pattern formation, to that observed for a single inclusion case, illustrated in Figs. 2.5-2.7, is seen in the case of a composite with the

Table 2.4 The magnitude and the location of the maximum stress (σ_{eff} and $\sigma_1 - \sigma_2$) for a single inclusion case and a unit uniaxial applied load as obtained analytically.

	Stress	E^c (ksi)						Angle
		1	30	120	450	9,000	90,000	
Matrix	σ_{eff}	0.995 r=1.25 a	1.07 r=1.25 a	1.33 r=1.25 a	1.40 r=1.267a	1.40 r=1.57 a	1.40 r=1.60 a	0°
	$\sigma_1 - \sigma_2$	1.01 r=1.25 a	1.25 r=1.25 a	1.41 r=1.25 a	1.35 r=1.43 a	1.35 r=1.73 a	1.35 r=1.77 a	
	σ_{eff}	2.96 r=1.25 a	2.17 r=1.25 a	1.33 r=1.25	1.00 r=∞	1.00 r=∞	1.00 r=∞	90°
	$\sigma_1 - \sigma_2$	2.96 r=1.25 a	2.25 r=1.25 a	1.45 r=1.25 a	1.00 r=∞	1.00 r=∞	1.00 r=∞	
Coating	σ_{eff}	0.034 r=1.06	0.624 r=1.07 a	1.13 r=1.125	1.40 r=1.25 a	1.55 r=1.25a	1.85 r=a	0°
	$\sigma_1 - \sigma_2$	0.254 r=1.06	0.496 r=1.15 a	0.955 r=1.22 a	1.32 r=1.25 a	1.61 r=1.25 a	2.10 r=a	
	σ_{eff}	0.012 r=1.25 a	0.227 r=1.25 a	0.434 r=1.25	0.663 r=1.25	1.30 r=1.25a	4.64 r=a	90°
	$\sigma_1 - \sigma_2$	0.014 r=1.25	0.256 r=1.25 a	0.503 r=1.25 a	0.736 r=1.25 a	1.31 r=1.25a	4.81 at r= a	
Inclusion	σ_{eff}	0.043	0.782	1.35	1.49	1.69	1.52	0°-90°
		$0 \le r \le a$						
	$\sigma_1 - \sigma_2$	0.047	0.844	1.42	1.50	1.66	1.67	
		$0 \le r \le a$						

23% volume fraction of randomly distributed inclusions (Figs. 2.9a-d). The values of the maximum shear stress (principal stress difference) in the matrix, obtained by the photoelastic method and also using finite element calculations, were compared in Table 2.5 and showed a good agreement. Fig. 2.9a gives the fringe patterns, which denote the contours of the difference in the in-plane principal stresses, $\sigma_1 - \sigma_2$, or the maximum in-plane shear stress, $\tau_{max} = (\sigma_1 - \sigma_2)/2$, for a composite with no coating ($E^c = E^m$) and Fig. 2.9c-d for a composite with a very compliant interphase (coating 1 and coating 2) for the same applied load of $\sigma_o = 492.5$ psi in the horizontal direction. Note that the stress fields in the matrix are very non-uniformly distributed in both cases and the stresses are much higher for compliant interphase cases (Fig. 2.9c-d) as expected. Note that the numbers denote the fringe numbers and the higher the number, the higher the stresses (Dally and Rilly, 1991).

In Figs. 2.10a-c the finite element outputs illustrate the joint effect of random arrangement and interface on σ_{eff} for the same arrangement of inclusions and the corresponding properties as in Figs. 2.9a, c-d. The finite element calculations also included three additional interphase cases given in Table 2 (Figs. 2.10d-f).

We observe that when the interface is very weak (interphase is very compliant - coating 1), then almost no load is transferred from the matrix to the inclusions and it is carried by the matrix (Fig. 2.10b). If the interface is weak (interphase is compliant - coating 2), but yet capable of transferring some loads to the inclusions, then the loads will be car-

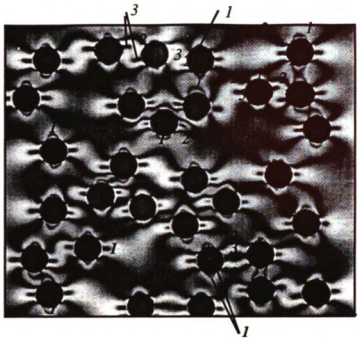

Fig. 2.9-a Isochromatic fringe patterns in an epoxy matrix with randomly distributed and perfectly bonded copper inclusions for an applied stress of $\sigma_0 = 492.3\ psi$ in the horizontal direction when the volume fraction $f = 23\%$.

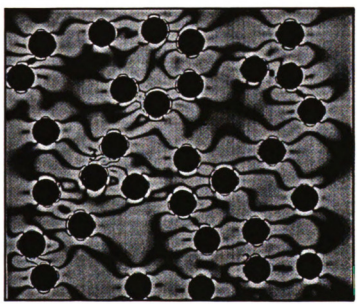

Fig. 2.9-b Isochromatic fringe patterns in an epoxy matrix with randomly distributed copper inclusions with a weak interface bonding for an applied stress of $\sigma_0 = 492.3\ psi$ in the horizontal direction when the volume fraction $f = 23\%$.

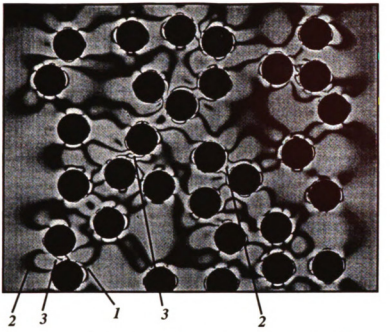

Fig. 2.9-c Isochromatic fringe patterns in an epoxy matrix with randomly distributed copper inclusion coated with coating 2 (E^c = *30 ksi)* for an applied stress of σ_0 = *492.3 psi* in the horizontal direction when f = 23%.

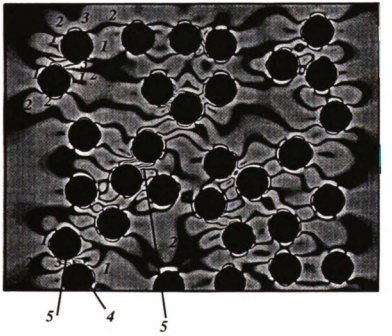

Fig. 2.9-d Isochromatic fringe patterns in an epoxy matrix with randomly distributed copper inclusion coated with coating 1 (E^c = *1 ksi*) for an applied stress of σ_0 = *492.3 psi* in the horizontal direction when f = 23%.

Table 2.5 A comparison between experimental and numerical and results for $(\sigma_1 - \sigma_2)/\sigma_o$ for multi-inclusion cases with volume fraction f = 23%.

	Experimental	FEM
Perfect bond	1.74	1.80
coating 1 $\Gamma^c = 1/450$	5.64	5.17
coating 2 $\Gamma^c = 1/15$	2.63	2.57

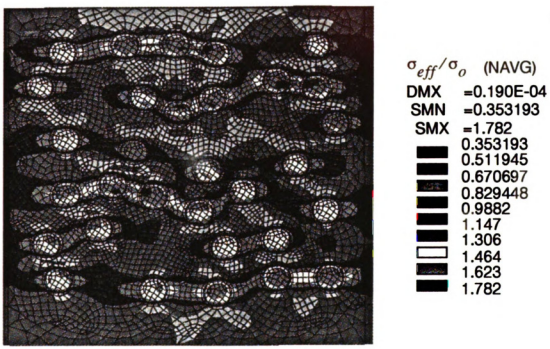

Fig. 2.10a σ_{eff}/σ_o in a model composite with volume fraction f = 23% of randomly distributed and perfectly bonded copper inclusions obtained by FEM for a uniaxial loading in the horizontal direction.

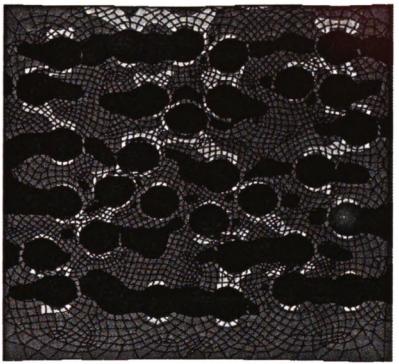

Fig. 2.10b σ_{eff}/σ_o in a model composite with volume fraction f = 23% of randomly distributed and coated inclusions with coating 1 *(E^c = 1 ksi)* obtained by FEM for a uniaxial loading in the horizontal direction.

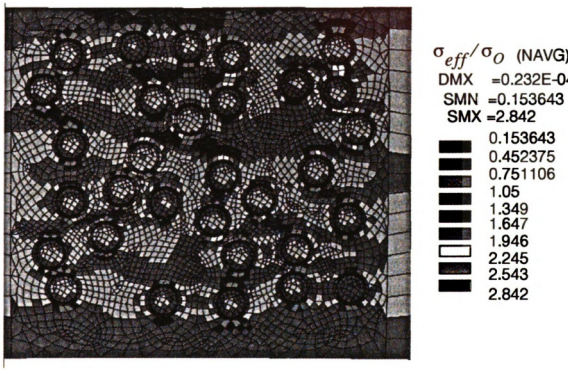

Fig. 2.10c σ_{eff}/σ_o in a model composite with volume fraction f = 23% of randomly distributed and coated inclusions with coating 2 (E^c = *30 ksi)* obtained by FEM for a uniaxial loading in the horizontal direction.

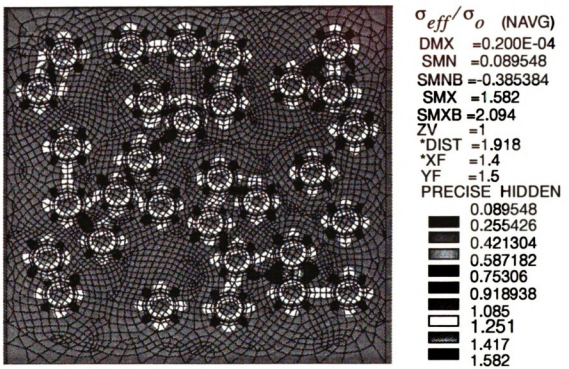

Fig. 2.10d σ_{eff}/σ_o in a model composite with volume fraction f = 23% of randomly distributed and coated inclusions with coating 4 ($E^c = 120$ *ksi*) obtained by FEM for a uniaxial loading in the horizontal direction.

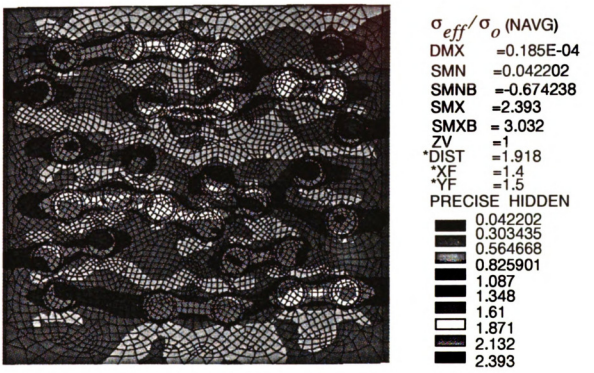

Fig. 2.10e σ_{eff}/σ_o in a model composite with volume fraction f = 23% of randomly distributed and coated inclusions with coating 5 *(E^c= 9000 ksi)* obtained by FEM for a uniaxial loading in the horizontal direction.

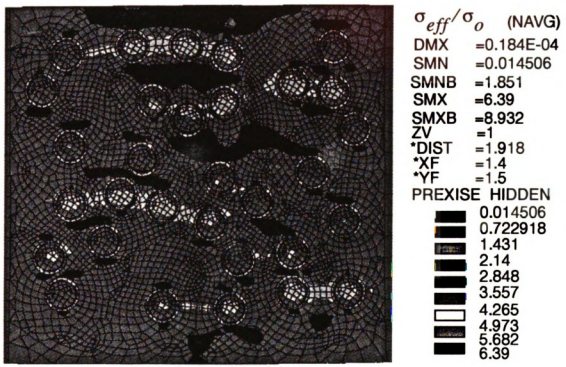

Fig. 2.10f σ_{eff}/σ_o in a model composite with volume fraction f = 23% of randomly distributed and coated inclusions with coating 6 (E^c = *90,000 ksi)* obtained by FEM for a uniaxial loading in the horizontal direction.

ried by both the inclusions and the matrix with the maximum stress occurring in the matrix (Fig. 2.10c). In case of optimum coating (minimum stress condition), the load will be shared almost equally between the matrix, the coating and the inclusion (Fig. 2.10d). If the interphase elastic modulus E^c increases further and a good bond is maintained between interfaces then the load will be carried by the stiff inclusions and the coatings (Fig. 2.10a). But if the coating is very stiff then the highest stress will occur in the coating (Fig. 2.10e-f). Note that a similar behavior, as observed for a single inclusion case and illustrated in Fig. 2.8, is present for the multi-inclusion case discussed here (Fig. 2.11).

In Fig. 2.10a there is bridging of stresses through the inclusions along the line of action of applied load. Inclusions close to each other and aligned in the direction of the load, behave like longitudinal fibers subjected to an axial loading. For inclusions with a compliant interphase, as shown in Fig. 2.10b-c, the maximum stress around each inclusion is located in a plane perpendicular to the applied loading, as was observed in the single inclusion case. A similar behavior occurs in elastic sheets with holes. Fig. 2.10a shows that the load is distributed very unevenly between the inclusions. This is in contrast to periodic arrangements in which inclusions share loads equally. In Fig. 2.10b-c we see a localization of maximum stress in the matrix. For a periodic arrangement this maximum stress would be distributed throughout the composite and be lower in magnitude as shown in Table 2.6. Thus, the non-uniform arrangement leads to stress localization and higher maximum stresses and thus to an earlier initiation of damage, and consequently, to a lower strength.

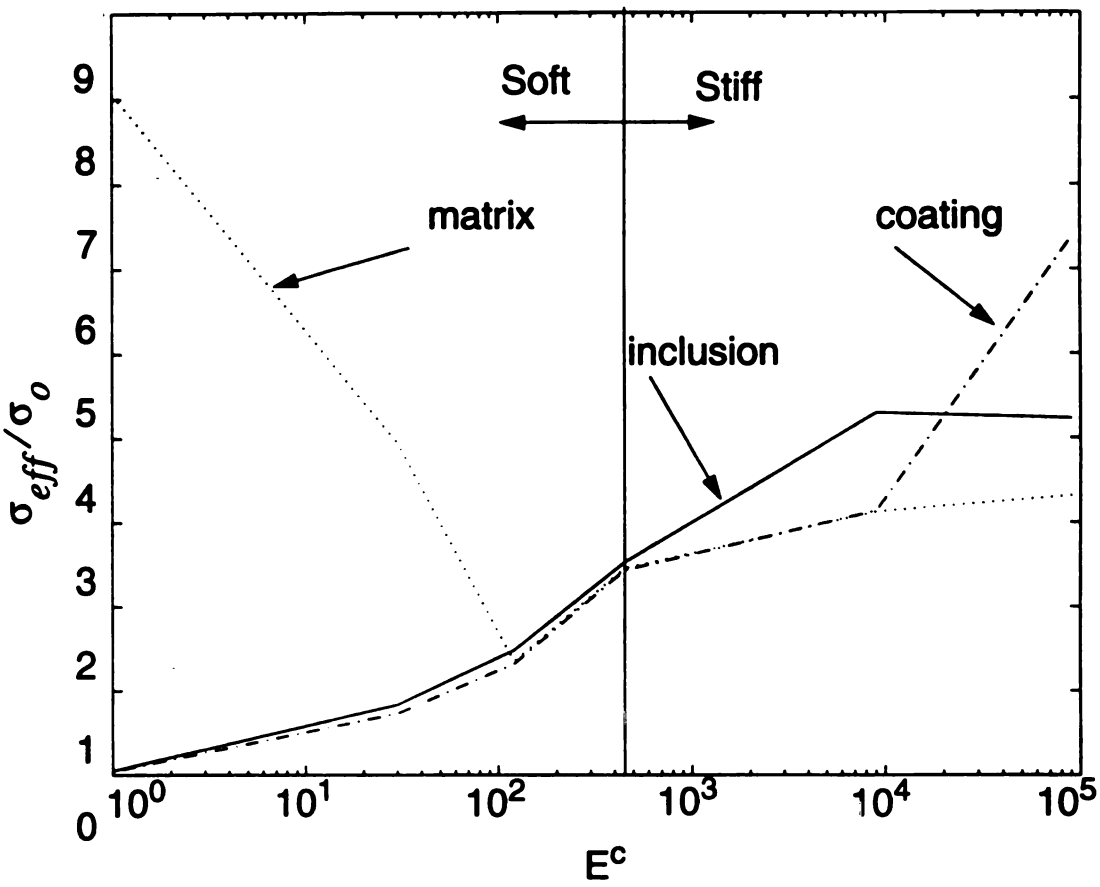

Fig. 2.11 The influence of the coating stiffness E^c on σ_{eff}/σ_o of the matrix, the coating and the inclusion for coated and randomly distributed inclusions case.

Table 2.6 Effect of the arrangement of inclusions on the maximum $(\sigma_1 - \sigma_2)/\sigma_o$ for a multi-inclusion composite as obtained by the FEM.

Arrangement		E^c (ksi)						
		1	30	120	450	9,000	90,000	
Square		3.38	2.29	1.42	2.03	2.47	2.52	Matrix
Triangular		3.10	1.81	1.15	1.32	2.02	2.09	
Random	AVG.	<8.17>	<4.07>	<1.51>	<2.41>	<3.09>	<2.98>	
	STD.	2.45	1.461	0.101	0.112	0.113	0.113	
Two from Random	AVG.	<5.20>	<3.51>	<1.50>	<2.50>	<3.20>	<3.19>	
	STD.	2.25	1.352	0.161	0.164	0.165	0.168	
Two in Effective m.	AVG.	<5.19>	<3.43>	<1.46>	<2.53>	<3.25>	<3.25>	
	STD.	2.04	1.33	0.157	0.160	0.162	0.165	
Square		0.003	0.534	1.24	2.13	2.40	4.07	Coating
Triangular		0.002	0.426	1.20	1.44	2.31	3.86	
Random	AVG.	<0.034>	<0.701>	<1.30>	<2.37>	<3.10>	<6.26>	
	STD.	0.007	0.068	0.104	0.113	1.541	2.32	
Two from Random	AVG.	<0.020>	<0.65>	<1.30>	<2.40>	<3.34>	<6.68>	
	STD.	0.007	0.054	0.055	0.063	1.523	2.24	
Two in Effective m.	AVG.	<0.011>	<0.643>	<1.29>	<2.38>	<3.30>	<6.43>	
	STD.	0.006	0.052	0.054	0.060	1.510	2.21	
Square		0.009	0.693	1.39	2.11	3.40	3.14	Inclusion
Triangular		0.001	0.599	1.26	1.58	2.80	2.62	
Random	AVG.	<0.044>	<0.745>	<1.46>	<2.50>	<4.78>	<4.11>	
	STD.	0.005	0.063	0.089	0.115	1.12	1.01	
Two from Random	AVG.	<0.018>	<0.601>	<1.46>	<2.30>	<5.19>	<4.65>	
	STD.	0.004	0.052	0.061	0.065	1.10	0.981	
Two in Effective m.	AVG.	<0.015>	<0.532>	<1.46>	<2.25>	<5.10>	<4.59>	
	STD.	0.004	0.049	0.054	0.062	0.995	0.976	

These issues were also discussed in detail in Basista and Krajcinovic (1991), Ostoja-Starzewski *et al.* (1994), Becker and Smelser (1994), Pyrz and Bochenek (1994), Pyrz (1994), Brockenbrough *et al.* (1991), Day *et al.* (1992), Snyder *et al.* (1992), Davis *et al.* (1994), Chen *et al.* (1995), and others.

A similar behavior in terms of load carrying mechanisms is observed for the maximum shear stress distribution $\sigma_1 - \sigma_2$ (Fig 2.12a-f and 2.13).

Table 2.6 summarizes the results of maximum $\sigma_1 - \sigma_2$ in the matrix, coating, and inclusions for seven random arrangements and two periodic arrangements (square and triangular). The volume fraction used in these calculations is 23% for both random and periodic arrangements. We also include the results for two isolated inclusions, embedded in an epoxy matrix or in an effective medium. The effective medium properties are determined by using the Mori-Tanaka method (Tong and Jasiuk, 1990). The location of these two inclusions is determined by their geometric arrangement and they have the maximum stress in their vicinity in the multi-inclusion configuration.

Table 2.6 shows that periodic arrangement underestimates the magnitude of the maximum stress present in a real composite where the fiber arrangement is non-uniform. This is due to a locatization of stresses as discussed before. Also, the triangular arrangement gives lower stresses than the square one for the same volume fraction. This is due to the fact that inclusions are further apart in the triangular arrangement for the same volume fraction.

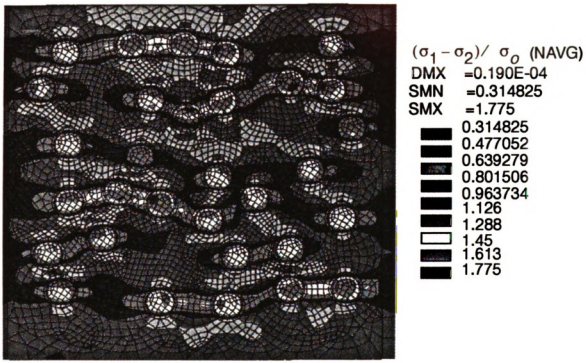

Fig. 2.12a $(\sigma_1 - \sigma_2)/\sigma_o$ in a model composite with volume fraction f = 23% of randomly distributed and perfecly bonded copper inclusions obtained by FEM for a uniaxial loading in the horizontal direction.

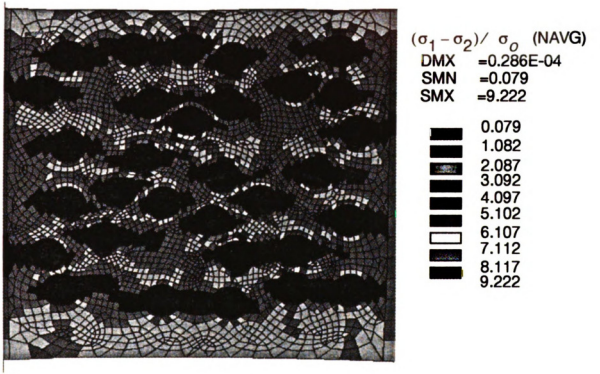

Fig. 2.12b $(\sigma_1 - \sigma_2)/\sigma_o$ in a model composite with volume fraction f = 23% of randomly distributed and coated inclusions with coating 4 *(E^c = 1 ksi)* obtained by FEM for a uniaxial loading in the horizontal direction.

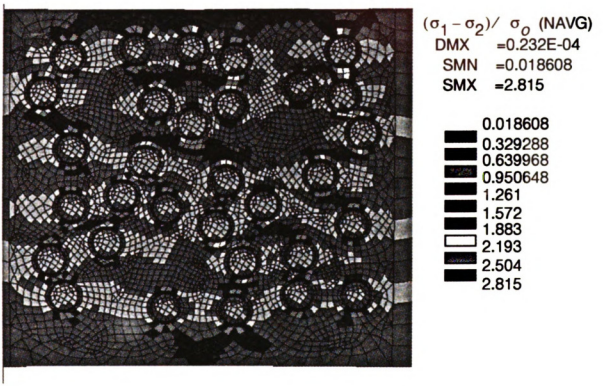

Fig. 2.12c $(\sigma_1 - \sigma_2)/\sigma_o$ in a model composite with volume fraction f = 23% of randomly distributed and coated inclusions with coating 2 *(E^c = 30 ksi)* obtained by FEM for a uniaxial loading in the horizontal direction.

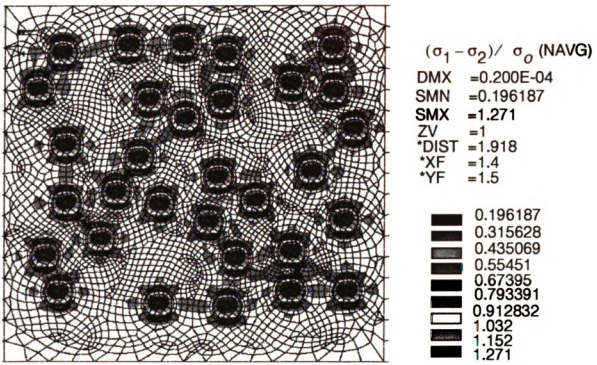

Fig. 2.12d $(\sigma_1 - \sigma_2)/\sigma_o$ in a model composite with volume fraction f = 23% of randomly distributed and coated inclusions with coating 4 (E^c = *120 ksi)* obtained by FEM for a uniaxial loading in the horizontal direction.

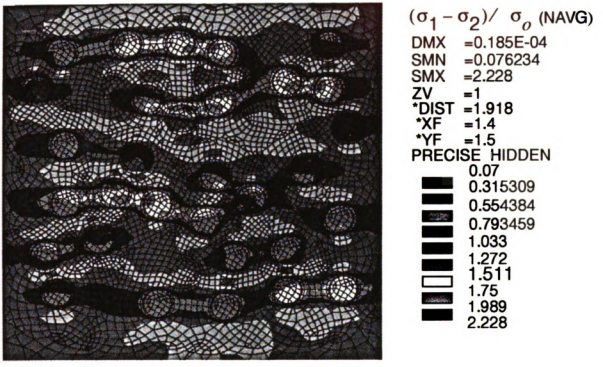

Fig. 2.12e $(\sigma_1 - \sigma_2)/\sigma_o$ in a model composite with volume fraction f = 23% of randomly distributed and coated inclusions with coating 5 *(E^c = 9000 ksi)* obtained by FEM for a uniaxial loading in the horizontal direction.

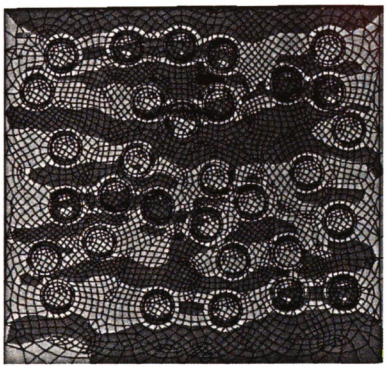

Fig. 2.12f $(\sigma_1 - \sigma_2)/\sigma_o$ in a model composite with volume fraction f = 23% of randomly distributed and coated inclusions with coating 6 (E^c = *90,000 ksi)* obtained by FEM for a uniaxial loading in the horizontal direction.

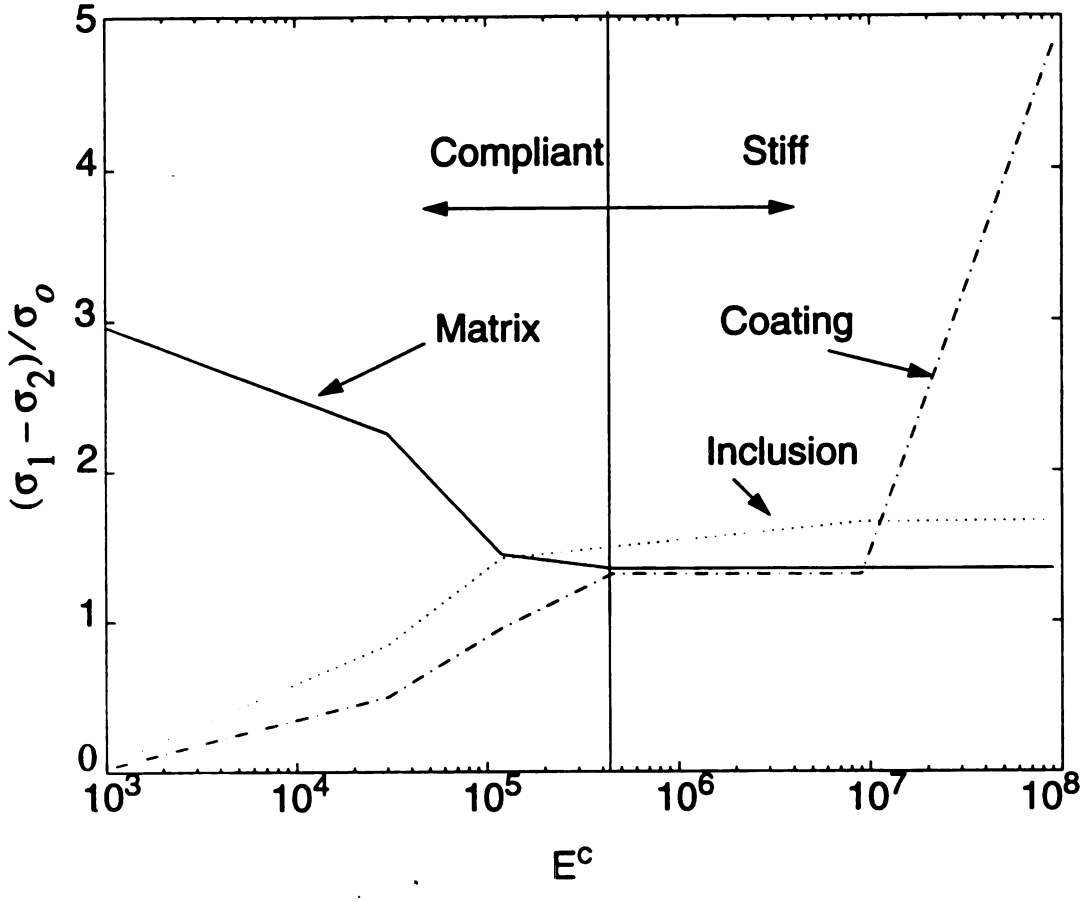

Fig.2.13 Influence of the coating stiffness E^c on $(\sigma_1-\sigma_2)/\sigma_o$ of the matrix, the coating and the inclusion for randomly distributed coated inclusions case.

For cases of compliant coating two inclusions embedded in either the matrix or the effective medium under a uniaxial loading give a lower magnitude of stress than the one in the actual composite, and the stresses are higher for the two inclusions in the matrix as expected because of a higher mismatch in elastic moduli. The opposite behavior is observed for cases of stiff coatings. Also, the maximum stresses in the matrix are highest when the interphase is most compliant. This is expected since in this case the matrix carries most of the load even though the inclusions are much stiffer than the matrix material. Another important observation is that there is a very large scatter in data for compliant coating cases and it decreases as the coating stiffness increases.

Two inclusions

In order to gain an insight into the inclusions' interaction we focus now on a two-inclusion solution. The local stress fields due to two inclusions are a function of the inclination angle between the two inclusions with respect to the applied loading, the separation distance between the two inclusions, and the presence of other inclusions. The angle of inclination θ_{inc} is the angle between the line connecting the centers of two inclusions and the line perpendicular to the applied uniaxial tension. We conduct this study numerically. We compared our numerical calculations for a very compliant coating (which has similar stress fields to those produced in an elastic sheet with holes) and for a perfect bonding case with the analytical solution of Kouris (1993) and found a very good agreement between our finite element and his analytical results (Fig. 2.14).

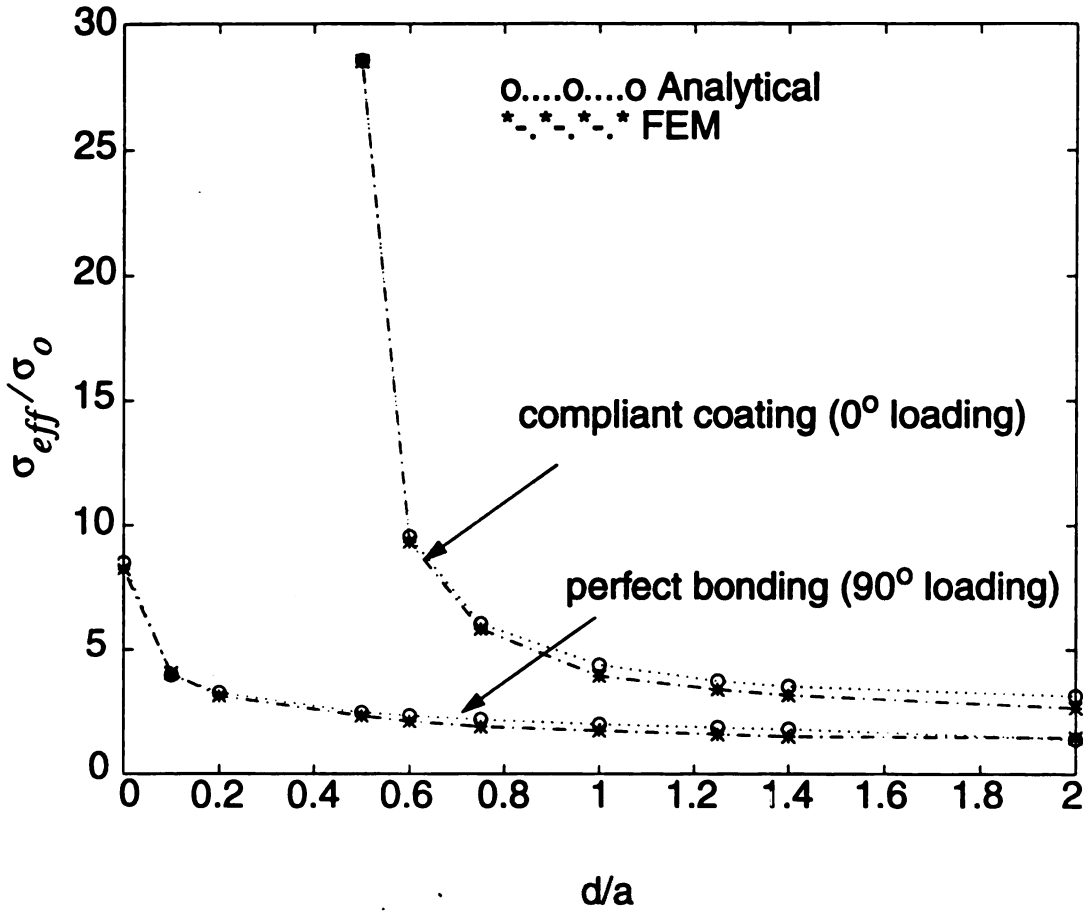

Fig. 2.14 Comparison between analytical (Kouris, 1991) and our numerical (FEM) results of σ_{eff}/σ_o around two inclusions separated by $d=a$.

1) Effect of the inclination angle on the local elastic stress fields

First, we explore the effect of the angle of inclination θ_{inc}. We consider numerically two coated inclusions separated by a constant distance $d = a$ and inclined by the angle θ_{inc}. The influence of the inclination angle on the effective stress σ_{eff} in the matrix, coating, and inclusion is shown in Figs. 2.15-2.17. The location of the maximum σ_{eff}^{m} is at around $\theta = 0$ for cases of compliant coating (when the two inclusions are aligned in a plane perpendicular to the applied loading). For cases of stiffer coatings, the location of the maximum σ_{eff}^{m} is at around $\theta = \pi/2$ (when the two inclusions are aligned along the line of action of the applied loading) as in the case of a single inclusion as discussed before. For the case of an optimum coating the effective stress (σ_{eff}) in the matrix will be the same at any angle of inclination of the two inclusions (Carman *et al.*, 1992). A similar behavior is observed for effective stresses in the coating and the inclusion. So we can define two extreme angles of inclinations: critical and optimum. We denote the critical angle of inclination as the angle which will produce the maximum stress. The optimum angle of inclination is the angle that gives the minimum stress. We are interested in the critical angle, which is for soft coatings at around $\theta = 0$ and for the stiff coatings at around $\theta = \pi/2$.

2) Effect of separation distance between two inclusions.

Next we vary the separation distance between the two coated inclusions inclined at either $\theta = 0$ or $\theta = \pi/2$. Figs. 2.18-2.19 show that increasing the separation distance

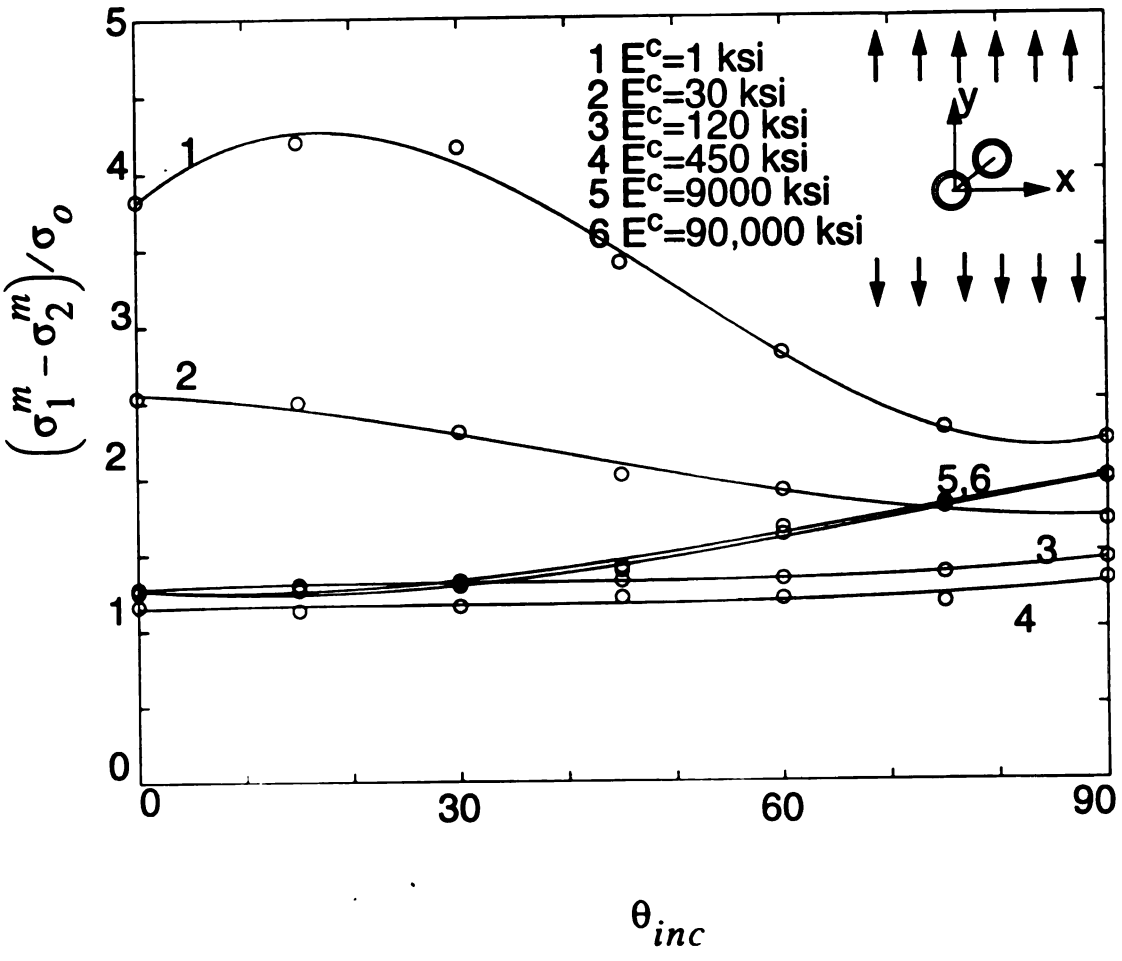

Fig. 2.15 Effect of the inclination angle θ on the maximum shear stress $(\sigma_1 - \sigma_2)/\sigma_o$ in the matrix for a two-inclusions solution.

$$\mathbf{B} \times \left(\overset{\circ}{\mathbf{B}} - \overset{\circ}{\mathbf{B}} \right)$$

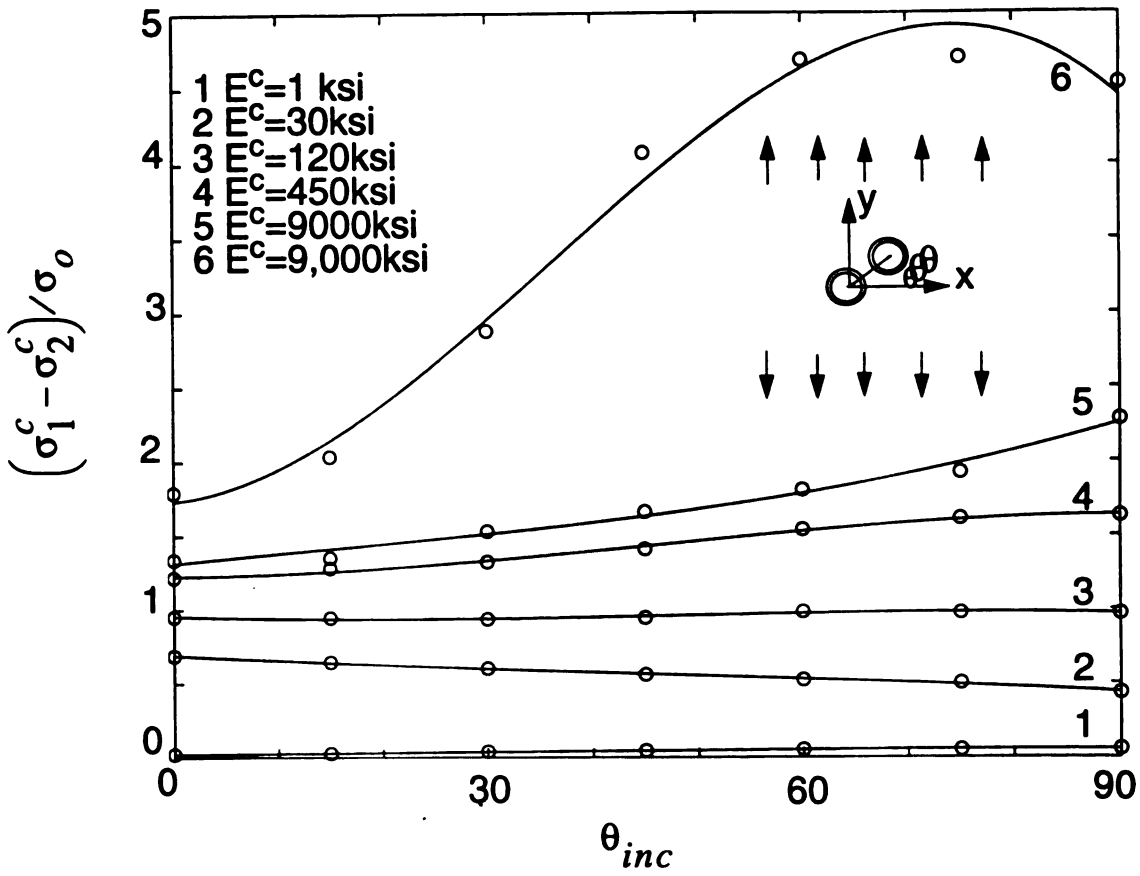

Fig. 2.16 Effect of inclination angle θ on the maximum shear stress $(\sigma_1 - \sigma_2)/\sigma_o$ in the coating for a two-inclusions solution.

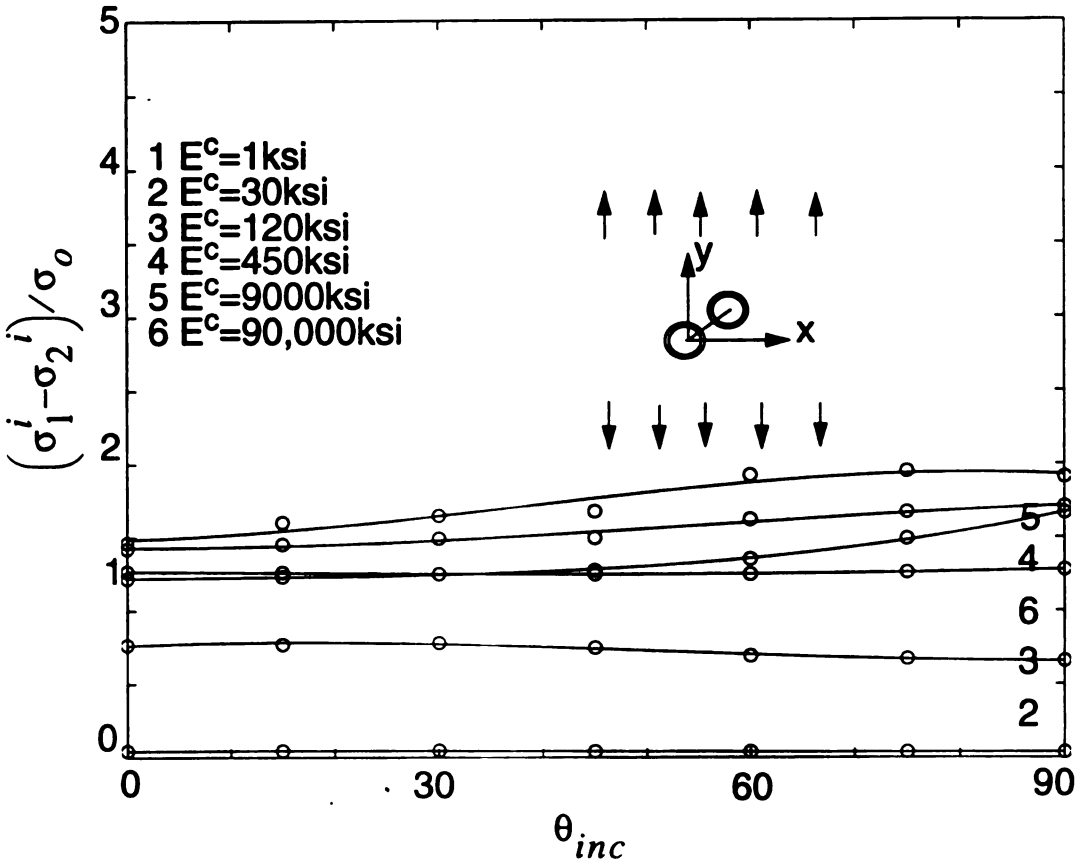

Fig. 2.17 Effect of inclination angle θ on the maximum shear stress $(\sigma_1 - \sigma_2)/\sigma_o$ in the inclusion for two-inclusions solution.

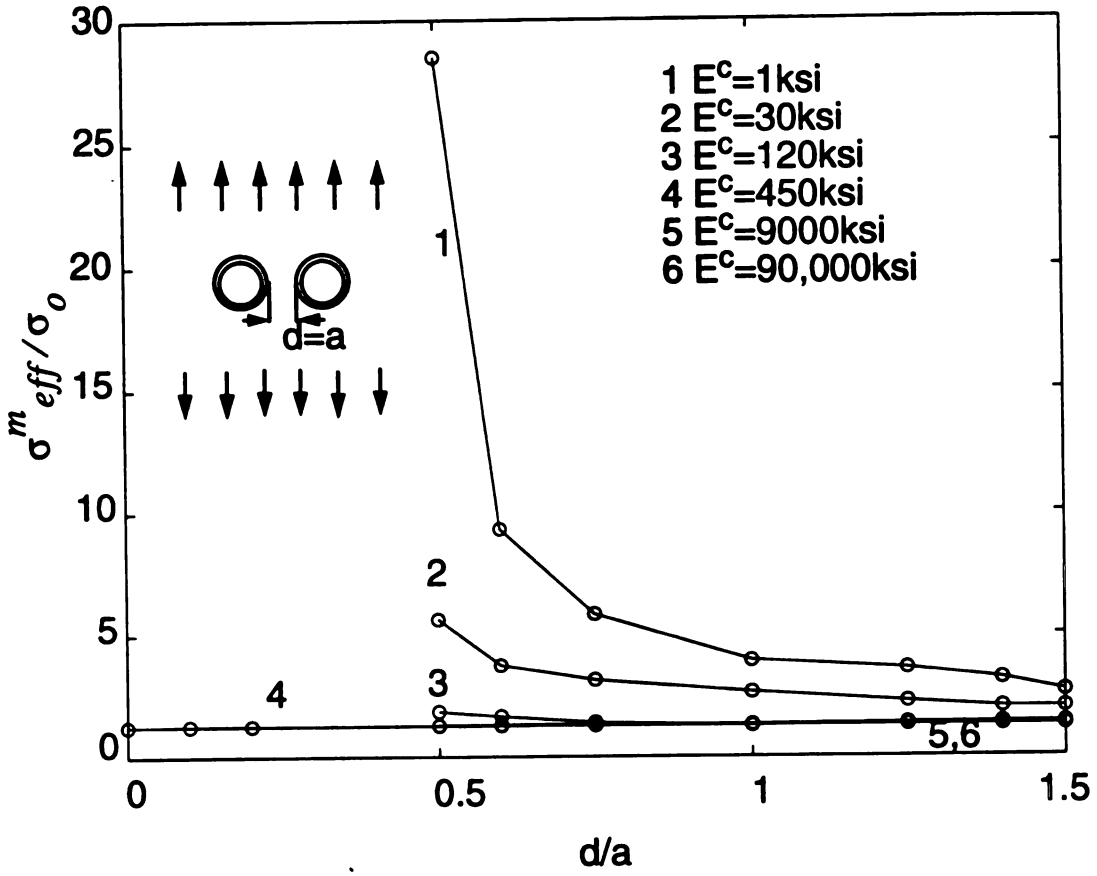

Fig. 2.18 Effect of separation distance between two inclusions on the effective stress in the matrix σ^m_{eff}/σ_o for a uniaxial loading σ_o and $\theta = 0^o$.

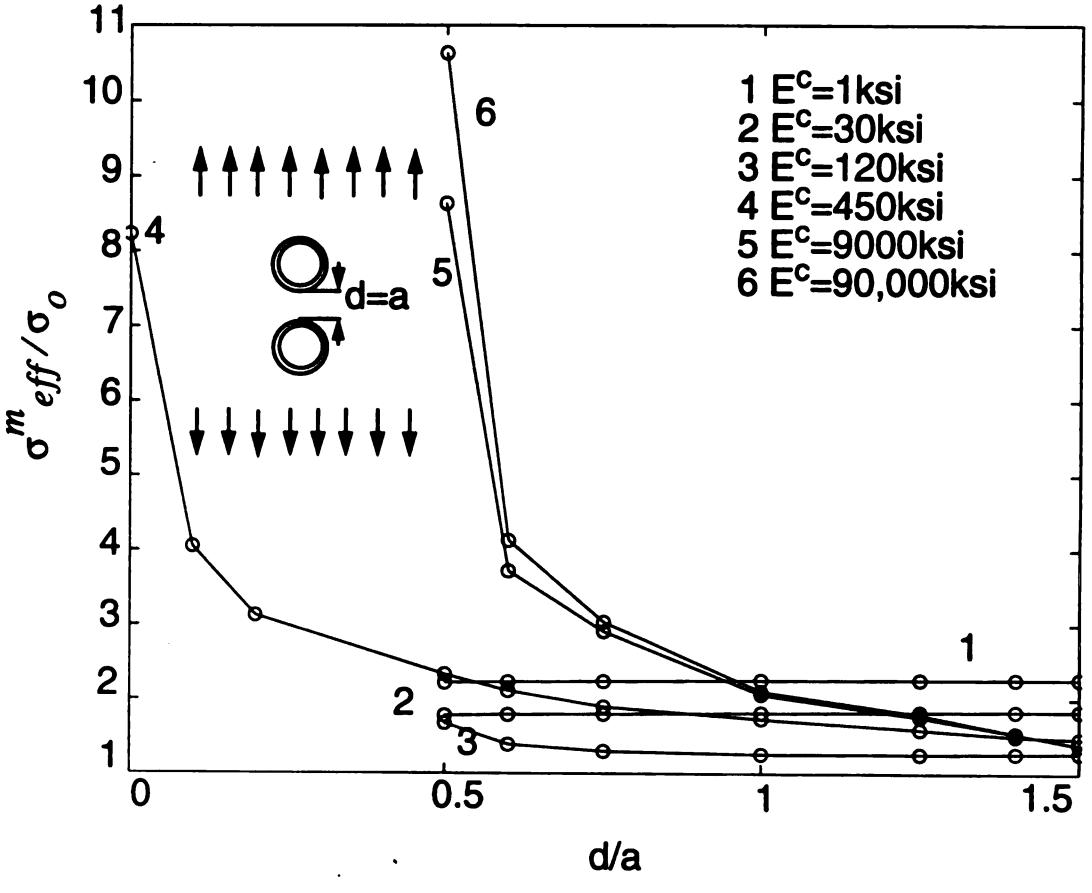

Fig. 2.19 Effect of separation distance between two inclusions on the effective stress in the matrix. $\sigma_{eff}{}^{m}/\sigma_o$ for a uniaxial tension σ_o and $\theta = \pi/2$.

reduces the local effective stress in the matrix, the coating, and the inclusion when the two inclusions are aligned along a critical path. On the other hand, increasing the separation distance will slightly

increase the effective stresses if the two inclusions are aligned along the optimum path.

3) effect of the presence of other inclusions.

Finally, we explore the effect of the presence of more than two inclusions on the stress field. We do so by considering three and four inclusions in a row aligned along a line perpendicular or parallel to the line of loading, which correspond to angles $\theta = 0$ and $\theta = \pi/2$, respectively, and three or four inclusions with their centers forming an equilateral triangle or a square, respectively.

a) effect of number of aligned inclusions along $\theta = 0$ *and* $\theta = \pi/2$.

Figs 2.20-2.21 show that when the inclusions are aligned at the critical angle, then, increasing the number of inclusions increases the effective stress in the matrix. However, if the inclusions are aligned along an optimum path, then, increasing the number of inclusions will decrease the effective stress in the matrix. The effect of inclusion number will decrease as inclusions are added. The similar behavior was observed for stresses in the coating and the inclusion.

b) effect of arrangement.

Three and four inclusions arranged in triangular or square arrangements and separated by a constant distance $d = a$ are studied and compared to the case of two inclusions sepa-

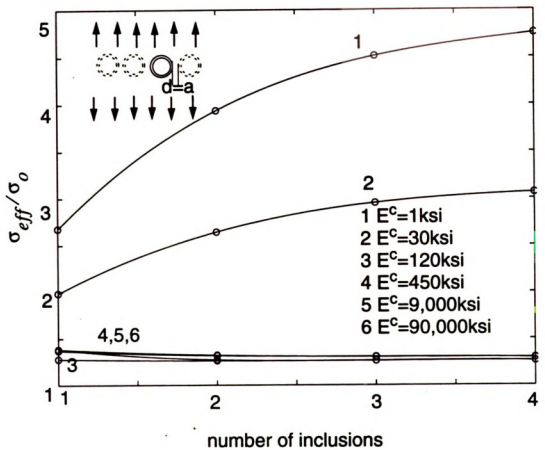

Fig. 2.20 Effect of number of inclusion on the maximum shear stress, $(\sigma_1 - \sigma_2)/\sigma_o$ in the matrix for a uniaxial loading σ_o when $\theta = 0$.

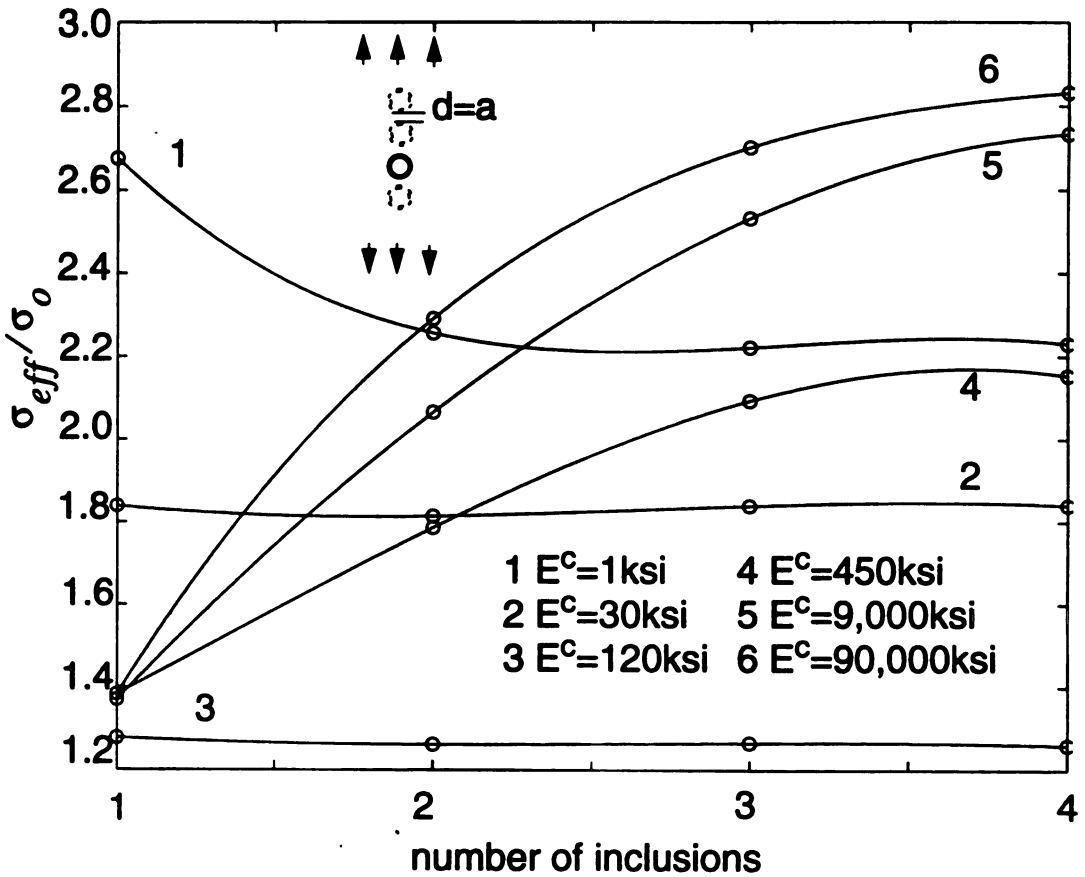

Fig. 2.21 Effect of number of inclusions on the maximum shear stress $(\sigma_1 - \sigma_2)/\sigma_o$ in the matrix for a uniaxial loading σ_o when $\theta = \pi/2$

rated by the same distance and subjected to the same transverse uniaxial loading (Table 2.7). For the four inclusions arrangement the effective stress σ^m_{eff} between any two inclusions is more than σ^m_{eff} between two isolated inclusions inclined along optimum path but slightly less than σ^m_{eff} between two inclusions aligned along critical path. Same behavior was observed for stresses in the coating and the inclusions.

Plane Stress Versus Plane Strain, Other Volume Fractions and Statistics

All our numerical examples are for a plane stress case because experimentally we used thin epoxy plates for the reasons mentioned on page 21. We also explored a comparison between plane stress and plane strain cases numerically and we found that the plane stress case is more critical for both single and multi-inclusions geometries (Figs 2.22a-d) .

We have also considered the case with volume fraction f = 0.46 for the cases of randomly distributed and either perfecly bonded or coated inclusions with compliant coatings (coatings 1 and 2). The magnitudes of the maximum stresses (σ_{eff} and $\sigma_1 - \sigma_2$) were found to be higher for f=0.46 than those for f = 23%. The actual numbers, however, depend on the given geometric arrangement. To study the correlation between geometric distribution of the non-uniformly distributed fibers and the stress fields, Delaunay networks with 10 different distributions are used (Fig. 2.23). Each vertex of the Delaunay cell represents the location of a fiber. Then the probability of inclination angles between each of the neighboring inclusions, $P(\theta)$, (Fig. 2.24), the probability of closest neighbor,

Table 2.7 The maximum effective stress in two, three, and four inclusion arrangement separated by a constant distance for a unit applied loading in the vertical direction.

E^c (ksi)	σ^m_{eff}	σ^c_{eff}	σ^i_{eff}
1	3.94	0.012	0.048
30	2.64	0.377	0.833
120	1.26	1.13	1.36
450	1.27	1.28	1.49
9,000	1.32	1.35	1.75
90,000	1.32	3.01	1.40

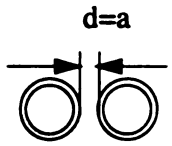

1	2.26	0.012	0.036
30	1.82	0.732	0.726
120	1.26	1.14	1.36
450	1.74	1.70	1.70
9,000	2.07	2.49	1.94
90,000	2.19	4.50	1.74

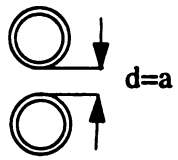

1	3.68	0.011	0.021
30	2.10	0.742	0.883
120	1.28	1.13	1.27
450	1.40	1.45	1.59
9,000	1.59	1.68	1.79
90,000	1.63	3.24	1.64

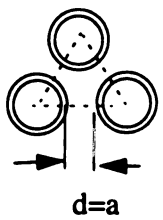

1	3.82	0.041	0.053
30	2.54	0.784	0.915
120	1.28	1.16	1.27
450	1.67	1.62	1.65
9,000	1.98	1.93	1.90
90,000	1.96	4.45	1.72

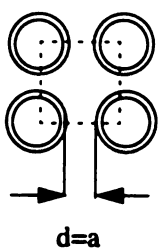

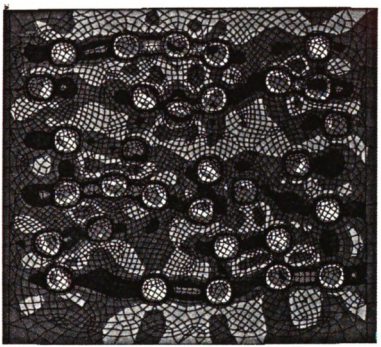

Fig. 2.22a σ_{eff}/σ_o in a model composite with volume fraction f = 23% of randomly distributed and perfectly bonded copper inclusions obtained by FEM (plane strain) for a uniaxial loading in the horizontal direction.

Fig. 2.22b σ_{eff}/σ_o in a model composite with volume fraction f = 23% of randomly distributed and coated inclusions with coating 1 (E^c = *1 ksi)* obtained by FEM (plane strain) for a uniaxial loading in the horizontal direction.

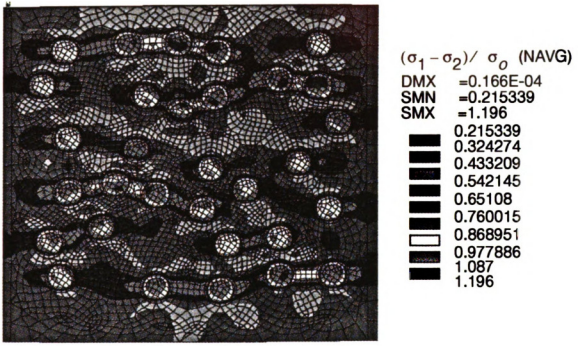

Fig. 2.22c $(\sigma_1 - \sigma_2)/\sigma_o$ in a model composite with volume fraction f = 23% of randomly distributed and perfecly bonded copper inclusions obtained by FEM (plane strain) for a uniaxial loading in the horizontal direction.

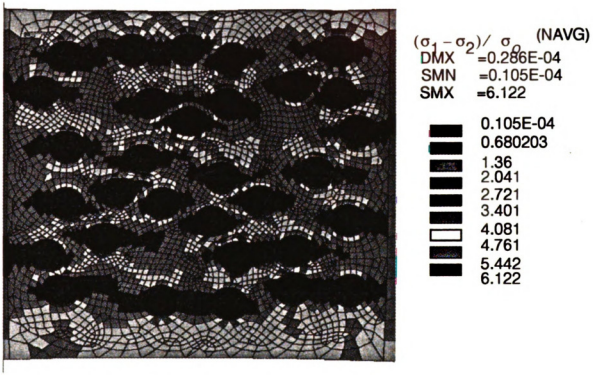

Fig. 2.22d $(\sigma_1 - \sigma_2)/\sigma_o$ in a model composite with volume fraction f = 23% of randomly distributed and coated inclusions with coating 4 *(E^c = 1 ksi)* obtained by FEM (plane strain) for a uniaxial loading in the horizontal direction.

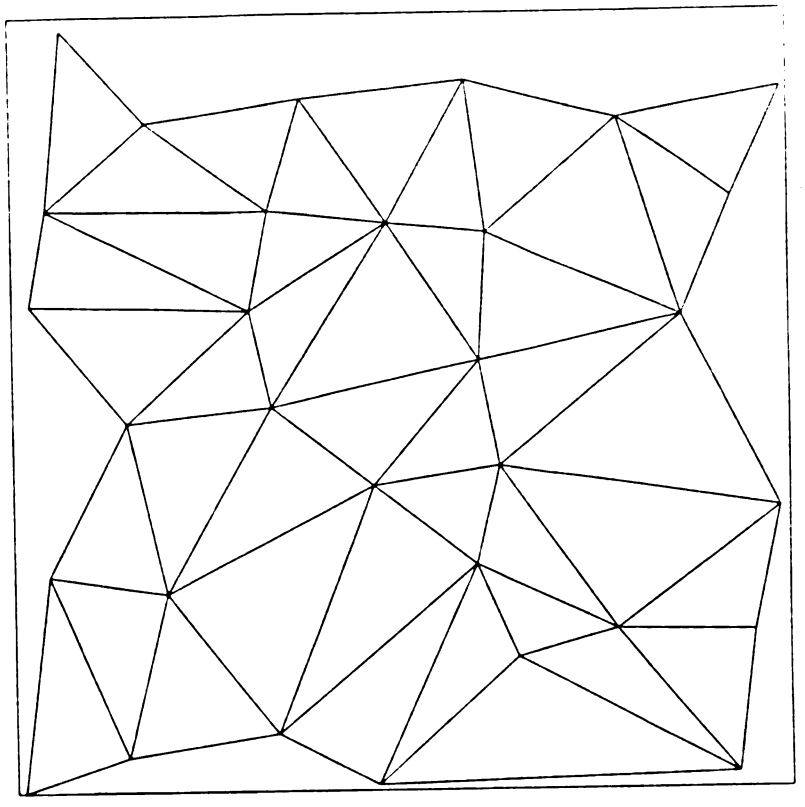

Fig. 2.23 A typical Delaunay network of randomly distributed fibers.

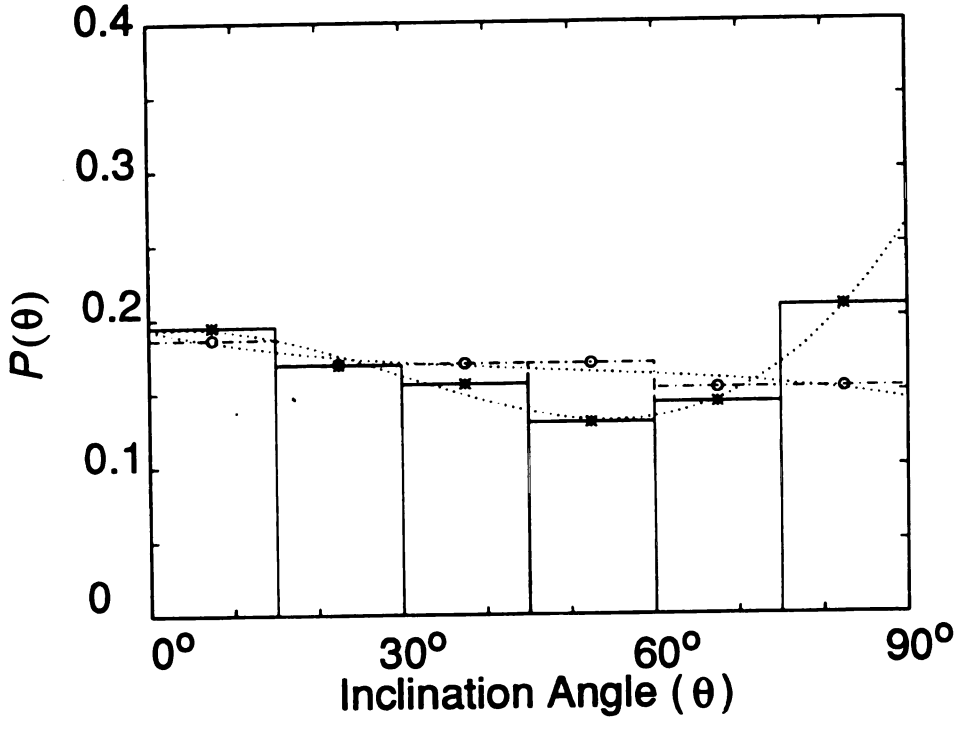

Fig. 2.24 Probability distribution of inclination angle between the closest neighboring inclusions.

P(n), (Fig. 2.25), and the separation distance, P(d), (Fig. 2.26) were studied. Since we have a finite medium bounded by the size of the specimen, then our results will be limited to the given geometry of the tested sample. Note that if we ignore the edge lines (effect of discontinuity of the model) then $P(\theta)$ will have a constant value (dashed line). Thus for the random arrangement, with restrictions of non-overlapping, we have no preferential angle, as expected.

CLOSURE

In this phase of the study we investigated the influence of the inclusion-matrix interface and the geometric arrangement on the local stress fields of a model composite having circular copper inclusions in the photoelastic matrix. We find that both of these factors significantly contribute to the local stress fields. We note that the study of the effects of geometric arrangement of inclusions requires a more complete statistical analysis. a more complete discussion of the results from this chapter is included in the conclusions section on pages 244-247.

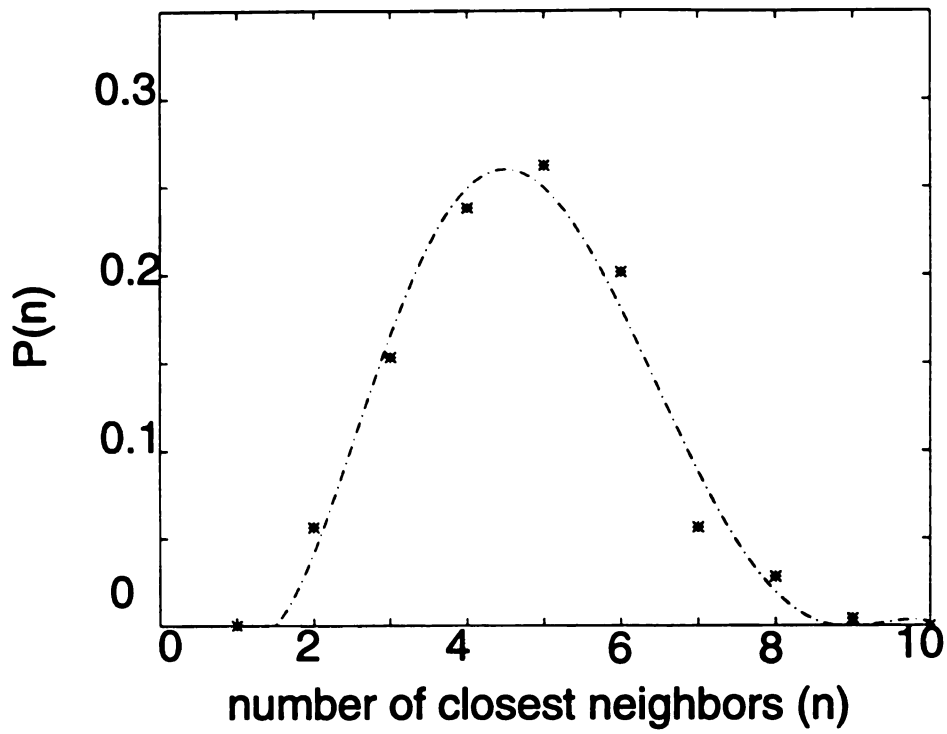

Fig. 2.25 Probability distribution of the number of closest neighboring inclusions.

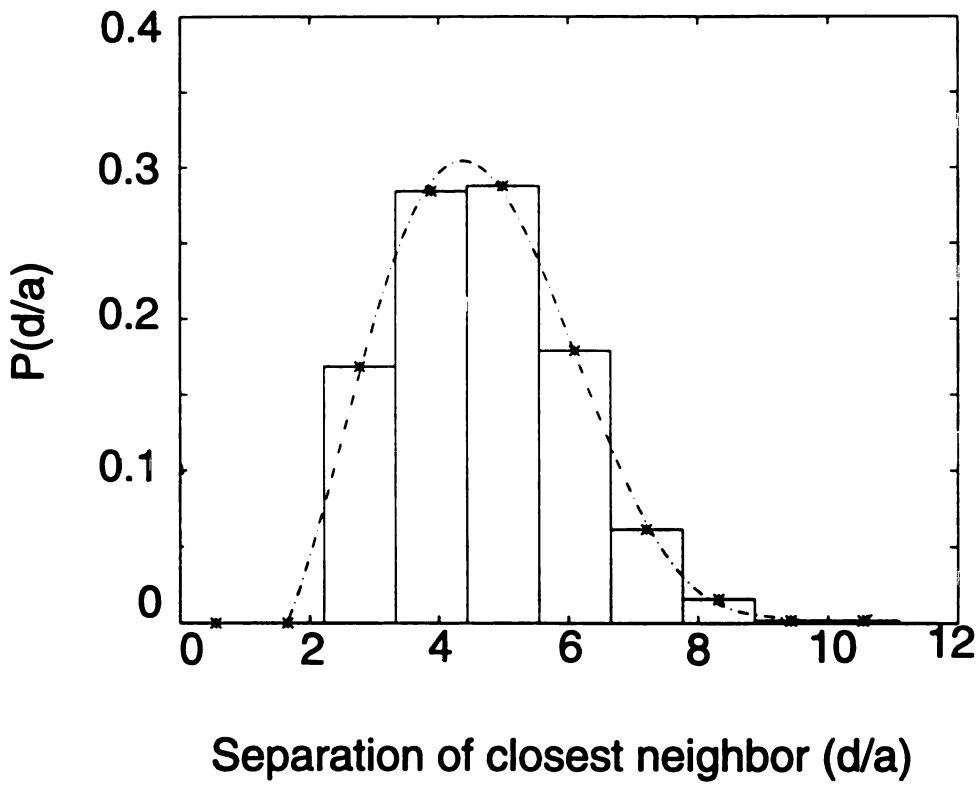

Fig. 2.26 Probability distribution of the separation distance between the closest neighboring inclusions.

CHAPTER 3

TASK 2: THE INFLUENCE OF INTERFACE AND RANDOM ARRANGEMENT OF INCLUSIONS ON THE RESIDUAL STRESSES IN A MODEL COMPOSITE MATERIAL

When a composite material is subjected to a temperature change, thermal stresses are created due to a mismatch in thermal expansion coefficients. The temperature change may be due to thermal cooling of a composite material after being manufactured at an elevated temperature; such stresses are called residual stresses. These thermal stresses cause stress concentrations, which may initiate yielding and / or cracking. Therefore, for design purposes it is important to know the magnitude of these stresses.

In this phase of study we analyse the local stress field in a model composite made of an epoxy matrix and coated copper inclusions. We study such a composite experimentally using a photoelastic technique and numerically using a finite element method. Experimentally we focus on studying the stress distributions around cast-in-place copper inclusions in either random or regular arrangement (triangular). More specifically we consider two random arrangements, one periodic arrangement, two inclusions separated by different separation distances, and a single inclusion configuration. Numerically, we study the local stress fields by considering two random arrangements and two periodic arrangements (triangular and square) of coated copper inclusions. In this case we vary both the elastic modulus of the coating E^c and the coefficient of thermal expansion (CTE) of the coating α^c.

THE SINGLE INCLUSION SOLUTION

Initially, we consider a single coated inclusion solution in order to gain a more basic understanding of the problem and we discuss the influence of different parameters on the thermal stress field in a composite with a dilute concentration of fibers.

We consider a three phase composite material consisting of a circular inclusion of radius a coated with a material of thickness t and embedded in an infinitely extended matrix. The inclusion, the coating layer and the matrix are assumed to be linearly elastic and isotropic. They have distinct material properties: the elastic modulus E, the Poisson's ratio ν and the coefficient of thermal expansion (CTE) α. In the notation used the super-scripts i, c, and m refer to the inclusion, coating and matrix, respectively.

When the above composite is subjected to a uniform temperature change ΔT, then the displacement and stress fields in polar coordinates (r, θ) are:

a) in the inclusion

$$\begin{aligned} u_r^i &= (\kappa^i - 1) rA/2\mu^i + U_r^i \\ \sigma_{rr}^i &= \sigma_{\theta\theta}^i = 2A \end{aligned} \tag{3.1}$$

b) in the coating

$$\begin{aligned} u_r^c &= C(\kappa^c - 1) r/2\mu^c - D/2\mu^c r + U_r^c \\ \sigma_{rr}^c &= 2C + D/r^2 \\ \sigma_{\theta\theta}^c &= 2C - D/r^2 \end{aligned} \tag{3.2}$$

c) in the matrix

$$u_r^m = -B/2r\mu^m + U_r^m$$
$$\sigma_{rr}^m = -\sigma_{\theta\theta}^m = B/r^2 \tag{3.3}$$

where

$$\kappa^s = \begin{cases} (3-\nu^s)/(1+\nu^s) & plane\ stress \\ 3-4\nu^s & plane\ strain \end{cases} \qquad s = i, c, m \tag{3.4}$$

The other displacement and stress components are zero due to a radial symmetry.

Note that the radial displacements in the constituents are the sums of the deformation due to thermal strain in the absence of the remaining components as given by

$$U_r^s = (1+\eta^s)\alpha^s \Delta T r \qquad s = i, c, m \tag{3.5}$$

where

$$\eta = \begin{cases} \nu & plane\ strain \\ 0 & plane\ stress \end{cases} \tag{3.6}$$

and the deformation due to elastic strains. A,B,C and D are the unknown constants to be determined using the boundary conditions. We assume perfect bonding boundary conditions at the inclusion-coating and coating-matrix interfaces, which are given as follows

$$\begin{aligned} \sigma_{rr}^i = \sigma_{rr}^c \qquad u_r^i = u_r^c \qquad & at\ r = a \\ \sigma_{rr}^c = \sigma_{rr}^m \qquad u_r^c = u_r^m \qquad & at\ r = a+t \\ \sigma_{rr}^m = 0 \qquad & at\ r \to \infty \end{aligned} \tag{3.7}$$

Note, that stresses in the matrix are chosen in such a way so that the condition of van-

ishing tractions at infinity is automatically satisfied.

THE MULTI INCLUSIONS SOLUTION

While finding local stress fields of a composite with a single inclusion is relatively simple, determining the local stress fields of a composite with many inclusions, where the interaction of inclusions' takes place, is very complicated to do analytically. Thus, alternatively, experimental and numerical techniques can be used.

Experimental Procedure

Sample Preparation

The epoxy resin used was Epon 828 which is based in diglycidyl ether of Bisphenol-A and has the following chemical structure (Gupta *et al.* 1985)

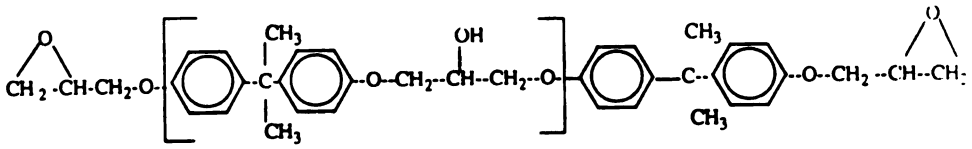

The curing agent used was metaphenylene diamine having the following chemical structure

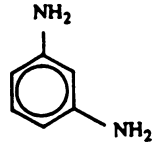

The curing agent concentration was calculated by Gupta *et al.* (1985) to be 14.5 parts per hundred parts of resin so that the epoxy amine ratio is 1:1.

To prepare the epoxy matrix, the resin and the curing agent were heated in separate containers at 75^0C for approximately 15 minutes (until the curing agent melted), then they were mixed together. The mixture was then vacuum-gassed. Next, the epoxy resin mixture was poured into silicone rubber models to form 1.6x3.5x0.125 inch rectangular specimens or dogbone standard shape control specimens. Inclusions were placed at least a distance of one diameter away from the free surface to minimize the free surface effect (Lee *et al.* 1992). The model epoxy-copper composite was then cured in a pre-programed oven. The curing cycle used was 75^0C (167 ^{o}F) for two hours followed by 125^{o}C (257 ^{o}F) for another two hours, then the composite was either heated to 160^{o}C (320 ^{o}F) ,which is the glass transition temperature for this epoxy, held for two hours and then cooled to room temperature at slow cooling at rate of 2.5^{o}C (5^0F)/hour (post curing), or cooled directly to room temperature without post curing (standard curing).

Mechanical Properties of Epoxy Matrix

To study the temperature dependence of various mechanical properties of the epoxy resin three sets of experiments were conducted. In the first set, the tensile tester (MTS) was used. Using a small environmental chamber, the stress-strain data and the axial-transverse strain data were recorded for 55^{o}C and 85^0C at a strain rate of 7%. The average results of three specimens for each case were used to find the elastic modulus and the Poisson's ratio for both post and standard curing conditions.

In the second set of experiments, Instron tensile measurements were used to find the mechanical properties of the epoxy matrix at room temperature. The laser extensometer was used to measure strain. Stress-strain curves of epoxy matrix for various temperatures

and for the two cooling conditions are plotted in Figures 3.1a and 3.1b. The dashed curve in Figure 3.1a was obtained by Gupta *et al.* (1985). Using a regression analysis, the variation of the elastic modulus of the epoxy matrix as a function of temperature T is given by

$$E^m(T) = 6.2974\,(10)^5 - 6.7798\,(10)^3 T + 49.7354 T^2 - 0.157799 T^3 \; psi \qquad (3.8)$$

This variation of elastic modulus with temperature is represented in Fig. 3.2 . The effect of temperature on the Poisson's ratio of the matrix is shown in Figure 3.3 and has the following form

$$\nu^m(T) = 0.2704417 + 0.00368067T - 1.335529\,T^2 - 4.26119 T^3 \qquad (3.9)$$

In the third set of experiments, the variation of thermal expansion with temperature was used to calculate the coefficient of thermal expansion (CTE) of the epoxy-matrix, coating materials and copper inclusions.

Deformation of epoxy, coating and inclusion samples as a function of temperature is plotted in Figures 3.4 through 3.7. The derivative of those curves will give a variation of thermal coefficients of expansion with temperature which are found using regression analysis

$$\alpha^m(T) = 2.91\,(10)^{-5} - 4.59\,(10)^{-6}T + 3.11\,(10)^{-7}T^2 - 1.18\,(10)^{-8}T^3 + 2.78\,(10)^{-10}T^4 - 4.21\,(10)^{-2}T^5 + 4.10\,(10)^{-14}T^6 - 2.48\,(10)^{-16}T^7 + 8.49\,(10)^{-19}T^8 - 1.25\,(10)^{-21}T^9 \; {}^{o}C \qquad (3.10)$$

Similar expressions were obtained for the coatings and the inclusion.

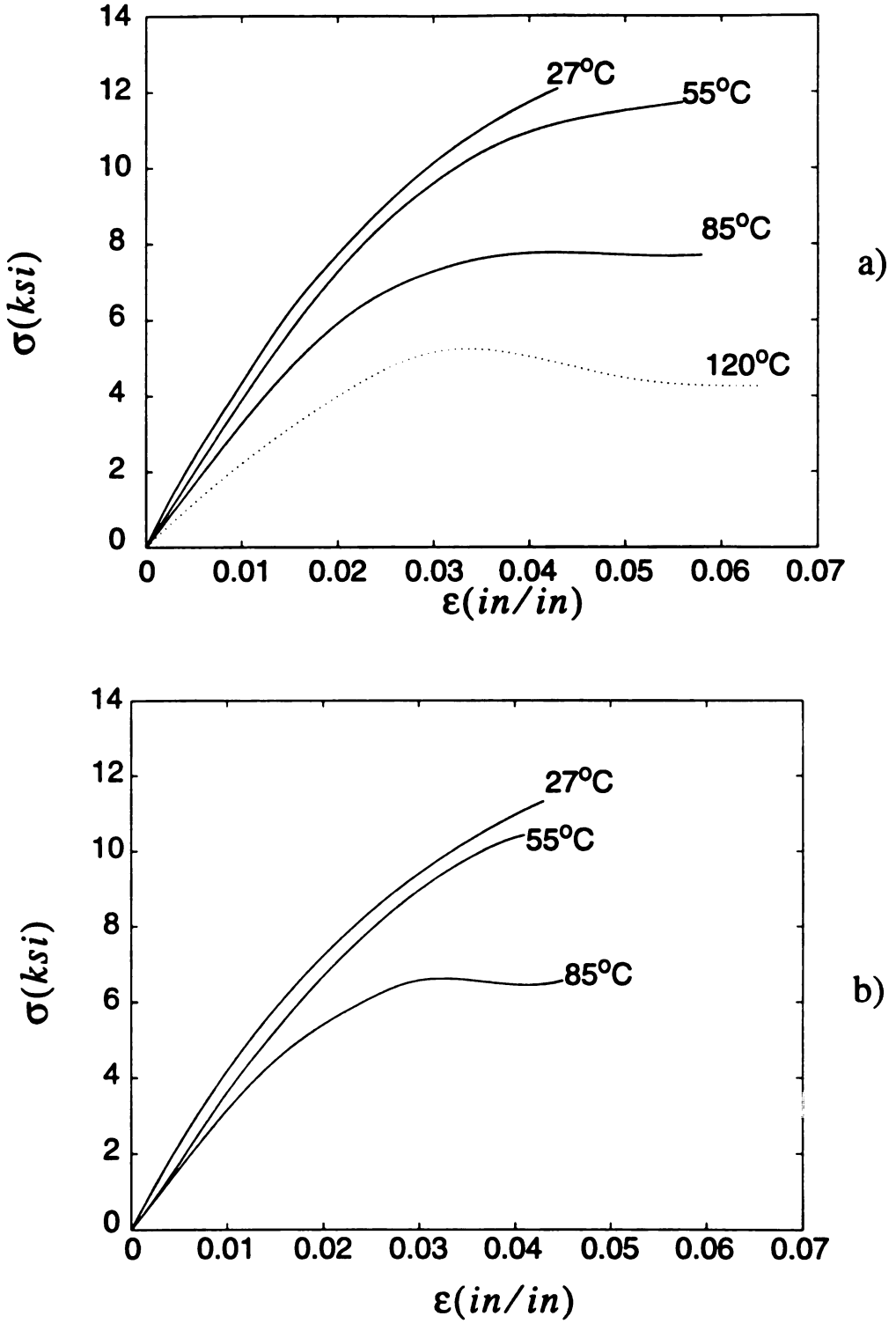

Fig. 3.1 Stress-strain curves of epoxy matrix (Epon 828) for various temperatures and for the two cooling conditions: a) standard curing and b) post curing.

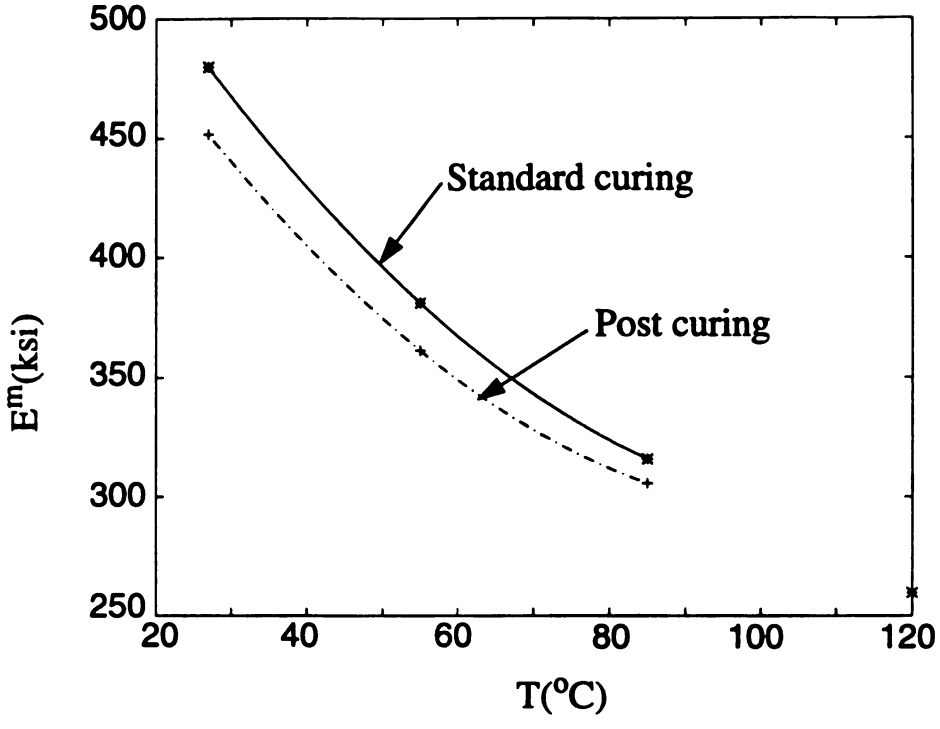

Fig. 3.2 Effect of temperature on the elastic Young's modulus of the epoxy matrix (E^m)

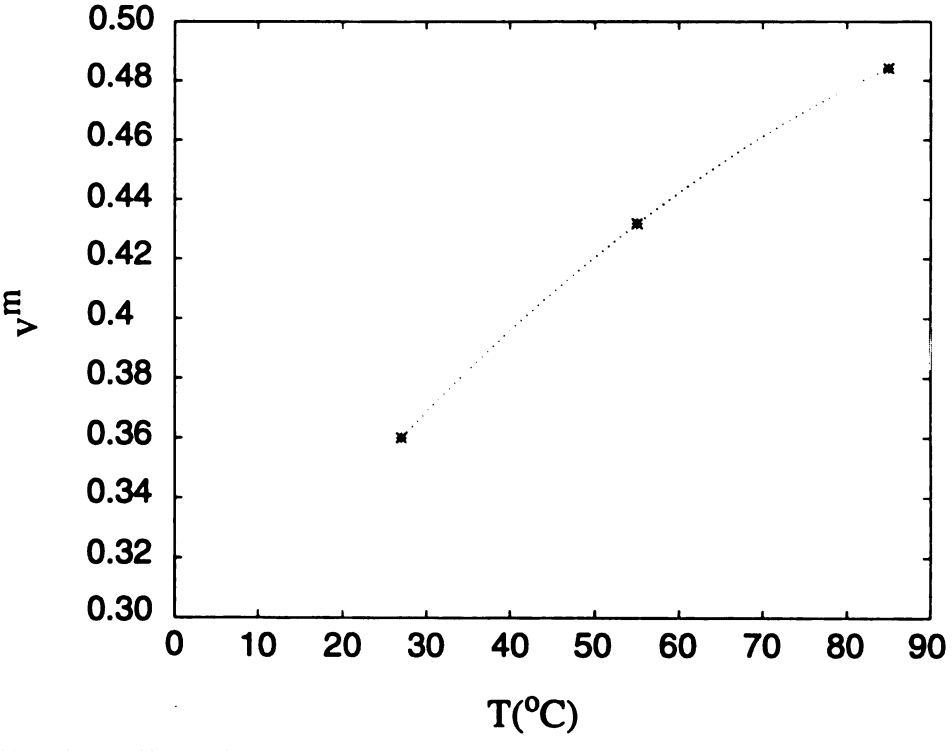

Fig. 3.3 Effect of temperature on the Poisson's ratio of the epoxy matrix (ν^m).

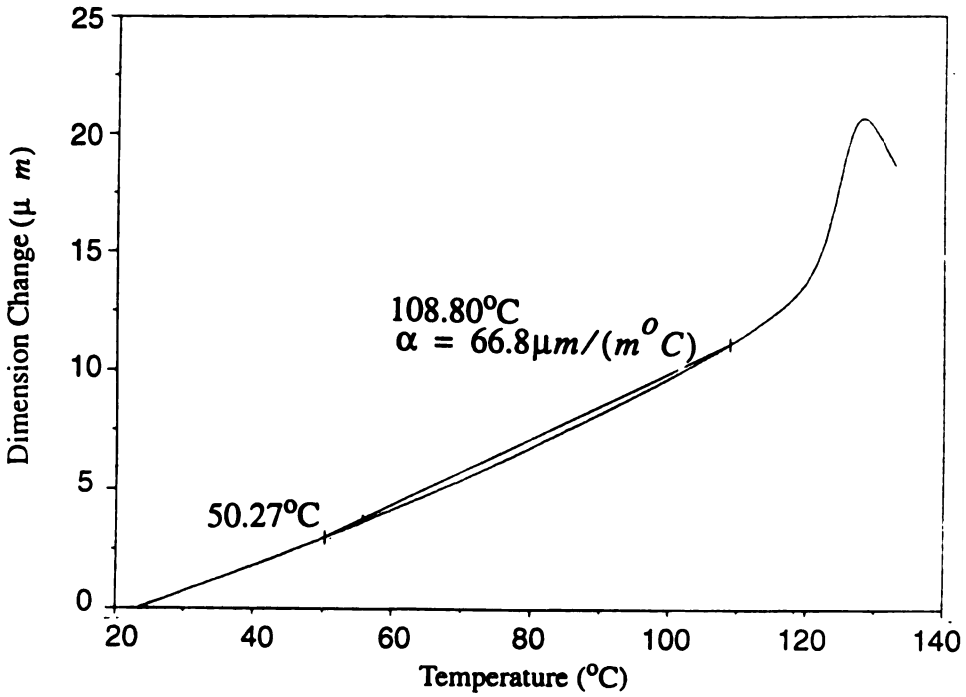

Fig. 3.4 Effect of temperature on the deformation of the epoxy matrix.

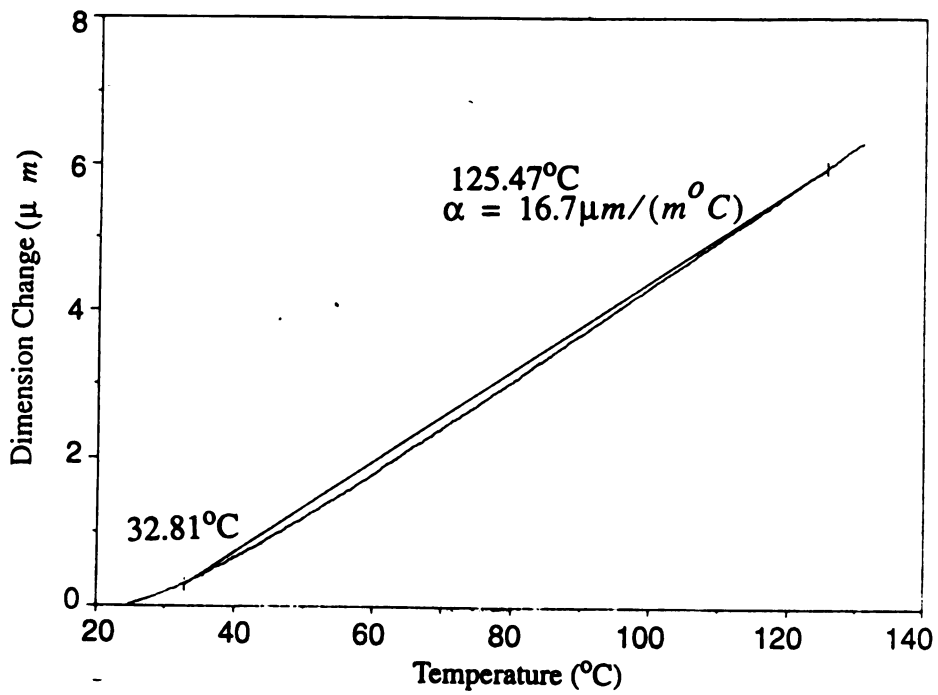

Fig. 3.5 Effect of temperature on the deformation of copper inclusions.

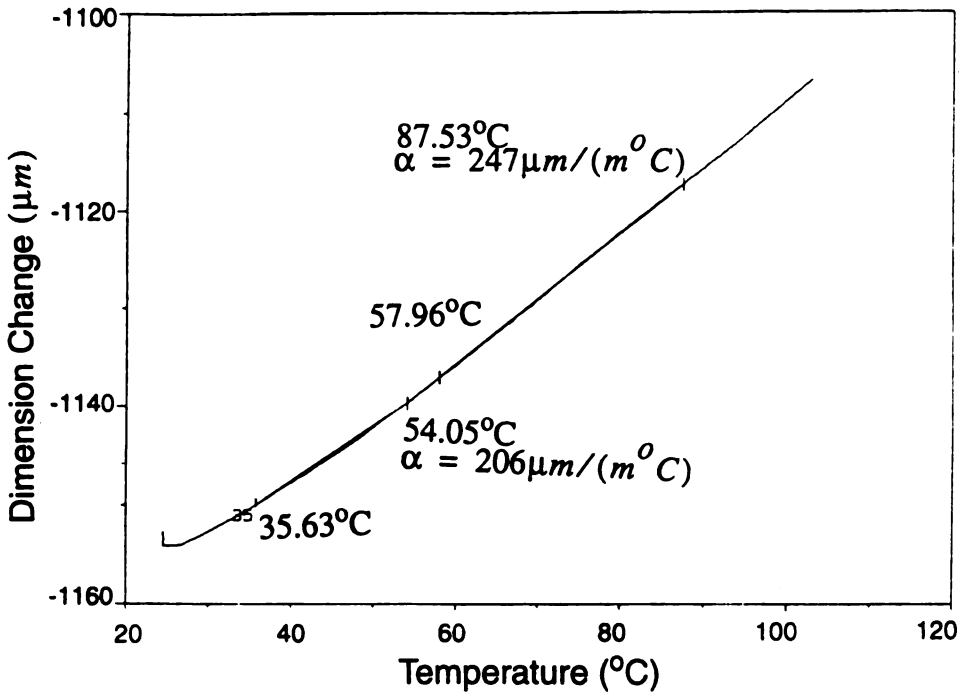

Fig. 3.6 Effect of temperature on the deformation of coating 1.

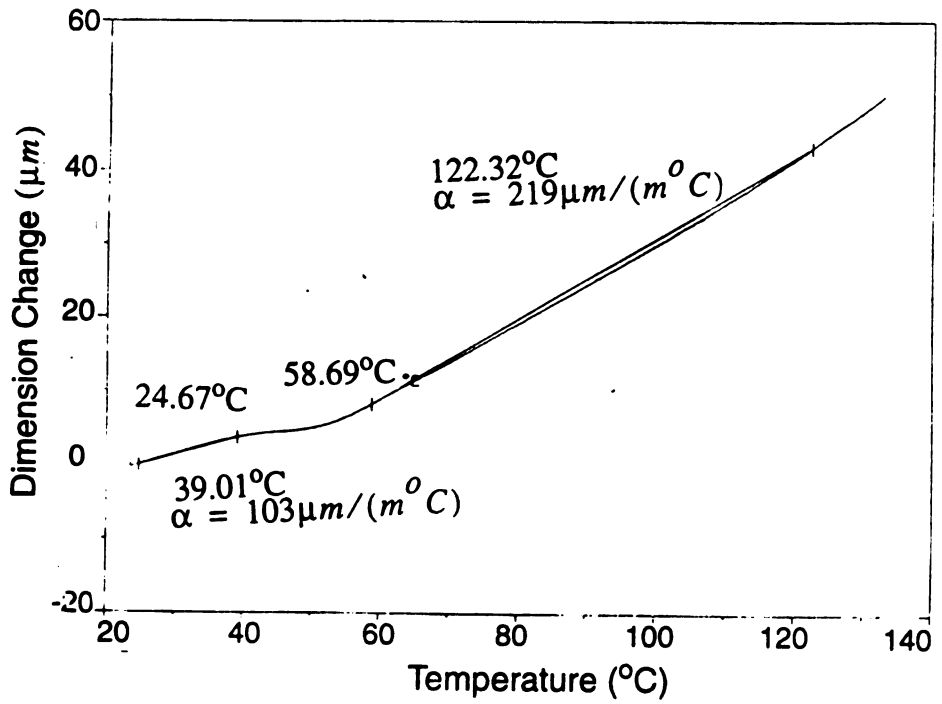

Fig. 3.7 Effect of temperature on the deformation of coating 2.

Photoelastic measurements.

The photoelasticity method was used to study the effect of interphase and random arrangement of inclusions on thermal stresses in composites with cast-in-place inclusions for two curing conditions: standard curing and post curing. In this analysis we used two compliant coatings. The mechanical properties of the epoxy matrix, inclusion and coatings are shown in Table 3.1.

To study the effect of geometric distribution, two random arrangements of inclusions with volume fraction 14% and 20% were used. The location of these fibers was digitized to be incorporated in the finite element analysis as will be mentioned in next section. For a comparison we also studied a periodic arrangement (triangular) with a volume fraction of 27.5%. The matrix was cured in accordance to standard curing for the case of randomly and regularly arranged inclusions.

In our study we considered the model composite in a form of a thin plate in order to simplify the experimental analysis. By having the plane stress case we reduce the free edge effects, i.e. the disturbance of the stresses near the two traction-free surfaces due to a relaxation of stresses there, and, in this case, we can see the photoelastic fringes more easily. Alternatively, we could simulate directly the plane strain case by using a fringe freezing technique as mentioned before.

In order to calibrate the epoxy matrix material for the fringe value f_σ different levels of loading were applied to a four-point-loaded beam (Figure 3.8). The average value of number of fringes was used to determine the material fringe value f_σ according to the formula $\sigma_1 - \sigma_2 = \frac{N f_\sigma}{h}$. For our case f was found to be 14.5 lb/in/fringe at room temperature.

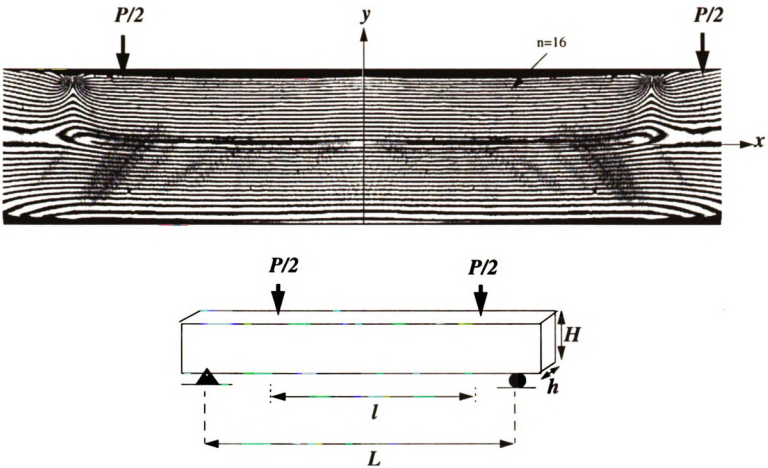

Fig. 3.8 Calibration of the epoxy matrix for photoelasticity measurements using a four-point-loading beam.

The Finite Element Solution

In this study we used a commercially available finite element package ANSYS 5.1. We utilized quadrilateral plane elements, such that each element was defined by eight nodes having two degrees of freedom: translations in the nodal x and y directions with the element edge size of.*25a*. We used the following boundary conditions: traction free conditions at three side edges and a symmetric boundary condition at the remaining edge.

We did two types of analyses. First, to study the effect of interface numerically, we varied the elastic properties of the coating keeping the same elastic properties of the matrix and the inclusion as that given in Table 3.1. In this case the random geometric distribution of fibers was generated by the computer as discussed in Chapter 2. We also studied two periodic arrangements: triangular and square. For more basic understanding we also studied single, two, and three inclusions in a row or in an equilateral arrangement.

In the second set of runs, to check the accuracy of our numerical and experimental results, we simulated the exact geometry of the experimental specimens (described in the previous section) and used the mechanical and thermal properties of tested materials as obtained experimentally (eqns. 3.8-3.10); thus we utilized a nonlinear analysis in this case.

RESULTS AND DISCUSSION

The Single Inclusion Solution.

In the parametric study of a single coated inclusion we studied the influence of four

Table 3.1. The elastic and thermal properties of composite's constituents used in the analytical solution.

	E^c *ksi (MPa)*	ν^c	α^c /^oC *($x10^{-6}$)*
matrix	450 ($3.11x10^3$)	0.36	64
inclusion	$1.74x10^3$ ($1.20x10^5$)	0.34	16.7
coating 1	1 (6.89)	0.36	246
coating 2	30 (206.84)	0.36	219

parameters characterizing the coating (interphase): the Young's modulus E^c, the Poisson's ratio ν^c, the thermal coefficient of expansion α^c and the thickness t, on the stress fields in the matrix. The com-

posite system is a thin epoxy plate with copper inclusions with the properties given in Table 3.1.

Fig. 3.9 illustrates the joint effect of the non-dimensionalized Young's modulus of the coating E^c with respect to the Young's modulus of the matrix E^m (E^c/E^m) and the non-dimensionalized thickness t with respect to the inclusion radius a (t/a) on σ_{rr}^m at $r = a + t$ *when* $\nu^c = 0.36$ and $\alpha^c = \alpha^m$. Observe that both the thickness t and the Young's modulus of the coating E^c contribute to the stress fields. The effect of changing the coating thickness is more pronounced for the cases of thin coating. Increasing the coating thickness will always increase the radial stress in the matrix regardless of the elastic modulus of the coating. If $E^c/E^m > 1$, thenand increasing the elastic modulus of the coating increases the radial stress in the matrix. The opposite behavior is observed when $E^c/E^m < 1$.

Increasing the thermal coefficient of expansion of the coating will increase the radial stresses (Figs. 3.10 and 3.11). This influence increases as the value of the elastic modulus of the coating E^c/E^m increases. The effect of changing the Poisson's ratio of the coating (ν^c) increases as the elastic modulus of the coating increases (E^c/E^m) as shown in Fig. 3.12. Also note that increasing the Poisson's ratio of the coating (ν^c) will increase the radial stress in the matrix (σ_{rr}^m) for the cases of compliant coatings; this effect will be

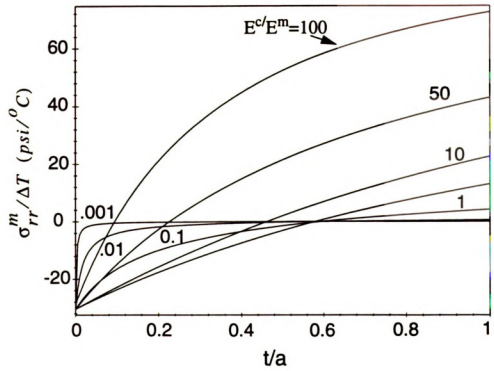

Fig. 3.9 The joint effect of the non-dimensionalized Young's modulus of the coating E^c with respect to the Young's modulus of the matrix E^m (E^c/E^m) and the non-dimensionalized thickness t with respect to the inclusion radius a (t/a) on $\sigma_{rr}^m/\Delta T$ at r = a + t when $\nu^c = 0.36$ and $\alpha^c = \alpha^m$.

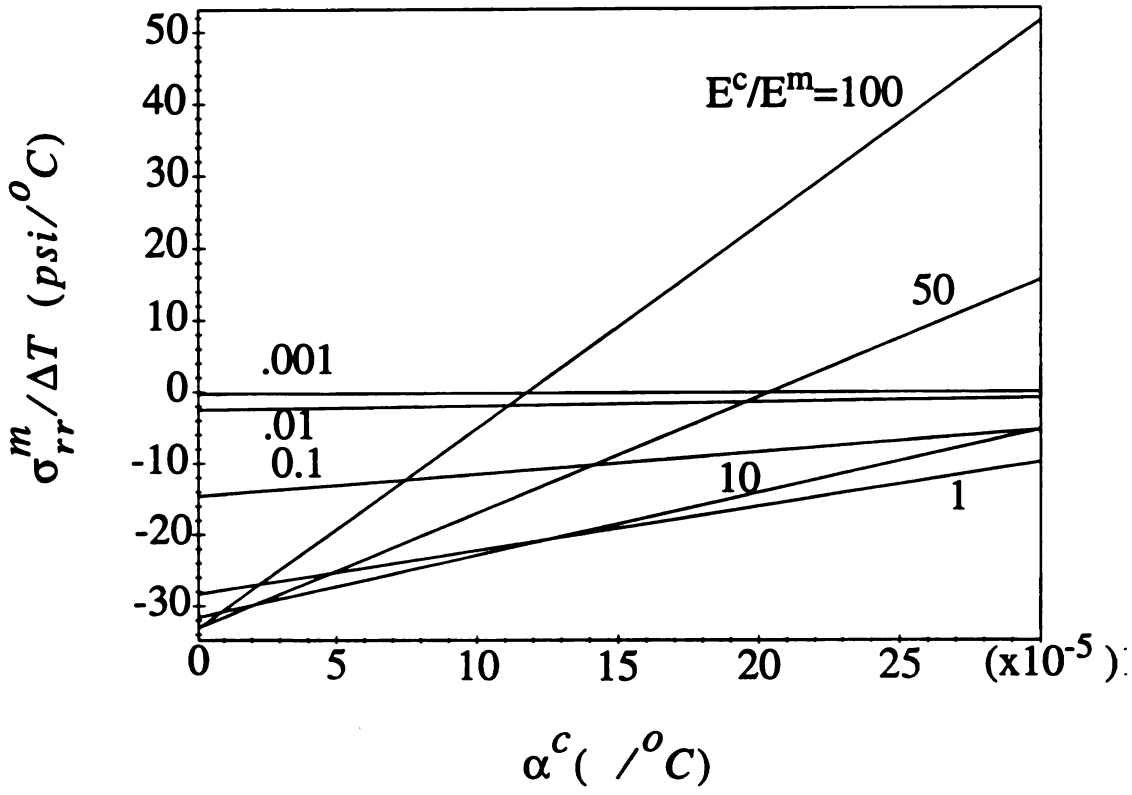

Fig. 3.10 The joint effect of the non-dimensionalized Young's modulus of the coating E^c with respect to the Young's modulus of the matrix E^m (E^c/E^m) and the coefficient of thermal expansion of the coating α^c on $\sigma^m_{rr}/\Delta T$ at r = a + t when ν^c = 0.36 and t/a = .25.

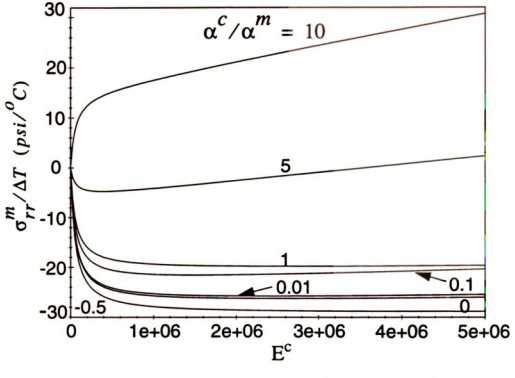

Fig. 3.11. The joint effect of the Young's modulus of the coating E^c and the non-dimensionalized coefficient of thermal expansion of the coating α^c with respect to the coefficient of thermal expansion of the matrix α^m on $\sigma^m_{rr}/\Delta T$ at r = a + t when ν^c = 0.36 and t/a= .25.

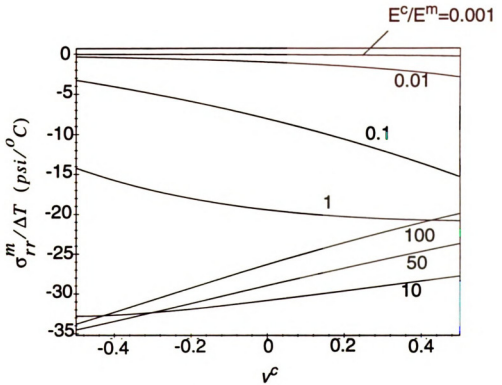

Fig. 3.12 The joint effect of the non-dimensionalized Young's modulus of the coating E^c with respect to the Young's modulus of the matrix E^m (E^c/E^m) and the Poisson's ratio of the coating v^c on σ^m_{rr} at $r = a + t$ when $t/a = .25$.

reversed in cases of stiff coatings.

Figs. 3.13 demonstrates the effect of the elastic modulus of the coating E^c on the effective stresses σ_{eff} in the matrix, coating and inclusion when $\alpha^c = \alpha^m$, $\nu^c = \nu^m$ and t $=.25\ a$. If the elastic modulus of the coating $E^c < E^m = 450\ ksi$ then the matrix, coating, and inclusion carry almost the same amount of loading. However when $E^c > E^m$ then the loading is carried by the coating and the inclusion with the maximum stress being in the matrix. Note that the stress in the matrix will be almost constant when $E^c > E^m$.

For a constant $t = .25a$, $E^c = E^m$ and $\nu^c = \nu^m$, increasing the coefficient of thermal expansion (CTE) of the coating α^c will reduce the effective stresses σ_{eff} in the matrix but will increase the effective stress in the coating and the stress in the inclusion will not change (Fig. 3.14). Figure 3.15 shows the distribution of $\sigma_1 - \sigma_2$ in the matrix, coating and inclusion along the radial direction for the case of a constant $t = .25a$, $\alpha^c = \alpha^m$ and ν^c $= \nu^m$. Note that the stresses are uniform inside the inclusion as expected from Eshelby's solution (1957).

To study the effect of curing conditions, experimental and numerical results of $\sigma_1 - \sigma_2$ stress distribution in the matrix along the radial direction were compared in Figure 3.16b for two curing conditions: post curing and standard curing for the case of perfectly bonded inclusions. In the finite element analysis the mechanical properties shown in Figures 3.1-3.8 were used. Fig. 3.16b shows that post curing will reduce residual stress in the matrix. Figure 3.16a represents typical stress patterns of both curing conditions as

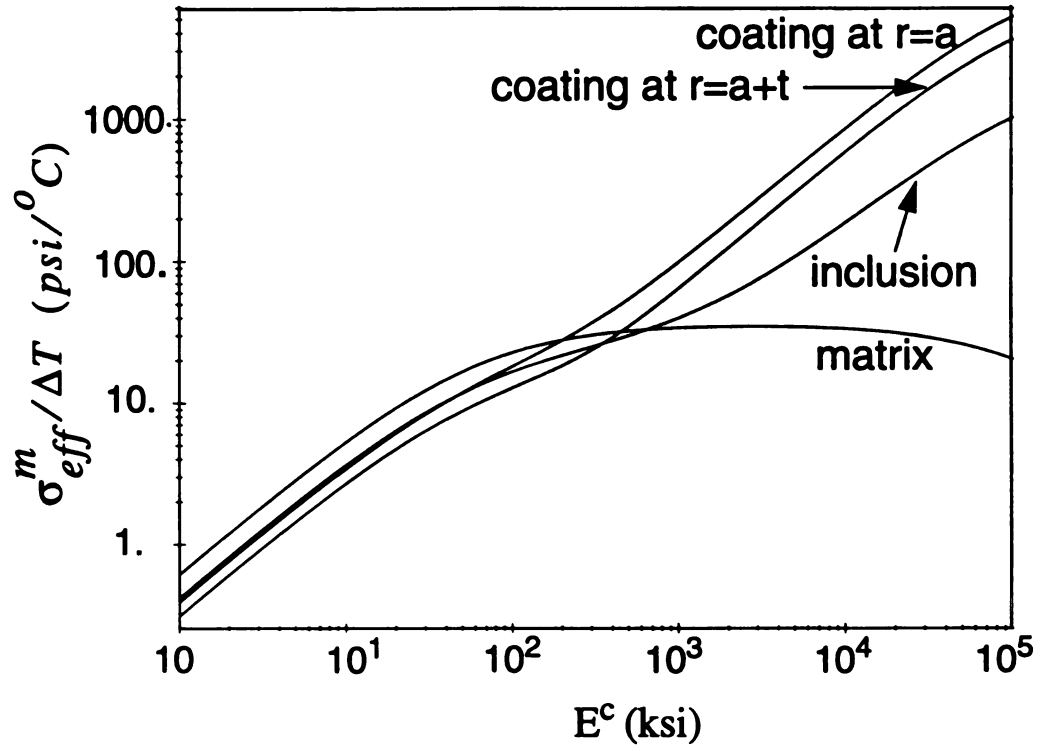

Fig. 3.13 The effect of the elastic modulus of the coating E^c on the effective stresses $\sigma_{eff}/\Delta T$ in the matrix, coating and inclusion when $\alpha^c = \alpha^m$, $\nu^c = \nu^m$ and $t = 0.25\ a$.

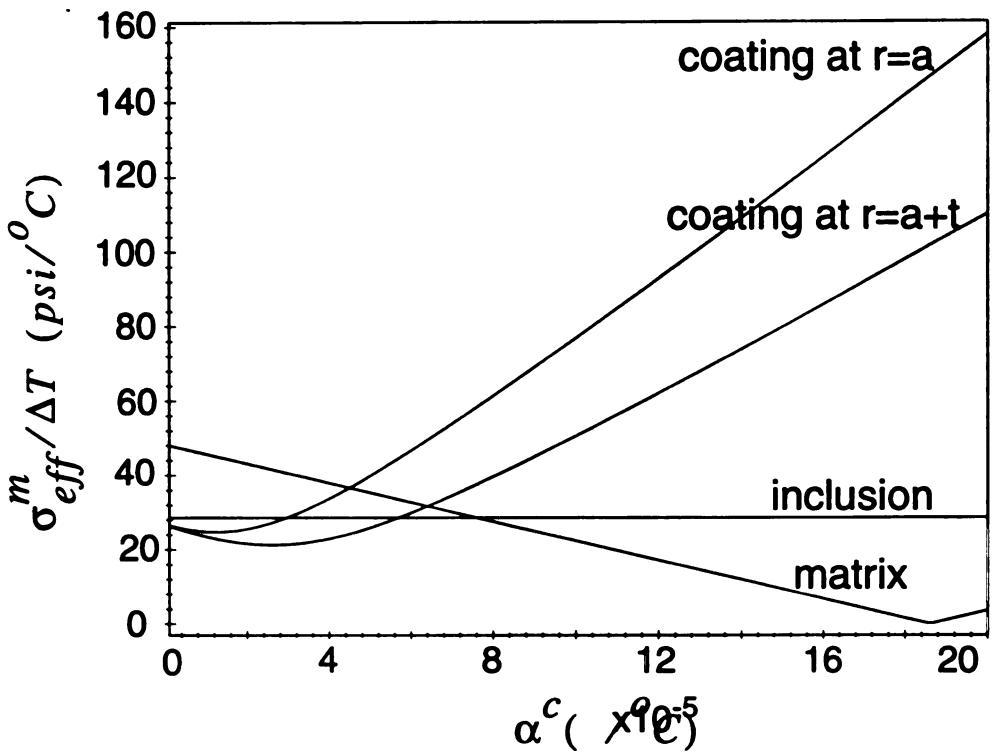

Fig. 3.14 The effect of the coefficient of thermal expansion of the coating α^c on the effective stresses $\sigma_{eff}/\Delta T$ in the matrix, coating and inclusion when $E^c = E^m$, $\nu^c = \nu^m$ and $t = .25\ a$.

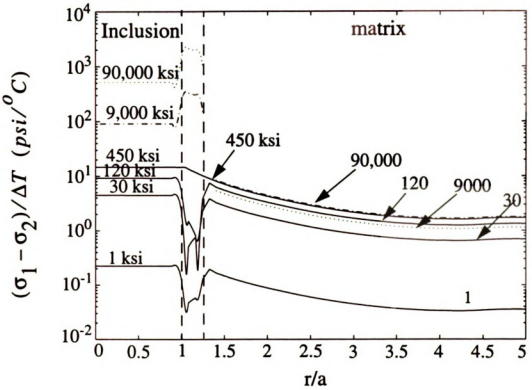

Fig. 3.15 The distribution of $(\sigma_1-\sigma_2)/\Delta T$ $(psi/^oC)$ in the matrix, coating and inclusion along the radial direction for the case of a constant t =.25a, $\alpha^c = \alpha^m$ and $\nu^c = \nu^m$.

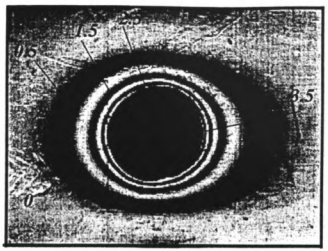

(i)

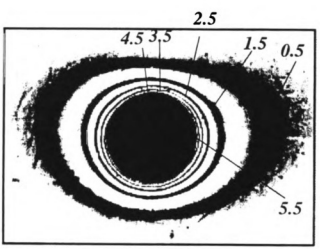

(ii)

Fig. 3.16a. Isochromatic fringe patterns around a cast-in-place copper inclusion in an epoxy matrix for two curing conditions: i) post curing, and ii) standard curing.

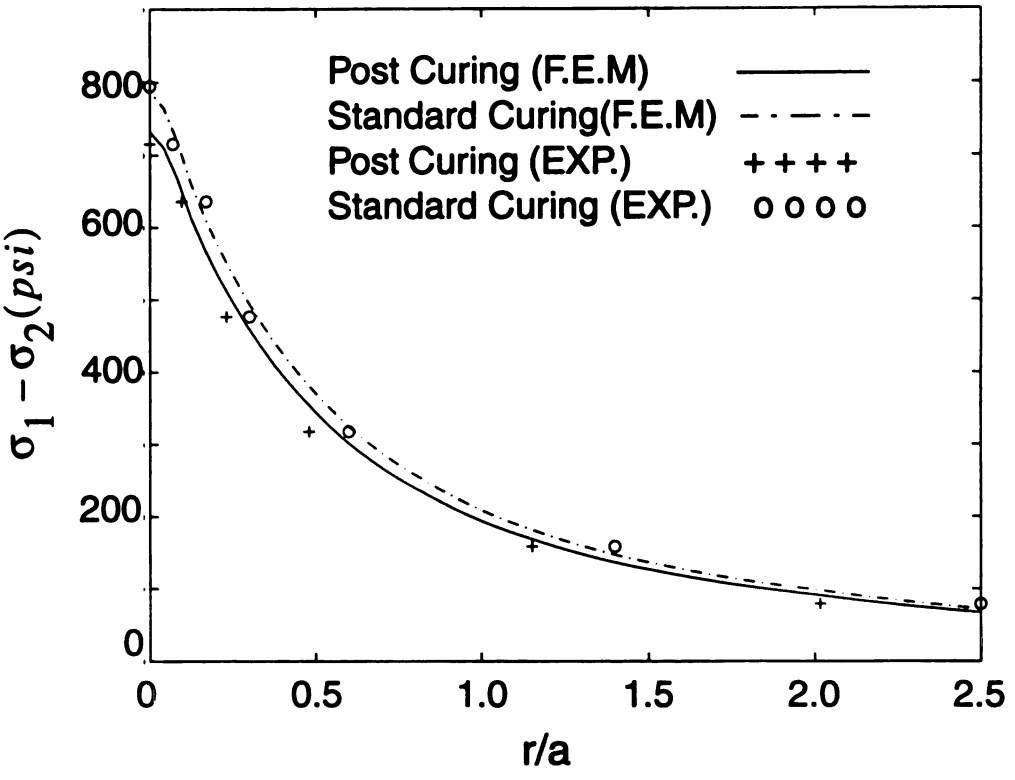

Fig. 3.16b. The effect of two curing conditions: experimental (EXP.) and numerical (F.E.M.) results for $\sigma_1 - \sigma_2$ stress distribution in the matrix along the radial direction.

obtained via photoelasticity.

In order to check the accuracy of both our photoelastic results and finite element outputs, we compared the contours of the max($\sigma_1^m - \sigma_2^m$), obtained numerically and experimentally with the analytical results. These results, given in Table 3.2, show a good agreement between our numerical, experimental, and analytical solutions. Note, also, the similarity in stress distributions of the three methods (Fig. 3.17a). In case of compliant coatings no stresses were observed in the birefringe material (Fig. 3.17bi-ii).

Two inclusions case.

In order to gain an insight about the inclusions' interaction we focus now on the two inclusions solution. The local stress fields due to two inclusions are a function of the separation distance between the two inclusions, and the presence of other inclusions.

1) Effect of separation distance between two inclusions.

Numerically, we vary the separation distance between the two coated inclusions. Figs. 3.18-3.22 show that increasing the separation distance reduces the local effective stress in the matrix, the coating, and the inclusion. For the case of the coating thickness t=.25a, the thermal coefficient of expansion of the coating $\alpha^c = \alpha^m = 64x10^{-6}\ /^oC$ and the Poisson's ratio of the coating $\nu^c = \nu^m = .36$ (Fig.3.16-3.18), the maximum stress between the two inclusions always increases as the elastic Young's modulus of the coating E^c increases. The same influence was observed for the case of $\alpha^c = 219x10^{-6}\ /^oC$

Table 3.2. A comparison of experimental, numerical and analytical results of the maximum $\left(\sigma_1^m - \sigma_2^m\right)/\Delta T$ $(psi/^oC)$ for the single inclusion case.

	Experimental	F.E.M	Analytical
perfect bond (no coating)	13.9	14.5	14.46
coating 1	0	6.61	6.32
coating 2	0	.203	0.185

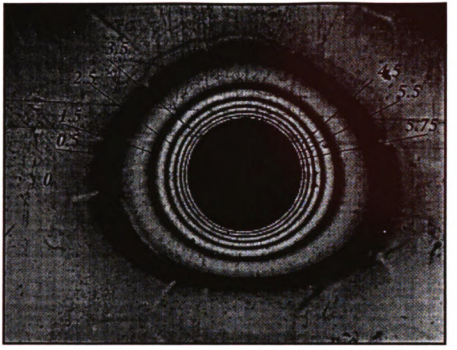

Fig. 3.17a-i. The contours of $\sigma_1 - \sigma_2$ in the epoxy matrix around a perfectly bonded single copper inclusion as obtained experimentally.

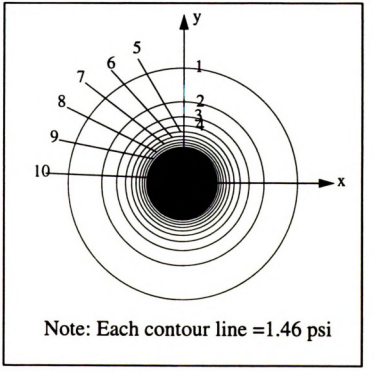

Fig. 3.17a-ii. The contours of $\sigma_1 - \sigma_2$ in the epoxy matrix around a perfectly bonded single copper inclusion as obtained analytically.

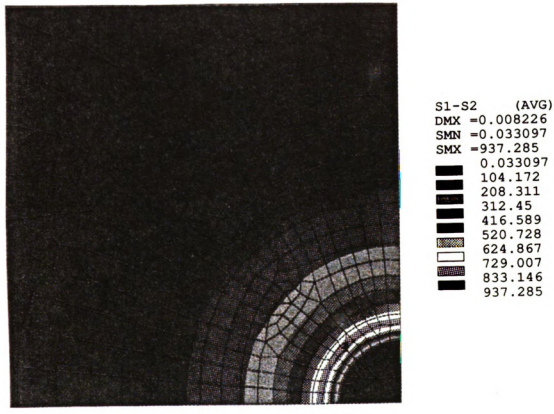

Fig. 3.17a-iii. The contours of $(\sigma_1 - \sigma_2)/\Delta T$ *(psi/°C)* in the epoxy matrix around a perfectly bonded single copper inclusion as obtained numerically.

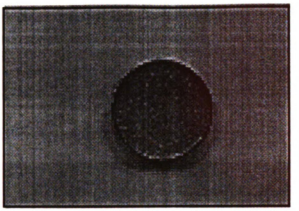

i)

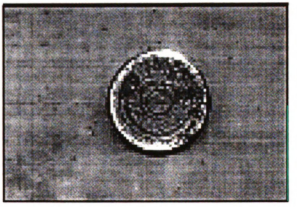

ii)

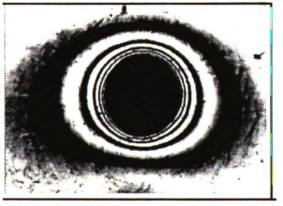

iii)

Fig. 3.17b. Isochromatic fringe pattern obtained by photoelasticity for an epoxy matrix with either coated single inclusion using i) coating 1 and ii) coating 2, or (iii) no coating case.

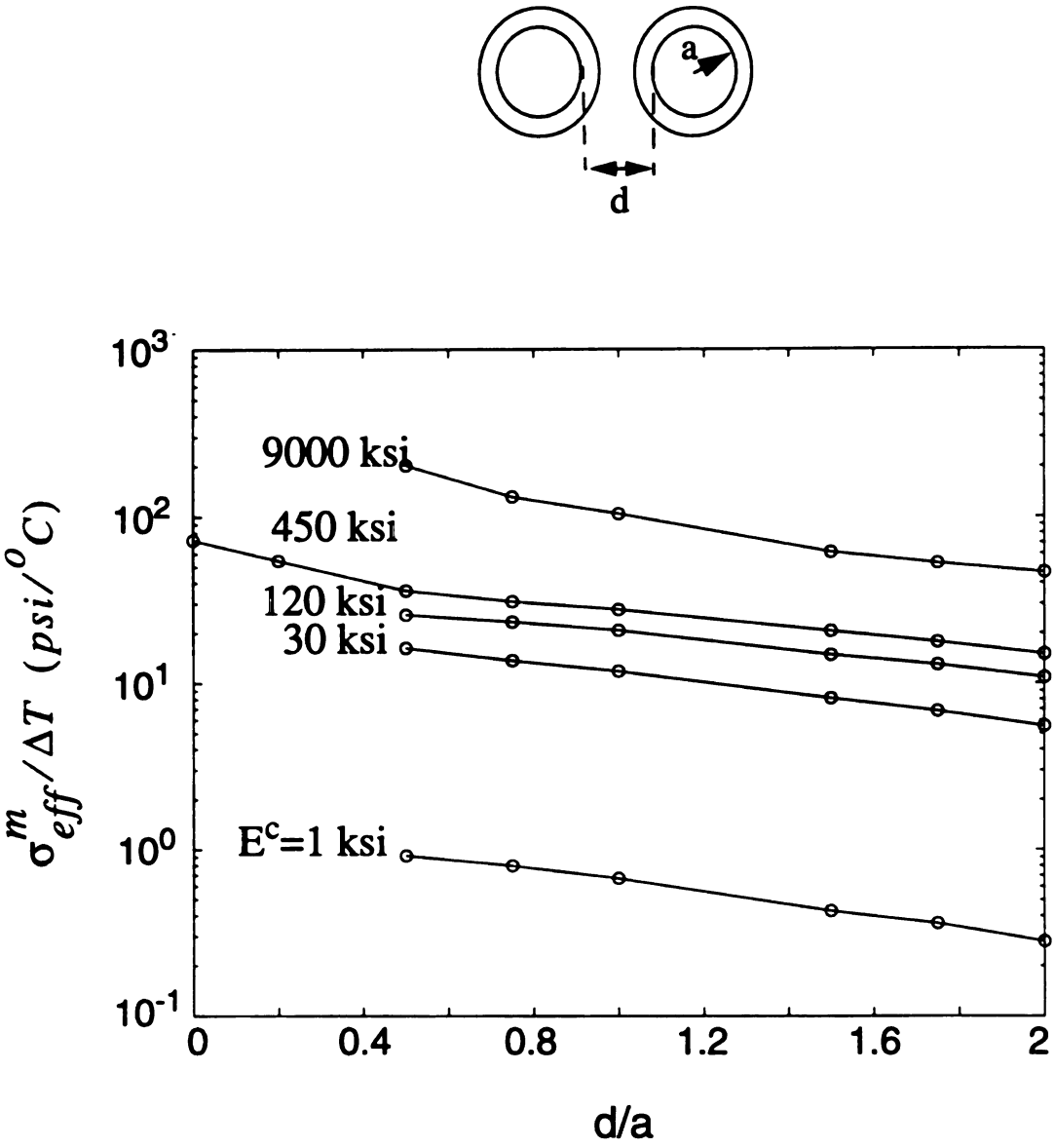

Fig. 3.18 Effect of separation distance d on the effective stress in the matrix $\sigma^m_{eff}/\Delta T$ $(psi/^oC)$ for a coating thickness $t = .25a$, the thermal coefficient of expansion of the coating $\alpha^c = \alpha^m = 64x10^{-6}$ $/^oC$ and the Poisson's ratio of the coating $v^c = v^m = 0.36$.

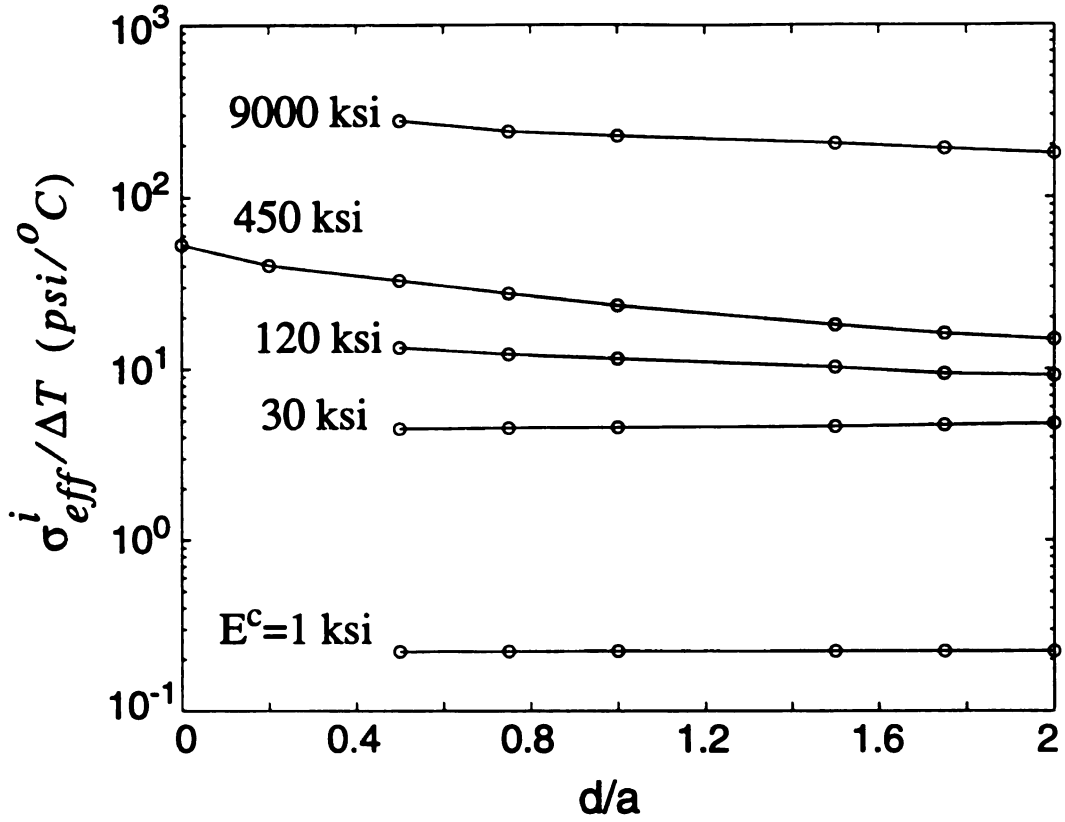

Fig. 3.19 Effect of separation distance d on the effective stress in the inclusion $\sigma^i_{eff}/\Delta T$ $(psi/^oC)$ for a coating thickness $t=.25a$, the thermal coefficient of expansion of the coating $\alpha^c = \alpha^m = 64x10^{-6}/^oC$ and the Poisson's ratio of the coating $\nu^c = \nu^m = 0.36$.

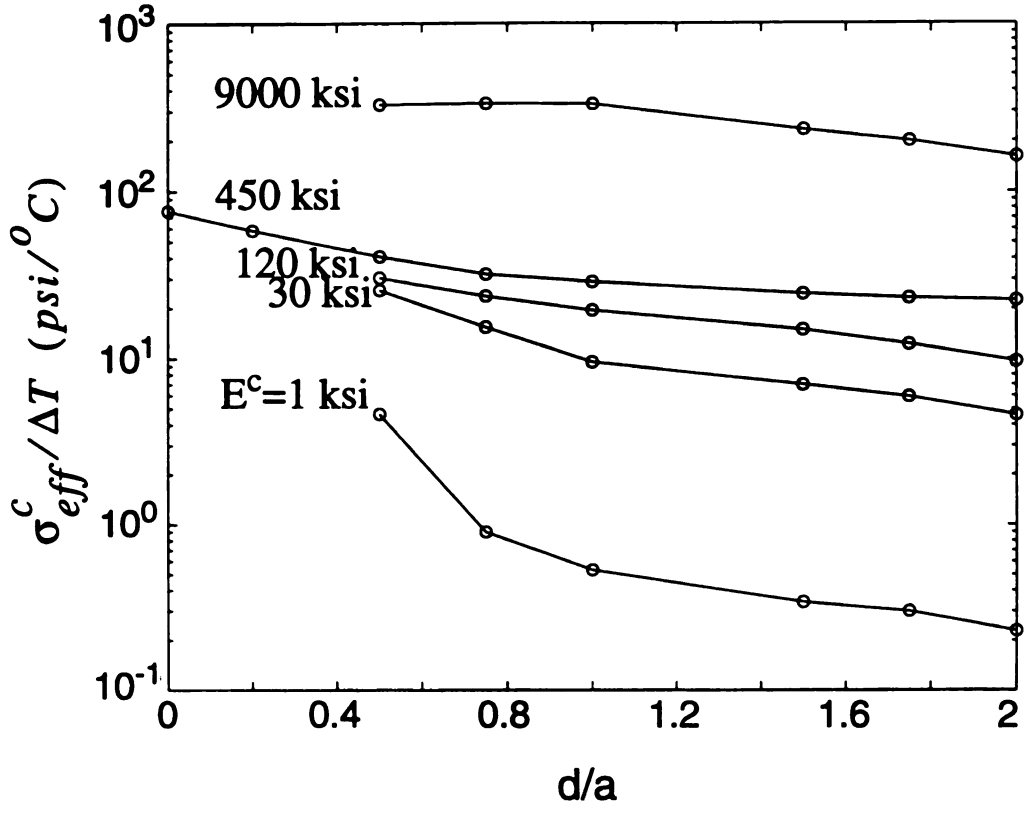

Fig. 3.20 Effect of separation distance d on the effective stress in the coating $\sigma^c_{eff}/\Delta T$ $(psi/^oC)$ for a coating thickness $t = .25a$, the thermal coefficient of expansion of the coating $\alpha^c = \alpha^m = 64x10^{-6}$ $/^oC$ and a Poisson's ratio of the coating $\nu^c = \nu^m = .3$.

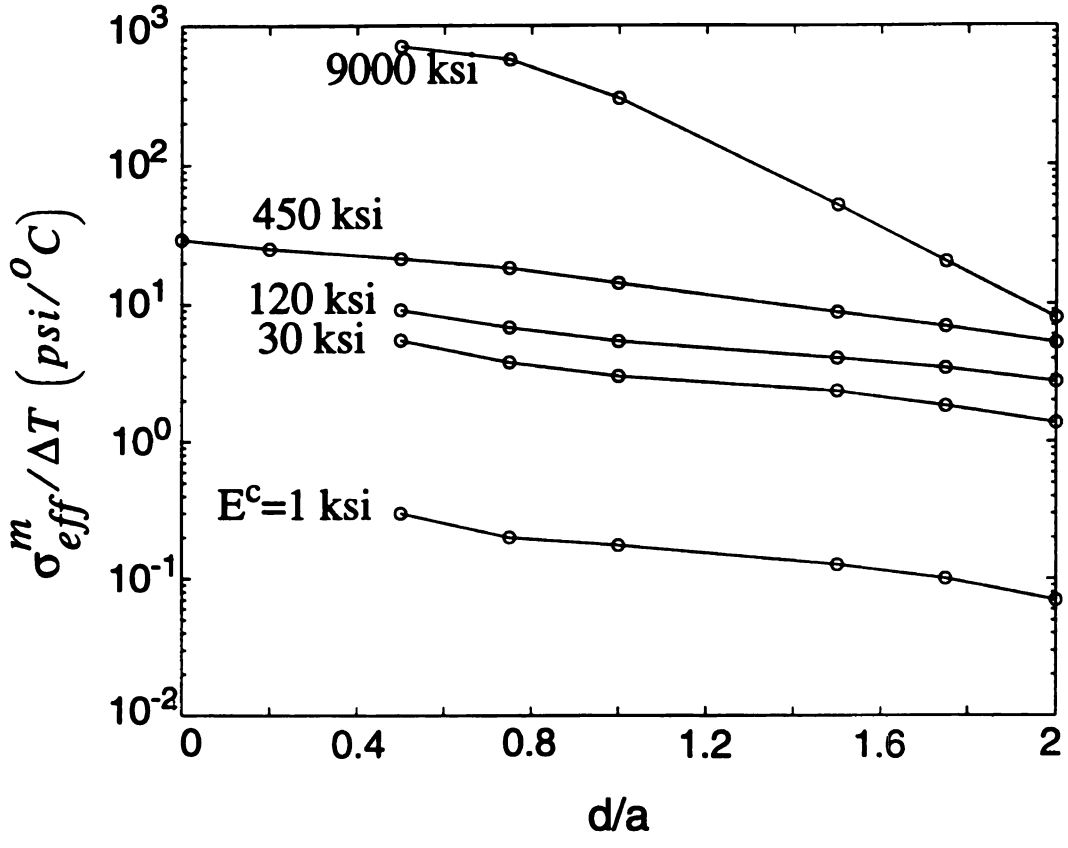

Fig. 3.21 Effect of separation distance d on the effective stress in the matrix $\sigma^m_{eff}/\Delta T\ \left(psi/^oC\right)$ for a coating thickness $t = 0.25a$, the thermal coefficient of expansion of the coating $\alpha^c = 219x10^{-6}$ /°C and the Poisson's ratio of the coating $\nu^c = \nu^m = 0.36$.

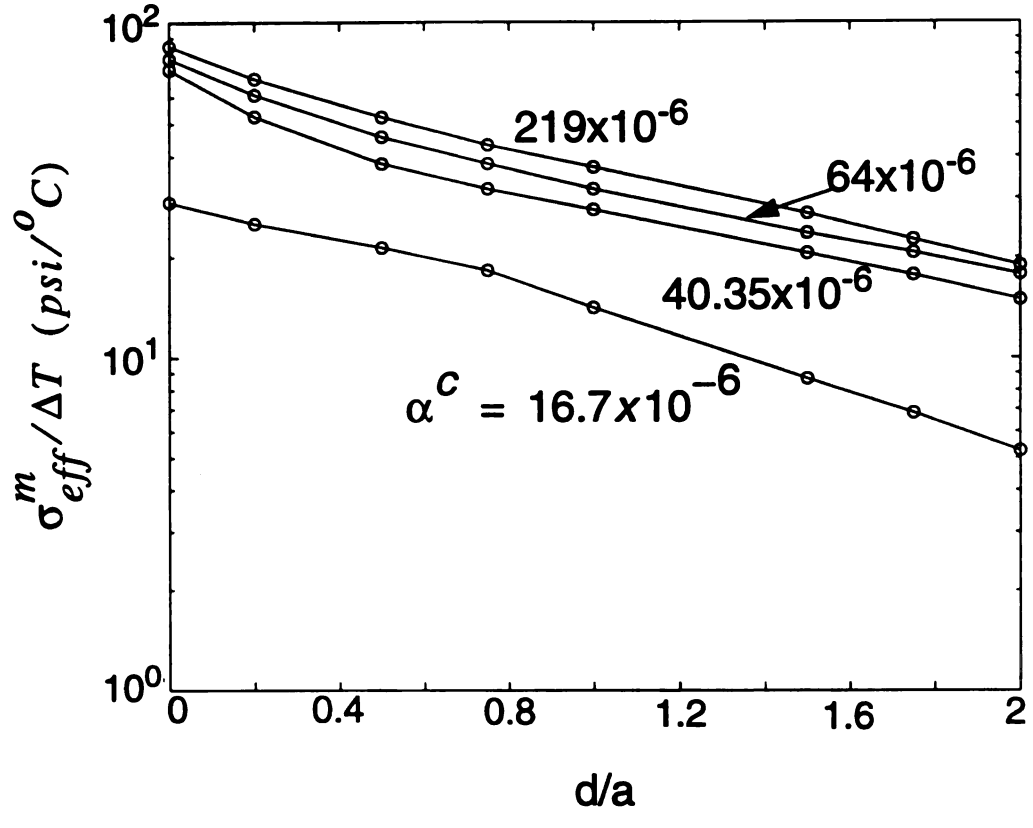

Fig. 3.22 Effect of separation distance d on the effective stress in the matrix $\sigma^m_{eff}/\Delta T$ $(psi/^oC)$ for a coating thickness t=.25a, an elastic Young's modulus of the coating $E^c = E^m$ and a Poisson's ratio of the coating $\nu^c = \nu^m = .36$.

(Fig.3.21). Fig. 3.22 shows that for the case of $E^c = E^m$, $t = .25$ and $\nu^c = \nu^m = .36$ the effective stress between two inclusions always increases by increasing the thermal coefficient of expansion α^c of the coating regardless of the separation distance between the two inclusions.

Experimentally, we vary the separation distance between two perfectly bonded inclusions and we use the standard curing condition (Fig. 3.23a-h). When we compared results of our numerical calculations for a perfect bonding case with our experimental results for the case of standard curing, we found a very good agreement between the finite element and experimental results of $\sigma_1^m - \sigma_2^m$ (Fig.3.24).

2) effect of the presence of other inclusions.

Finally, we explore the effect of the presence of more than two inclusions on the stress field. We do so by considering three inclusions in a row and three inclusions with their centers forming an equilateral triangle. We study these effects for the case of either a two-phase material (no coating) or a three phase material (with a coating). For the case of two phase material system we vary the mismatch between the two materials (E^i/E^m) and we use Kouris' solution (1991). Fig. 3.25 shows that increasing the number of inclusions in a row increases the compressive of radial stress in the matrix regardless of degree of mismatch between the inclusion and the matrix. This effect decays as we increase the number of inclusions. Fig. 3.25 also shows that three inclusions in the row configuration will produce a larger compressive stress than the three inclusions in a triangular arrangement.

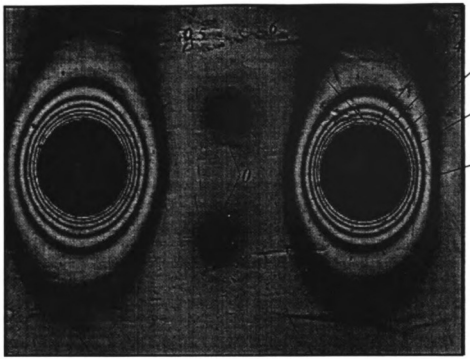

Fig. 3.23a. Isochromatic fringe pattern obtained by photoelasticity for an epoxy matrix of thickness t=0.124 in. with two perfectly bonded copper inclusions located at a/D=0.154.

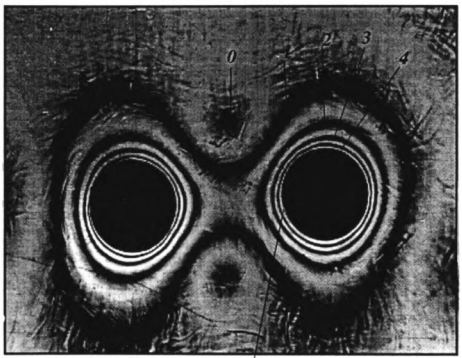

Fig. 3.23b. Isochromatic fringe pattern obtained by photoelasticity for an epoxy matrix of thickness t=0.95 in. with two perfectly bonded copper inclusions located at a/D=0.222

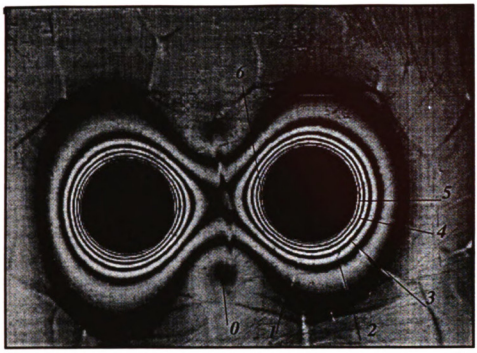

Fig. 3.23c. Isochromatic fringe pattern obtained by photoelasticity for an epoxy matrix of thickness t=0.115 in. with two perfectly bonded copper inclusions located at a/D=0.257.

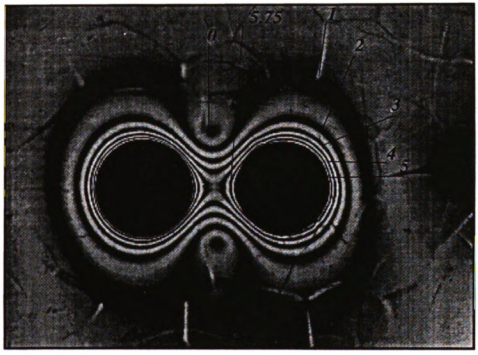

Fig. 3.23d. Isochromatic fringe pattern obtained by photoelasticity for an epoxy matrix of thickness t=0.0877 in. with two perfectly bonded copper inclusions located at a/D=0.347.

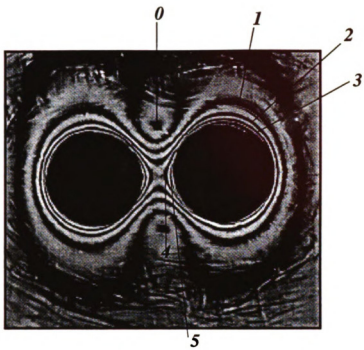

Fig. 3.23e. Isochromatic fringe pattern obtained by photoelasticity for an epoxy matrix of thickness t=0.071 in. with two perfectly bonded copper inclusions located at a/D=0.348

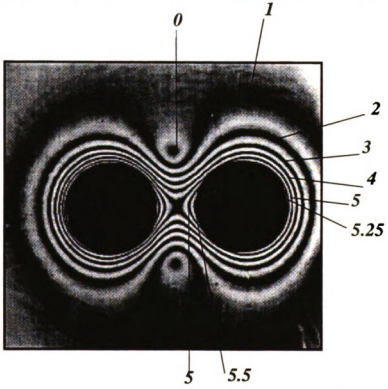

Fig. 3.23f. Isochromatic fringe pattern obtained by photoelasticity for an epoxy matrix of thickness t=0.074 in. with two perfectly bonded copper inclusions located at a/D=0.396.

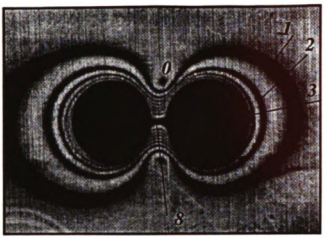

Fig. 3.23g. Isochromatic fringe pattern obtained by photoelasticity for an epoxy matrix of thickness t=0.075 in. with two perfectly bonded copper inclusions located at a/D=0.442.

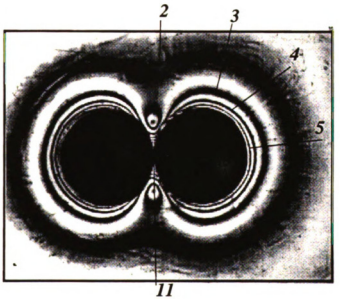

Fig. 3.23h. Isochromatic fringe pattern obtained by photoelasticity for an epoxy matrix of thickness t=0.081 in. with two perfectly bonded copper inclusions located at a/D=0.4803.

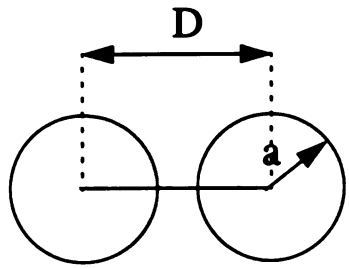

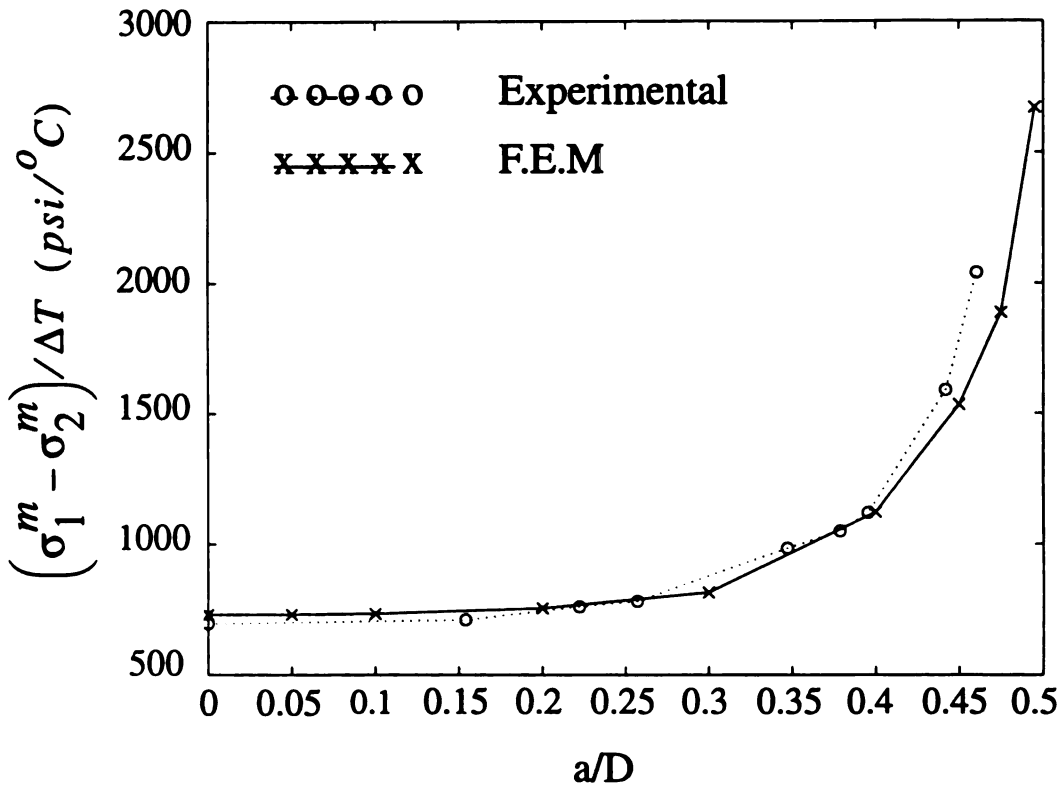

Fig. 3.24 Effect of separation distance between two perfectly bonded copper inclusions in an epoxy matrix on $\left(\sigma_1^m - \sigma_2^m\right)/\Delta T$ *(psi/°C)* experimentally and numerically.

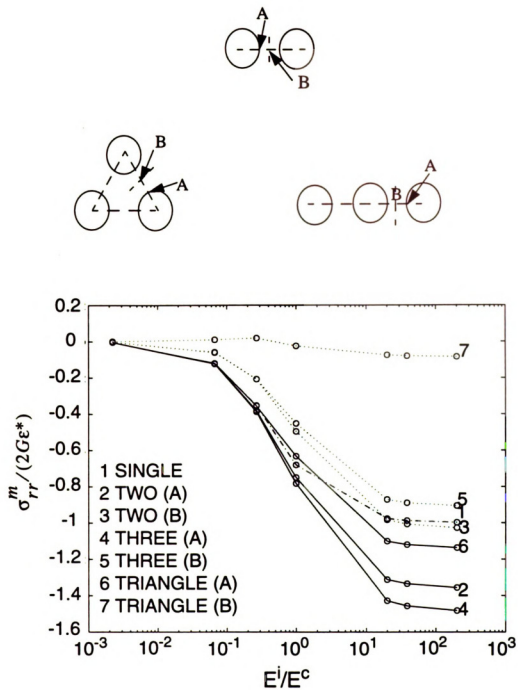

Fig. 3.25 Effect of elastic the mismatch in elastic Young's modulus between the inclusions and the matrix in a two-phase material on $\sigma^m_{rr}/(2G\epsilon^*)$ for $\nu^c = \nu^m = .36$ using the solution Kouris (1993).

Radial compressive stress in the matrix is found to be larger at the inclusion/matrix interface than the stress at the mid-distance between the two inclusions; actually the stress becomes tensile at the mid-distance between the two inclusion in the case of triangular arrangement (Fig. 3.25). Note that $\varepsilon^* = (\alpha^m - \alpha^i)\Delta T$ where α^m, α^i are CTE of the matrix and inclusion respectively and G is the shear modulus of the matrix. These effects are observed to be the same for the case of a coated inclusion subjected to a uniform thermal change (Fig. 3.26).

The Multi-Inclusions Solution.

The values of the maximum shear stress (principal stress difference, $\sigma_1^m - \sigma_2^m$) in the matrix, obtained by the photoelastic method and also using finite element calculations for the case of perfectly bonded inclusions for two random randomly arranged inclusions of volume fractions 14% (Fig. 3.27) and 20% (Fig. 3.28) and a regular arrangement for the volume fraction of 27% (Fig. 3.29) were compared in Table 3.3 which shows a good agreement between experimental and numerical results. Table 3.3 shows that increasing the volume fraction of the inclusions will increase the maximum shear stress. The periodic arrangement produces a lower stress than that of random arrangement even if the volume fraction of the periodic arrangement is higher. Note the similarity between stress field contours obtained experimentally (Figs 3.27-3.29) and numerically (Figs. 3.30-3.32).

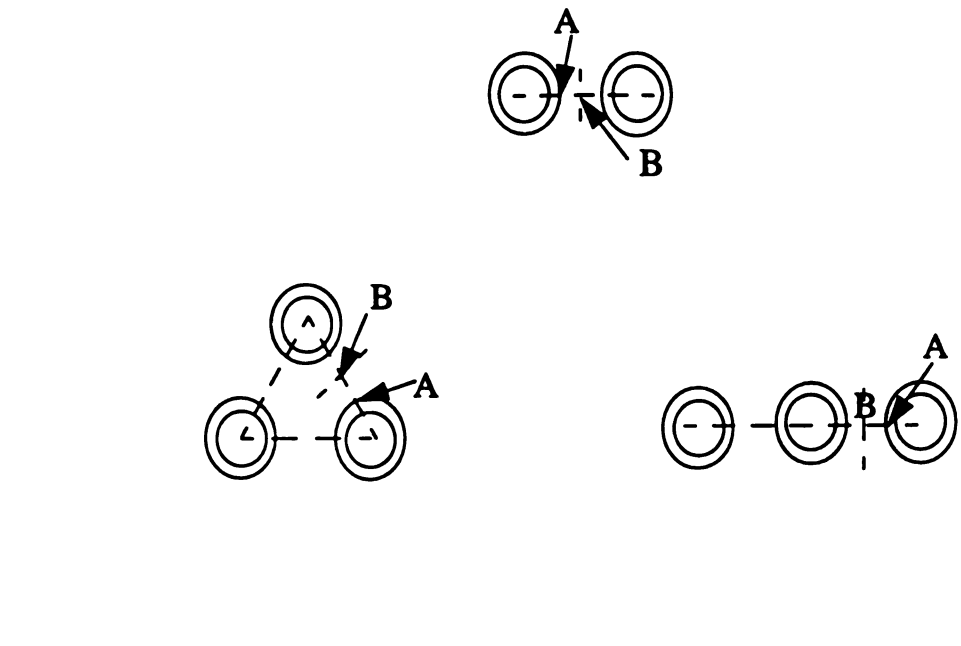

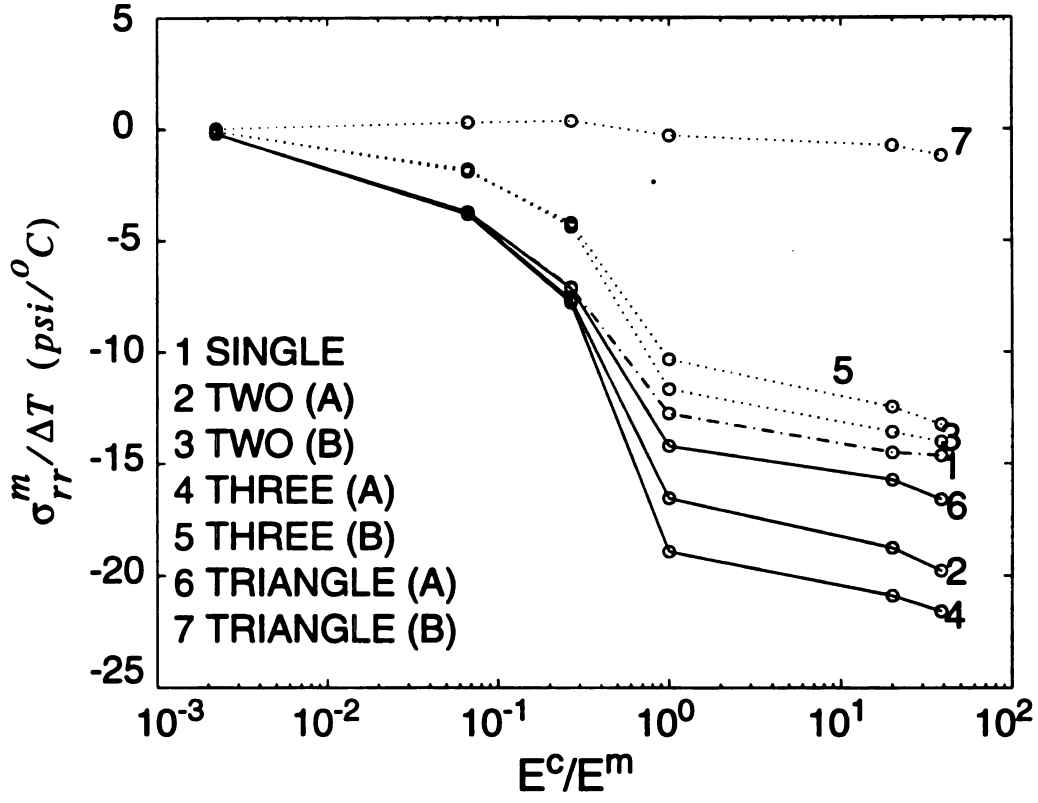

Fig. 3.26 Effect of elastic Young's modulus of the coating E^c on radial stress in the matrix $\sigma^m_{rr}/(\Delta T)$ for $v^c = v^m = .36$ using a finite element method.

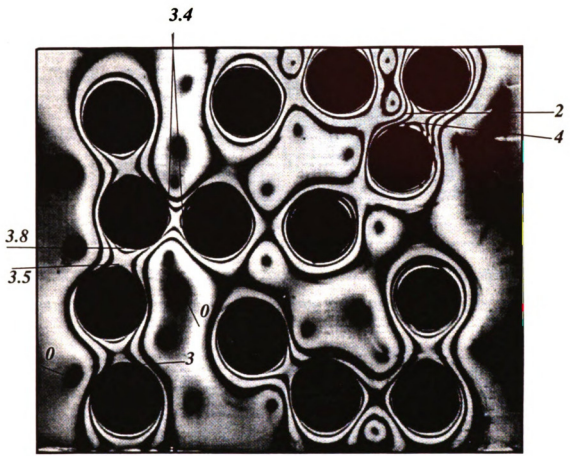

Fig. 3.27 Isochromatic fringe patterns obtained by photoelasticity for an epoxy matrix with a 14% volume fraction of cast-in-place and randomly arranged copper inclusions.

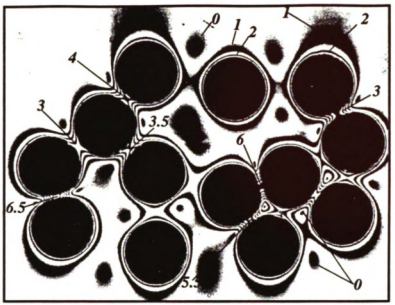

Fig. 3.28 Isochromatic fringe patterns obtained by photoelasticity for an epoxy matrix with a 17% volume fraction of cast-in-place and randomly arranged copper inclusions.

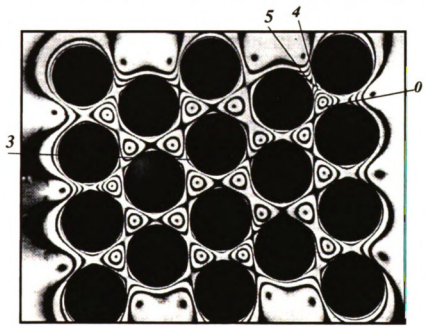

Fig. 3.29 Isochromatic fringe patterns obtained by photoelasticity for an epoxy matrix with a 20% volume fraction of cast-in-place copper inclusions arranged in a periodic arrangement...

Table 3.3. A comparison of experimental and numerical results of the maximum $\left(\sigma_1^m - \sigma_2^m\right)/\Delta T \ \ (psi/^oC)$ for the case of perfectly bonded and randomly distributed multi-inclusions.

Arrangement	Experimental	F.E.M
random (f=0.17)	899.6	911.6
random (f=.14)	504.3	540.4
periodic (f=0.2)	690 (max) 414 (mid)	723 (max) 390 (mid)

Note: (max) represents the maximum stress value in the matrix for the entire sample considered numerically, and (mid) represents the maximum stress value in the matrix at the middle portion of the same sample (i.e. away from the free surface effect).

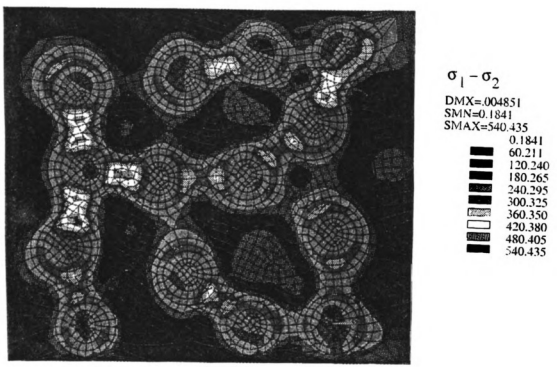

Fig. 3.30 $\sigma_1 - \sigma_2$ (psi) in a model composite with volume fraction f = 14% of randomly distributed and perfectly bonded copper inclusions obtained by FEM for a uniform temperature loading of ΔT = -50°C using a non-linear analysis.

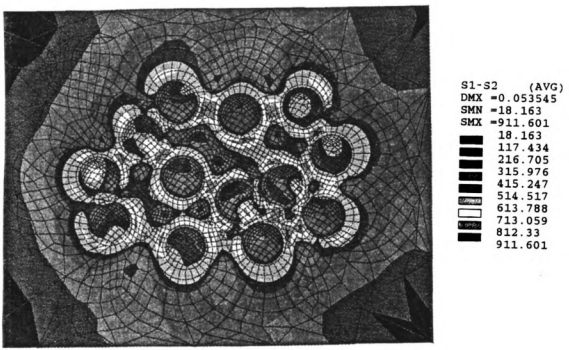

Fig. 3.31 $\sigma_1 - \sigma_2$ (psi) in a model composite with volume fraction f = 17% of randomly distributed and perfectly bonded copper inclusions obtained by FEM for a uniform temperature loading of ΔT = -50°C using a non-linear analysis.

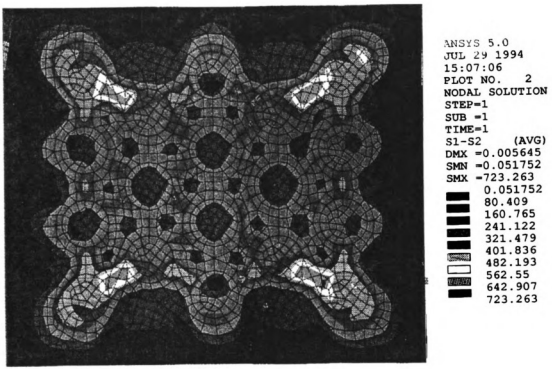

Fig. 3.32 $\sigma_1 - \sigma_2$ (psi) in a model composite with volume fraction f = 20% of randomly distributed and perfectly bonded copper inclusions in a regular arrangement obtained by FEM for a uniform temperature loading of ΔT = -50°C using a non-linear analysis.

Figs. 3.33-3.34 show the influence of the elastic modulus of the coating E^c on the location and maximum value of effective stress and principal stress difference for the case of $t = .25a$, $\nu^c = \nu^m = .36$ and either $\alpha^c = 219x10^{-6}/^oC$ or $\alpha^c = 64x10^{-6}/^oC$ with the properties of the matrix and inclusion given in Table 3.1. Note that (c) and (m) notations represent the location of the maximum stress (i.e. in the matrix (m) or in the coating (c)). Figs. 3.33-3.34 show that increasing the elastic modulus of the coating will always increase the maximum stress in the composite material. Whereas for the case of $\alpha^c = 219x10^{-6}/^oC$ the maximum stress is always in the coating material, the maximum stress will be in the matrix for the case of $E^c < E^m$ when $\alpha^c = 64x10^{-6}/^oC$.

The effect of the thermal coefficient of expansion α^c is shown in Figs. 3.35-3.36. The maximum stress in the composite material will increase by increasing the thermal coefficient of expansion of the coating. For the case of no coating the maximum stress is always in the matrix and for a stiff coating material (E^c=9000 ksi) the maximum stress is basically carried by the coating.

We compared the effect of the inclusions' arrangement using two periodic arrangements (square and triangular) and random arrangements (Tables 3.4-7). Using random arrangement always gives higher values of stresses than regular arrangements. This effect is more noticeable when the maximum stress is located in the matrix. Typical stress field contours (σ_{eff}) due to thermal residual stresses are shown in Figs. 3.37-3.44.

We also studied the local stresses around a single inclusion at elevated temperature by

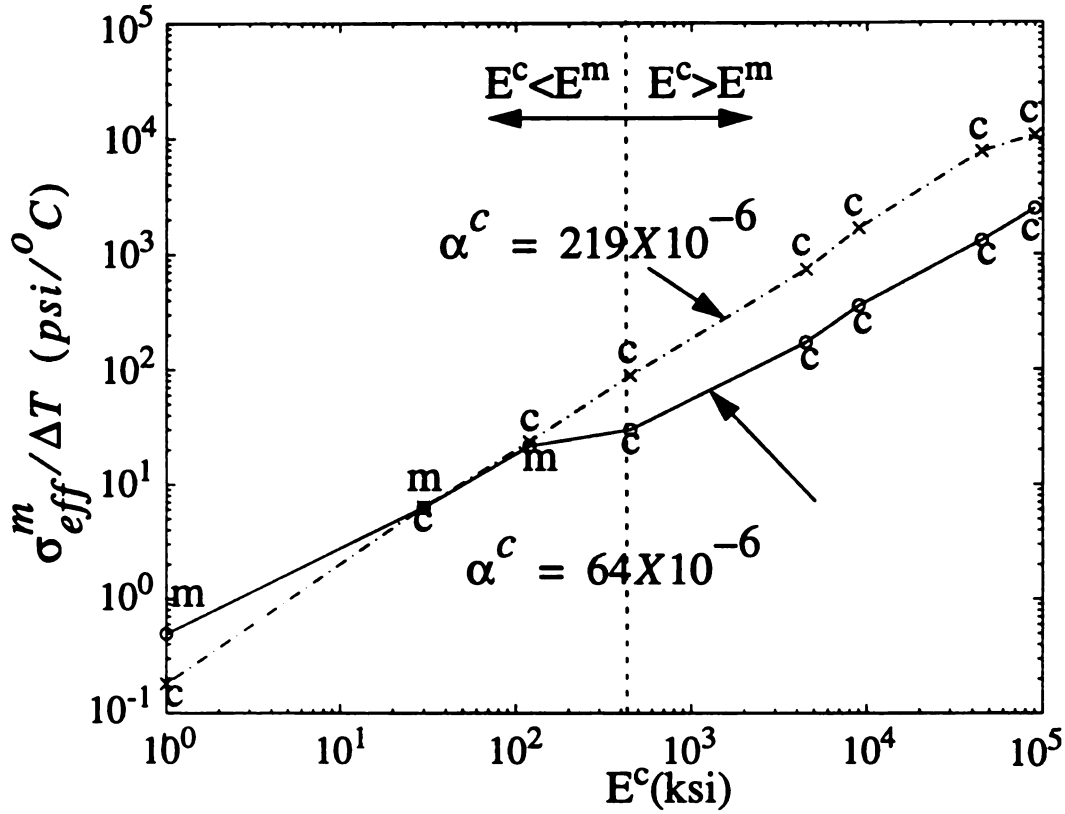

Fig. 3.33 The influence of elastic modulus of the coating E^c on the effective stress $\sigma_{eff}/\Delta T$ for the case of $t = .25a$, $\nu^c = \nu^m = .36$.

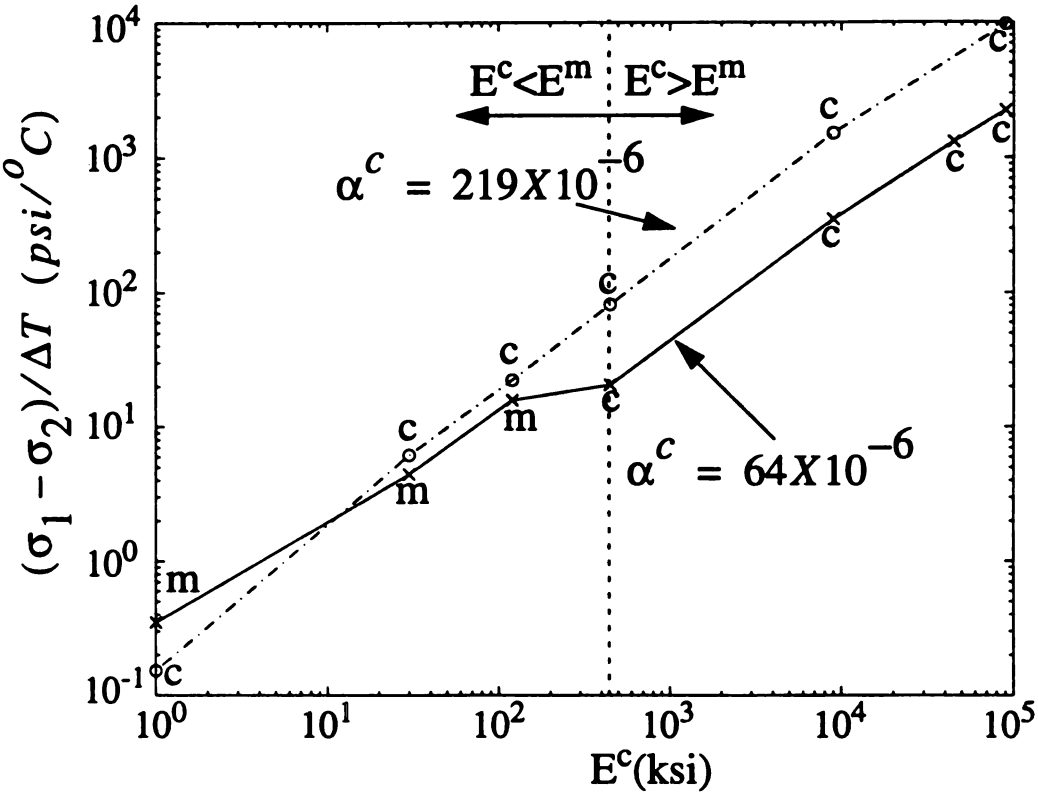

Fig. 3.34 The effect of elastic modulus of the coating E^c on $(\sigma_1 - \sigma_2)/\Delta T$ for the case of $t = .25a$, $v^c = v^m = .36$.

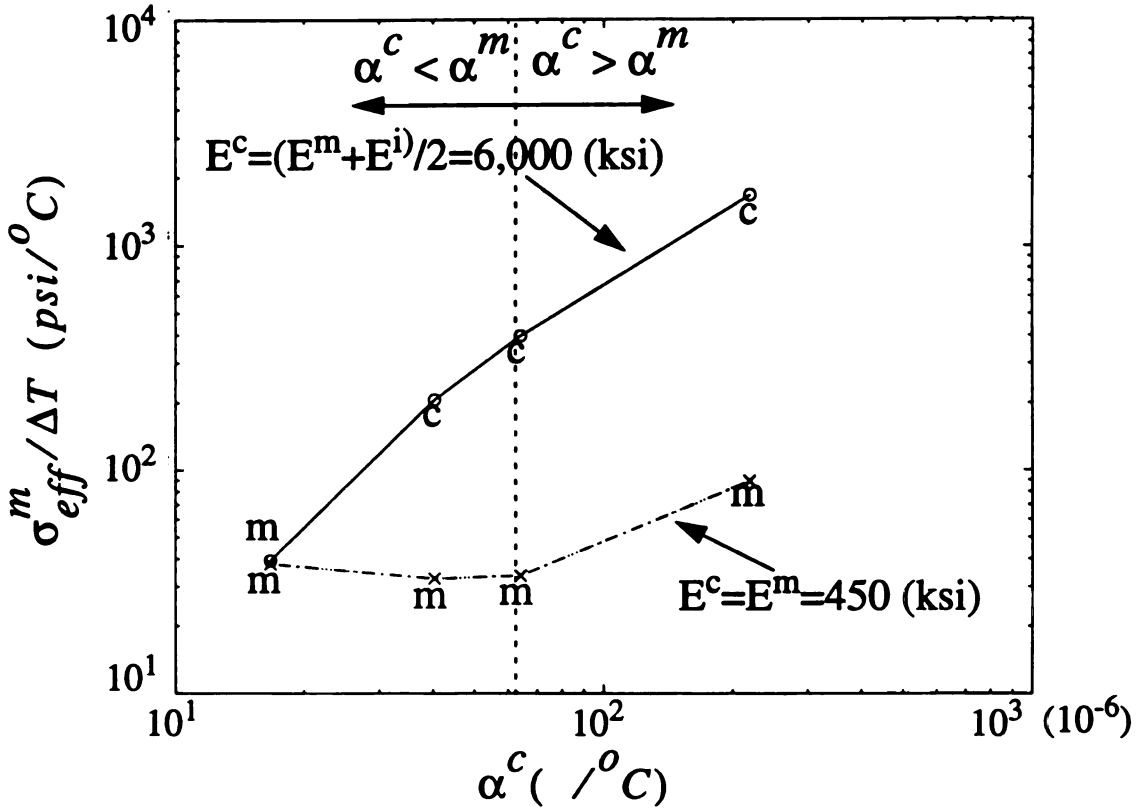

Fig. 3.35 The effect of coefficient of thermal expansion of the coating (α^c) on the effective stress $\sigma_{eff}/\Delta T$ for the case of $t = 0.25a$, $\nu^c = \nu^m = 0.36$.

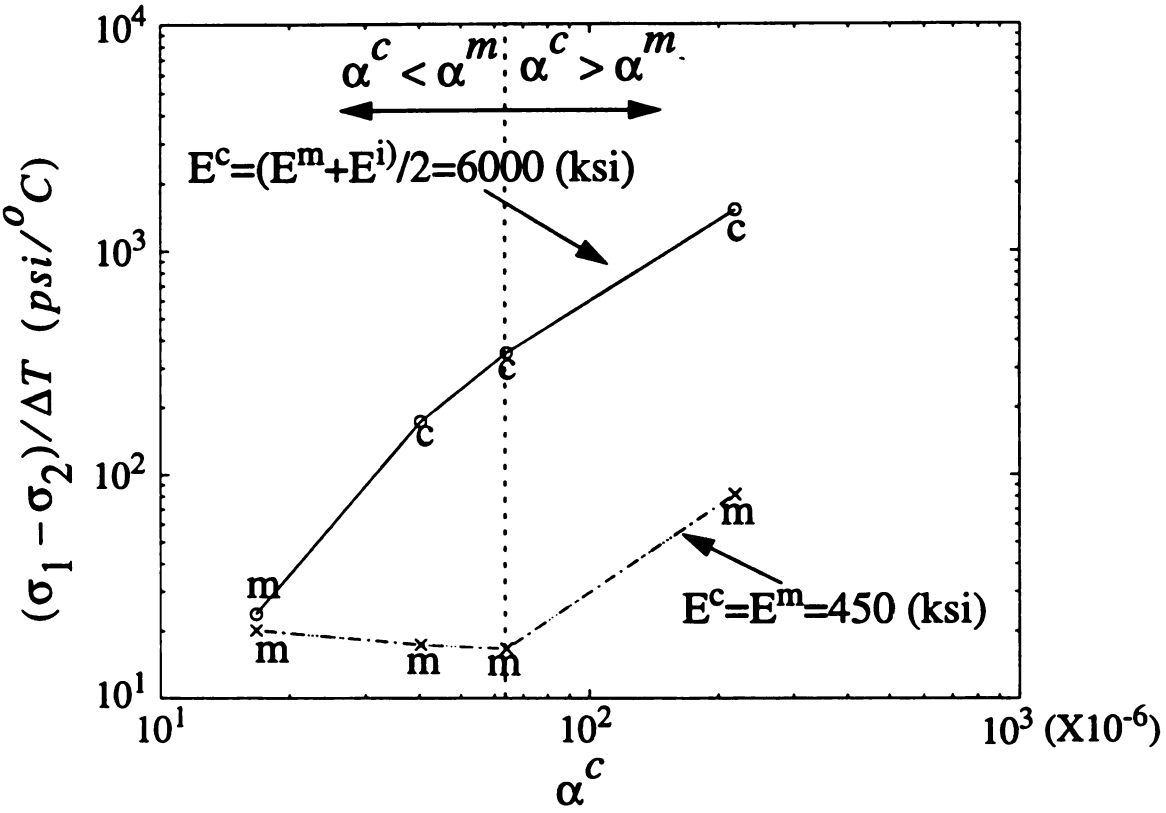

Fig. 3.36 The effect of coefficient of thermal expansion of the coating (α^c) on $(\sigma_1 - \sigma_2)/\Delta T$ for the case of $t = .25a$, $\nu^c = \nu^m = .36$.

Table 3.4. Effect of arrangement on the maximum stress in a model composite material when $\alpha^c = \alpha^m = 64x10^{-6}/^oC$, $t = .25a$ and $\nu^c = \nu^m = 0.36$ for various values of E^c.

Stress (psi/°C)	E^c=*1 (ksi)*	*30 (ksi)*	*120 (ksi)*	*450 (ksi)*	*4500 (ksi)*	*9000 (ksi)*	*45000 (ksi)*	*90000 (ksi)*	
$\sigma_{eff}/\Delta T$	0.49 (m)	6.3 (m)	21.7 (m)	33.7 (c)	172.2 (c)	397.4 (c)	1313 (c)	2475 (c)	Random
$(\sigma_1-\sigma_2)/\Delta T$	0.45 (m)	4.4 (m)	15.9 (m)	20.9 (c)	350.0 (c)	375.3 (c)	1312 (c)	2238 (c)	
$\sigma_{eff}/\Delta T$	0.28 (m)	5.2 (m)	17.2 (m)	22.2 (c)	170.0 (c)	391.2 (c)	1293 (c)	2404 (c)	Square
$(\sigma_1-\sigma_2)/\Delta T$	0.27 (m)	3.24(m)	13.0 (m)	15.3 (c)	341.2 (c)	369.3 (c)	1297 (c)	2210 (c)	
$\sigma_{eff}/\Delta T$	0.22 (m)	4.3 (m)	12.3 (m)	19.1 (c)	161.8 (c)	382.7 (c)	1287 (c)	2372 (c)	Triangular
$(\sigma_1-\sigma_2)/\Delta T$	0.20 (m)	3.0 (m)	11.4 (m)	13.4 (c)	337.1 (c)	361.9 (c)	1290 (c)	2201 (c)	

Note: (c and m) represent the location of the maximum stress i.e. in the coating (c) or in the matrix (m). The random arrangement results are the average values obtained from three different arrangements of the same volume fraction.

Table 3.5. Effect of arrangement on the maximum stress in a model composite material when $\alpha^c = 219x10^{-6}\ /^oC$, $t=.25a$ and $\nu^c = \nu^m = 0.36$ for various values of E^c.

Stress (psi/°C)	$E^c=1$ *(ksi)*	*30 (ksi)*	*120 (ksi)*	*450 (ksi)*	*4500 (ksi)*	*9000 (ksi)*	*45000 (ksi)*	*90000 (ksi)*	
$\sigma_{eff}/\Delta T$	0.18 (m)	6.4 (c)	23.7 (c)	89.2 (c)	740 (c)	1675 (c)	7717 (c)	10669 (c)	Random
$(\sigma_1-\sigma_2)/\Delta T$	0.15 (c)	6.2 (c)	22.4 (c)	81.8 (c)	710 (c)	1519 (c)	7250 (c)	9683 (c)	
$\sigma_{eff}/\Delta T$	0.18 (c)	5.7 (c)	20.1 (c)	69.3 (c)	610 (c)	1590 (c)	7003 (c)	9290 (c)	Square
$(\sigma_1-\sigma_2)/\Delta T$	0.15 (c)	4.3 (c)	19.0 (c)	62.0 (c)	601 (c)	1485 (c)	6810 (c)	8710 (c)	
$\sigma_{eff}/\Delta T$	0.17 (c)	5.0 (c)	18.3 (c)	54.4 (c)	550 (c)	1410 (c)	6520 (c)	7230 (c)	Triangular
$(\sigma_1-\sigma_2)/\Delta T$	0.13 (c)	3.6 (c)	17.6 (c)	53.3 (c)	532 (c)	1390 (c)	6010 (c)	6960 (c)	

Table 3.6. Effect of arrangement on the maximum stress in a model composite material when $E^c=E_{avg}=9x10^3$ *psi*, $t = .25a$ and $\nu^c = \nu^m = 0.36$ for various values of thermal coefficients of expansions.

Stress (*psi*/^oC)	α = *16.7* ($10^{-6}/^oC$)	*40.35* ($10^{-6}/^oC$)	*64* ($10^{-6}/^oC$)	*219* ($10^{-6}/^oC$)	
$\sigma_{eff}/\Delta T$	39.3 (m)	206.5 (c)	397.45 (c)	1675 (c)	Random
$(\sigma_1 - \sigma_2)/\Delta T$	23.8 (m)	173.0 (c)	375.31 (c)	1519 (c)	
$\sigma_{eff}/\Delta T$	26.9 (m)	170.4 (c)	391.24 (c)	1590 (c)	Square
$(\sigma_1 - \sigma_2)/\Delta T$	20.3 (m)	152.3 (c)	369.3 (c)	1485 (c)	
$\sigma_{eff}/\Delta T$	24.0 (m)	159.3 (c)	382.7 (c)	1410 (c)	Triangular
$(\sigma_1 - \sigma_2)/\Delta T$	17.3 (m)	143.6 (c)	361.9 (c)	1390 (c)	

Table 3.7. Effect of arrangement on the maximum stress in a model composite material when $E^c = E^m = 450$ *ksi*, $t = .25a$ and $\nu^c = \nu^m = 0.36$ for various values of thermal coefficients of expansions.

Stress ($psi/^oC$)	α = 16.7 ($10^{-6}/^oC$)	40.35 ($10^{-6}/^oC$)	64 ($10^{-6}/^oC$)	219 ($10^{-6}/^oC$)	
$\sigma_{eff}/\Delta T$	37.9 (m)	32.6 (m)	33.7 (c)	89.1 (c)	Random
$(\sigma_1 - \sigma_2)/\Delta T$	20.1 (m)	17.3 (m)	20.9 (c)	81.7 (c)	Random
$\sigma_{eff}/\Delta T$	24.6 (m)	20.1 (m)	22.2 (c)	69.3 (c)	Square
$(\sigma_1 - \sigma_2)/\Delta T$	17.6 (m)	14.9 (m)	15.4 (c)	62.0 (c)	Square
$\sigma_{eff}/\Delta T$	22.3 (m)	19.0 (m)	19.1 (c)	54.4 (c)	Triangular
$(\sigma_1 - \sigma_2)/\Delta T$	15.9 (m)	13.0 (m)	13.4 (c)	53.3 (c)	Triangular

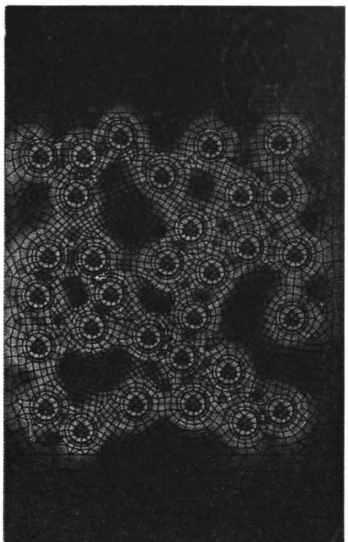

Fig. 3.37 σ_{eff} (psi) in a model composite with volume fraction f = 23% randomly arranged of coated copper inclusions with elastic modulus of the coating $E^c = 1ksi$, thermal coefficient of expansion of the coating $\alpha^c = 64x10^{-6}/^oC$ obtained by FEM for a uniform temperature loading of ΔT = -1°C using a linear analysis.

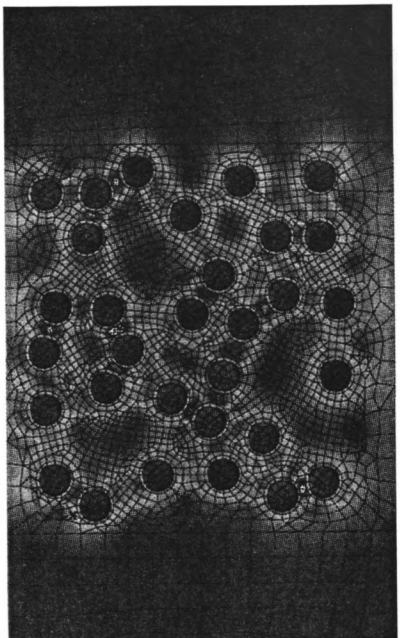

Fig. 3.38 σ_{eff} (psi) in a model composite with volume fraction f = 23% randomly arranged of coated copper inclusions with elastic modulus of the coating E^c=*30 ksi*, thermal coefficient of expansion of the coating $\alpha^c = 64x10^{-6}$ /°C obtained by FEM for a uniform temperature loading of ΔT = -1°C using a linear analysis.

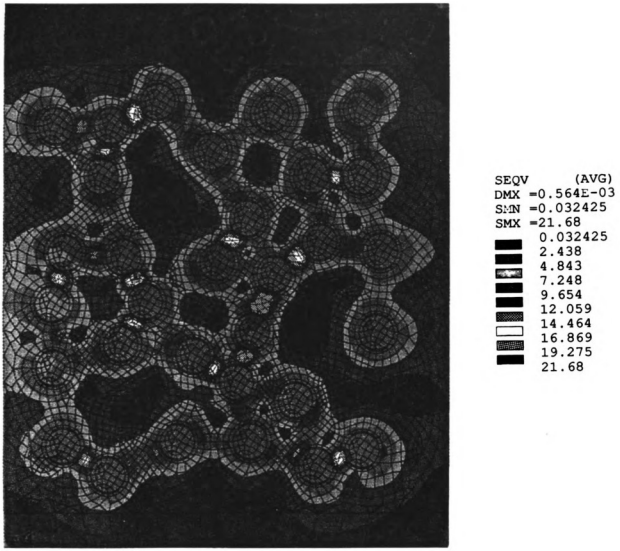

Fig. 3.39 σ_{eff} (psi) in a model composite with volume fraction f = 23% randomly arranged of coated copper inclusions with elastic modulus of the coating E^c=*120 ksi*, thermal coefficient of expansion of the coating $\alpha^c = 64x10^{-6}$ /°C obtained by FEM for a uniform temperature loading of ΔT = -1°C using a linear analysis.

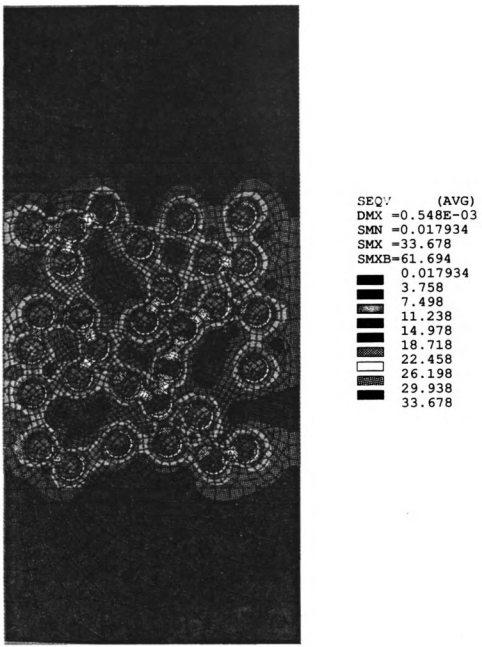

Fig. 3.40 σ_{eff} (psi) in a model composite with volume fraction $f = 23\%$ randomly arranged of coated copper inclusions with elastic modulus of the coating $E^c = E^m =$ *450 ksi,* thermal coefficient of expansion of the coating $\alpha^c = 64x10^{-6}$ $/^oC$ obtained by FEM for a uniform temperature loading of $\Delta T = -1^oC$ using a linear analysis.

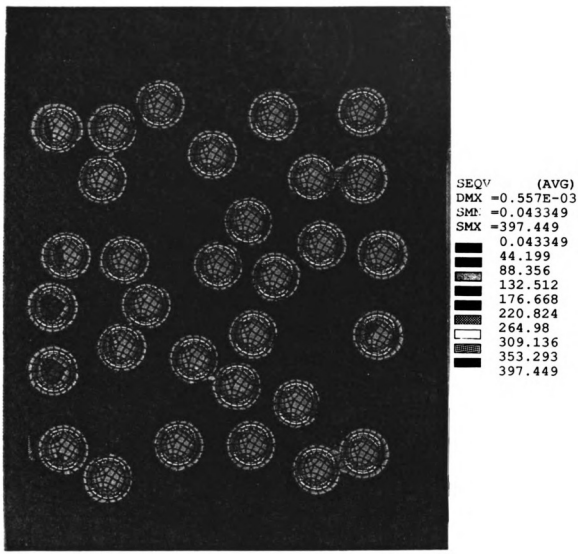

Fig. 3.41 σ_{eff} (psi) in a model composite with volume fraction f = 23% randomly arranged of coated copper inclusions with elastic modulus of the coating E^c=*9000 ksi*, thermal coefficient of expansion of the coating $\alpha^c = 64x10^{-6}$ /°C obtained by FEM for a uniform temperature loading of ΔT = -1°C using a linear analysis.

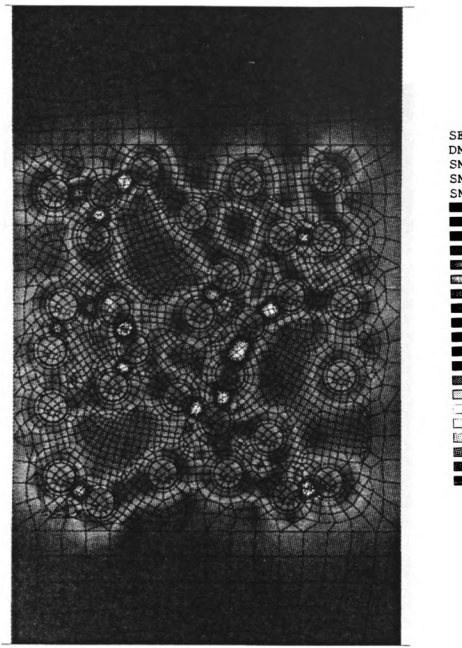

Fig. 3.42 σ_{eff} (psi) in a model composite with volume fraction f = 23% randomly arranged of coated copper inclusions with elastic modulus of the coating $E^c = E^m$ = *450 ksi,* thermal coefficient of expansion of the coating $\alpha^c = 16.7x10^{-6}/^oC$ obtained by FEM for a uniform temperature loading of ΔT = -1°C using a linear analysis.

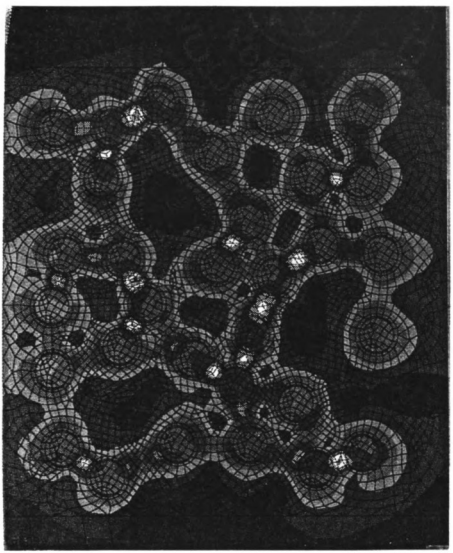

Fig. 3.43 σ_{eff} (psi) in a model composite with volume fraction $f = 23\%$ randomly arranged of coated copper inclusions with elastic modulus of the coating $E^c = E^m = 450\ ksi$, thermal coefficient of expansion of the coating $\alpha^c = 40.35x10^{-6}/^oC$ obtained by FEM for a uniform temperature loading of $\Delta T = -1^oC$ using a linear analysis.

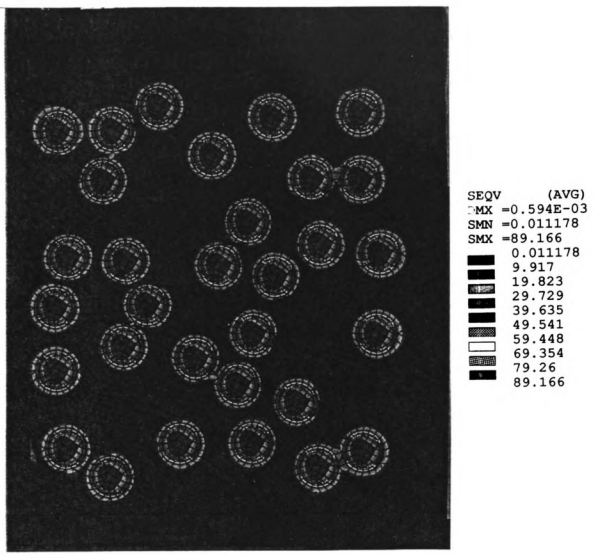

Fig. 3.44 σ_{eff} (psi) in a model composite with volume fraction f = 23% randomly arranged of coated copper inclusions with elastic modulus of the coating $E^c = E^m$ = *450 ksi,* thermal coefficient of expansion of the coating $\alpha^c = 219x10^{-6}/^oC$ obtained by FEM for a uniform temperature loading of ΔT = -1°C using a linear analysis.

considering cast-in-place copper inclusions in an epoxy matrix and subjected it to a continuous increase in temperature. The specimen was placed in a small chamber and the change in stresses was monitored and recorded continuously. The results of stresses at six selected temperatures are shown in Fig. 3.45. The experimental and numerical results of $\sigma_1^m - \sigma_2^m$ are in good agreement at relatively low temperatures ($T<77\,^oC$) as shown in Fig 3.46. At high temperature, there is a big difference between the two methods. This could be due to viscoelastic effect and change of birefringe coefficient with temperature. These two effects were not considered in our calculations.

CLOSURE

In this phase of the study we investigated the influence of the inclusion-matrix interface and the geometric arrangement on the residual stresses in a model composite made of an epoxy matrix and circular copper inclusions. We find that both of these factors significantly contribute to the local stress fields. The study of the effects of geometric arrangement of inclusions requires a more complete statistical analysis and more study is needed to investigate the viscoelastic effect,

specially at high temperatures.

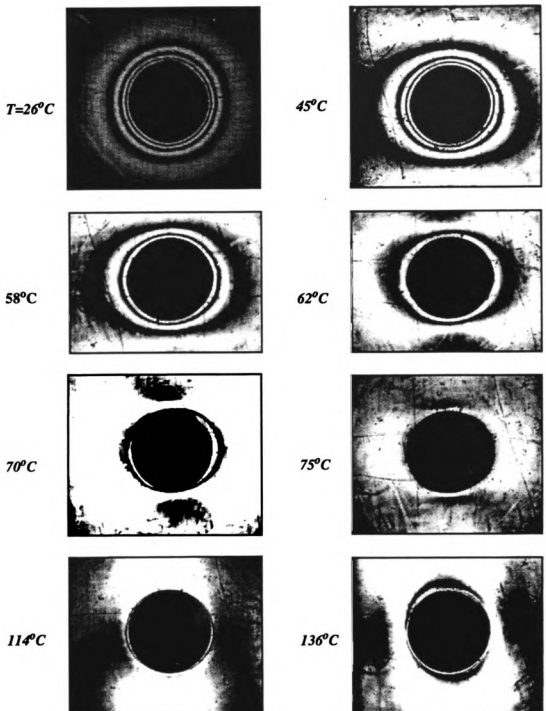

Fig. 3.45. Isochromatic fringe pattern obtained by photoelasticity around a single cast-in-place copper inclusion subjected to a continuous increase in temperature.

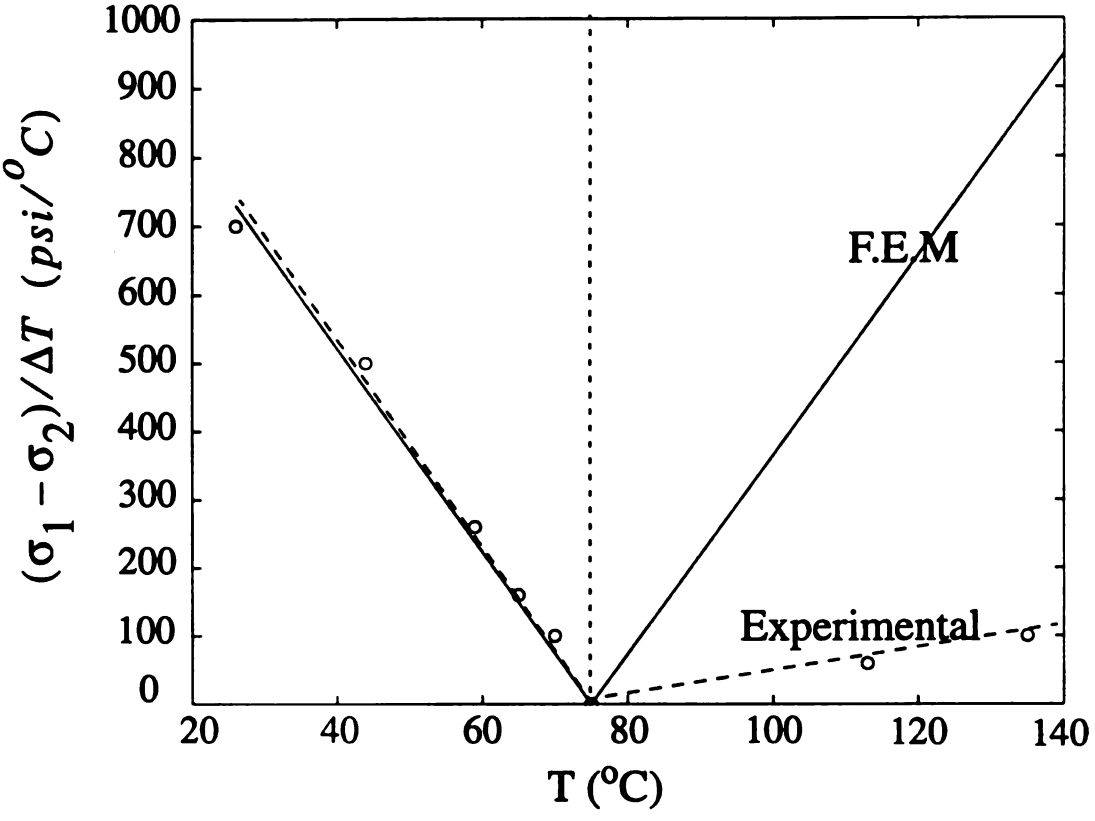

Fig. 3.46. Comparison between experimental and numerical results of maximum $(\sigma_1 - \sigma_2)/\Delta T$ $(psi/^oC)$ in an epoxy matrix around a cast-in-place copper inclusion subjected to thermal heating.

CHAPTER 4

TASK 3: THE DAMAGE INITIATION AND PROPAGATION IN A MODEL COMPOSITE WITH AN EMPHASIS ON CRACK INITIATION AND PROPAGATION IN AN ELASTIC PLATE WITH RANDOMLY DISTRIBUTED HOLES.

In this chapter we consider the crack initiation and propagation in elastic-brittle (epoxy) and elasto-plastic (aluminum) thin sheets containing randomly arranged circular holes. The specimens are subjected to a uniaxial tension. We study a single configuration of a random arrangement both numerically, by using a finite element method, and experimentally. The goal of this study is to predict numerically the crack path which is in agreement with the crack patterns obtained experimentally. This study will set a framework for a fracture analysis of more complex two or three phase composite materials with randomly arranged inclusions.

EXPERIMENTAL STUDY

The experimental set-up involved thin perforated sheets made of either an epoxy or an aluminum, each containing 31 randomly distributed non-overlapping circular holes of the same size (volume fraction of holes is 23% in the portion of the specimen away from the edges). The distribution of holes was obtained by generating random numbers to simulate the loci of the holes' centers. We imposed restrictions that the holes did not overlap, they

were located at least one diameter away from the edges of the specimen and the distance between the holes was at least 0.1 a, where a was the hole radius. The dimensions of each epoxy plate were 3.5"x13.0"x0.125" and the holes were 0.25" in diameter. The holes were introduced in the following way. For the case of an epoxy material the plates were placed one at a time between the two steel plates and drilled at a slow speed to reduce residual stresses caused by machining. Then, the remaining residual stresses were removed by annealing the epoxy plate to a temperature beyond the glass transition temperature which was for our case 160°C. For the case of aluminum sheets the holes were drilled according to the desired random arrangement.

After the preparation of the epoxy samples the photoelasticity method was used to find the stress distributions in these birefringent perforated plates. In order to determine the material fringe value f_σ for the epoxy material used, different levels of loading were applied to either specimens with a hole or to a four-point-loaded beam. It is known from theory of plane elasticity (Michell, 1899; Timoshenko and Goodier, 1956) that, when a material with holes is subjected to tractions and the resultant of forces over each hole boundary vanishes, the stress field is independent of elastic constants. Thus, the stresses obtained from the analysis of fringe patterns are applicable for both material systems studied, when they are in the elastic range.

The crack propagation tests were conducted using an Instron testing machine that could apply a constant displacement rate boundary condition. An ASTM standard D2343 requires the use of a cross head speed of 2 mm/min. This recommended cross head speed is used by many other ASTM standards in cases where the stress is distributed uniformly along the tested cross section. In a material with holes the stress is not uniform and thus

the stress concentration is more than 1.0. In our experiments we used a cross head speed of 0.1 mm/min. (.04 in/min). To monitor crack propagation and final crack pattern a high speed camera, which could capture 3000 frames/sec., was used. The video camera was connected to an image digitizer and the output was directed either to a super VCR or a thermal printer. The recorded image was then stored in the computer and studied frame by frame to determine a site of crack initiation and crack paths. This experiment was done for a single random configuration of holes only but it was repeated on several epoxy and aluminum specimens. More details on experimental set up is included in the Appendix (pp. 272-280).

NUMERICAL SIMULATIONS OF FRACTURE

In addition to conducting experiments we also studied the above problem numerically. We used a commercial finite element program ANSYS 5.1 to explore the issue of crack initiation and propagation in elastic-brittle epoxy and elasto-plastic aluminum sheets perforated with circular and randomly arranged holes of equal size as described in the previous section. We subjected the boundary of the tested specimens to the kinematic boundary conditions $u_i = \varepsilon^0_{ij} x_j$ where $\varepsilon^0_{ij} = \varepsilon^0_{yy}$. In the modeling of crack initiation and growth we used the approach involving a removal of elements. For the epoxy sheet we simulated cracking by either removing the elements with the highest strain energy or the elements that had a maximum principal stress exceeding the tensile strength of the material. In the second case for example, if the largest of the in-plane principal stresses σ_1 and σ_2 in an element exceeded a tensile strength of the matrix, we removed that element and repeated the same steps under the same loading until a stable condition was reached (i.e. no element

had a stress exceeding the tensile strength of the matrix); then we increased the load by a small increment and repeated the procedure until the whole specimen fractured. For the aluminum sheet we employed the criterion used by Becker and Smelser (1994) which predicts the onset of fracture when the strain in the thickness direction ε_{zz} in a shin sheet is reduced by 25%. We also used two different mesh sizes by assigning element sizes of $0.2a$ and $0.4a$ around the boundary of each hole. In our numerical modeling we were interested not only in the final crack patterns but also in the crack growth. We may also point out that we did not do remeshing, i.e. we stayed with the same fine mesh for the whole crack simulation process. We have used this crude approach for simplicity. Also, we only did a static fracture analysis and neglected viscoelastic effects.

RESULTS AND DISCUSSION

The local stress fields

Studying the local stress field will give an insight in the damage initiation, especially for brittle materials. The local stress field in a material with randomly arranged holes under a remote tension, as considered in our numerical examples and experiments, is very complex and will differ for each random arrangement. Thus, in order to gain a fundamental understanding of the stress fields and the sites of crack initiation in a material with randomly arranged and interacting holes we first consider simpler geometries involving a single hole and two holes. The single hole solution is applicable for the dilute case in which holes are far away from each other and they don't interact, but it also gives a basic understanding of the stress fields in a perforated sheet with many holes. The results of a single hole solution using analytical, numerical and experimental techniques are illus-

trated in Figs. 4.1-4.3 and the Table 4.1 which shows a good agreement between our solutions using these three methods. The fringes around a single hole start forming in a plane perpendicular to the applied loading, at $\theta = 0$, which is a location of the maximum stress, then migrate along its line of action, $\theta = \pi/2$.

When more than one hole is present the problem of finding local stresses becomes very complex due to the elastic fields interaction. The elasticity problems of two holes or inclusions were solved analytically by Kouris and Tsuchida (1991), and the problem of multiple holes or inclusions by Gong and Meguid (1993). These solutions involved a considerable mathematical effort. In this chapter, for simplicity, we use the photoelasticity and finite element methods to evaluate the stress field in a sheet with randomly distributed holes.

A similar behavior, in terms of the fringe pattern formation, to that observed for a single hole case, illustrated in Figs. 4.1-3, is seen in the case of a composite with the 23% and 31% volume fraction of randomly distributed holes both experimentally (Figs. 4.4-5) and numerically (Figs 4.6-7). Figs. 4.4-5 show the isochromatic fringe patterns obtained by the photoelasticity method for an epoxy matrix with randomly distributed holes of volume fractions of 23% and 31%. In the latter case the holes' centers are in the same locations but the hole size is larger and it is 0.3125" in diameter. Figs. 4.6-7 give typical finite element stress contours of $(\sigma_1 - \sigma_2)/\sigma_o$. Both numerical and experimental results show a good agreement (Table 4.2). For the same geometric distribution, the stress field in the perforated sheet with a higher volume fraction of holes (larger holes) is higher in magnitude, which means an earlier sign of cracking and a lower overall strength. Figs. 4.4-7 show a localization and a nonuniform distribution of stresses between the holes. This

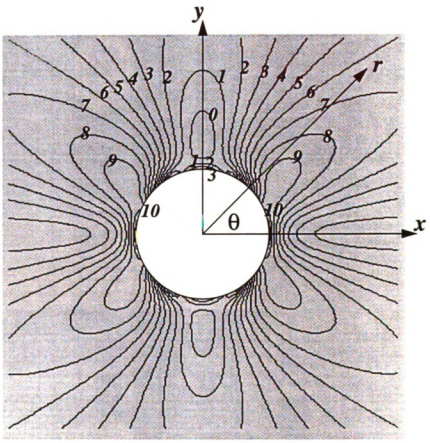

Note: contour value=0.3

Figure 4.1 Analytical stress contours of $(\sigma_1 - \sigma_2)/\sigma_0$ around an isolated hole for an applied loading in the vertical direction.

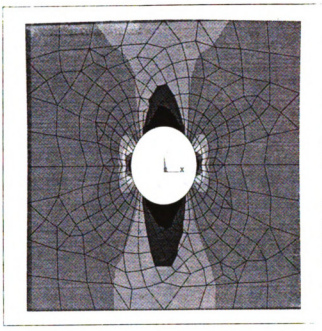

a)

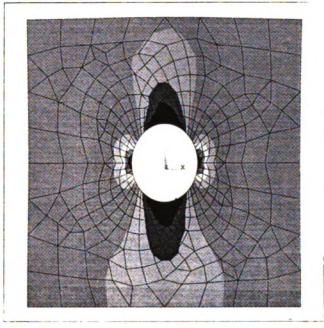

b)

Figure 4.2 Finite element contours of a) $(\sigma_1 - \sigma_2)/\sigma_0$ and b) $(max(\sigma_1, \sigma_2))/\sigma_o$ around an isolated hole for an applied uniaxial tensile loading in the vertical direction.

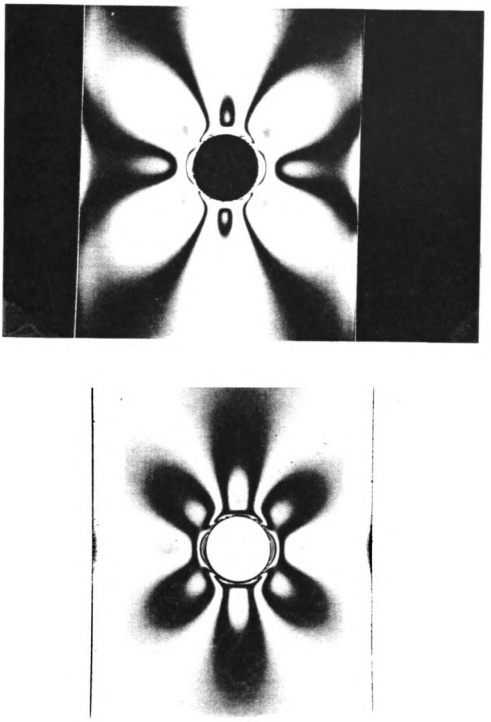

Fig. 4.3 Isochromatic fringe pattern obtained by photoelasticity for an epoxy matrix with a holes and subjected to a uniaxial tensile loading of 1 ksi.

4.1 A comparison between analytical, experimental and numerical results for $\left(\sigma_1^m - \sigma_2^m\right)/\sigma_o$ for an elastic plate with a single hole.

		Analytical	Experimental	Numerical
$\left(\sigma_1^m - \sigma_2^m\right)/\sigma_o$	$\theta = 0$	3.0	3.0	2.8
	$\theta = \pi/2$	1.0	0.9	0.9

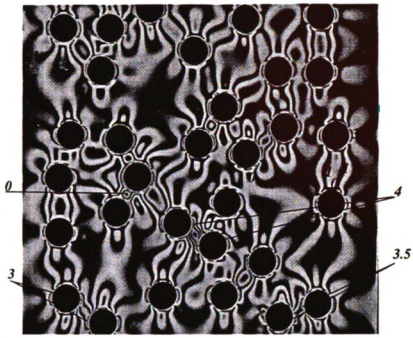

Fig. 4.4 Isochromatic fringe pattern obtained by photoelasticity for an epoxy with a 23% volume fraction holes at the middle portion of specimen and subjectedto uniaxial transverse loading of 492.5 psi in the vertical direction.

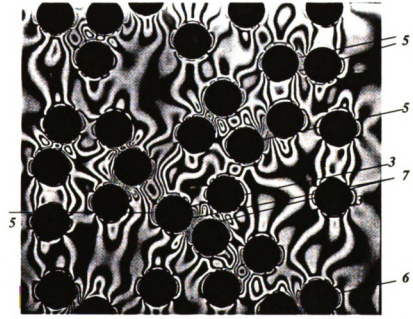

Fig. 4.5 Isochromatic fringe pattern obtained by photoelasticity for an epoxy matrix with a 31% volume fraction holes at the middle portion of the specimen and subjected to a uniaxial load of 492.5 psi in the vertical direction.

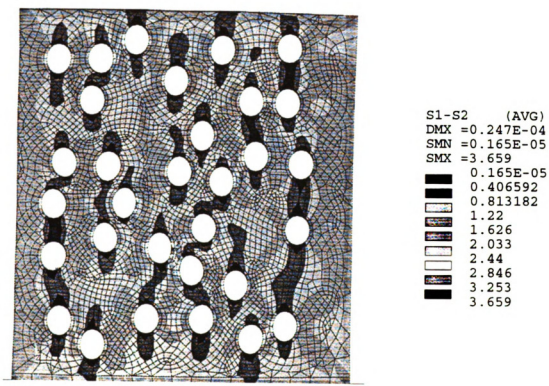

Fig. 4.6 Stress contours of $(\sigma_1 - \sigma_2)/\sigma_o$ in an elastic sheet with holes of volume fraction 23% and subjected to a uniaxial tensile loading in the vertical direction.

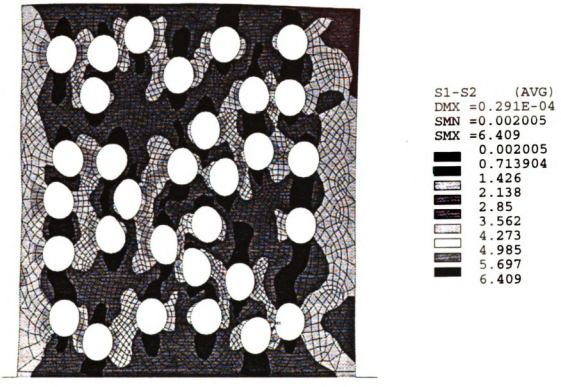

Fig. 4.7 Stress contours of $(\sigma_1 - \sigma_2)/\sigma_o$ in an elastic sheet with holes of volume fraction 31% and subjected to a unit uniaxial tensile loading in the vertical direction.

4.1 A comparison between analytical, experimental and numerical results for $\left(\sigma_1^m - \sigma_2^m\right)/\sigma_o$ for an elastic plate with randomly arranged holes holes.

	volume fraction (f)	Experimental	Numerical
$\left(\sigma_1^m - \sigma_2^m\right)/\sigma_o$	0.23	3.5	3.7
	0.31	6.2	6.4

is in contrast with the periodic arrangement in which the distribution of stresses is more uniformly distributed and each hole will have the same stress in its vicinity. The maximum stress and thus the possible location of damage initiation in an elastic sheet with randomly distributed holes will be between the two inclusions arranged in the most critical geometric arrangement. The stress field disturbed by the presence of two holes depends on the separation distance between the holes, their location with respect to the applied loading, and the surrounding environment (neighboring inclusions). Figs. 4.8a-c show the stress contours of the maximum in-plane principal stress, $max(\sigma_1, \sigma_2)$, in an elastic sheet with two holes aligned at different inclination angles. Note that the maximum stress is always at a plane perpendicular to the applied loading regardless of the inclination of the two holes with respect to one another. Thus, the worst scenario of arrangement of two holes will occur when the holes are aligned in a direction almost perpendicular to the applied loading, as shown in Fig. 4.9, which represents the maximum principal stress between two holes separated by a constant distance d, which we take as $d = a$. This is not surprising as that geometry resembles the nucleation of a crack from a chain of voids.

When the holes are aligned along the line of action of the applied loading, the stress is minimum and less or equal to the one in the case of an isolated hole, which has a stress concentration of 3, depending on the separation distance. As the two holes get closer to each other the stress concentration increases if the two holes are aligned in a plane perpendicular to the applied loading but it decreases if they are aligned along the line of action of the applied loading as illustrated in Fig. 4.10. The effect of adding more holes along a particular path is summarized in Fig. 4.11 and Table 4.3.

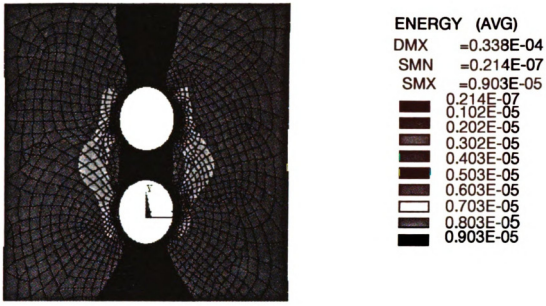

Fig. 4.8a Stress contours of $(max(\sigma_1, \sigma_2))/\sigma_o$ in an elastic sheet with two hole alignedat $\theta_{inc} = \pi/2$ for an applied loading in the vertical direction.

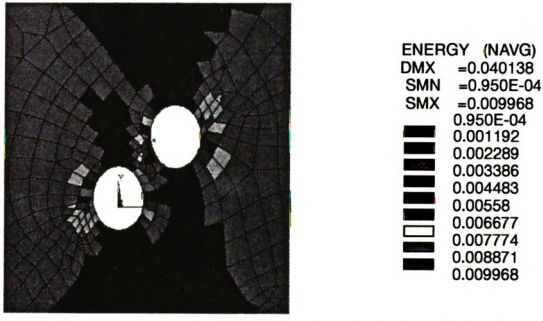

Fig. 4.8a Stress contours of $(max(\sigma_1, \sigma_2))/\sigma_o$ in an elastic sheet with two hole alignedat $\theta_{inc} = \pi/4$ for an applied loading in the vertical direction.

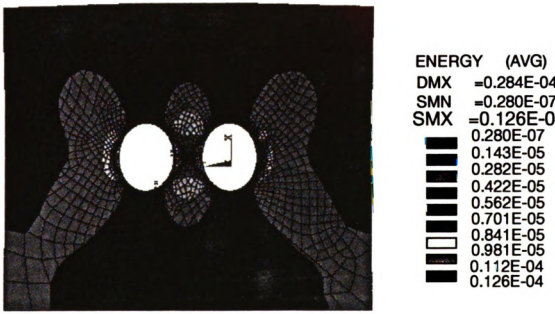

Fig. 4.8c Stress contours of $(max(\sigma_1, \sigma_2))/\sigma_o$ in an elastic sheet with two hole aligned at $\theta_{inc} = 0$ for an applied loading in the vertical direction.

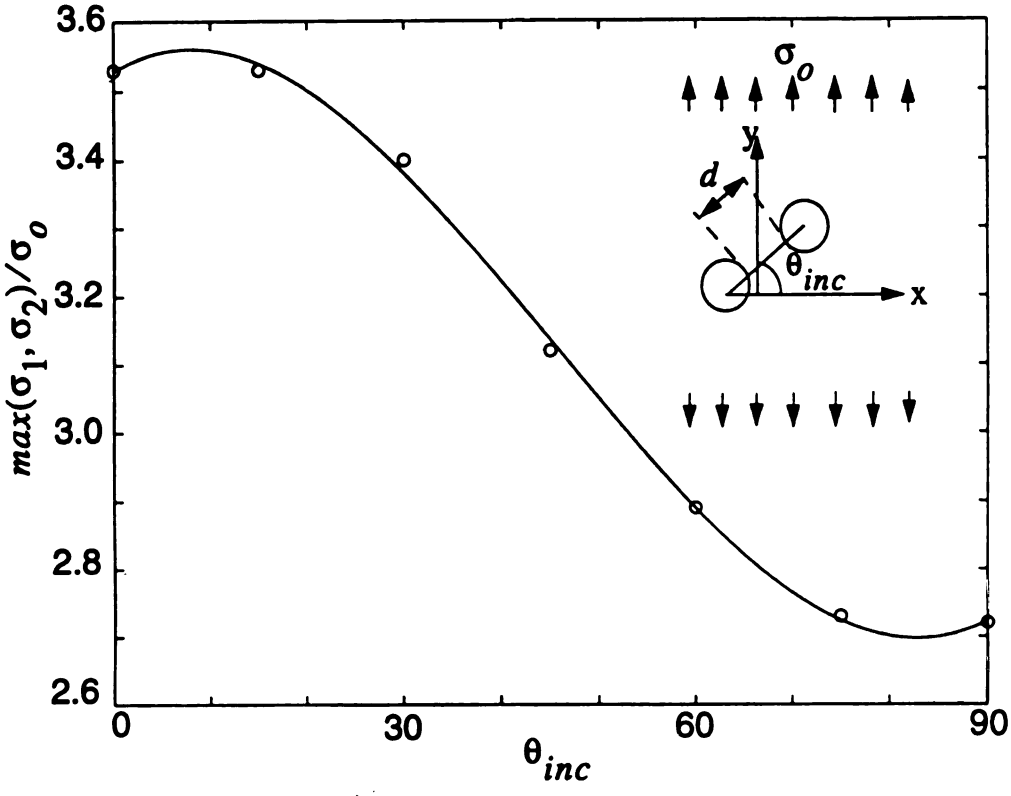

Fig. 4.9 Effect of inclination angle θ_{inc} on the maximum principal stress $(max(\sigma_1, \sigma_2))/\sigma_o$ in an elastic sheet with two holes separated by a constant distance d = a.

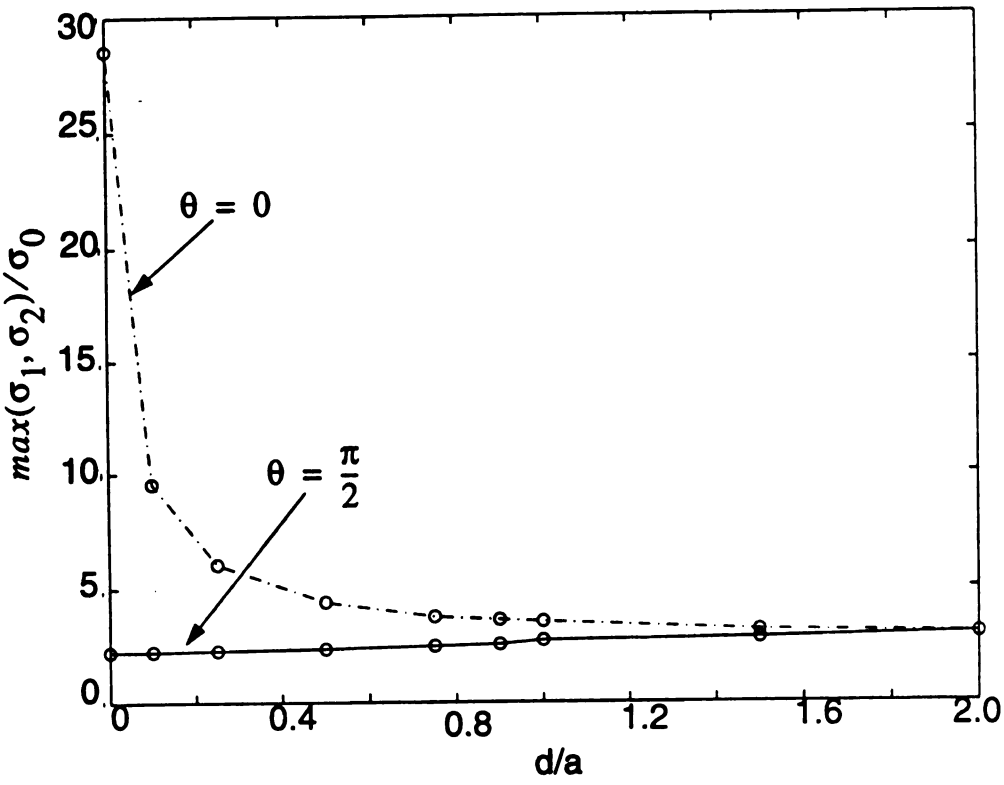

Fig 4.10 Effect of separation distance between two holes inclined at $\theta_{inc} = 0$ or $\theta_{inc} = \pi/2$ on the maximum principal stress $(max(\sigma_1, \sigma_2))/\sigma_o$ in an elastic sheet.

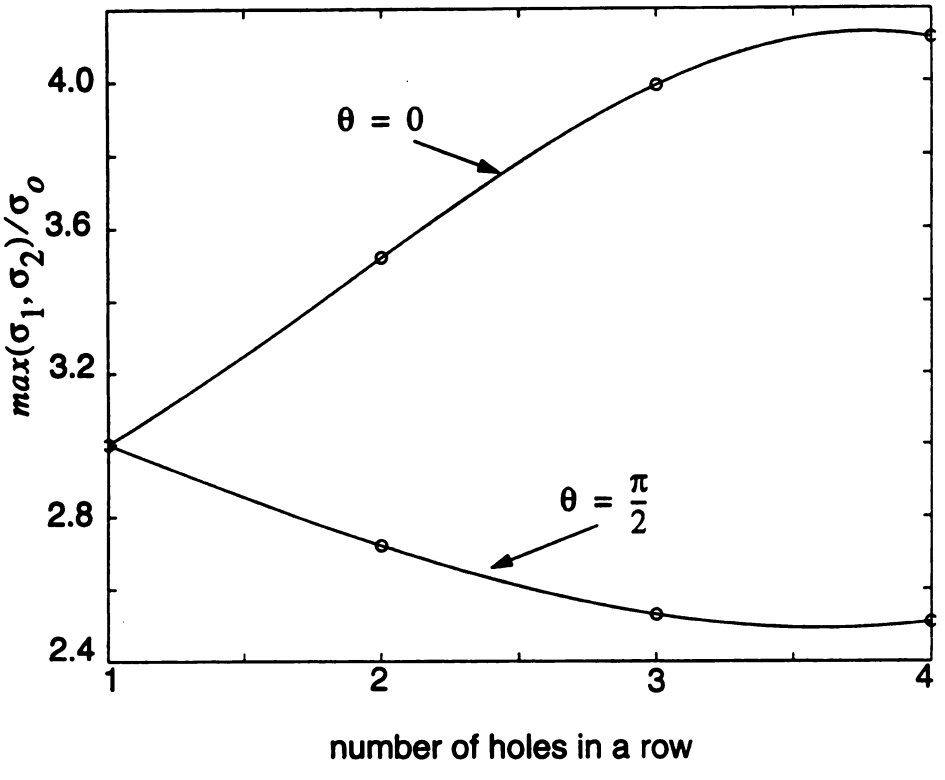

Fig 4.11 Effect of number of holes in a row inclined at $\theta_{inc} = 0$ or $\theta_{inc} = \pi/2$ with a separation distance of $d = a$ between each two holes on the maximum principal stress in an elastic sheet.

Table 4.3. Effect of arrangement on maximum principal stress in an elastic brittle sheet with holes.

Arrangement	$max(\sigma_1, \sigma_2)/\sigma_0$
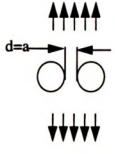	3.52
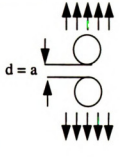	2.72
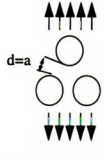	3.34
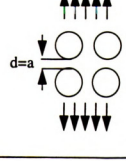	3.41

Crack initiation and propagation in a sheet with non-uniformly arranged holes.

To study the crack initiation and propagation experimental and numerical techniques were used. Numerically, crack propagation was simulated by removal of elements and either adaptive meshing (Fig. 4.12a) or random meshing (4.12b). Experimentally a high speed camera was used to monitor the crack initiation and propagation. Note that in Figure 4.12b, where both holes are located along the line of action of the applied uniaxial tensile loading, $\theta_{inc} = \pi/2$, and if we assume that the material is perfectly homogeneous and the holes are identical, both holes give rise to the same stress concentration factor and thus have the same chance for the crack initiation. However, due to small numerical differences, small differences in the mesh, one of them will have a slightly higher stress concentration factor and the crack will initiate at that hole. The similar behavior can be observed experimentally and is due to material imperfections, for example.

Cracking of a brittle material

Fig. 4.13 demonstrates crack progress in an epoxy matrix with 31% volume fraction holes as recorded by a high speed camera with 1000 frames/second. Fig. 4.14 shows a crack propagation in two epoxy samples with 23% volume fraction using a high speed camera with 1000 and 2000 frames/ second. Our experimental study of crack initiation and propagation in a brittle material (epoxy) with randomly distributed holes indicates a catastrophic failure, as shown in Figs. 4.13 and 4.14, where the crack propagates with a speed approximately equal to the sonic speed (1020 ft/s or 340 m/s). In our numerical study of a specimen with 31 randomly arranged holes four fracture criteria are used to identify the location of a crack initiation, namely the maximum principal stress criterion,

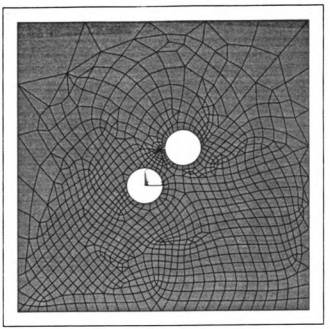

a)

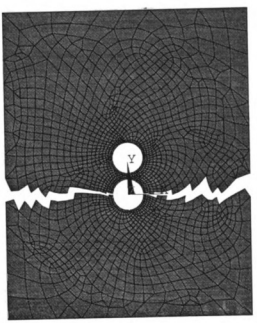

b)

Fig. 4.12 Crack propagation between two isolated holes using a) adaptive meshing technique b) a relatively crude mesh.

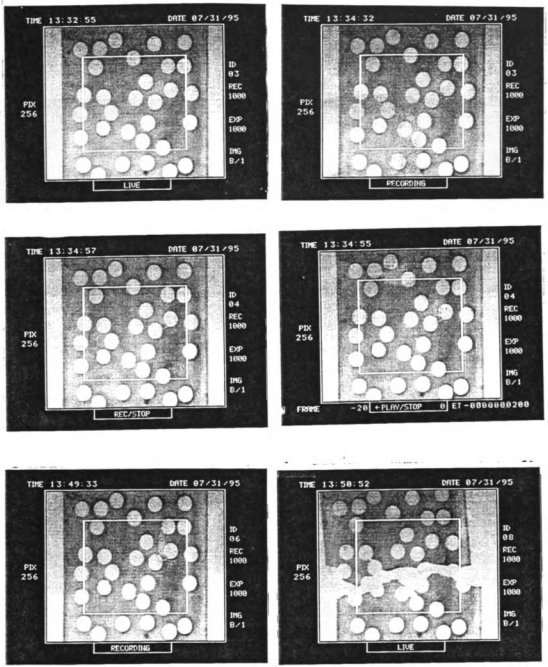

Fig. 4.13 Crack initiation and propagation in an epoxy sheet, with randomly distributed holes of volume fraction f = 31%, subjected to a uniaxial displacement in the vertical direction (experimentally).

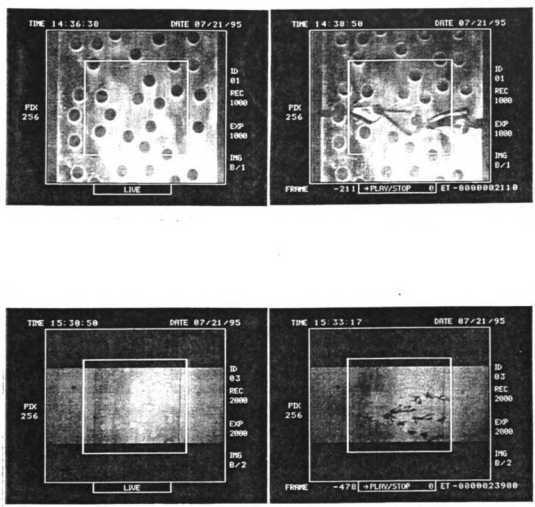

Fig. 4.14 Crack initiation and propagation in an epoxy sheet with randomly distributed holes of volume fraction (f = 23%), subjected to a uniaxial displacement loading (experimentally), for two different samples.

the minimum strain energy criterion, the maximum circumferential stress criterion, and the minimum thickness criterion. In Fig. 4.15 the minimum strain energy criterion was used and twelve selected steps of crack propagation are shown as obtained using FEM. The location of the crack initiation is found to be the same regardless of the criterion used and it is between the two most closely spaced holes as shown, for example, in Figs. 4.6-7. This agrees with our experimental and numerical results for all samples considered. However our numerical results using finite element (Figs. 4.16-17) and finite difference (Ostoja-Starzewski and Lee, 1996) (Fig. 4.18) methods show different crack paths for different failure criteria.

Similarly, we obtain experimentally several different crack patterns by fracturing several specimens with the identical hole arrangements; different crack patterns are shown in Figs. 4.19 and 4.20 for cases of volume (area) fraction f = 31% and f = 23%, respectively. Schematic plot of final crack paths of seven specimens of the same geometric arrangement with f = 23% and subjected to the same loading conditions is shown in Fig. 4.21. A similar response in terms of crack scatter was observed for the case of a higher volume fraction of f = 31% (Fig. 4.22).

In spite of the crude way of simulating the crack propagation, at least two of the crack patterns (the outer crack paths shown in Fig. 4.21) are predicted numerically by using two different fracture criteria: the maximum principal stress criterion (Figs. 4.18a,b) and the minimum elastic strain energy (Fig. 4.18c) and using the spring removal technique in the finite difference approach (Fig. 4.20). However, the middle path of Figs. 4.21 is not predicted numerically by using a deterministic static analysis. The scatter in crack pattern is larger at the right portion of the test specimens. Since, as observed experimentally, this

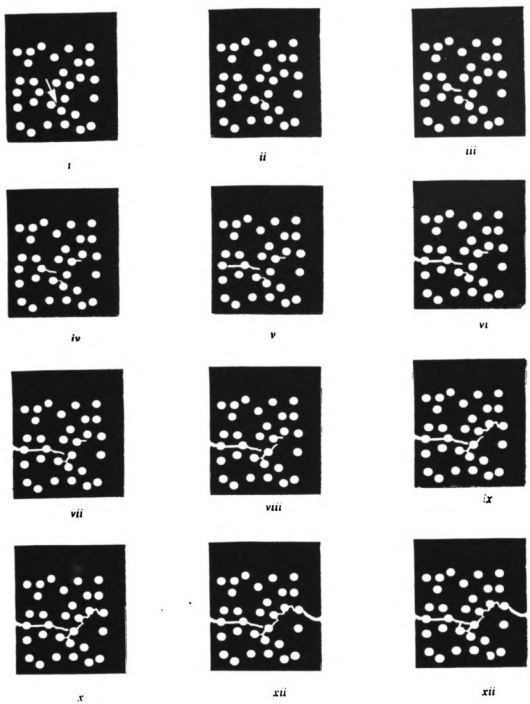

Fig. 4.15 Crack initiation and propagation in an epoxy sheet, with randomly distributed holes, subjected to a uniaxial tensile loading using the elastic strain energy fracture criterion with a mesh size = 0.4a around the holes (selected 12 steps) as obtained by a finite element method.

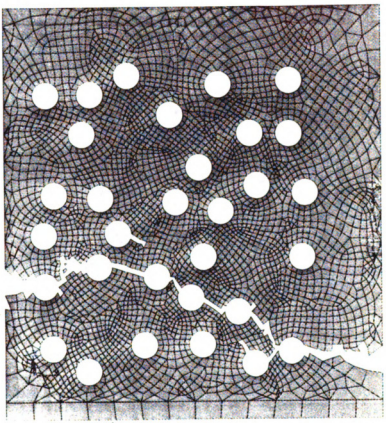

Fig. 4.16a The final crack pattern obtained numerically by finite element method using the maximum principal stress criterion with a mesh size of *0.4a* around the holes for a brittle elastic material with volume fraction f=23% of holes for the vertical uniaxial displacement.

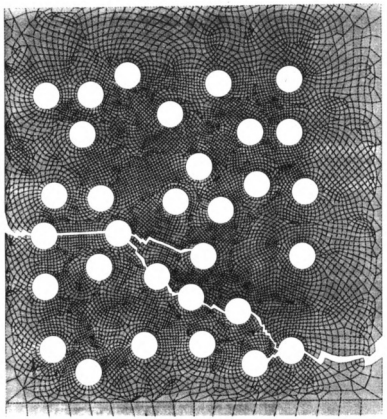

Fig. 4.16b The final crack pattern obtained numerically by finite element method using the maximum principal stress fracture criterion with a mesh size of $0.2a$ around the holes for a brittle elastic material with volume fraction f=23% of holes for the vertical uniaxial displacement.

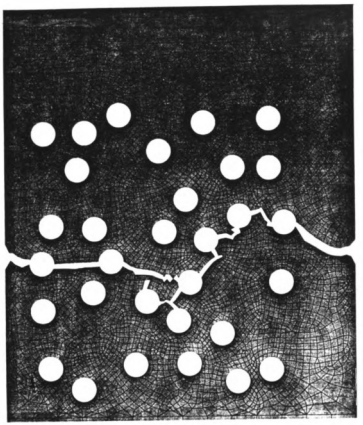

Fig. 4.16c The final crack pattern obtained numerically by finite element method using the elastic strain energy fracture criterion with a mesh size of *0.4a* around the holes for a brittle elastic material with volume fraction f=23% of holes for the vertical uniaxial displacement.

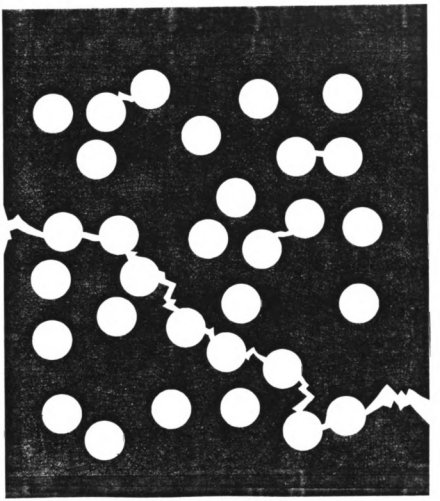

Fig. 4.17a The final crack pattern obtained numerically by finite element method using the maximum principal stress criterion with a mesh size of *0.4a* around the holes for a brittle elastic material with volume fraction f=31% of holes for the vertical uniaxial displacement.

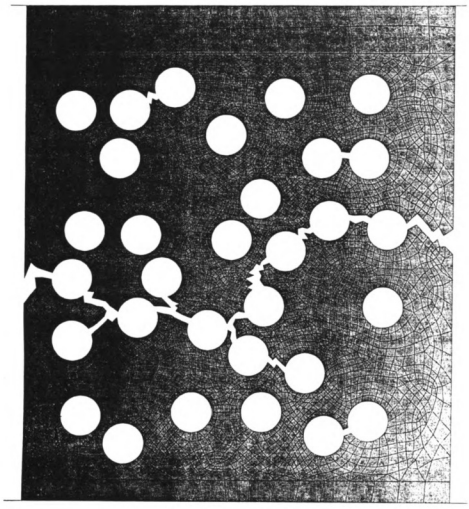

Fig. 4.17b The final crack pattern obtained numerically by finite element method using the elastic strain energy fracture criterion with a mesh size of *0.4a* around the holes for a brittle elastic material with volume fraction f=31% of holes for the vertical uniaxial displacement.

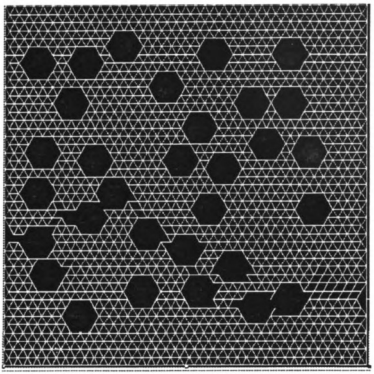

Fig. 4.18a Final crack pattern in a brittle elastic material with holes of volume fraction f = 23% obtained numerically using the finite difference method for a mesh size of *0.67a*.

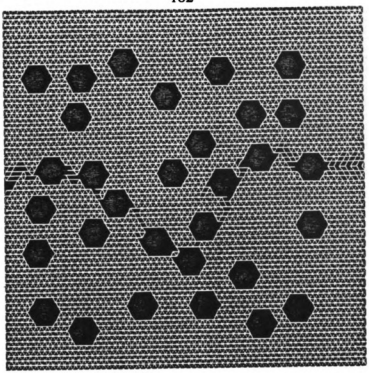

Fig. 4.18b Final crack pattern in a brittle elastic material with holes of volume fraction f = 23% obtained numerically using the finite difference method for a mesh size of *0.4a*.

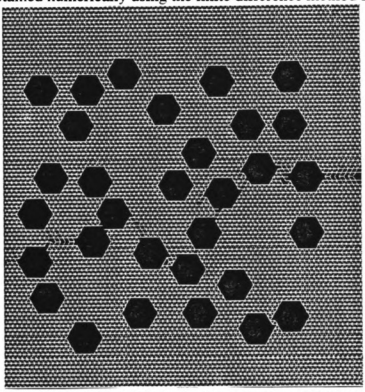

Fig. 4.18c Final crack pattern in a brittle elastic material with holes of volume fraction f = 23% obtained numerically using the finite difference method for a mesh size of *0.25a*.

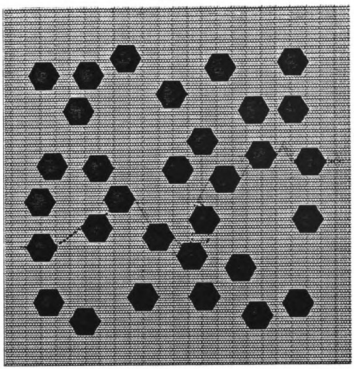

Fig. 4.18d Final crack pattern in a brittle elastic material with holes of volume fraction f = 23% obtained numerically using the finite difference method for a mesh size of *0.2a*.

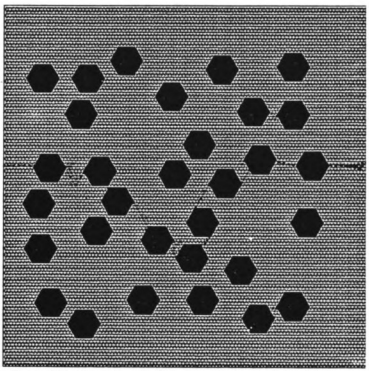

Fig. 4.18e Final crack pattern in a brittle elastic material with holes of volume fraction f = 23% obtained numerically using the finite difference method for a mesh size of *0.167a*.

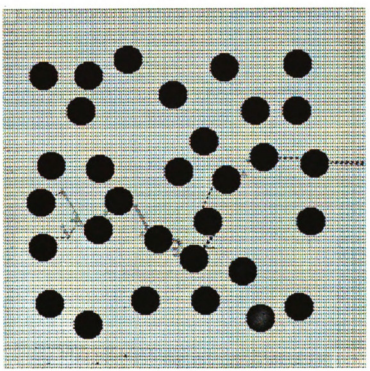

Fig. 4.18f Final crack pattern in a brittle elastic material with holes of volume fraction f = 23% obtained numerically using the finite difference method for a mesh size of $0.13a$.

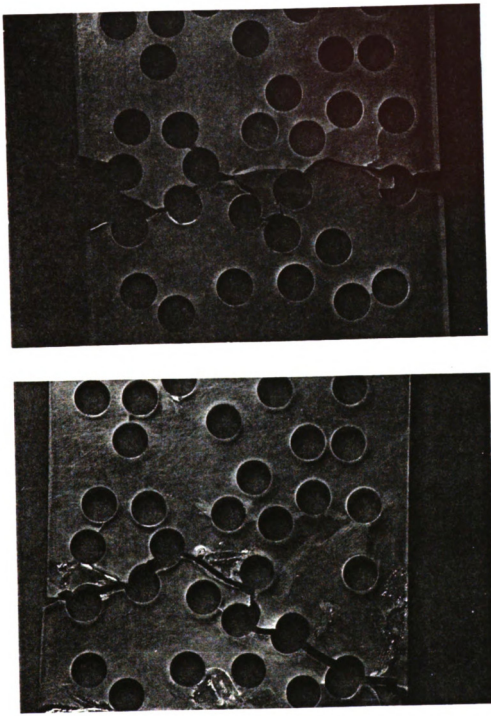

a)

b)

Fig. 4.19 Final crack pattern in an epoxy sheet with randomly distributed holes, subjected to a uniaxial displacement loading, obtained experimentally from two samples with the same hole arrangement with volume fraction f = 31%.

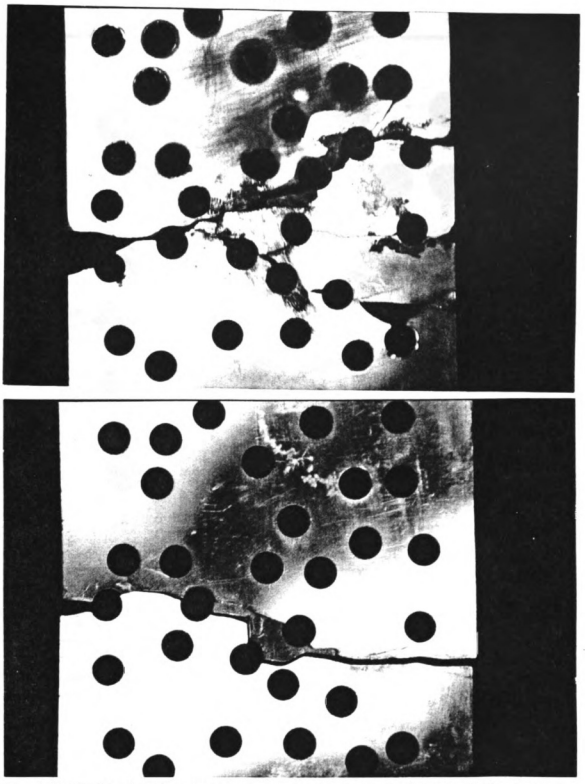

Fig. 4.20 Final crack pattern in an epoxy sheet with randomly distributed holes, subjected to a uniaxial displacement loading as obtained experimentally from two samples with the same hole arrangement with volume fraction f = 23%.

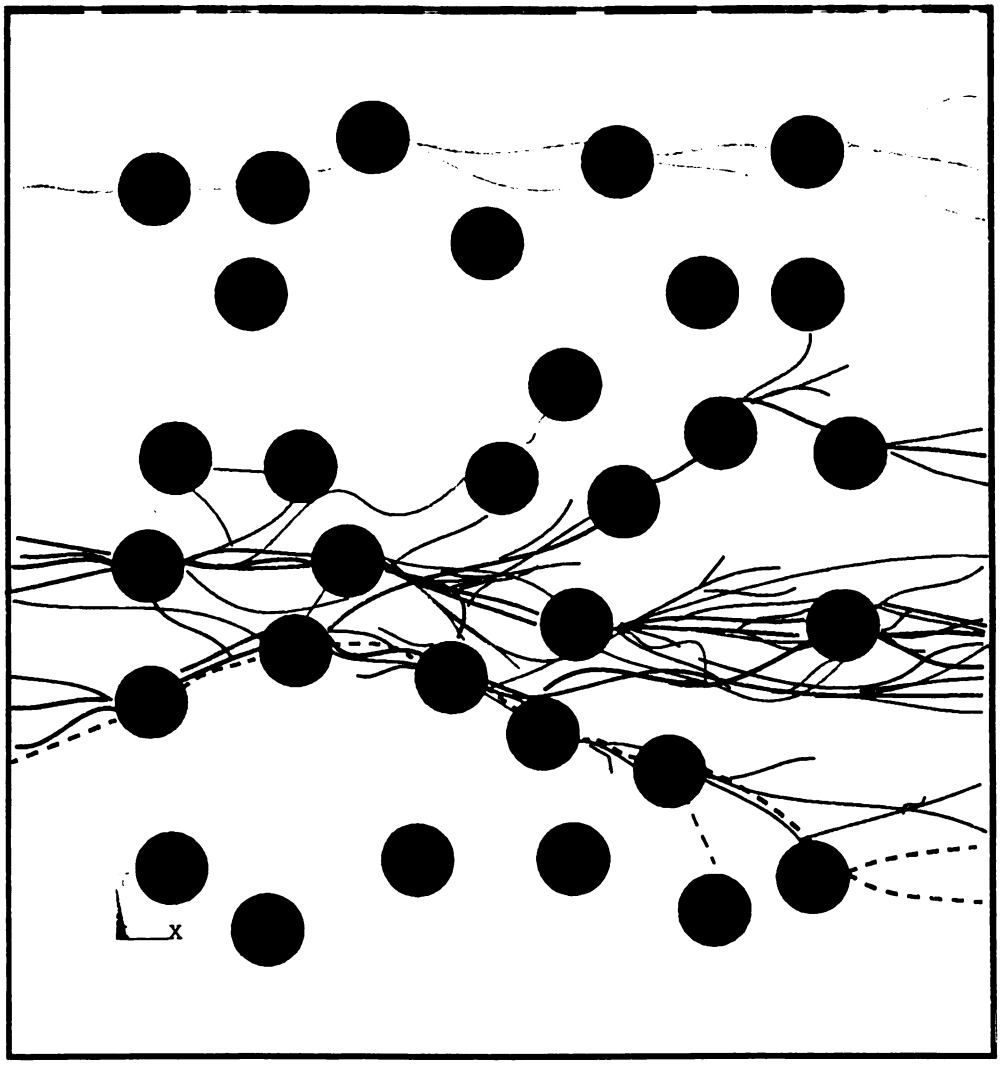

Fig. 4.21 Schematic plot of the final crack pattern in an epoxy sheet with randomly distributed holes and subjected to a uniaxial displacement loading, obtained experimentally, from seven samples with the same hole arrangement with volume fraction f=23%.

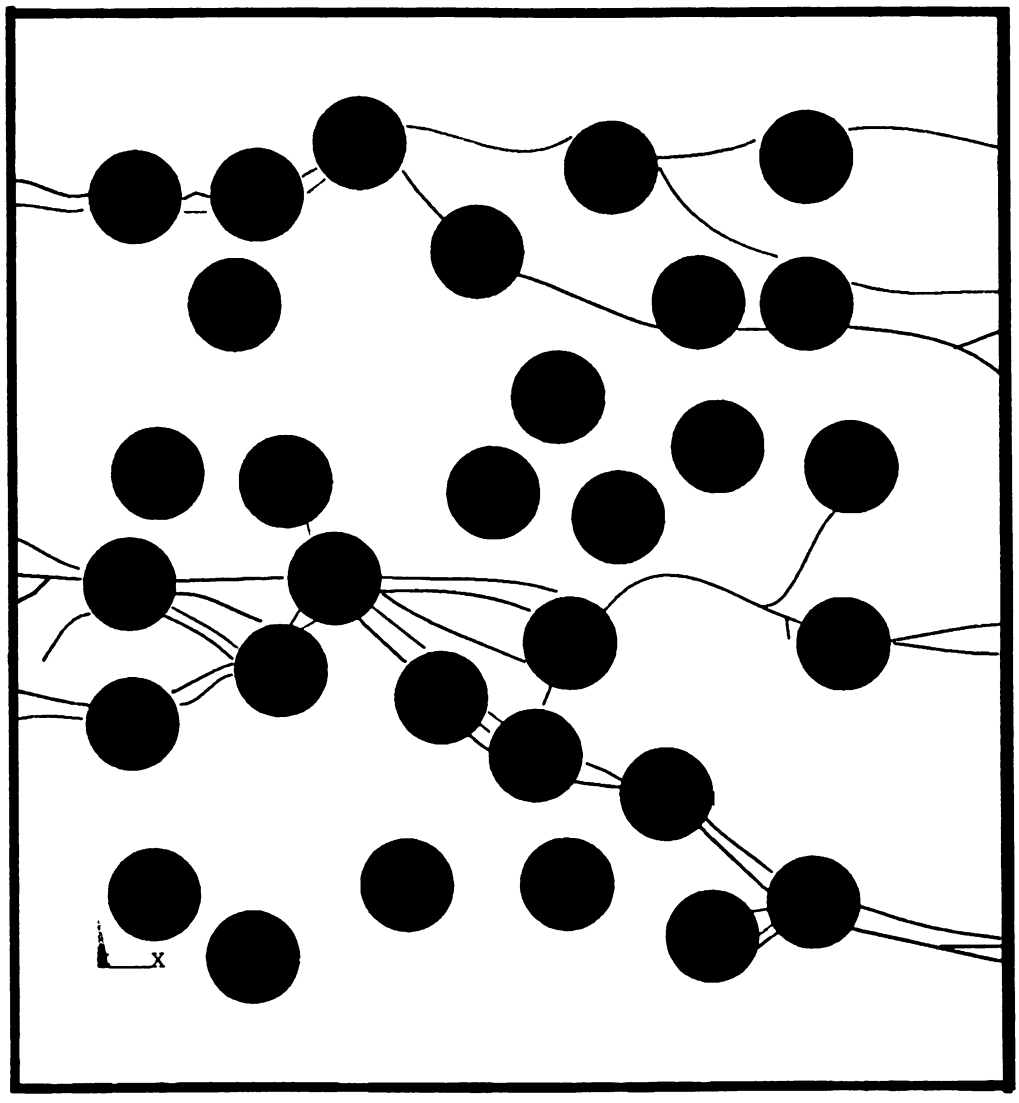

Sample # 1
Sample #2
Sample # 3
Sample # 4
Sample # 5

Fig. 4.22 Schematic plot of the final crack pattern in an epoxy sheet with randomly distributed holes, subjected to a uniaxial displacement loading, obtained experimentally from five samples with the same hole arrangement with volume fraction f = 31%.

is the final portion of the crack and the crack length is already large, we have a catastrophic failure with a dynamic crack propagation. Therefore, a dynamic analysis will be considered in the future.

We also studied crack initiation and propagation in an epoxy matrix with randomly arranged inclusions coated with a very compliant layer. Since the local stress field of such composite is very similar to the stress field around circular holes (Fig. 2.10a) of volume fraction of 31% we combine the results of crack paths in case of random holes with f=31% (Fig. 4.22) with crack paths obtained in case of a compliant coating (Fig. 4.23). The results are shown in Fig. 4.24. Fig. 4.25a represents crack propagation in an epoxy matrix with randomly distributed and coated inclusions with a compliant coating. Note the similarity with the results obtained in the case of a similar random arrangement of holes of the same size. Note also branching of cracks in case of cracking of a brittle material (Fig. 4.25b). The non-uniqueness of the experimental results may be understood as follows: in a sheet with thirty one inclusions there is, on purely combinatorial grounds, a very large number of geometrically acceptable crack paths cutting the specimen across. The energy release values associated with all these paths do not differ much from one another, and thus, a subset of them has practically the same numerical value. Therefore, minute material and geometric imperfections decide which crack path will actually take place in a particular specimen that is nominally (on the macroscopic scales) the same as the rest of the bunch. Thus, both experimental and numerical methods showed that the crack path is not unique and several crack paths were observed.

However, there are two major paths that are most likely for the specimen to crack along. To understand the cracking behavior better we considered partially cracked speci-

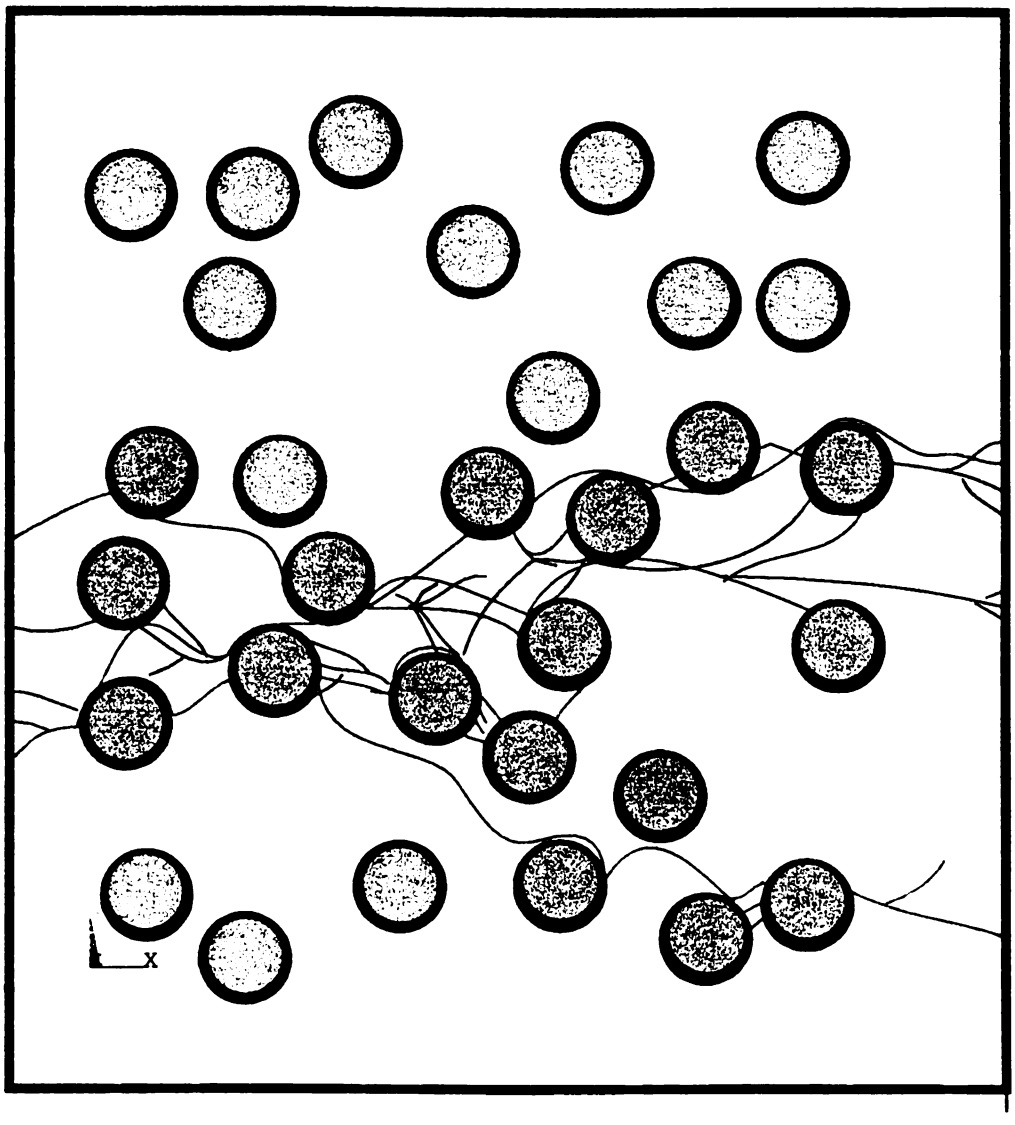

Fig. 4.23 Schematic plot of the final crack pattern in an epoxy sheet with randomly distributed coated inclusions with a compliant coating subjected to a uniaxial displacement loading, obtained experimentally from four samples with the same arrangement.

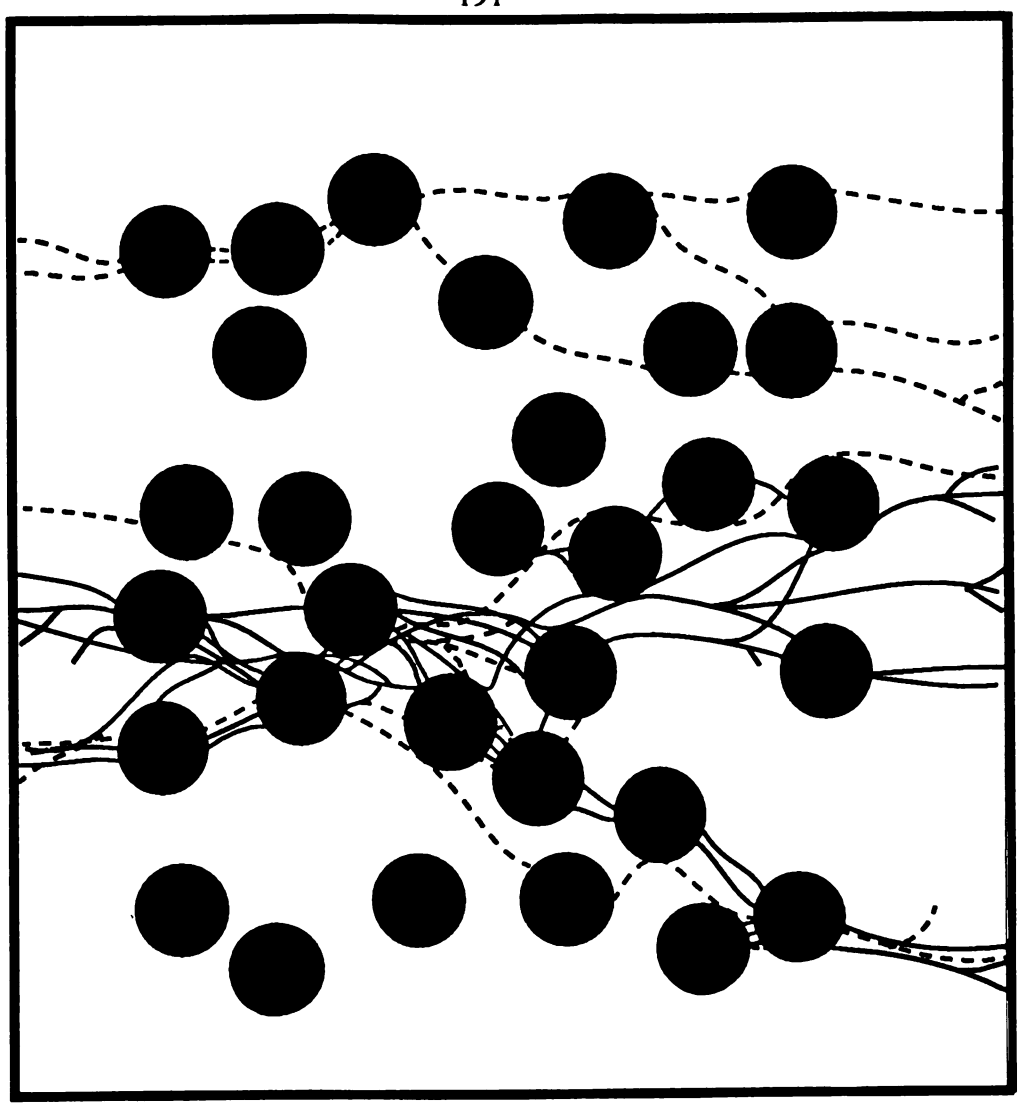

——————— *Sample # 1*
——————— *Sample #2*
——————— *Sample # 3*
——————— *Sample # 4*
——————— *Sample # 5*
- - - - - - - - *Sample # 6*
---------- *Sample # 7*
- — - — - — *Sample # 8*
- — - — - — *Sample # 9*

Fig. 4.24 Schematic plot of the final crack pattern in an epoxy sheet with randomly distributed holes or inclusions coated with a compliant coating and subjected to a uniaxial displacement loading obtained experimentally from nine samples with the same hole arrangement.

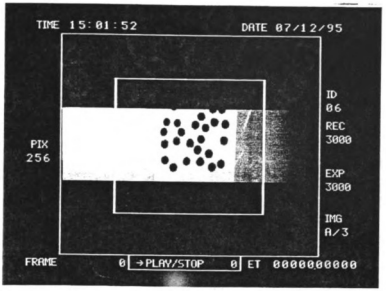

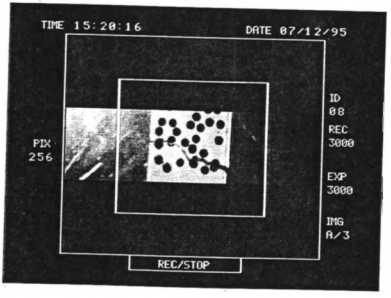

Fig. 4.25a. Crack initiation and propagation in an epoxy sheet with randomly distributed **Co**ated inclusions subjected to a uniaxial displacement loading (experimentally)

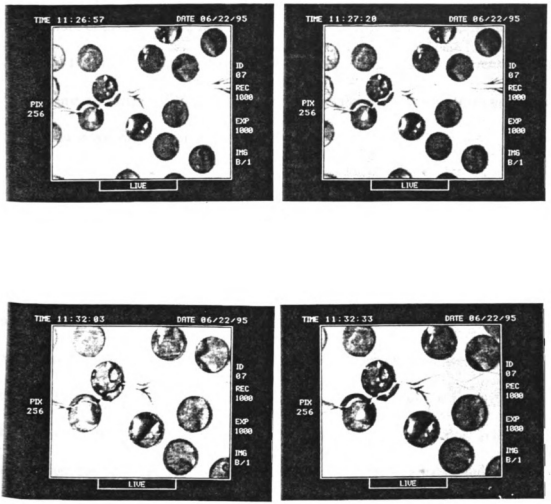

Fig. 4.25b Crack branching in an epoxy sheet with randomly distributed coated inclusions.

mens experimentally (Fig. 4.26) and numerically (Fig. 4.27). Both experimental and numerical results of partially cracked specimens show that all stresses are localized along two paths which are the major cracking paths. Also, to understand the relation between stress field and the final crack path we compare Figures 4.28 and 4.21 which show that the final crack path distribution is the same as the localized maximum stress distributions.

Failure of the epoxy matrix with randomly distributed holes is a brittle failure as shown in Fig. 4.29, which represents the stress-strain curve of seven different specimens of the same geometry and loading conditions. The failure load is higher for the specimens with a lower volume fraction of holes, as expected.

Cracking of ductile material

To further understand the nature of the crack propagation problem we also conducted experiments using aluminum sheets of the same geometry as the epoxy samples and the same distribution of holes which allow a slow crack propagation (Figs. 4.30 and 4.33). Whereas the final crack path of the brittle material contains many branches (Fig. 4.22 b), the final crack path of the aluminum sheet is associated with a plastic flow (Fig.4.31 and Fig.4.34). Experiments on the aluminum sheet show a major plastic flow in the two directions, then one path will dominate, and cracking will proceed in that direction. The schematics of the final crack paths in cases of f = 23% and f = 31% are shown in Figs. 4.32 and 4.35, and typical cracked specimens are shown in Figs. 4.31 and 4.34. Note both the plastic flow and the cracking in these figures. Numerically we used a minimum strain criterion (necking between holes) (Fig. 4.36). The aluminum sheet will crack if ε_{zz} is about -0.25, this value is based on an empirical formula (Becker and Smelser, 1994). Before cracking

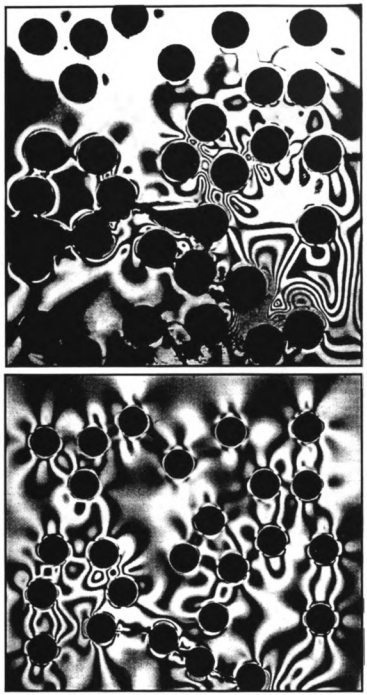

Fig. 4.26 Isochromatic fringe patterns of two partially cracked specimen using photoelasticity

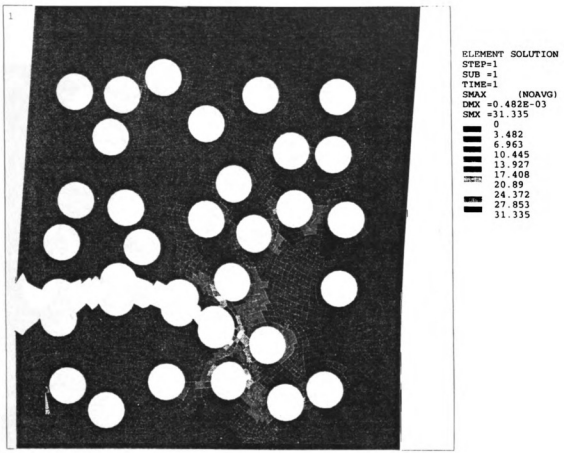

Fig 4.27 Stress contours of $(max(\sigma_1, \sigma_2))/\sigma_o$ of a partially cracked specimen subjected to a uniaxial tensile loading in the vertical direction using FEM.

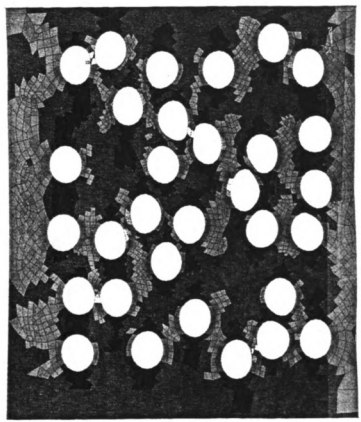

Fig 4.28 Stress contours of $(\sigma_1 - \sigma_2)/\sigma_o$ of an elastic material perforated with holes of f = 31% and subjected to a uniaxial tensile loading in the vertical direction which shows a localization of stresses.

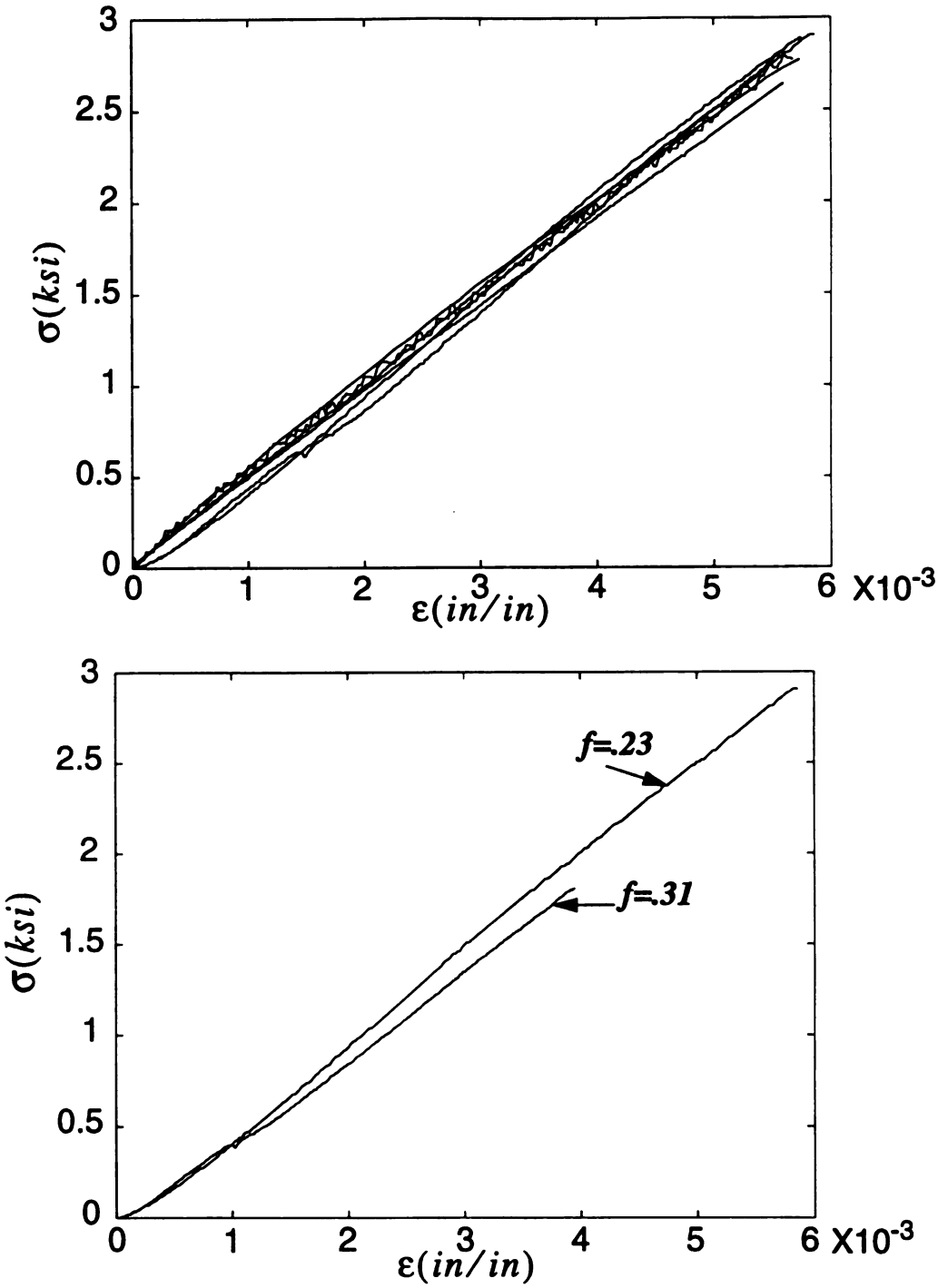

Fig 4.29 A typical stress-strain curve of an epoxy sheet with perforated holes a) seven different specimens of the same geometric arrangement with f=23% b) a comparison between elastic response of two sheets having two volume fractions of holes but same locations of hole centers.

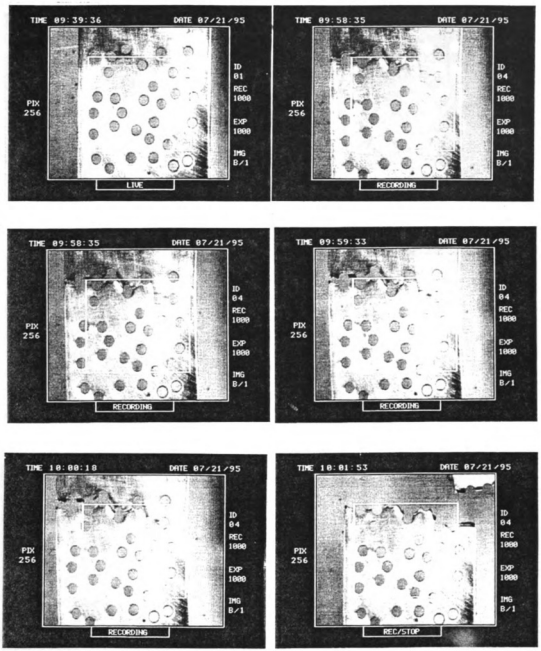

Fig. 4.30a Crack initiation and propagation in an aluminum sheet, with randomly distributed holes of volume fraction (f=23%), subjected to a uniaxial displacement loading (experimentally) for a selected sample.

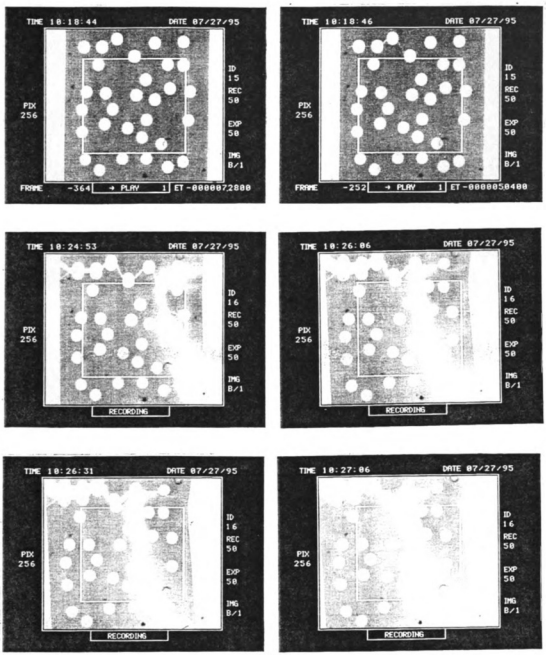

Fig. 4.30b Crack initiation and propagation in an aluminum sheet, with randomly distributed holes of volume fraction (f=23%), subjected to a uniaxial displacement loading (experimentally) for another selected sample.

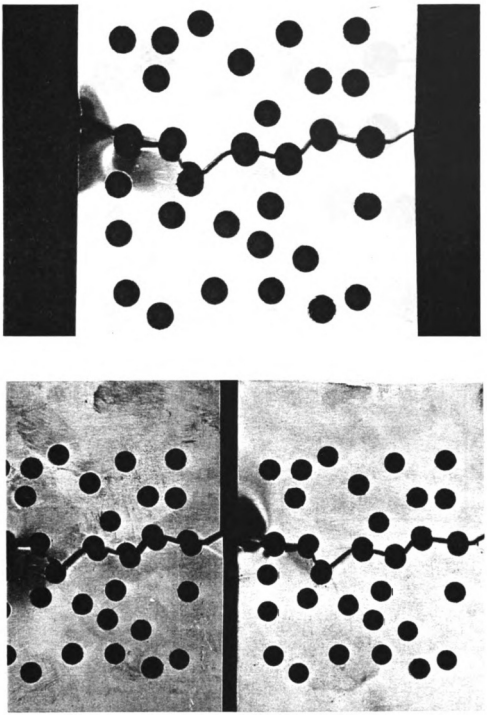

Fig. 4.31 Final crack pattern in an aluminum sheet, with randomly distributed holes, subjected to a uniaxial displacement loading obtained experimentally from three selected samples with the same hole arrangement with volume fraction f= 23%.

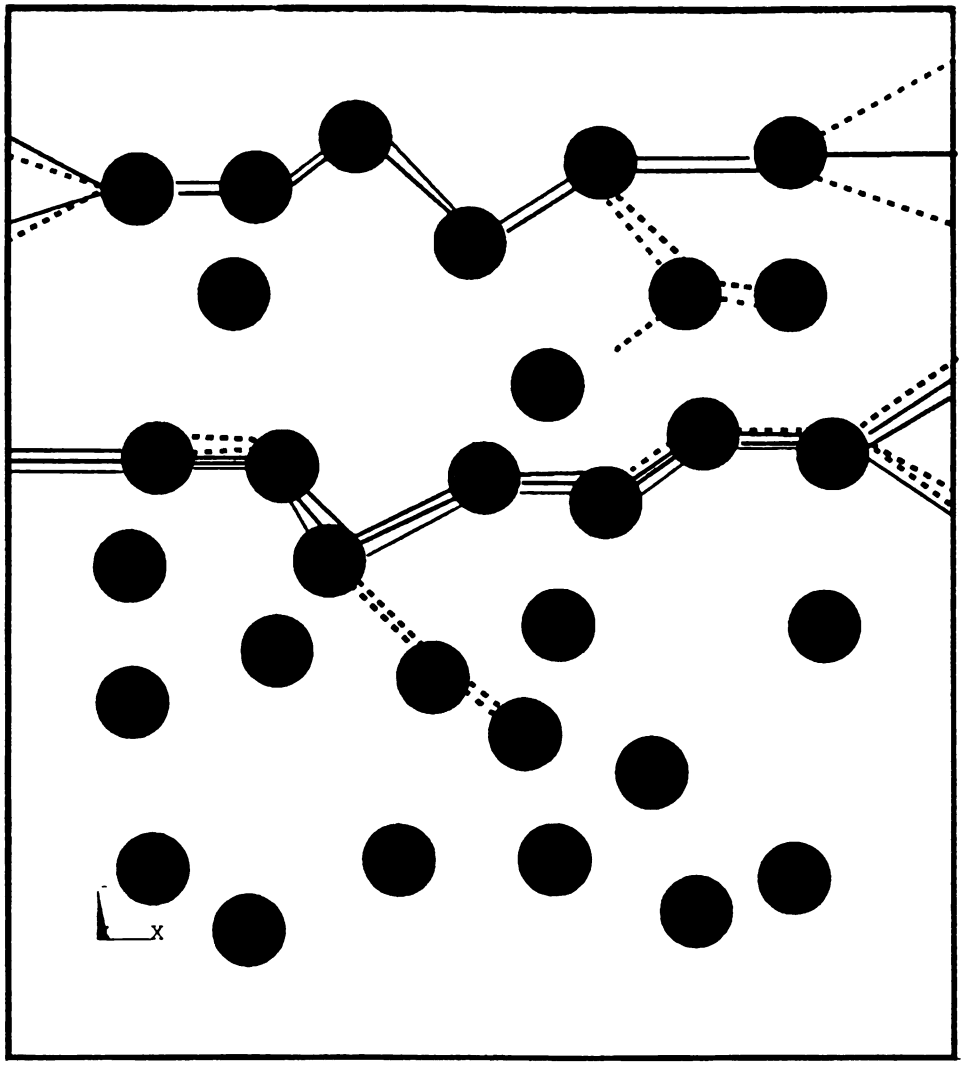

Sample # 1 (Cracking)
Sample # 1 (Plastic deformation)
Sample # 2 (Cracking)
Sample # 2 (Plastic deformation)
Sample # 3 (Cracking)
Sample # 3 (Plastic deformation)
Sample # 4 (Cracking)
Sample # 4 (Plastic deformation)
Sample # 5 (Cracking)
Sample # 5 (Plastic deformation)

Fig. 4.32 Schematic plot of the final crack pattern in an aluminum sheet, with randomly distributed holes and subjected to a uniaxial displacement loading, obtained experimentally from seven samples with the same hole arrangement with volume fraction f= 23%.

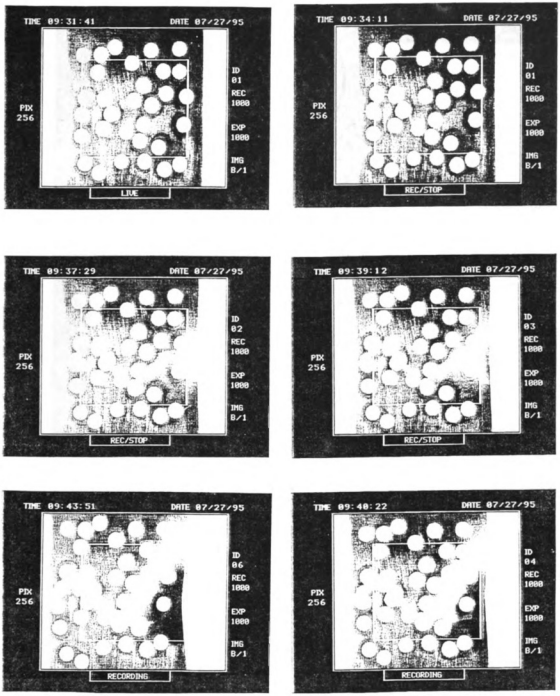

Fig. 4.33a Crack initiation and propagation in an aluminum sheet, with randomly distributed holes of volume fraction f= 31% and subjected to a uniaxial displacement loading (experimentally), for a selected sample.

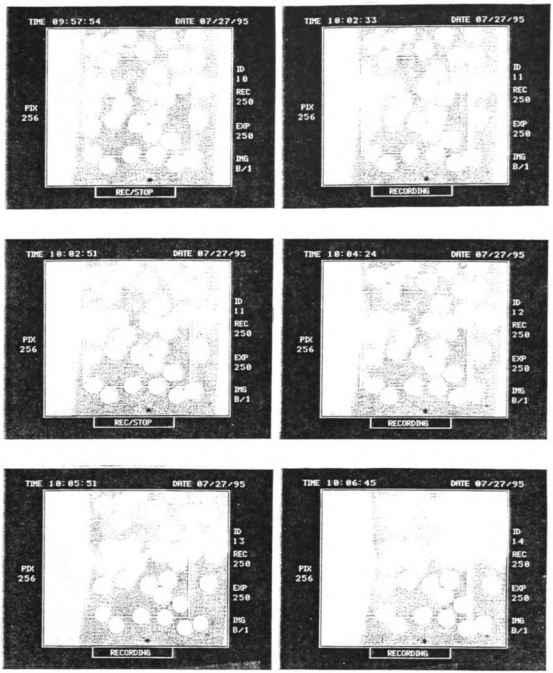

Fig. 4.33b Crack initiation and propagation in an aluminum sheet, with randomly distributed holes of volume fraction f= 31% and subjected to a uniaxial displacement loading (experimentally), for another selected sample.

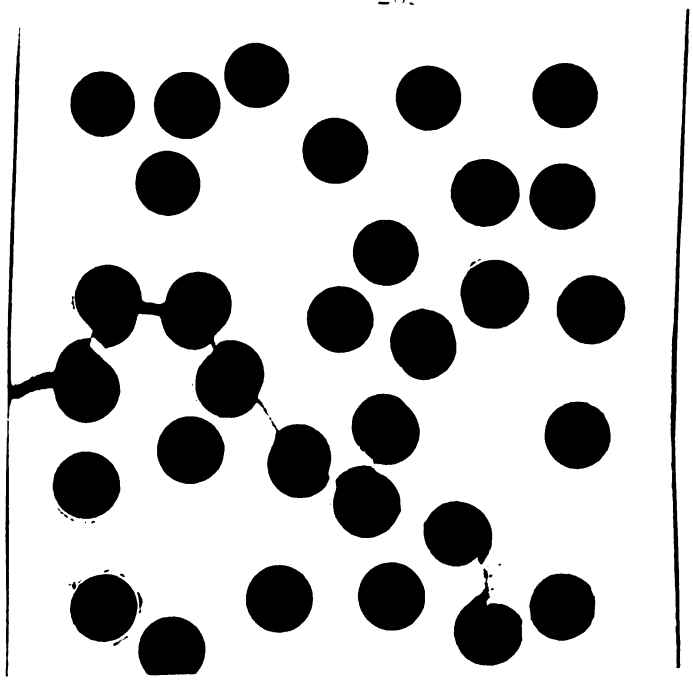

a)

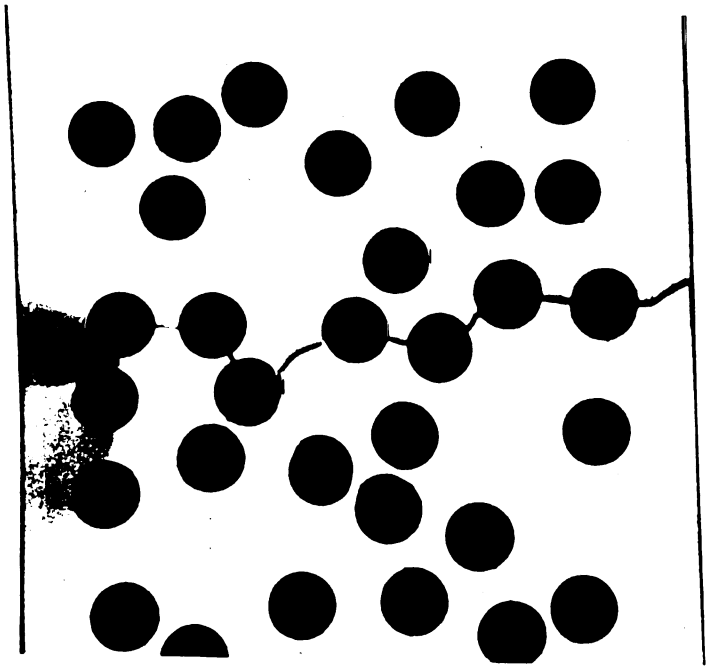

b)

Fig. 4.34 Final crack pattern in an aluminum sheet, with randomly distributed holes, subjected to a uniaxial displacement loading obtained experimentally from two samples with the same hole arrangement with volume fraction f = 31%.

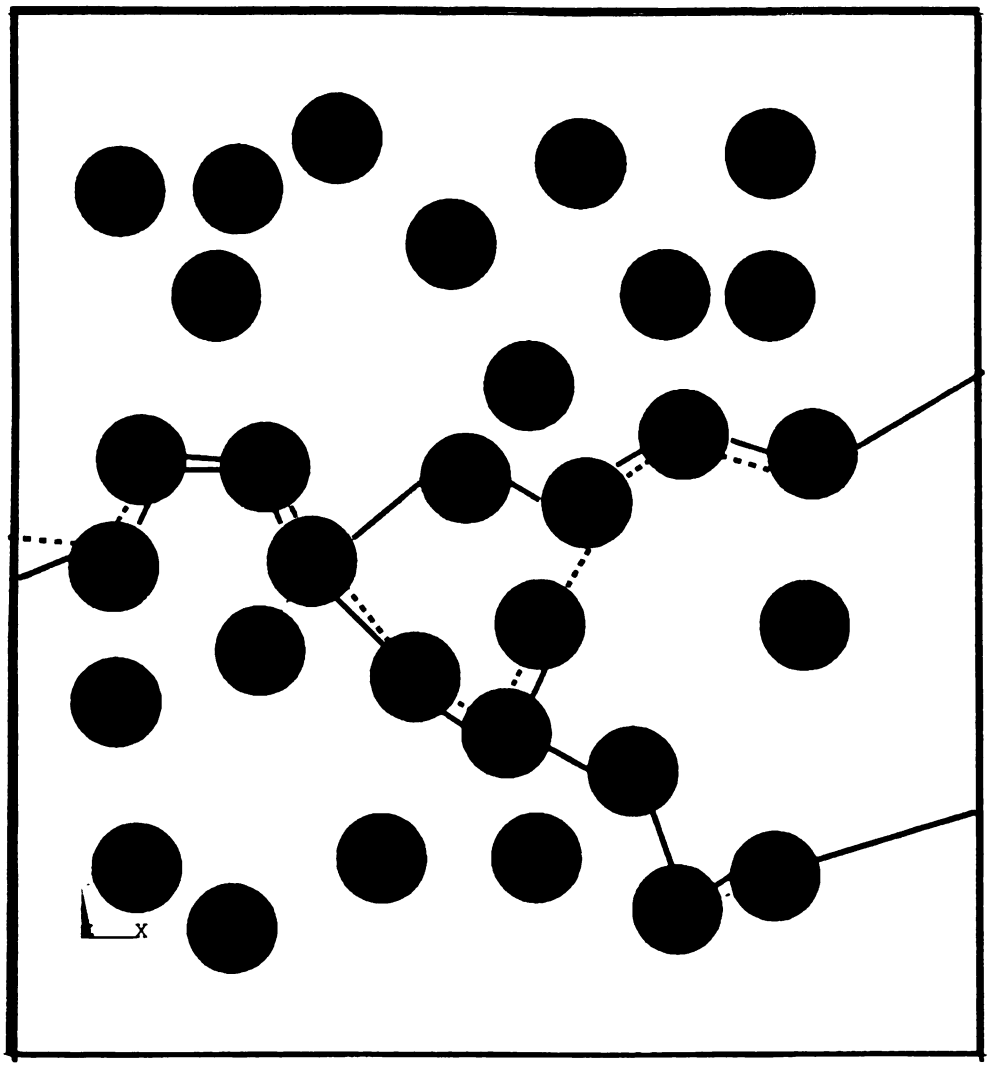

Fig. 4.35 Schematic plot of the final crack pattern in an aluminum sheet, with randomly distributed holes and subjected to a uniaxial displacement loading, obtained experimentally from seven samples with the same hole arrangement with volume fraction f = 31%.

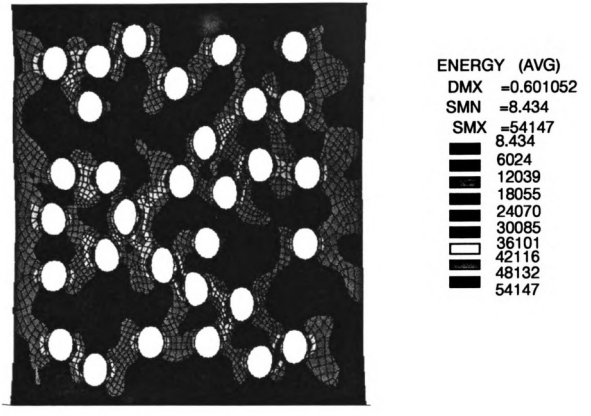

Fig. 4.36a Strain energy density contours using finite elements around randomly distributed holes of volume fraction f=23% in an aluminum sheet at the initiation of cracking when $\varepsilon_{zz} \approx -0.25$ for an applied loading in the vertical direction.

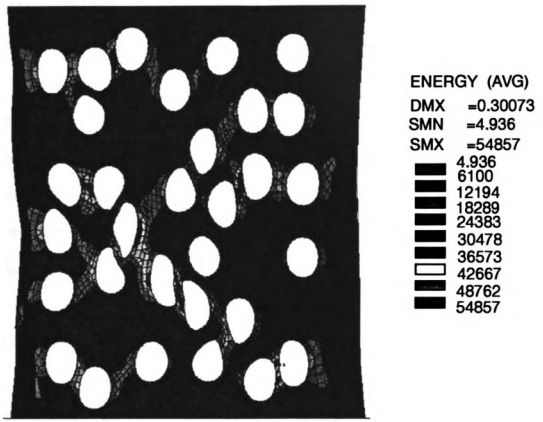

Fig. 4.36b Strain energy density contours using finite elements around randomly distributed holes of volume fraction f=31% in an aluminum sheet at the initiation of cracking when $\varepsilon_{zz} \approx -0.25$ for an applied loading in the vertical direction.

the aluminum sheet undergoes a very large plastic deformation as shown in Figs. 4.37, which illustrates the non-dimensionalized σ_{eff}/σ_y when $\varepsilon_{zz} = -.25$, where σ_y is the yield stress of aluminum. Note that if $\sigma_{eff}/\sigma_y > 1$ then plasticity will start. Our numerical results of the final crack path using minimum thickness criterion are shown in Fig 4.38.

Stress-strain curves of five different samples of aluminum sheets with randomly distributed holes of volume fraction 23% are shown in Fig. 4.39a. Fig. 4.39b represents a comparison between the stress-strain curve of two aluminum sheets with different volume fractions for the same random distribution of holes. In Fig. 4.39b the sudden drop in the stress value in the case of f = 31% was associated with the first cracking between two holes.

CLOSURE

In this study we have considered the problem of a crack initiation and propagation in materials containing randomly arranged holes. We have observed that the location of the crack initiation depends on a distance between the holes and their orientation with respect to the applied loading. The crack propagation obtained numerically depended on the mesh shape, size, and orientation of elements. Also, experimental results gave several different crack paths for the same hole arrangement. This may be due to material imperfections and an unstable crack growth. Thus, we have obtained non-unique crack paths both numerically and experimentally. This research illustrates the complexity of fracture phenomena and a need for a stochastic fracture analysis.

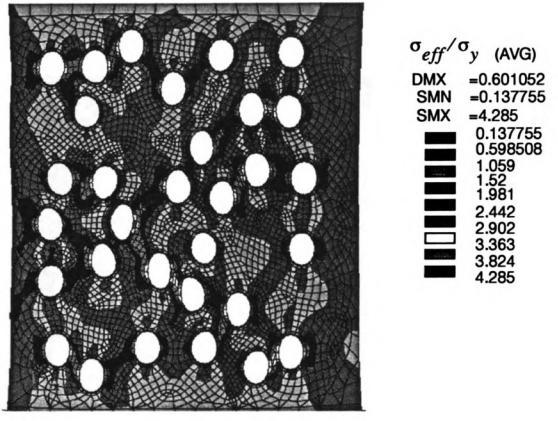

Fig. 4.37a σ_{eff}/σ_y stress contours using finite element around randomly distributed holes of volume fraction f=23% in an aluminum sheet at the initiation of cracking when $\varepsilon_{zz} \approx -0.25$ for an applied loading in the vertical direction.

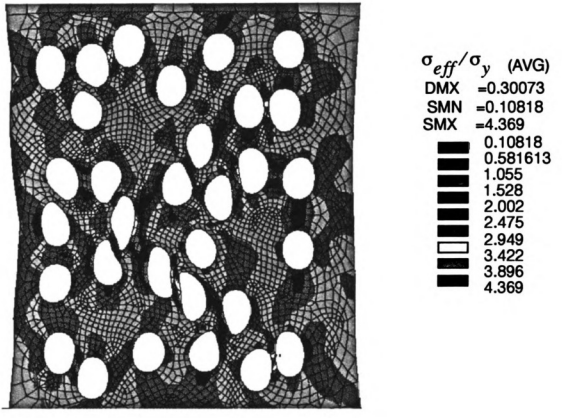

Fig. 4.37b σ_{eff}/σ_y stress contours using finite elements around randomly distributed holes of volume fraction f=31% in an aluminum sheet at the initiation of cracking when $\varepsilon_{zz} \approx -0.25$ for an applied loading in the vertical direction.

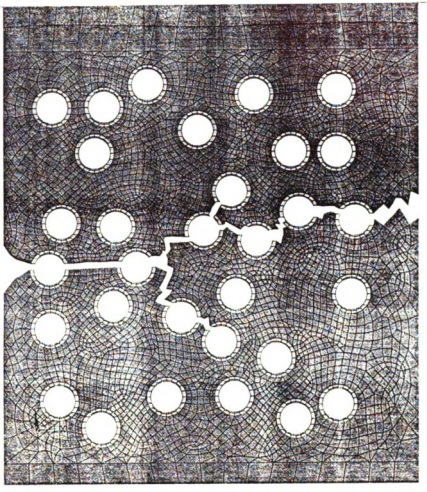

Fig. 4.38a Final crack pattern obtained numerically by finite element method using the minimum strain criterion with a mesh size of *0.4a* around the holes for f = 23%.

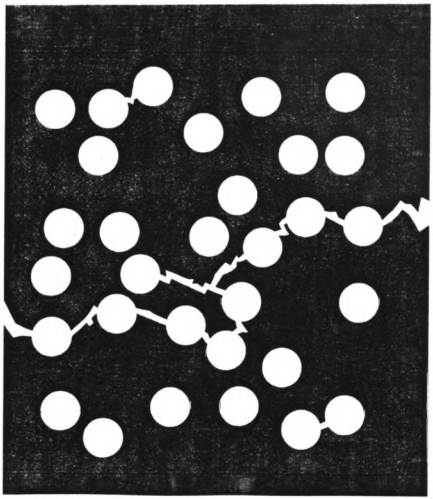

Fig. 4.38b Final crack pattern obtained numerically by finite element method using the minimum strain criterion with a mesh size of *0.4a* around the holes for f = 31%.

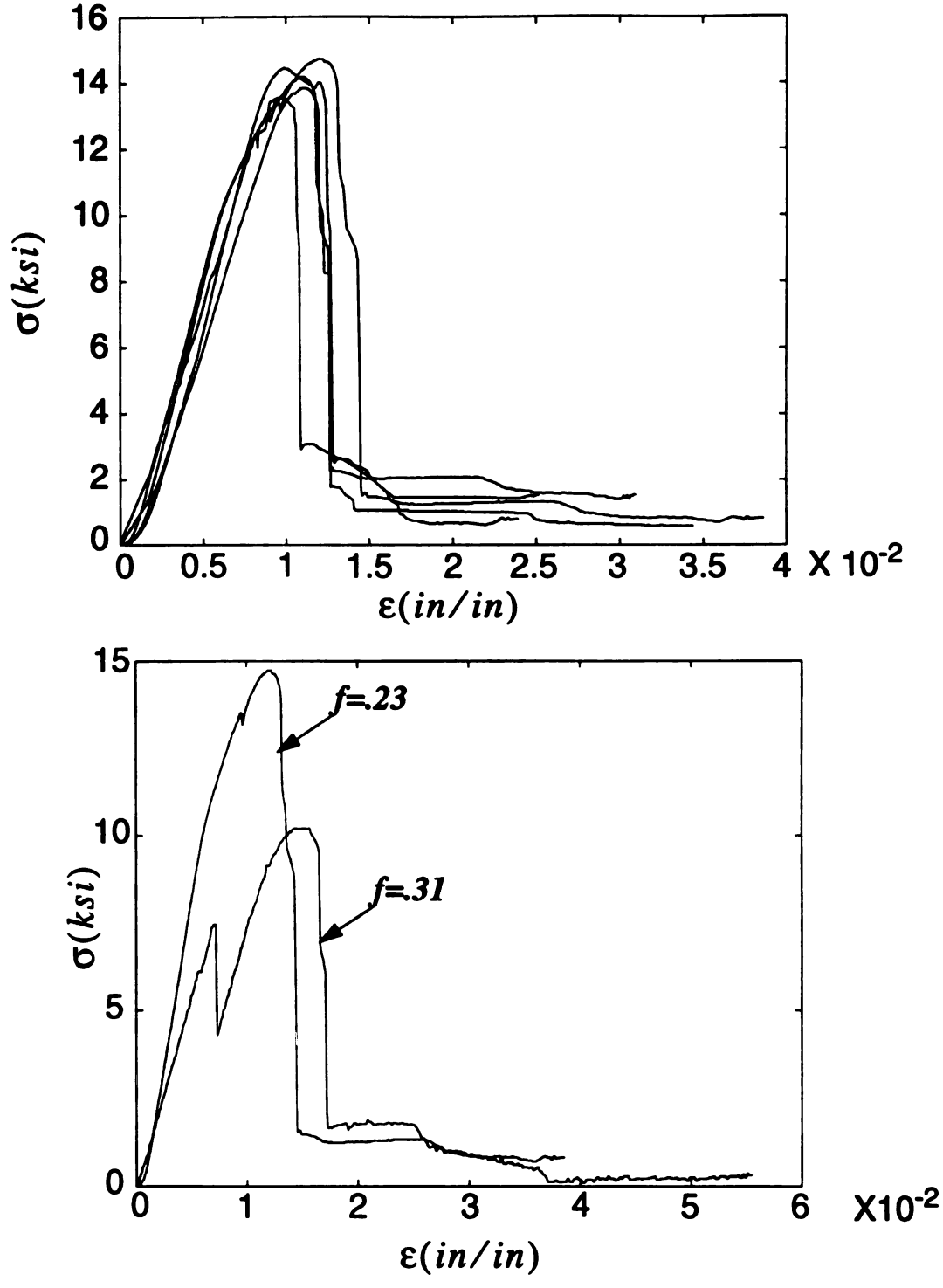

Fig 4.39 A typical stress-strain curve of an aluminum sheet with holes a) five different **specimens** of the same geometric arrangement with f=23% b) a comparison between **elastic** response of two sheets having two volume fractions of holes when centers are **at** the same location.

CHAPTER 5

TASK 4: AN ELASTIC CIRCULAR INCLUSION IN A HALF-PLANE: THE EFFECT OF BOUNDARY CONDITIONS ON STRESS CONCENTRATIONS

In the previous sections we focussed on the joint effect of the geometric arrangement of inclusions and the interface. Of interest there was the fact that stress field is affected by inclusions interactions. There we considered multi-inclusions embedded in an infinite plane.

Another important factor influencing the stress is the interaction of inclusions with the surface; this surface can be a neighboring lamina or an edge of a specimen, for example. The proximity of such a surface may give rise to high stress concentrations. In this chapter we investigate this issue by considering a single inclusion in a half-plane and vary the boundary conditions at the edge of the half-plane as well as at the inclusion-matrix interface.

In this phase of study we extend the results obtained by Lee *et al.* (1992) by considering the plane elasticity problem of an elastic circular (or cylindrical) inclusion embedded in a half-plane. The inclusion undergoes an eigenstrain (Mura, 1987), which can be a transformation strain, a thermal strain, a plastic strain, or a misfit strain. The matrix-inclusion interface is either perfectly bonded or allows slip without friction, while the edge of

the half-plane is either fixed or is allowed to move in the horizontal direction. We compare these results with a recent solution of a circular inclusion in a half-space with a traction-free edge (Lee *et al.*, 1992).

METHOD OF SOLUTION

We study the elastic fields when a circular inclusion is embedded in an elastic half-plane and subjected to an eigenstrain loading of non-shear type. Both the inclusion and the matrix are linear elastic and isotropic and they have distinct elastic constants. The interface between the inclusion and the matrix is either perfectly bonded (displacements and tractions are continuous) or is allowed to slip without friction with no separation in the normal direction (tractions and normal displacements are continuous, and shear tractions vanish), while the straight edge of the half-plane is either fixed (constrained in motion - displacements are zero) or frictionless (can move freely in the horizontal direction - vertical displacement and shear traction are zero). The method of analysis is similar to the one used in Lee *et al.* (1992). In this chapter we briefly summarize the method of solution and focus on the results.

In the analysis we use the Cartesian coordinate system (x,y) and the polar coordinates (r, θ). We let the origin of coordinates be at the center of the circular inclusion (see Fig. 5.1) and the x-axis be directed down into the interior of the half-plane. We set the edge of

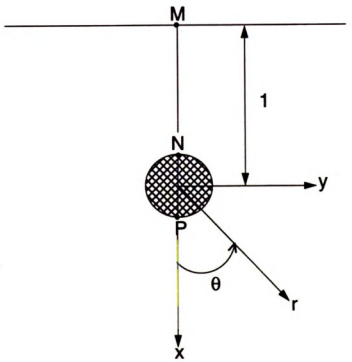

Fig. 5.1 A circular inclusion in a half-plane.

the half-plane at $x = -1$ and denote the radius of the inclusion by $r = a$.

The boundary conditions are as follows:

a) At the surface at $x = -1$

- either a fixed surface

$$(u_x)_{x=-1} = (u_y)_{x=-1} = 0 \tag{5.1}$$

- or a surface which is allowed to move with no restriction in the horizontal direction (or to slip with no friction with respect to a rigid material in contact with an elastic half-plane); we refer to this surface as frictionless

$$(u_x)_{x=-1} = (\sigma_{xy})_{x=-1} = 0 \tag{5.2}$$

- or a traction-free surface condition

$$(\sigma_{xx})_{x=-1} = (\sigma_{xy})_{x=-1} = 0 \tag{5.3}$$

which was solved by Lee *et al.* (1992), and is included here for a comparison;

b) At the inclusion-matrix interface at $r = a$

- either slipping with no friction and no separation in the normal direction

$$(\sigma_{rr})_{r=a} = (\bar{\sigma}_{rr})_{r=a} \qquad (u_r)_{r=a} = (\bar{u}_r)_{r=a}$$

$$(\sigma_{r\theta})_{r=a} = (\bar{\sigma}_{r\theta})_{r=a} = 0 \tag{5.4}$$

where the quantities denoted by the bar refer to the inclusion (Note that in this chapter we do not use the superscripts to denote the matrix and the inclusion in order to simplify the notation),

- or perfect bonding conditions

$$(\sigma_{rr})_{r=a} = (\bar{\sigma}_{rr})_{r=a} \qquad (\sigma_{r\theta})_{r=a} = (\bar{\sigma}_{r\theta})_{r=a}$$

$$(u_r)_{r=a} = (\bar{u}_r)_{r=a} \qquad (u_\theta)_{r=a} = (\bar{u}_\theta)_{r=a} \tag{5.5}$$

c) Vanishing tractions at infinity

$$\sigma_{kl} = 0 \qquad k, l = x, y \tag{5.6}$$

We solve the above boundary value problems by using Papkovich-Neuber displacement potentials ϕ_0 and ϕ_1, which for the matrix ($r > a$) are

$$(I)\begin{cases} \phi_0 = -A_0 \log r + \sum_{m=1}^{\infty} A_m \frac{\cos m\theta}{r^m} \\ \phi_1 = \sum_{m=1}^{\infty} B_m \frac{\cos m\theta}{r^m} \end{cases} \tag{5.7}$$

$$(II)\begin{cases} \phi_0 = \int_0^{\infty} \psi_1(\lambda) e^{-\lambda x} \cos \lambda y d\lambda \\ \phi_1 = \int_0^{\infty} \lambda \psi_2(\lambda) e^{-\lambda x} \cos \lambda y d\lambda \end{cases} \tag{5.8}$$

and for the inclusion ($r < a$) are

$$(III)\begin{cases} \phi_0 = \sum_{n=1}^{\infty} \bar{A}_n r^n \cos n\theta \\ \phi_1 = \sum_{n=1}^{\infty} \bar{B}_n r^n \cos n\theta \end{cases} \tag{5.9}$$

where A_n, B_n, $\bar{A}_n$, $\bar{B}_n$ are the unknown constants and $\psi_1(\lambda)$, $\psi_2(\lambda)$ are the unknown functions. Note that the potentials *(I)* account for the disturbance in the matrix due to the presence of the inclusion, while the potentials *(II)* allow to satisfy the boundary conditions at the surface at

$x = -1$. Since the applied loading is the non-shear eigenstrain in the inclusion with components ε_{xx}^*, ε_{yy}^*, and ε_{zz}^* the displacements inside the inclusion are the sum of the displacements in the unconstrained inclusion with no matrix present given by

$$\begin{aligned} \bar{u}_r^* &= \frac{r}{2}\{2\bar{\eta}\varepsilon_{zz}^* + (\varepsilon_{xx}^* + \varepsilon_{yy}^*) + (\varepsilon_{xx}^* - \varepsilon_{yy}^*)\cos 2\theta \\ u_\theta^* &= \frac{r}{2}(\varepsilon_{xx}^* - \varepsilon_{yy}^*)\sin 2\theta \end{aligned} \tag{5.10}$$

where

$$\bar{\eta} = \begin{cases} \bar{\nu} & \text{for plane strain} \\ 0 & \text{for plane stress} \end{cases} \tag{5.11}$$

and the elastic displacements obtained from the potentials *(III)*, which account for trac-

tions imposed by the matrix. In (5.11) $\bar{\nu}$ denotes the Poisson's ratio of the inclusion.

In order to satisfy the boundary conditions (5.1), (5.2), or (5.3) at the surface x = -1 we use the following mathematical relations

$$\frac{\cos m\theta}{r^m} = \frac{(-1)^m}{(m-1)!}\int_0^\infty \lambda^{m-1} e^{\lambda x}\cos\lambda y d\lambda$$
$$\frac{\sin m\theta}{r^m} = \frac{(-1)^m}{(m-1)!}\int_0^\infty \lambda^{m-1} e^{\lambda x}\sin\lambda y d\lambda \qquad x<0 \qquad (5.12)$$

Then, we can express potentials *(I)* in the Cartesian coordinates via eqn. (5.12) and use the potentials *(I)* and *(II)*, now both expressed in terms of integrals, to find the stresses and displacements in the matrix, and to satisfy the boundary conditions at the surface x = -1. Then, the quantities for the conditions (5.1) and (5.2) at x = -1 are

$$(2Gu_x)_{x=-1} = \int_0^\infty [A_0 e^{-\lambda} - \lambda\psi_1(\lambda)e^{\lambda} + \sum_{m=1}^{\infty}\frac{(-1)^m}{(m-1)!}\lambda^m e^{-\lambda}A_m + \lambda^2\psi_2(\lambda)e^{\lambda} -$$
$$\sum_{m=1}^{\infty}\frac{(-1)^m}{(m-1)!}B_m\lambda^m e^{-\lambda} - \kappa\lambda\psi_2(\lambda)e^{\lambda} - \kappa\sum_{m=1}^{\infty}\frac{(-1)^m}{(m-1)!}B_m e^{-\lambda}\lambda^{m-1}]\cos\lambda y d\lambda = 0 \qquad (5.13)$$

$$(2Gu_y)_{x=-1} = \int_0^\infty [-A_0 e^{-\lambda} - \lambda\psi_1(\lambda)e^{\lambda} - \sum_{m=1}^{\infty}\frac{(-1)^m}{(m-1)!}A_m\lambda^m e^{-\lambda} + \lambda^2\psi_2(\lambda)e^{\lambda}$$
$$+ \sum_{m=1}^{\infty}\frac{(-1)^m}{(m-1)!}B_m\lambda^m e^{-\lambda}]\sin\lambda y d\lambda = 0 \qquad (5.14)$$

$$(\sigma_{xy})_{x=-1} = \int_0^\infty \lambda^2 [\ \psi_1(\lambda)e^{\lambda} + \left(\frac{\kappa-1}{2} - \lambda\right)\psi_2(\lambda)e^{\lambda} - \sum_{m=1}^{\infty} A_m \frac{(-1)^m}{(m-1)!}\lambda^{m-1}e^{-\lambda} + \sum_0^\infty B_m \frac{(-1)^m}{(m-1)!}\left(\frac{\kappa-1}{2} + \lambda\right)\lambda^{m-2}e^{-\lambda} - A_0\lambda^{-1}e^{-\lambda}]\sin\lambda y d\lambda = 0 \tag{5.15}$$

where

$$\kappa = \begin{cases} 3-4\nu & \text{for plane strain} \\ \dfrac{(3-\nu)}{1+\nu} & \text{for plane stress} \end{cases} \tag{5.16}$$

and G denotes the shear modulus.

For the case of a fixed surface, with the boundary conditions given by (5.1), we set the quantities in brackets in equations (5.13) and (5.14) to zero. Thus, we have two equations for the two unknown functions $\psi_1(\lambda)$ and $\psi_2(\lambda)$, which we find to be

$$\psi_1(\lambda) = A_0 e^{-2\lambda}(-\lambda^{-1} + 2\kappa^{-1}) + \sum_{m=1}^{\infty} \frac{(-1)^m}{(m-1)!} A_m \lambda^m e^{-2\lambda}(-\lambda^{-1} + 2\kappa^{-1}) - 2\sum_{m=1}^{\infty} \frac{(-1)^m}{(m-1)!} B_m \lambda^m e^{-2\lambda}\kappa^{-1} \tag{5.17}$$

$$\psi_2(\lambda) = 2A_0 e^{-2\lambda}\lambda^{-1}\kappa^{-1} + 2\sum_{m=1}^{\infty} \frac{(-1)^m}{(m-1)!} A_m \lambda^{m-1} e^{-2\lambda}\kappa^{-1} - \sum_{m=1}^{\infty} \frac{(-1)^m}{(m-1)!} B_m\ e^{-2\lambda}(2\lambda^{m-1}\kappa^{-1} + \lambda^{m-2}) \tag{5.18}$$

Similarly for the case of the frictionless edge, with the boundary conditions given by (5.2), we find $\psi_1(\lambda)$ and $\psi_2(\lambda)$ by setting the quantities in brackets in equations (5.13) and (5.15) to zero. These functions are found to be

$$\psi_1(\lambda) = A_0\lambda^{-1}e^{-2\lambda} + \sum_{m=1}^{\infty} A_m\frac{(-1)^m}{(m-1)!}\lambda^{m-1}e^{-2\lambda} - 2\sum_{0}^{\infty} B_m\frac{(-1)^m}{(m-1)!}\lambda^{m-1}e^{-2\lambda} \tag{5.19}$$

$$\psi_2(\lambda) = -\sum_{0}^{\infty} B_m\frac{(-1)^m}{(m-1)!}\lambda^{m-2}e^{-2\lambda} \tag{5.20}$$

In order to satisfy the boundary conditions at the inclusion-matrix interface, given by either (5.4) or (5.5), we use the following relation

$$e^{-\lambda x}\cos\lambda y = \sum_{n=0}^{\infty}(-1)^n\frac{(\lambda r)^n}{n!}\cos n\theta \tag{5.21}$$

Then we rewrite potentials *(II)* by using eqn. (5.21) as follows

$$(II)^*\begin{cases}\phi_0 = C_0\sum_{n=0}^{\infty}\alpha_n r^n\cos n\theta \\ \phi_1 = C_0\sum_{n=0}^{\infty}\beta_n r^n\cos n\theta\end{cases} \tag{5.22}$$

where

$$\begin{aligned}\alpha_n &= \int_0^{\infty}\psi_1(\lambda)\frac{(-1)^n\lambda^n}{n!}d\lambda \\ \beta_n &= \int_0^{\infty}\lambda\psi_2(\lambda)\frac{(-1)^n\lambda^n}{n!}d\lambda\end{aligned} \tag{5.23}$$

It is convenient to express eqn. (5.23) in the following form

$$\alpha_n = A_0\alpha_{n1} + \sum_{m=1}^{\infty} \alpha_{n2}^m A_m + \sum_{m=1}^{\infty} \alpha_{n3}^m B_m$$
$$\beta_n = A_0\beta_{n1} + \sum_{m=1}^{\infty} \beta_{n2}^m A_m + \sum_{m=1}^{\infty} \beta_{n3}^m B_m \tag{5.24}$$

where for the case of a fixed-surface at $x = -1$

$$\alpha_{n1} = \frac{2}{\kappa}\gamma_n^0 + \varepsilon_n \qquad \alpha_{n2}^m = \gamma_n^{m-1} + \frac{2}{\kappa}m\gamma_n^m \qquad \alpha_{n3}^m = -\frac{2}{\kappa}m\gamma_n^m$$

$$\beta_{n1} = \frac{2}{\kappa}\gamma_n^0 \qquad \beta_{n2}^m = \frac{2}{\kappa}m\gamma_n^m \qquad \beta_{n3}^m = \gamma_n^{m-1} - \frac{2}{\kappa}m\gamma_n^m \tag{5.25}$$

and for the case of a frictionless-surface at $x = -1$

$$\alpha_{n1} = -\frac{1}{n}\gamma_{n-1}^0 \qquad \alpha_{n2}^m = \gamma_n^{m-1} \qquad \alpha_{n3}^m = 2\gamma_n^{m-1}$$

$$\beta_{n1} = \beta_{n2}^m = 0 \qquad \beta_{n3}^m = \gamma_n^{m-1} \tag{5.26}$$

where

$$\gamma_n^m = \frac{(-1)^{m+n}}{m!n!}\int_0^{\infty} \lambda^{m+n} e^{-2\lambda} d\lambda = \frac{(-1)^{m+n}}{m!n!}\frac{(m+n)!}{2^{m+n+1}} \tag{5.27}$$

and

$$\varepsilon_n = \begin{cases} \log 2 & n = 0 \\ \dfrac{\gamma_{n-1}^0}{n} & n \geq 1 \end{cases} \tag{5.28}$$

since

$$\int_0^\infty e^{-ax} x^b dx = \frac{b!}{a^{b+1}} \qquad a,b > 0 \tag{5.29}$$

$$\int_0^\infty \frac{1}{\xi} e^{-\xi z} d\xi = -\log z \tag{5.30}$$

Then, using the boundary conditions at the matrix-inclusion interface, either (5.4) or (5.5), we have four sets of equations to find the unknown constants A_n, B_n, $\bar{A}_n$, $\bar{B}_n$. We evaluate these constants by truncating the infinite series to $n = N$; for more details see Lee *et al.* (1992).

In the potentials *(II*)* the constants α_1 and β_0 correspond to the same rigid body motion of the matrix in the x-direction. We set one of these constants to zero. In the potentials *(III)* the constants $\bar{A}_1$ and $\bar{B}_0$ represent the same rigid body motion of the inclusion in the x-direction. Thus, again, we can set one of these constants to zero. For the cases of fixed and frictionless surfaces at $x = -1$ we need to allow for the rigid body displacements in both the matrix and the inclusion. Thus, we take $\alpha_1 \neq 0$ and $\bar{A}_1 \neq 0$, while $\beta_0 = \bar{B}_0 = 0$ ($\beta_0 \neq 0$, $\bar{B}_0 \neq 0$, and $\alpha_1 = \bar{A}_1 = 0$ would give the same results). For the traction-free surface case, discussed in Lee *et al.* (1992), only one rigid body displacement

needed to be specified. Thus, we allowed for the rigid body motion of the inclusion and took $\bar{A}_1 \neq 0$, while $\alpha_0 = \beta_0 = \bar{B}_0 = 0$. Again $\bar{B}_0 \neq 0$ with the other constants vanishing would give the same solution.

RESULTS AND DISCUSSION

In the numerical examples we assume a plane strain case. This case is of interest when the inclusion represents a long cylindrical reinforcing bar in concrete or a continuous fiber in a composite material, for example. In most figures, unless otherwise stated, we assume the same Poisson's ratio of the inclusion and the matrix such that $\nu = \bar{\nu} = 0.3$ and consider dilatational eigenstrains $\varepsilon_{xx}^* = \varepsilon_{yy}^* = \varepsilon_{zz}^*$ in the inclusion as a loading. Physically, these eigenstrains may represent thermal strains such that $\varepsilon_{xx}^* = \bar{\alpha}\Delta T$ when $\alpha = 0$, for example. Also, we take the ratio of the shear moduli of the inclusion and matrix $\Gamma = \bar{G}/G = 100$. We choose such a high mismatch so the differences between perfect bonding and sliding cases are more pronounced. In each of these figures we give the results for both types of boundary conditions at the inclusion-matrix interface: perfect bonding (PB), denoted by solid lines, and sliding (SL), denoted by dashed lines, and for the three cases of boundary conditions at $x = -1$: fixed (FIXED), frictionless (FRICL) and traction-free (FREE). In Figs. 5.2-9 the radius, denoted by an a, ranges from 0 to 0.98, while the distance from the center of the inclusion to the closest point on the straight edge is unity. Thus, the radius a close to zero corresponds to the limit case of an inclusion in the infinite material while a close to 1 implies that the inclusion is located very close to the surface given by $x = -1$.

Fig. 5.2 gives the hoop stress $\sigma_{yy} = \sigma_{\theta\theta}$ in the matrix versus the radius a on the surface $x = -1$ at point M (see Fig. 5.1) for the six cases (both types of boundary conditions at the inclusion-matrix interface and the three types of conditions at the surface $x = -1$). Note that the boundary conditions at the surface begin influencing the hoop stress when the inclusion radius is about 0.1, i.e. the inclusion is a distance of about 9 radii away from the surface. Perfect bonding and sliding conditions at the inclusion-matrix interface enter later when a is about 0.5, i.e the inclusion is located a distance of one radius away from the surface. The highest tensile stress in the matrix develops when the surface is traction-free for the sliding inclusion case, with a frictionless surface with a sliding inclusion also giving a high stress. The high compressive stress develops in the frictionless and fixed surface cases with a perfectly bonded inclusion when the inclusion is very close to the surface. The interesting tendency is observed for the case of the perfectly bonded inclusion near the frictionless surface as the hoop stress changes a sign and becomes compressive when $a > 0.9$.

Fig. 5.3 illustrates the hoop stress $\sigma_{yy} = \sigma_{\theta\theta}$ at the matrix-inclusion interface at point N (see Fig. 5.1). When the inclusion has a radius of about 0.2 or less, which implies that it is two or more diameters away from the edge, then the results are almost indistinguishable for the six cases being considered. In the limit case when the inclusion is very small, which corresponds to the case of inclusion embedded in the infinite matrix, $\sigma^{m}_{\theta\theta}/2G\varepsilon_{xx}^{*} = 1.2948$. When the distance between the inclusion and the edge decreases the hoop stress increases to high tensile values for the cases of traction free and frictionless surfaces when sliding occurs at the inclusion-matrix interface as at point M. For the

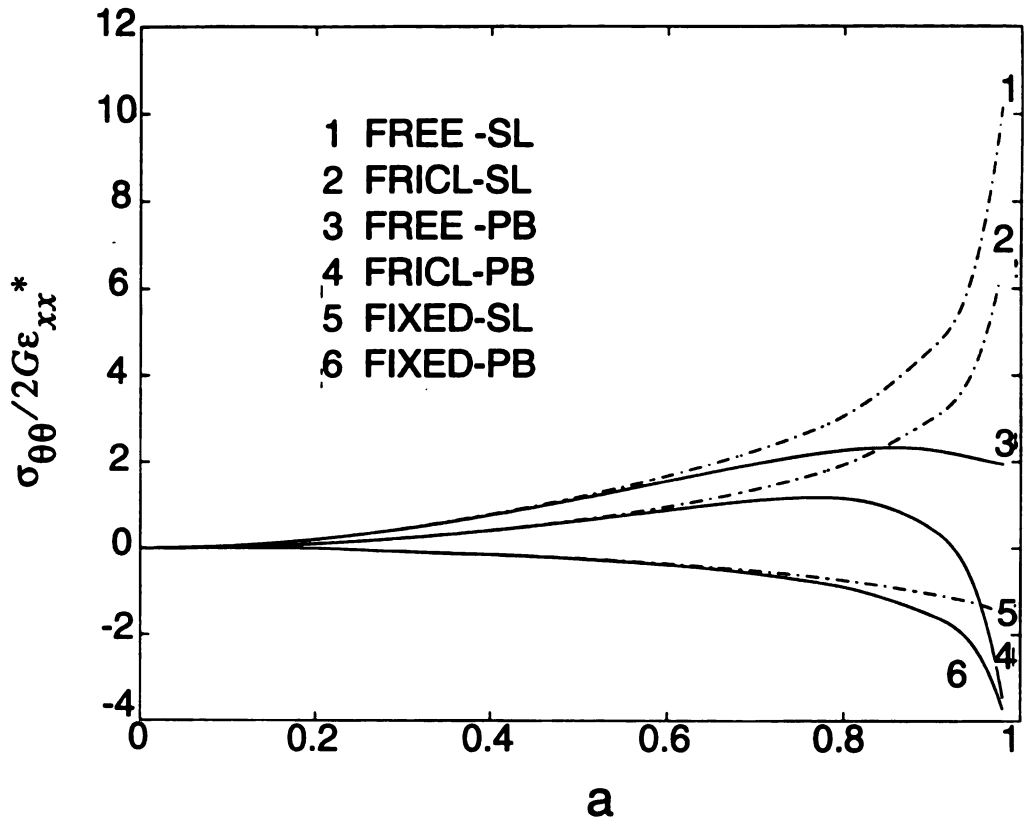

Fig. 5.2 The hoop stress $\sigma_{\theta\theta} = \sigma_{yy}$ in the matrix at point M versus the inclusion radius a when $\varepsilon_{xx}^* = \varepsilon_{yy}^* = \varepsilon_{zz}^*$ and $\Gamma = 100$.

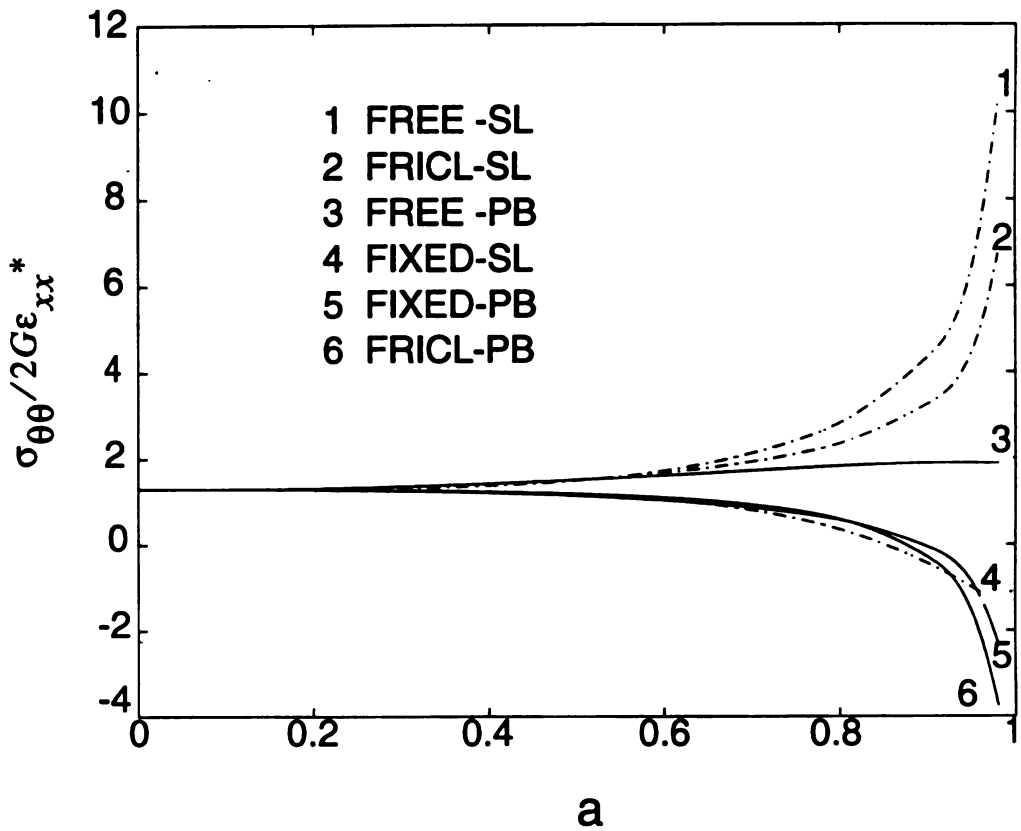

Fig. 5.3 The hoop stress $\sigma_{\theta\theta} = \sigma_{yy}$ in the matrix at point N versus the inclusion radius a when $\varepsilon_{xx}^* = \varepsilon_{yy}^* = \varepsilon_{zz}^*$ and $\Gamma = 100$.

case of a traction-free edge and a perfectly bonded inclusion case the magnitude of the hoop stress remains almost unchanged while for the cases of a fixed edge with a perfectly bonded inclusion and fixed and frictionless edges with a slipping inclusion the stress decreases and at around a = 0.9 becomes negative.

Fig. 5.4 illustrates the hoop stress $\sigma_{yy} = \sigma_{\theta\theta}$ in the matrix at the matrix-inclusion interface at point P (see Fig. 5.1). Here the effects of both edge and matrix-inclusion interface boundary conditions are small for all six cases, as expected, and for the radius a close to zero, i.e. the case of inclusion embedded in the infinite medium, the non-dimensionalized hoop stress equals to 1.2948 as expected. The hoop stress in the matrix remains tensile for all six cases with a small increase observed for the frictionless and fixed edges with a slipping inclusion cases and the traction-free and perfectly bonded inclusion case, and a small decrease observed for the remaining three cases.

Fig. 5.5 illustrates the radial stress $\sigma_{xx} = \sigma_{rr}$ in the matrix at the edge (x = -1) at point M. As expected the stress field is zero when a is close to zero, i.e. an inclusion is embedded in an infinite plate. Then, as the size of the inclusion increases, for the traction free edge the stress is tensile but very small, while for the frictionless and fixed edge it becomes compressive with the highest compressive stress being for the frictionless edge case and both matrix-inclusion interface conditions cases. Note that the effect of boundary conditions at the inclusion-matrix interface is almost negligible for the traction free and frictionless edge cases but it is noticeable for the fixed edge case when $a > 0.5$, with the perfect bonding case giving the higher compressive stress than the sliding inclusion case.

Fig. 5.6 illustrates the radial stress $\sigma_{xx} = \sigma_{rr}$ at the matrix-inclusion interface at

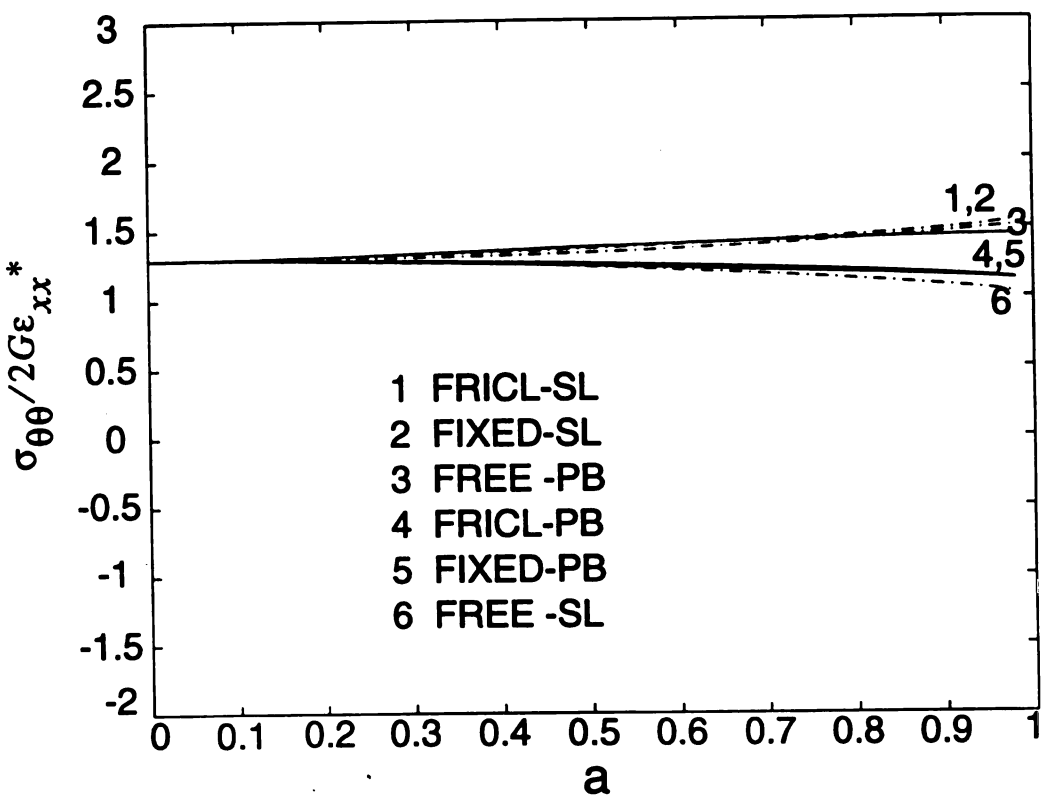

Fig. 5.4 The hoop stress $\sigma_{\theta\theta} = \sigma_{yy}$ in the matrix at point P versus the inclusion radius a when $\varepsilon_{xx}^* = \varepsilon_{yy}^* = \varepsilon_{zz}^*$ and $\Gamma = 100$.

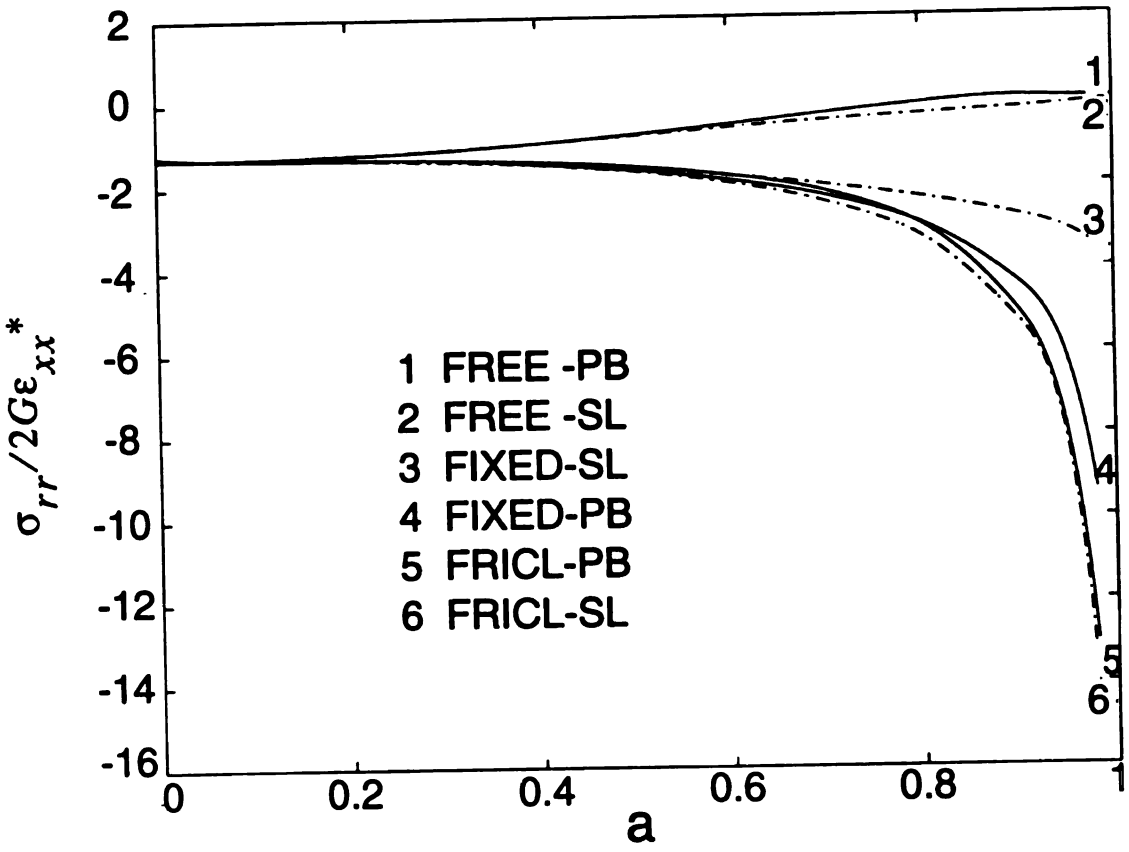

Fig. 5.5 The radial stress $\sigma_{rr} = \sigma_{xx}$ in the matrix at point M versus the inclusion radius a when $\varepsilon_{xx}^* = \varepsilon_{yy}^* = \varepsilon_{zz}^*$ and $\Gamma = 100$.

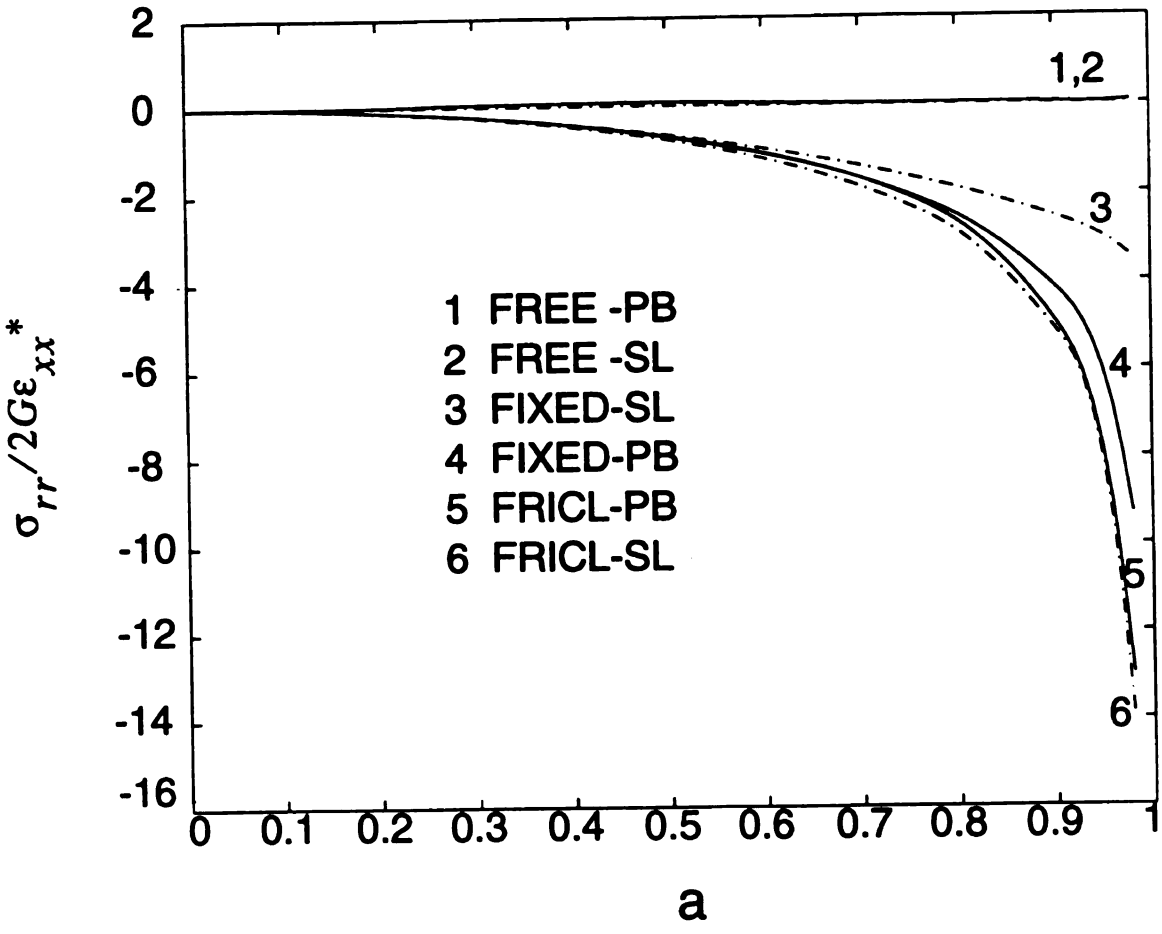

Fig. 5.6 The radial stress $\sigma_{rr} = \sigma_{xx}$ in the matrix at point N versus the inclusion radius a **when** $\varepsilon_{xx}^* = \varepsilon_{yy}^* = \varepsilon_{zz}^*$ and $\Gamma = 100$.

point N. When a is close to zero, i.e. the inclusion is very small, $\sigma_{rr}/2G\varepsilon_{xx}^* = -1.2948$ as expected. As the inclusion radius increases the stress behavior is similar to the one at point M (Fig. 5.5) but with a difference that the stress remains compressive for all cases and the whole range of a.

Fig. 5.7 gives $\sigma_{xx} = \sigma_{rr}$ at the matrix-inclusion interface at point P. The stress is compressive for all six cases and all geometries with rather small differences between each case. Thus, again the effect of boundary conditions at this point is small.

In summary, the effect of boundary conditions is pronounced at points M and N, illustrated in Figs. 5.2-3 and 5.5-6, but small at point P as given in Figs. 5.4 and 5.7.

Figs. 5.8-9 give the effective stress σ_{eff} which is defined, using the Huber-Mises criterion(e.g. Mendelson, 1986), as

$$\sigma_{eff} = \frac{1}{\sqrt{2}}[(\sigma_{rr}-\sigma_{\theta\theta})^2+(\sigma_{\theta\theta}-\sigma_{zz})^2+(\sigma_{zz}-\sigma_{rr})^2+6(\sigma_{r\theta}^2+\sigma_{\theta z}^2+\sigma_{zr}^2)]^{1/2} \quad (5.31)$$

where $\sigma_{z\theta} = \sigma_{rz} = 0$ for plane elasticity and $\sigma_{zz} = \nu(\sigma_{rr}+\sigma_{\theta\theta})$ for a plane strain case and $\sigma_{zz} = 0$ for a case stress case. Physically, this quantity defines the onset of plasticity in metals. Fig. 5.8 gives σ_{eff} at point M and Fig. 5.9 at point N. In both cases a sliding inclusion embedded in a half-plane with a frictionless edge gives the highest effective stress, then a sliding inclusion near a free surface and a perfectly bonded inclusion near a frictionless surface follow, while the cases of a perfectly bonded inclusion near a traction-free surface and a slipping inclusion near a fixed edge give the lowest effective stresses, and thus will cause yielding last.

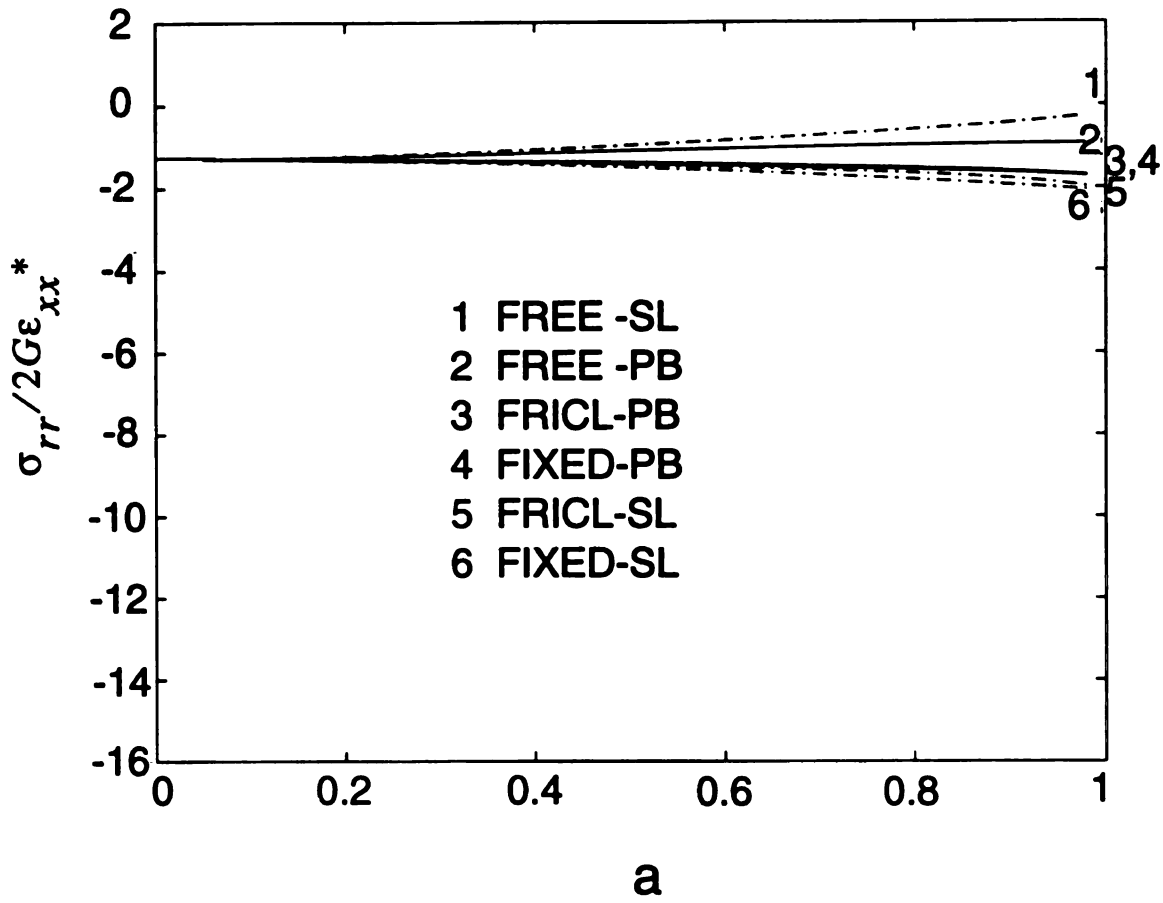

Fig. 5.7 The radial stress $\sigma_{rr} = \sigma_{xx}$ in the matrix at point P versus the inclusion radius a **when** $\varepsilon_{xx}^* = \varepsilon_{yy}^* = \varepsilon_{zz}^*$ and $\Gamma = 100$.

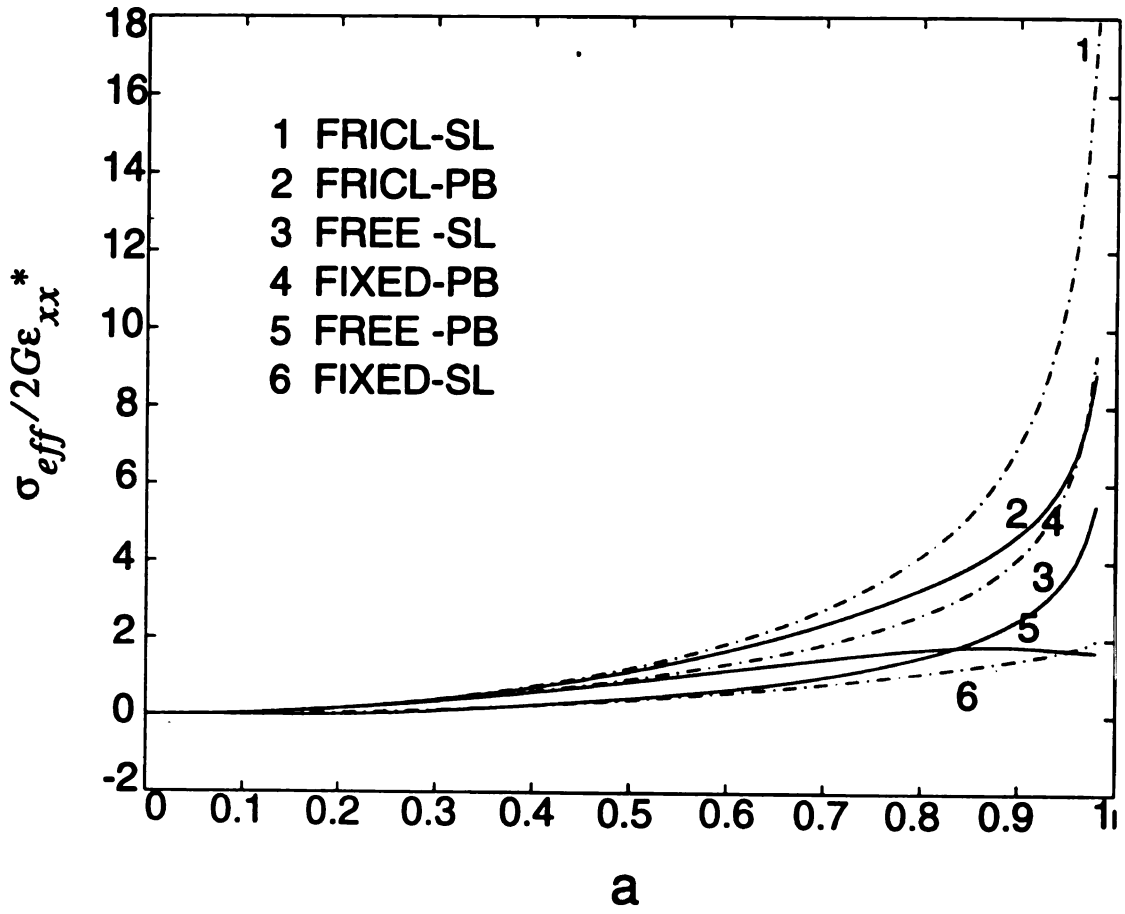

Fig. 5.8 The effective stress σ_{eff} in the matrix at point M versus the inclusion radius a **when** $\varepsilon_{xx}^* = \varepsilon_{yy}^* = \varepsilon_{zz}^*$ and $\Gamma = 100$.

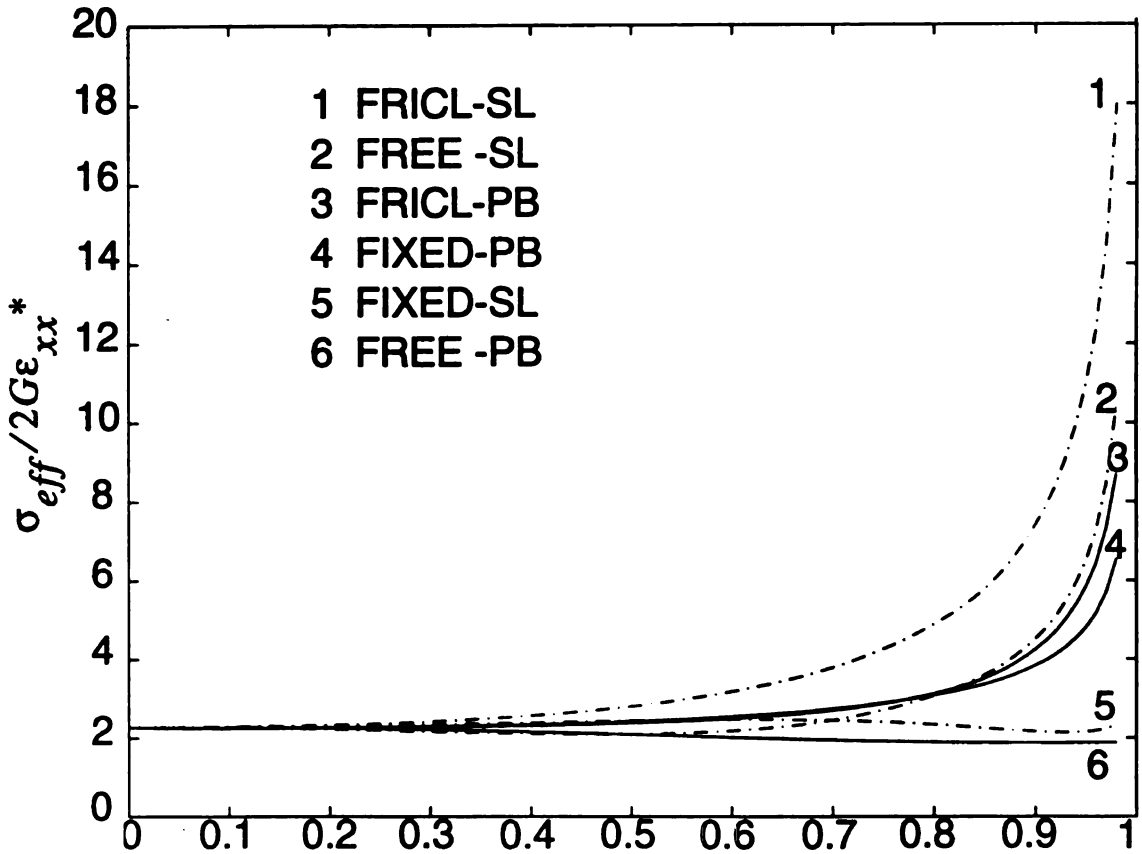

Fig. 5.9 The effective stress σ_{eff} in the matrix at point N versus the inclusion radius a **when** $\varepsilon_{xx}^* = \varepsilon_{yy}^* = \varepsilon_{zz}^*$ and $\Gamma = 100$.

Fig. 5.10 gives the hoop stress $\sigma_{yy} = \sigma_{\theta\theta}$ in the matrix versus $\Gamma = \bar{G}/G$ at point N when when $\varepsilon_{xx}^* = \varepsilon_{yy}^* = \varepsilon_{zz}^*, \nu = \bar{\nu} = 0.3$, and $a = 0.8$. Note that the effect of Γ on stress is very pronounced when Γ is small and the stress remains almost unchanged for Γ greater than about 20. Again, the effect of boundary conditions is pronounced as the stress varies from about 0.5 to 3. It is interesting to note that the fixed and traction-free surfaces with sliding inclusions behave very similarly when Γ is large.

Fig. 5.11 illustrates the radial stress $\sigma_{xx} = \sigma_{rr}$ in the matrix versus Γ at point N when $a = 0.8$. Note that there is a large influence of Γ on stress when Γ is less than about 5 and the stress remains almost unchanged when $\Gamma > 10$ for both traction-free cases with both a perfectly bonded and slipping inclusion and when Γ is greater 20 to 40 for the other four cases. Again the influence of boundary conditions is pronounced with stress being compressive and close to zero for traction-free and perfect bonding inclusion case and approximately -3 for the frictionless surface with sliding inclusion case. Fixed and frictionless surfaces with perfectly bonded inclusions behave similarly to each other in the whole range of Γ.

Fig. 5.12 gives the stress σ_{yy} in both the inclusion and the matrix along the x-axis when $\varepsilon_{xx}^* = \varepsilon_{yy}^* = \varepsilon_{zz}^*$, $\nu = \bar{\nu} = 0.3$, $\Gamma = 100$, and $a = 0.6$ for the six cases. Note that the stress is not uniform in the perfectly bonded inclusion (Eshelby, 1957) due to the presence of the surface. The stress is lower in the inclusion than in the matrix as expected due to the high shear modulus mismatch (high Γ). The effect of boundary conditions is quite pronounced near the surface and this effect decreases as the distance from the sur-

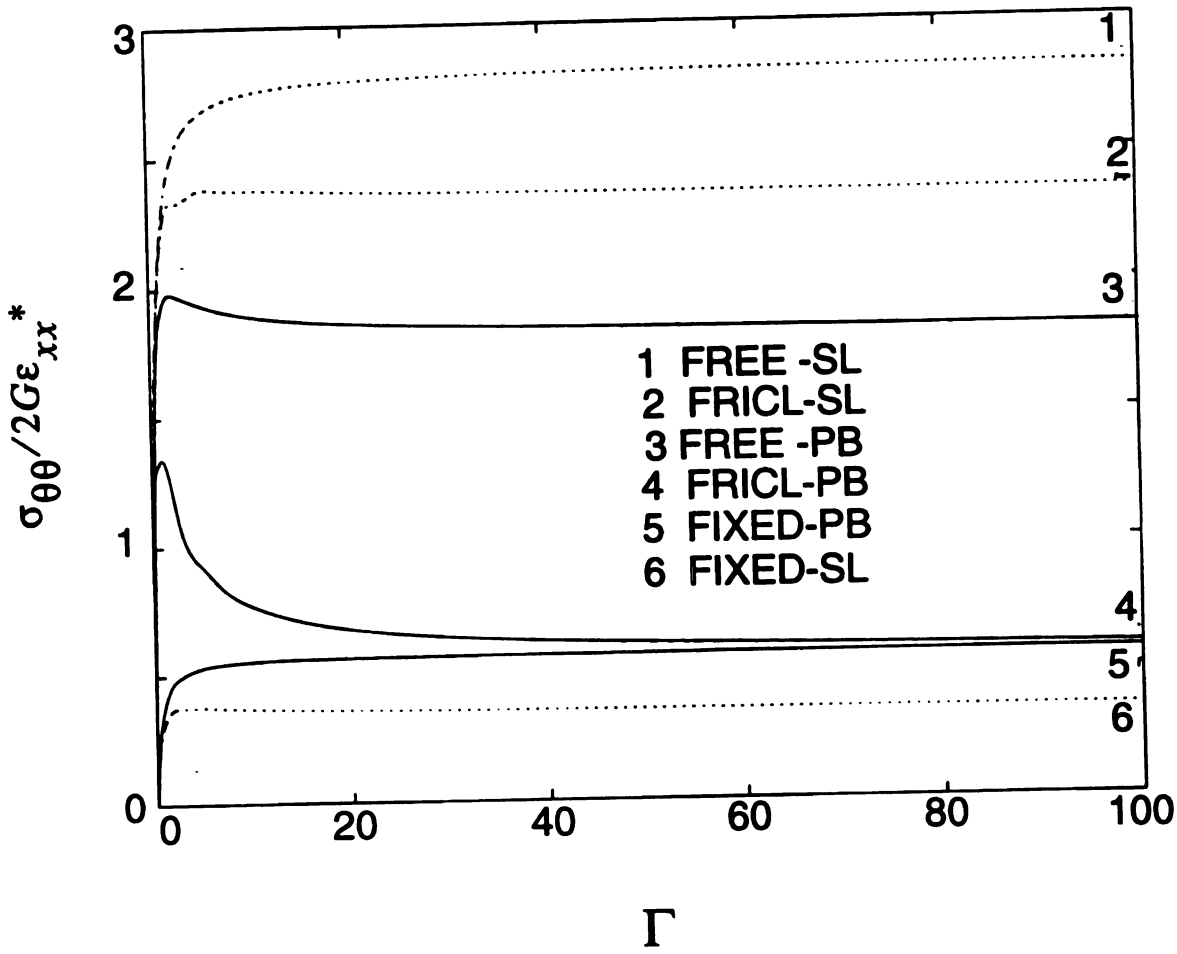

Fig. 5.10 The hoop stress $\sigma_{\theta\theta} = \sigma_{yy}$ in the matrix at point N versus Γ when $\nu = \bar{\nu} = 0.3$, $\varepsilon_{xx}^* = \varepsilon_{yy}^* = \varepsilon_{zz}^*$, and $a = 0.8$.

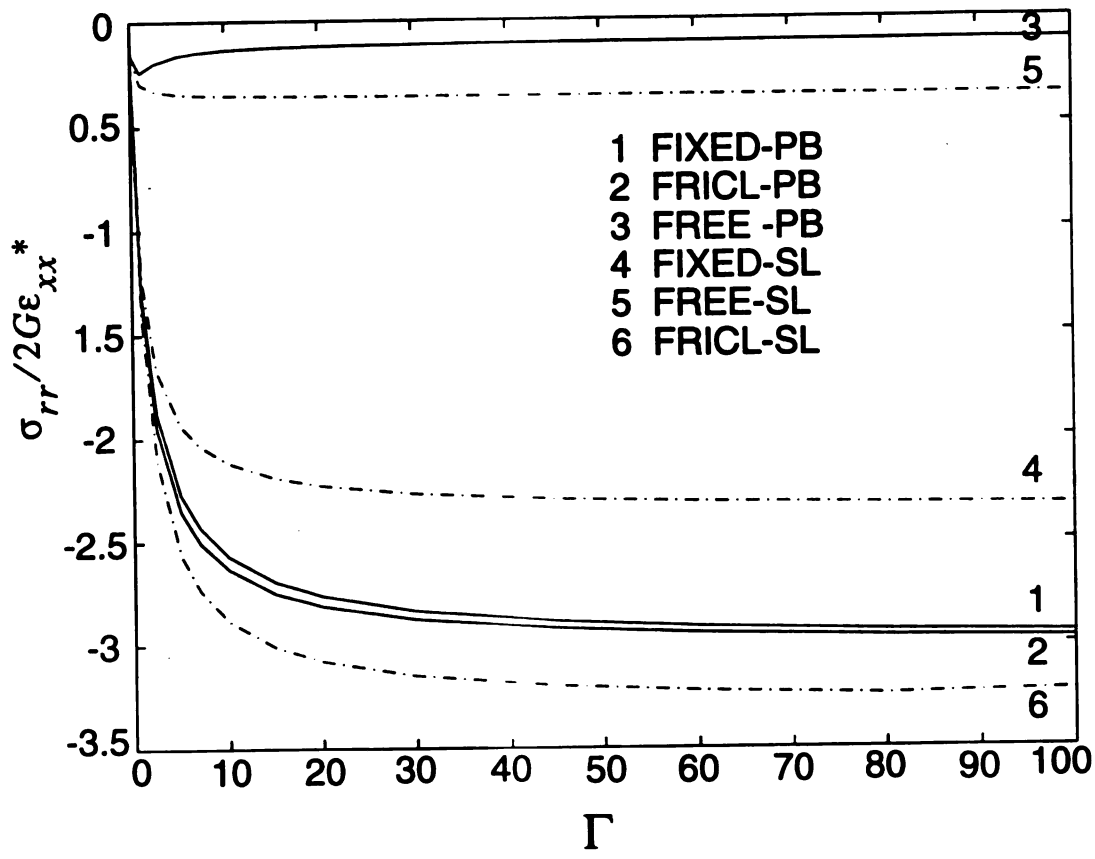

Fig. 5.11 The radial stress $\sigma_{rr} = \sigma_{xx}$ in the matrix at point N versus the shear moduli **ratio** Γ when $\varepsilon_{xx}^* = \varepsilon_{yy}^* = \varepsilon_{zz}^*$, $\nu = \bar{\nu} = 0.3$, and $a = 0.8$.

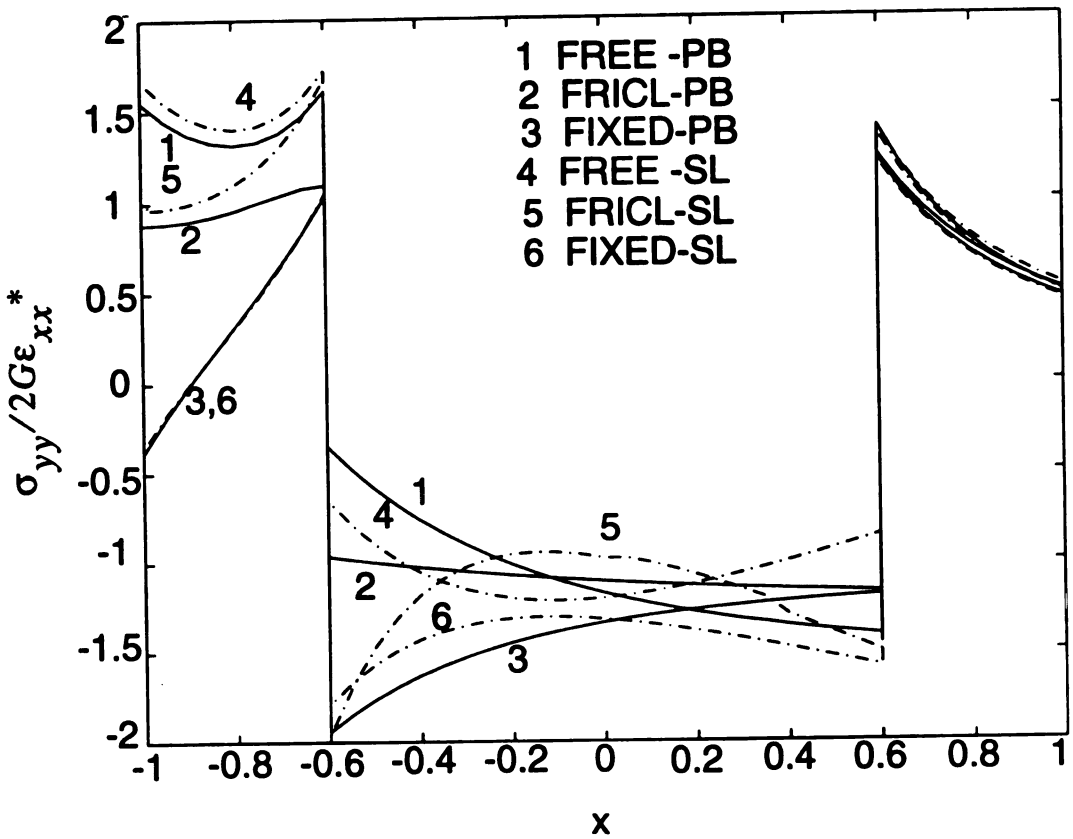

Fig. 5.12 The stress σ_{yy} in the matrix and in the inclusion along the x-axis when

$\varepsilon_{xx}^* = \varepsilon_{yy}^* = \varepsilon_{zz}^*$, $\nu = \bar{\nu} = 0.3$, $\Gamma = 100$, and $a = 0.6$.

face increases. The more complete information on the stress at x = -1 (point M) is included in Fig. 5.2 and at x = -0.6 (point N) in Fig. 5.3. The stress in the inclusion is negative and the highest compressive values are at x = -0.6 for the frictionless surface with sliding inclusion and the fixed surface with perfectly bonded inclusion cases.

Figs. 5.13, 5.15-5.16 show the tangential stress $\sigma_{r\theta}$ at the matrix-inclusion interface versus the angle θ for the perfect bonding case when $\nu = \bar{\nu} = 0.3$, $\Gamma = 100$, and a = 0.8, for different eigenstrain loadings. Fig. 5.15 corresponds to the dilatational eigenstrain case, such that $\varepsilon_{xx}^* = \varepsilon_{yy}^* = \varepsilon_{zz}^*$, considered in all the previous discussions of the results, while Fig. 5.17 gives the loading $\varepsilon_{xx}^*/2 = \varepsilon_{yy}^* = \varepsilon_{zz}^*$, and Fig. 5.18 the case of $\varepsilon_{xx}^* = 2\varepsilon_{yy}^* = \varepsilon_{zz}^*$. Note that when $\varepsilon_{xx}^* = \varepsilon_{yy}^* = \varepsilon_{zz}^*$ and the inclusion is embedded in the infinite plane then the shear stress is zero for all angles θ due to the radial symmetry. This is not the case anymore when the inclusion is embedded near a surface (Fig. 5.15).

Fig. 5.16 gives a jump in the tangential displacement $2G[u_\theta]$ for the same parameters as in Fig. 5.15. Note that both $\sigma_{r\theta}$ and $2G[u_\theta]$ are zero at $\theta = 0$ and 180° due to symmetry about the x axis.

CLOSURE

There is a strong influence of boundary conditions on the local stress concentration due to a cricular inclusion in a half plane. This influence becomes more pronounced as the inclusion approaches the surface.

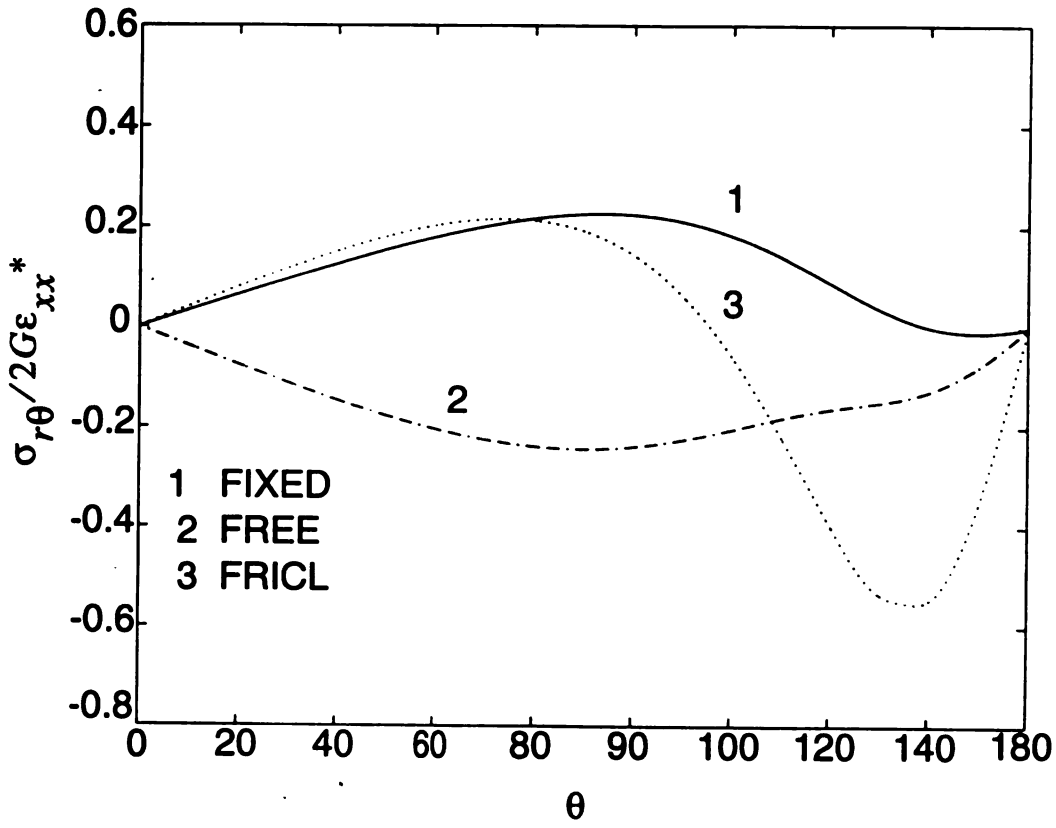

Fig. 5.13 The stress $\sigma_{r\theta}$ along the matrix-inclusion interface versus the angle θ when

$\varepsilon_{xx}^* = \varepsilon_{yy}^* = \varepsilon_{zz}^*$, $\nu = \bar{\nu} = 0.3$, $\Gamma = 100$, and $a = 0.6$.

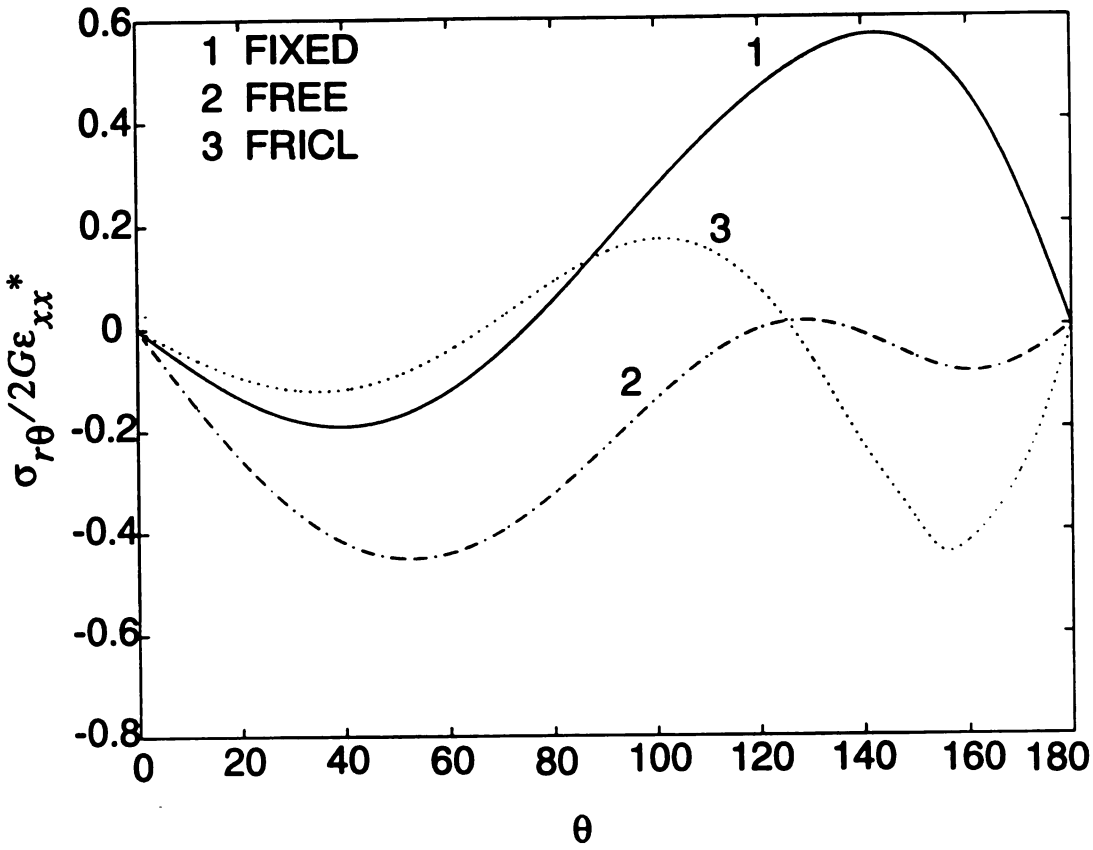

Fig. 5.14 The jump in the tangential displacement $2G[u_\theta]$ along the matrix-inclusion interface versus the angle θ when $\varepsilon_{xx}^* = \varepsilon_{yy}^* = \varepsilon_{zz}^*$, $\nu = \bar{\nu} = 0.3$, $\Gamma = 100$, and $a = 0.6$.

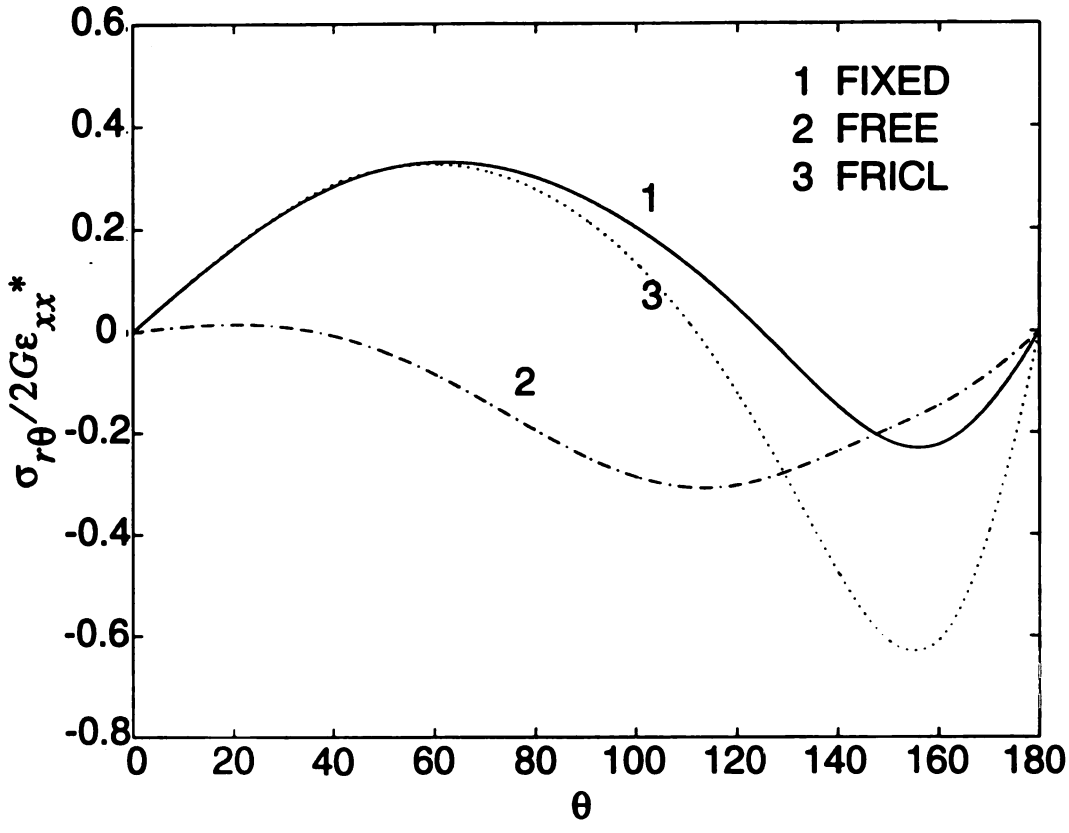

Fig. 5.15 The stress $\sigma_{r\theta}$ along the matrix-inclusion interface versus the angle θ when

$\varepsilon_{xx}^* = 2\varepsilon_{yy}^* = \varepsilon_{zz}^*$, $\nu = \bar{\nu} = 0.3$, $\Gamma = 100$, and $a = 0.8$.

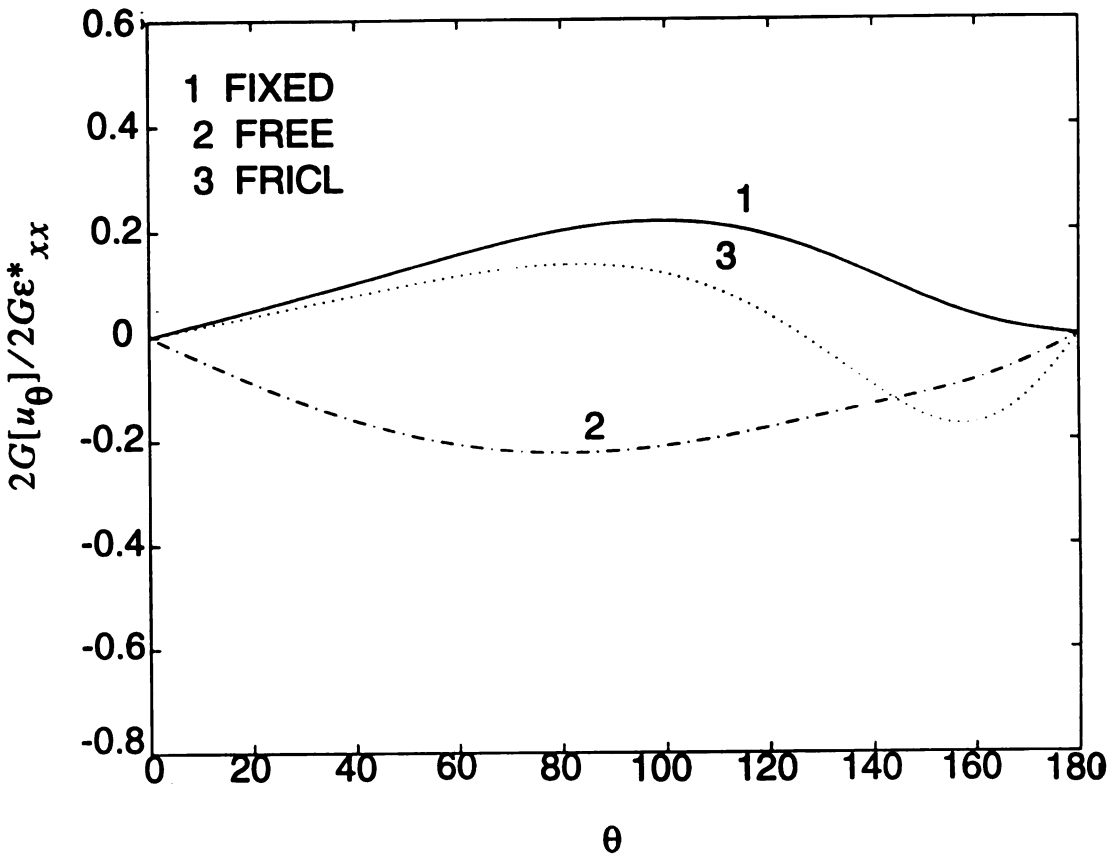

Fig. 5.16 The stress $\sigma_{r\theta}$ along the matrix-inclusion interface versus the angle θ when

$2\varepsilon_{xx}^* = \varepsilon_{yy}^* = \varepsilon_{zz}^*$, $\nu = \bar{\nu} = 0.3$, $\Gamma = 100$, and $a = 0.8$.

CONCLUSIONS

STRESS LOCALIZATION DUE TO RANDOM ARRANGEMENT FOR A UNIAXIAL TRANSVERSE LOADING.

Single-Inclusion case.

1-Both the thickness t and the Young's modulus of the coating E^c contribute to the stress fields.

2-The effect of the Young's modulus of the coating E^c on the stresses in the matrix is more pronounced when the coating is very compliant and is highly influenced by the thickness. This effect of E^c is higher on $\sigma^m_{\theta\theta}$ at $\theta = \pi/2$ when the thickness is very small while the opposite behavior is true for σ^m_{rr} at $\theta = 0$.

3-The effect of the Poisson's ratio of the coating material is very small in comparison to the influence of the other two parameters. This effect increases somewhat as the thickness increases.

4- In the case of perfect bonding, experimentally, the fringes start forming at the inclusion-matrix interface along the line of action of the applied load and then they propagate to the

other side of the inclusion. The opposite behavior is observed in cases of an inclusion with a compliant coating or a hole, where fringes start forming in a plane perpendicular to the line of action of the applied load and eventually migrate to the line of action of the applied load.

5- In the case of a compliant coating the maximum stress is located in the matrix, and the inclusion and coating carry almost no load, even though the inclusion is much stiffer. As the value of E^c increases both the coating and the inclusion start carrying the load. In the case of a stiff coating the maximum stress in the composite is located in the coating.

Two-inclusion case.

1-The location of maximum σ^m_{eff} is at $\theta = 0$ for cases of compliant coating (when the two inclusions are aligned in a plane perpendicular to the applied loading) and for cases of stiffer coatings, the location of the maximum σ^m_{eff} is at $\theta = \pi/2$ (when the two inclusions are aligned along the line of action of the applied loading).

2- Increasing the separation distance reduces the local effective stress in the matrix, the coating, and the inclusion when the two inclusions are aligned along a critical path. On the other hand increasing the separation distance will slightly increase the effective stresses if the two inclusions are aligned along the optimum path.

3- When the inclusions are aligned at the critical angle then increasing the number of inclusions increases the effective stress in the matrix. However if the inclusions are aligned along an optimum path then increasing the number of inclusions will decrease the effective stress in the matrix. 4-The effect of inclusion number on the local stress fields in the matrix, coating and inclusion will decrease as inclusions are added.

Multi-inclusion cases.

1- When the coated inclusions are distributed unevenly in the matrix the stresses are distributed unevenly between the inclusions. Thus, the non-uniform arrangement leads to stress localization and higher maximum stresses and therfore to an earlier initiation of damage, and consequently, to a lower strength. This in contrast to the periodic arrangement in which inclusions share the load equally.

2- When the interface is very weak (interphase is very compliant - coating 1), then almost no load is transferred from the matrix to the inclusions and it is carried by the matrix. If the interface is weak (interphase is compliant - coating 2), but yet capable of transferring some loads to the inclusions, then the loads will be carried by both the inclusions and the matrix with the maximum stress occurring in the matrix.

3- In case of optimum (minimum stress condition) coating the load will be shared almost equally between the matrix, the coating and the inclusion.

4- If a good bond is maintained between interfaces then the load will be carried by the stiff inclusions and the coatings. But if the coating is very stiff then the highest stress will occur in the coating.

5- For the case of no bonding (perfect bonding), the load is carried by the stiff inclusions lying in the direction of the load and there is bridging of stresses through the inclusions along the line of action of applied load. Inclusions close to each other and aligned in the direction of the load behave like longitudinal fibers subjected to an axial loading.

6-For inclusions with a compliant interphase, the maximum stress around each inclusion is located in a plane perpendicular to the applied loading, as was observed in the single inclusion case. A similar behavior occurs in elastic sheets with holes.

7-The periodic arrangements of inclusions under estimate the magnitude of the maximum local stress given by random arrangements.

8-When the interface is more compliant the difference between the maximum stress in random versus periodic arrangements is more pronounced.

9- The two-inclusion model gives a good approximation to the stresses in muti-inclusion

method in the case of stiff coating only.

10-The local stresses depend on number of neighboring inclusions, volume fraction, the separation distance between them, the inclination angle and the interface conditions.

STRESS LOCALIZATION DUE TO RANDOM ARRANGEMENT FOR A THERMAL LOADING.

Single-inclusion case.

1-The effect of changing the coating thickness is more pronounced for the cases of thin coating. Increasing the coating thickness will always increase the radial stress in the matrix regardless of the elastic modulus of the coating if $E^c/E^m<1$, and increasing the elastic modulus of the coating increases the radial stress in the matrix. The opposite behavior is observed when $E^c/E^m>1$.

2- Increasing the thermal coefficient of expansion of the coating will increase the radial stresses. This influence increases as the value of the elastic modulus of the coating E^c/E^m increases.

3-The effect of the rate of change in the Poisson's ratio of the coating (ν^c) increases as the elastic modulus of the coating increases (E^c/E^m). Also, increasing the Poisson's ratio of

the coating (ν^c) will increase the radial stress in the matrix (σ_{rr}^m) for the cases of compliant coatings; this effect will be reversed in cases of stiff coatings.

4- If the elastic modulus of the coating $E^c < E^m = 450\ ksi$ then the matrix, coating, and inclusion carry almost the same amount of loading. However when $E^c > E^m$ then the loading is carried by the coating and the inclusion with the maximum stress being in the matrix.

5- For a constant $t = .25a$, $E^c = E^m$ and $\nu^c = \nu^m$, increasing the coefficient of thermal expansion (CTE) of the coating α^c will reduce the effective stresses σ_{eff} in the matrix but will increase the effective stress in the coating and the stress in the inclusion will not change.

6- Experimental and numerical results indicate that post curing will reduce residual stresses in the used composite material as compared to standard curing.

7- Although we have used a constant value for the material fringe coefficient (f_σ), and we have used a nonlinear elasticity method of analysis (no viscoelastic effect), there is a good agreement between numerical and experimental stress values of residual stresses at room temperature. On the other hand, there is a large disagreement between both experimental

and numerical results of stresses for the case of stresses at elevated temperature.

Two inclusions case.

1-The effective stress between two inclusions always increases by decreasing the separation distance between the two inclusions.

2- Increasing the number of inclusions in a row increases the radial stress in the matrix regardless of degree of mismatch between the inclusion and the matrix. This effect decays as we increase the number of inclusions.

3-Although we used a constant value for the material fringe coefficient (f_σ), and nonlinear elasticity (no viscoelastic effect), there was a good agreement between numerical and experimental stress values.

The Multi-Inclusions Solution.

1-Increasing the volume fraction of the inclusions will increase the maximum shear stress in the matrix.

2-The periodic arrangement produces a lower stress than that of random arrangement even if the volume fraction of the periodic arrangement is higher.

3- Increasing the elastic modulus of the coating will always increase the maximum stress in the composite material.

4-Whereas for the case of $\alpha^c = 219x10^{-6}/^oC$ the maximum stress is always in the coating material, the maximum stress will be in the coating only if $E^c < E^m$ for the case of $\alpha^c = 64x10^{-6}/^oC$.

5- The maximum stress in the composite material will increase by increasing the thermal coefficient of expansion of the coating.

6- For the case of no-coating the maximum stress is always in the matrix and for a stiff coating material (E^c=9000 ksi) the maximum stress is basically carried by the coating.

7-Using random arrangement always gives higher values of stresses than regular arrangements. This effect is more noticeable when the maximum stress is located in the matrix.

.CRACK INITIATION AND PROPAGATION.

1- Fracture in composite materials is a highly localized phenomenon depending on geometric and material disorder.

2- In order to investigate the local stress fields in a composite with random distribution of fibers, the unit cell concept is not sufficient.

3- In case of uniaxial loading, the crack initiation depends on both the distance between holes and their orientation with respect to the applied loading.

4- The numerically predicted crack pattern is highly dependent on the mesh size, shape and the used fracture criterions. Experimentally, we don't get unique crack also.

5- In case of randomly distributed holes there is a very large number of geometrically acceptable crack paths cutting across the specimen. The energy release or maximum stress values associated with all these paths do not differ much from one another, and thus, a subset of them has practically the same numerical value. Therefore, minute material and geometric imperfections decide which crack path will actually take place in a particular specimen that is normally (on the macroscopic scales) the same as the rest of the bunch. Thus, both experimental and numerical methods showed that the crack path is not unique and several crack paths were observed.

6- While crack propagation in ductile materials (aluminum) is slow, the crack propagation in brittle epoxy matrix is very fast causing catastrophic failure. Thus, in this case dynamic fracture analysis needs to be considered.

7- Using a very crude way in simulating the crack propagation we could predict closely the crack paths obtained experimentally.

EFFECT OF BOUNDARY CONDITIONS ON STRESS CONCENTRATIONS DUE TO AN ELASTIC CIRCULAR INCLUSION IN A HALF-PLANE.

In this phase of the study, an exact elasticity solution (given in a series form) is presented for either a sliding or perfectly bonded circular inclusion embedded in a half plane in order to investigate the joint defect of boundary conditions and interface on the local stress and displacement fields.

1- There is a strong influence of boundary conditions on the local stress concentration due to a circircular inclusion in a half-plane. This influence becomes more pronounced as the inclusion approaches the surface.

2-The effect of interface (sliding or perfect bonding) is more noticeable when the inclusion is stiffer than the matrix.

3-The effect of material mismatch ($\Gamma = \bar{G}/G$) on both radial (σ_{rr}) and hoop ($\sigma_{\theta\theta}$) stresses at point N is pronounced when Γ is small and the stress remains unchanged for large Γ.

REFERENCES

Achenbach, J., 1990 " Effect of Interphase on Micro and Macro Behavior of Hexagonal Array Fiber Composites" *Journal of Applied Mechanics*, Vol. 57 pp. 956-968.

Al-Ostaz, A. and Jasiuk, I., 1994, "Effect of Interface and Random Geometric Arrangement of Inclusions on the Local Stresses in Composite Materials,"*Durability of Composite Materials* (R.C. Wetherhold, ed.), 1994 ASME Winter Annual Meeting, Chicago, November 1994, pp. 207-217.

Arnold, S. and Wilt, T., 1993,"Influence of Engineered Interface on Residual Stresses and Mechanical Response in Metal Matrix Composites," *Composite Interfaces*, Vol. 1, pp. 381-402.

Axelsen, M.S., and Pyrz, R., 1995, "Correlation Between Fracture Toughness and the Microstructure Morphology in Transversely Loaded Unidirectional Composites," in *IUTAM Symposium of Microstructure- Property Interactions in Composite Materials* (ed. R. Pyrz) pp. 15-26, Kluwer Academic Publishers.

Balander, J.E., Ebihara, T., and Hikosaka, H., 1994, "Evaluating Concrete Mesoscale Properties Using Neural Networks," in Infrastructure: New Materials and Methods of Repair, Proceedings of the Third Materials Engineering Conference, San Diego, Nov. 1994, pp. 475-482.

Balander, J.E., Hikosaka, H., and He, W.J., 1995, "Large-scale Analyses through Adaptive Remeshing," preprint.

Basista, M. and Krajcinovic, D., 1991, "Brittle Deformation of Disordered Solids," *Compos. Engr.* Vol. 1, pp. 103-112.

Bazant, Z.P., Tabbara, M.R., Kazemi, M.T., and Pijaudier-Cabot, G., 1990, "Random Particle Model for Fracture of Aggregate or Fiber Composites," *J. Engng. Mech.*, Vol. 116, pp. 1686-1705.

Becker R., and Smelser, R.E., 1994, "Simulation of Strain Localization and Fracture Between Holes in an Aluminum Sheet," *J. Mech. Phys. Solids,* Vol. 42, pp. 773-790.

Belytschko, T., Lu, Y.Y., and Gu, L., 1994, "Element-Free Galerikin Method," *Int. J. Num. Meths. in Eng.*, Vol 37, pp. 229-256.

Belytschko, T., Lu, Y.Y., and Gu, L., 1995 "Crack Propagation by Element-Free Galerkin Method," *Engineering Fracture Mechanics*, Vol. 51, pp. 295-315.

Benveniste, G., 1985, "The Effective Mechanical Behavior of Composite Materials with Imperfect Contact Between Constituents," *Mechanics of Materials,* Vol. 4, pp. 197-208.

Benveniste, G., Dvorak, G., and Chen, T.,1989, " Stress Field in Composites with Coated Inclusions," *Mechanics of Materials*, Vol. 7, pp. 305-317.

Bird, M., and Steele, C., 1992, "A Solution Procedure for Laplace's Equation on Multiply Connected Circular Domains," *Transaction of the ASME*, Vol. 59, pp. 398-404.

Breysse, D., Fokwa, D., and Drahy, F., 1994, " Spatial Variability in Concrete: Nature, Structure, and Consequences." *Appl. Mech. Rev.* Vol. 47, pp S184-S196.

Brockenbrough, J.R., and Suresh, S., and Wienecke, H.A., 1991, "Deformation of Metal-Matrix Composites with Continuous Fibers: Geometrical Effects of Fiber Distribution and Shape," *Acta Metal. Mater.*, Vol. 39, pp. 735-752.

Carman G., Averil, R., Reifsnider, K., and Reddy, J., 1993, "Optimization of Fiber Coatings to Minimize Stress Concentrations in Composite Materials," *Journal of Composite Materials,* Vol. 27, pp. 589-612.

.

Chen, J., Thorpe, M., and Davis, L., 1995, "Elastic Properties of Rigid Fiber- Reinforced Composites," *J. Appl. Phys.* Vol. 77, pp. 4349-4360.

Chudnovsky, A., and Kunin, B., 1987, " A Probablistic Model of Brittle Crack Formation." J. Appl. Phy. Vol. 62, pp. 4124-4129.

Daniel, I., and Durelli, A.,1962, "Shrinkage Stresses around Rigid Inclusions," *Experimental Mechanics*, Vol. 2, pp. 240-245.

Davis, L., Hass, K., Chen, J. and Thorpe, M., 1994, "Elastic Moduli of Composites with Random, Rigid Inclusions," *Appl. Mech. Rev.*, Vol. 47, Part 2, S5-S9.

Day, A., Snyder, K., Garboczi, E., and Thorpe, M., 1992, "The Elastic Moduli of a Sheet Containing Circular Holes," J. Mech. Phys. Solids, Vol. 40, pp. 1031-1051.

Drzal, L., 1983, "Composite Interphase Characterization," SAMPLE J., pp. 7-13.

Durelli, A., Parks, V., Feng, H., and Chiang, F., 1967," Strains and stresses in matrices with inserts," *Mechanics of Composites*, pp. 265-337.

Erdogan, F., and Sih , S.,1963 , "On Crack Extention in Plates under Plane Loading and Transverse Shear," *ASME J. Basic Engng.*, Vol. 85. pp. 123-131.

Eshelby, J.D., 1957, "The Determination of the Elastic Field of an Ellipsoidal Inclusion, and Related Problems," *Proc. Roy. Soc.*, Vol. A241, pp. 376-396.

Ghosh, S. and Mukhopadhyay, S., 1993, "A Material Based Finite Element Analysis of Heterogeneous Media Involving Dirichlet Tessellations", *Comput. Methods Appl. Mech. Eng.* Vol. 104. pp. 211-247.

Gong, S. X., and Meguid, S. A., 1993, " Interacting Circular Inhemogeneties in Plane Elastostatics," *Acta Mechanica.* Vol. 99, pp. 49-60.

Griffith, A.A., 1921, "The Phenomena of Rupture and Flow in Solids," *Phil. Trans. R. Soc.*, Vol. 221, pp. 163-198.

Gupta, V.B.,Drzal, L.T., Lee, C.,Y-C., and Rich, M.J.,1985, "The Temperature-Dependance of Some Mechanical Properties of a Cured Epoxy Resin System," *Polymer Engineering and Science,* Vol. 25, pp. 812-823.

Gupta, V.B., Drzal, L.T., lee, C., Y-C., and Rich, M . J., 1984, " The Effects of Stoichiometry and Structure on the Dynamic Torsional Properties of a Cured Epoxy Resin System", *Journal of Macromolecular Science*, Vol. 24, pp. 435-466.

Hashin, Z., 1990, "Thermoelastic Properties of Fiber Composites with Imperfect Interface" , *Mechanics of Materials* , pp. 333-348.

Hashin, Z., 1991, "Extremum Principals of Elastic Hetrogenous Media with Imperfect Interface and There Application to Bounding of Effective Moduli", J. *Mech. Phys. Solids.* Vol. 40, No. 4, pp. 767-781.

Herrera-Franco, P. and Drzal, L, 1992, "Comparison of methods for the Measurement of Fiber/Matrix Adhesion in Composites," *Composites*, Vol. 23, pp. 2-27.

Herrmann, H. J., Hansen, H., and Roux, S., 1989, "Fracture of Disordered Lattices in Two Dimensions," *Phys. Rev. B.*, Vol. 39, pp. 637-648.

Herrmann, H. J., and Roux, S., eds., 1990, *Statistical Models for Fracture of Disordered Media,* Elsevier.

Hughes, J. D. H.,1991, "The Carbon Fiber/Epoxy Interface - A Review", *Composites Science and Technology*, Vol. 41, pp. 13-45.

Jagota, A., and Bennison, S.J., 1994, "Spring Network and Finite Element Models for Elasticity and Fracture," in *Breakdown and Non-Linearity in Soft Condensed Matter* (K.K. Bardhan, B.K. Chakrabarti, and A. Hansen, eds.) Springer Verlag, Berlin, preprint.

Javornicky, J., 1970, "Photoelastic Investigation of Cast Plates with Inclusions," *Experimental Stress Analysis*, pp. 39-82.

Jeffery, G. B., 1920, "Plane Stress and Plane Strain in Bipolar Coordinates," *Transactions of Royal Society, London*, Series A, Vol. 221, pp. 256-293.

Jeulin, D., 1994, " Fracture Statistics Models and Crack Propagation in Random Media." *Appl. Mech. Rev.* Vol. 47, pp. S141-S150.

Jirasek, M., and Bazant, Z., 1994/1995, "Macroscopic Fracture Characteristics of Random Particle Systems," Int. J. Fract. Vol. 69, pp. 201-228.

Kerans, R. J., Hay, R. S., Pagano, N. J., and Parthasarathy, T.A., 1989, "The Role of the Fiber-Matrix Interface in Ceramic Composites," *Ceramics Bulletin,* Vol. 68, pp. 429-442.

Kouris, D. and Tsuchida, E., 1991, "On the Elastic Interaction Between Two Fibers in a Continuous Fiber Composite under Thermal Loading," *Mechanics of Materials*, Vol. 12, pp. 131-146.

Kouris, D., 1993, "Stress Concentration Due to the Interaction Between Two Imperfectly Bonded Fibers in a Continuous Fiber Composite," *J. Appl. Mech.*, Vol. 60, pp. 203-206.

Kouris D., and Marshall, 1994 " Damage Mechanisms in Ti_3Al Matrix Composite" *Journal of Engineering Materials and Technology.* Vol. 166, pp. 319-324.

Kunin, B., and Gorelik, M., 1991, " On Representation of fracture profiles by Fractional Integrals of Wiener Process." *J. Appl. Phys.* Vol. 70, pp.7651-7653.

Kunin, B. I., 1994, "A stochastic Model for Slow Crack Growth in Brittle Materials.," *Applied Mechanics Reviews.*, Vol. 47, pp. S175-S183.

Lee, M., Jasiuk, I., and Tsuchida, E., 1992 "The Sliding Circular Inclusion in an Elastic Half-Plane,", *Journal of Applied Mechanics,* Vol. 59, pp. 57-64.

Lin, Y. K., and Yang. J. N., 1983, "On Statistical Moments of Fatigue Crack Propagation," *Engineering Fracture Mechanics.* Vol. 18, pp. 243-256.

Magnusen, P.E., Dubensky, E.M., and Koss, D.A., 1988, "The Effect of Void Arrays on Void Linking During Ductile Fracture," *Acta Metall.* Vol. 36. pp. 1503-1509.

Marloff, R., and Daniel, I., 1969, "Three-Dimensional Photoelastic Analysis of a Fiber-Reinforced Composite Model," *Experimental Mechanics,* Vol. 9, pp. 156-162.

Mikata, Y. and Taya, M., 1985, "Stress Field in a Coated Continuous Fiber Composite Subjected to Thermo-Mechanical Loading," *Journal of Composite Materials,* Vol. 19, pp. 554-579.

Mindlin, R. D., 1948, "Stress Distribution around a Hole Near the Edge of a Plate Under Tension," *Proceedings of the Society for Experimental Stress Analysis,* Vol. 5, pp. 56-68.

Moet, A., Mostafa, I., Chudnovsky, A., and Kunin, B., 1992, "Probabilistic Fracture Mechanisc of 2D Carbon-Carbon Composite." *International Journal of Fracture,* Vol. 55, pp. 179-191.

Mura, T., 1987, *Micromechanics of Defects in Solids,* 2nd ed., Martinus Nijhoff, Dordrecht.

Mura, T, and Furuhashi, R., 1984, "The Elastic Inclusion with a Sliding Interface," *Journal of Applied Mechanics,* Vol. 51, pp. 308-310.

Muskhelishvili, N.I., 1953, *Some Basic Problems of the Mathematical Theory of Elasticity,* P. Noordhoff Ltd., Groningen, Holland, pp. 214-217.

Needleman, A., and Kushner, A.S., 1990, "An Analysis of Void Distribution Effects on Plastic Flow in Porous Solids," *Eur. J. Mech., A/ Solids.* Vol. 9, pp. 193-206.

Ostoja-Starzewski,M and Lee, J.D., "Damage maps of Disorded composites : a Spring Network Approach," *Int. J. Fracture*, submitted.

Pagano, N.J. and Tandon, C.P., 1988, "Elastic Response of Multidirectional Coated Fiber Composites , " *Composites Science and Technology,* Vol. 31, pp. 273-293.

Pukanszky, B., and Voros, G., 1993, "Mechanism of Interfacial Interaction in Particulate Filled Composites." *Composite Interfaces*, Vol. 1, pp. 411-427.

Pyrz, R., and Bochenek, B., 1994, "Statistical Model of Fracture in Materials with Disordered Microstructure," *Science and Engineering of Composite Materials.* Vol. 3, pp. 95-109.

Pyrz, R., and Bochenek, B., 1995, "Discrete Model of Fracture in Disordered Two-Phase Materials," in *IUTAM Symposium of Microstructure- Property Interactions in Composite Materials* (ed. R. Pyrz), pp. 313-326, Kluwer Academic Publishers.

Pyrz, R., 1994, "Quantitative Description of the Microstructure of Composites. Part I: Morphology of Unidirectional Composite Systems" *Compos. Sci. & Tech. Vol.* 50, pp. 197-208.

Richardson, M., K., 1969, "Interference Stress in a Half Plane Containing an Elastic Disk of Same Material," *ASME Journal of Applied Mechanics*, Vol. 36, pp. 128-130.

Schlangen, E., 1993, *Experimental and Numerical Analysis of Fracture Process in Concrete,* Ph.D. thesis: Delft University of Technology, The Netherlands.

Saleme, E., M., 1958, "Stress Distribution Around a Circular Inclusion in a Semi-Infinite Elastic Plate," *ASME Journal of Applied Mechanics,* Vol. 25, pp. 129-135.

Shioya, S., 1967, "On a Semi-Infinite Thin Plate With Circular Inclusion Under Uniform Tension," *Bulletin of JSME,* Vol. 10, pp. 1-9.

Schlangen, E., and Garboczi, 1995 " New Method for Simulating Fracture Using and Elastically Uniform Random Geometry Lattice", *Int. J. Engr. Sci.*, submitted.

Schlangen, E., and van Mier, J.G.M., 1992, "Experimental and Numerical Analysis of Micromechanics of Fracture of Cement- Based Composites," *Cement & Concrete Compos.* Vol. 14. pp. 105-118.

Sih, G.,1974 "Strain-Energy-Density Factor Applied to Mixed-Mode Crack Problems'" *Int, J. Fracture Mech.* Vol 10, pp. 311-321.

Snyder, K.A., Garboczi, E.J., and Day, A, 1992, "The Elastic Moduli of a Simple 2-D Isotropic Composite: Computer Simulation and Effective Medium Theory," J. *Appl. Phys.*, Vol. 72, pp. 5948-5955.

Theocaris, P. S.,1995 "Failure Criteria for Isotropic Bodies Revised," *Engng. Fract. Mech.*, Vol. 51, pp. 239-264

Thorpe, M., and Day, A., 1994, "Comparison of Computed Elastic Moduli with Second and Third order Bounds for Fiber Aligned Composites," submitted.

Tvergaard, V.,1982, "On Localization in Ductile Materials Containing Spherical Voids," *Int. J. Fracture.* Vol. 18, pp. 237-251.

Ugural, A.C. and Fenster, S.K., 1995, A*dvanced Strength and Applied Elasticity, 3rd ed.* Prentice Hall, Englewood Cliffs, NJ, p. 161.

Wright, W. W., 1990, "The Carbon Fiber/epoxy Resin Interphase - A Review - Part II," *Composites Polymers*, Vol. 3, pp. 360-401.

Xu, X., and Needleman, A., 1991, "Simulations of Ductile Failure with Two Size Scales of Voids," *Eur. J. Mech., A/ Solids*. Vol. 10, pp. 459-484.

Zhang, J., and Katsube, N. 1995, "A Hybrid Finite Element Method For Heterogeneous Materials with Randomly Dispersed Elastic Inclusions," *Finite Elements Analysis and Design.* Vol. 19, pp. 45-55.

Zhang, X.S., 1988, "An Infinite Sheet Weakened by Doubly Periodic Circular Holes with Two Unequal Radial Cracks," *Engng. Fracture Mech.*, Vol. 31, pp. 837-845.

Zhu, H. and Achenbach, J., 1991, "Radial Matrix Cracking and Interphase Failure in Transversely Loaded Fiber Composites," *Mech. Mater.*, Vol. 11, pp. 347-356.

Zubelewicz, A., and Bazant, Z., 1987, "Interface Element Modeling of Fracture in Aggregate Composites," J. *Engng. Mech.*, Vol. 113, pp. 1619-1630.

APPENDIX

EXPERIMENTAL SET-UP

TASK1: THE INFLUENCE OF INTERFACE AND RANDOM ARRANGEMENT OF INCLUSIONS ON LOCAL STRESSES IN COMPOSITE MATERIALS

Sample Preparation

The experimental set-up involved epoxy plates manufactured by the Measurement Group, Inc. (PHOTOELASTIC DIVISION. MEASUREMENT GROUP, INC. P. O. BOX 27777, RALEIGH, NORTH CAROLINA 27611, USA. TELEPHONE (919) 365-3800. FAX (919) 365-365-3945) under a commercial name of PSM-5. The epoxy plates were cut with a band saw, operated at a slow rate to the dimensions of 3.2x13.0x0.125 inches. The pitch of the teeth on the band saw blade was about 0.1 in. so that at least two teeth are always in contact with the edge of the epoxy plate. Then the cut edges were milled using a vertical milling machine, cutting on the side of an end mill using sharp cutters with an air jet directed at the point of tool contact with the model to minimize heating. The cutlers used were 0.125 in. in diameter and the used cutter speed was 750 rpm. Then 31 randomly distributed non-overlapping coated circular copper inclusions (Fig. 2.2), which were 0.25 inches in diameter (volume fraction of inclusions is approximately 23% in the middle portion of the specimen) were introduced in the epoxy plates. To create a non-uniform arrangement of inclusions the random numbers, indicating the centers of inclusions, were

generated by a computer according to a planar Poisson's distribution. We imposed restrictions that the coated inclusions didn't overlap, were located at least one diameter away from the edge of the specimen, and there was a minimum clear distance $0.1a$ between any two inclusions (a is the inclusion radius). Inclusions were introduced in the following way. After cutting the epoxy plates to the desired dimensions (3.2x13x0.125 inches), the epoxy plates were placed one at a time between two steel plates and holes were drilled at a slow speed of 1000 rpm with a steady but slow feeds of the material to reduce residual stresses and to minimize microcracks. The holes were drilled according to the random distribution as described above and they were of the size equal the combined size of inclusions and the coatings. To remove any remaining residual stresses due to machining, the specimens were heated to $260^{o}F$ (which is beyond the glass transition temperature), were held at this temperature for two hours and then cooled at the rate of $(5^{o}F)/hr$ to $150^{o}F$, and finally cooled in 7 hours to a room temperature. In order to allow free expansion of the model, the epoxy surface was coated with a very thin uniform layer of releasing agent, then it was placed on a smooth flat plate in the oven to support the model during annealing. To simulate different interphases the inclusions were coated with two different adhesive materials with a coating thickness equal to 0.25 a (coating 1 and coating 2) or using a thin adhesive material which had the same properties of the matrix to simulate a no coating condition (coating 4). The mechanical properties of these materials are shown in Table 2.1. All coatings (adhesives) were purchased from the MEASUREMENT GROUP, INC. and all of

them were Bisphenol-A based epoxy resin materials made of two components: a resin and a hardener. One gram of mixed adhesive would cover approximately 1.5 $in.^2$ area. The mixing proportion for coating 1 which had a commercial name of PC-1 were 90.9% resin to 9.1% hardener and a mixture proportion of 50% of resin to 50% of hardener was used to prepare coating 2 which had a commercial name of PC-6. Coating 3 had a commercial name PC-11. The used mixture proportions for PC-11 were 40% of resin to 60% of hardener. Whereas PC-11 and PC-6 can be mixed at room temperature, PC-11 required a preheating prior to mixing order to obtain a smooth homogeneous mixture of a highly viscous material. The pot life of all used adhesives was approximately 20-30 minutes. Both the surface of the inclusions and the holes needed to be clean before spreading the adhesives, so we used Asiton to clean those surfaces. Also, it is recommended that the test part surface to be warmed prior to spreading of the adhesive material in case of using PC-11 adhesive. After preparation of the adhesives masking tape was used to place the inclusions at the centers of the holes then the gaps between the holes and inclusions were filled with the desired coating material. The coatings were allowed to set for at least 24 hours before testing.

Photoelastic measurements.

After the preparation of samples the photoelasticity method was used to find the stress distributions in these birefringent composite plates subjected to a uniaxial transverse load-

ing. The loading was applied by fixing the bottom side of the specimen and then applying a uniaxial force on the other side of the specimen. We used Modular Transmission Polariscope model 061 manufactured by the MEASUREMENT GROUP. This instrument was equipped with glass laminated paralyzer, analyzer, and quarter wave plate filters. The angular readings of this set up were readable to 1/2 degree. In the circular polariscope condition, the analyzer was independently rotatable to provide fractional fringe measurement by Tardy Compensation. The analyzer rotation was shown on the measuring dial and was readable to 0.1 of a fringe. To have a monochromatic light we used a sodium lamp with a wave length of 589 nm. In order to calibrate the epoxy matrix material for the fringe value f_σ different levels of loading were applied to either specimens involving thin sheets with a hole or to a two-point-loaded beam. The average value of number of fringes was used to determine the material fringe value f_σ. For our case f_σ was found to be 53 lb/in/ fringe at room temperature.

TASK 2: THE INFLUENCE OF INTERFACE AND RANDOM ARRANGEMENT OF INCLUSIONS ON THE RESIDUAL STRESSES IN A MODEL COMPOSITE MATERIAL

Sample Preparation

The epoxy resin used was Epon 828 which is based in diglycidyl ether of Bisphenol-A and has the following chemical structure (Gupta *et al.* 1985)

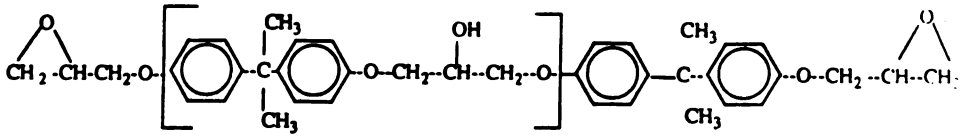

The curing agent used was metaphenylene diamine having the following chemical structure

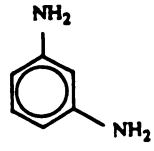

The curing agent concentration was calculated by Gupta *et al.* (1985) to be 14.5 parts per hundred parts of resin so that the epoxy amine ratio is 1:1.

To prepare the epoxy matrix, the resin and the curing agent were heated in separate containers at 75^0C (167^oF) for approximately 15 minutes (until the curing agent melted), then they were mixed together. The mixture was then vacuum-gassed. Next, the epoxy resin mixture was poured into silicone rubber models to form 1.6x3.5x0.125 inch rectangular specimens or dogbone standard shape control specimens. Inclusions were placed in random at the middle portion of the specimen and they were at least a distance of one diameter away from the free surface to minimize the free surface effect (Lee *et al.* 1992). We used either uncoated copper inclusions or coated copper inclusions. The coating was applied to the inclusions and allowed to set for at least 24 hours before placing the coated inclusions in the liquid epoxy matrix. Pre-made silicone molds with cavities equal to the combined size of the inclusions and the coatings were used, the inclusions were placed in

the center of theses cavities and the coating adhesives were used to fill the remaining gap. In this task we used the same coatings described in task 1. The mechanical properties of the epoxy matrix, inclusion and coatings used in this phase of the study are shown in Table 3.1.

To study the effect of geometric distribution, two random arrangements of inclusions with volume fraction 14% and 20% were prepared. The location of these fibers was digitized to be incorporated in the finite element analysis. For a comparison we also prepared periodic arrangement (triangular) with a volume fraction of 27.5% samples..

The model epoxy-copper composite was then cured in a pre-programed oven. The curing cycle used was 75^0C (167 ^{o}F) for two hours followed by 125^{o}C (257 ^{o}F) for another two hours, then the composite was either heated to 160^{o}C (320 ^{o}F), which is the glass transition temperature for this epoxy, held for two hours and then cooled to room temperature at slow cooling at rate of 2.5^{o}C (5^0F)/hour (post curing), or cooled directly to room temperature without post curing (standard curing).

In our study we considered the model composite in a form of a thin plate in order to simplify the experimental analysis. By having the plane stress case we reduce the free edge effects, i.e. the disturbance of the stresses near the two traction-free surfaces due to a relaxation of stresses there, and, in this case, we can see the photoelastic fringes more easily. Alternatively, we could simulate directly the plane strain case by using a fringe freezing technique as mentioned before.

Mechanical Properties of Epoxy Matrix

To study the temperature dependence of various mechanical properties of the epoxy

resin three sets of experiments were conducted. In the first set, the tensile tester (MTS) was used. Using a small environmental chamber, the stress-strain data and the axial-transverse strain data were recorded for $55^{o}C$ and $85^{0}C$ at a strain rate of 7%. The average results of three specimens for each case were used to find the elastic modulus and the Poisson's ratio for both post and standard curing conditions.

In the second set of experiments, Instron tensile measurements were used to find the mechanical properties of the epoxy matrix at room temperature. The laser extensometer was used to measure strain. Stress-strain curves of epoxy matrix for various temperatures and for the two cooling conditions are plotted in Figures 3.1a and 3.1b. The dashed curve in Figure 3.1a was obtained by Gupta *et al.* (1985). Using a regression analysis, the variation of the elastic modulus of the epoxy matrix as a function of temperature T is given by:

$$E^{m}(T) = 6.2974\,(10)^{5} - 6.7798\,(10)^{3}T + 49.7354T^{2} - 0.157799T^{3}\ psi \qquad (3.8)$$

This variation of elastic modulus with temperature is represented in Fig. 3.2. The effect of temperature on the Poisson's ratio of the matrix is shown in Figure 3.3 and has the following form

$$\nu^{m}(T) = 0.2704417 + 0.00368067T - 1.335529\,T^{2} - 4.26119T^{3} \qquad (3.9)$$

In the third set of experiments, the variation of thermal expansion with temperature was used to calculate coefficient of thermal expansion (CTE) of the epoxy-matrix, coating materials and copper inclusions.

Deformation of epoxy, coating and inclusion samples as a function of temperature is plotted in Figures 3.4 through 3.7. The derivative of those curves will give a variation of thermal coefficients of expansion with temperature which are found using regression analysis

$$\alpha^{m}(T) = 2.911\,(10)^{-5} - 4.595\,(10)^{-6}T + 3.10816\,(10)^{-7}T^{2} - 1.1816\,(10)^{-8}T^{3} + 2.7798\,(10)^{-10}T^{4} - 4.205\,(10)^{-2}T^{5} + 4.096\,(10)^{-14}T^{6} - 2.4814\,(10)^{-16}T^{7} + 8.487\,(10)^{-19}T^{8} - 1.25342\,(10)^{-21}T^{9} \qquad (3.10)$$

Similar expressions were obtained for the coatings and the inclusion.

Photoelastic measurements.

Photoelasticity method was used to study the effect of interphase and the random arrangement of inclusions on thermal stresses in composites with cast-in-place inclusions for two curing conditions: standard curing and post curing. In this analysis we used two compliant coatings. We used in the phase the same polariscope described in the previous section. In order to calibrate the epoxy matrix material for the fringe value f_σ different levels of loading were applied to a two point loaded beam (Figure 3.8). The average value of number of fringes was used to determine the material fringe value f_σ according to the formula $\sigma_1 - \sigma_2 = \frac{N f_\sigma}{h}$. For our case f was found to be 14.5 lb/in/fringe at room temperature.

TASK 3: THE DAMAGE INITIATION AND PROPAGATION IN A MODEL COMPOSITE WITH AN EMPHASIS ON CRACK INITIATION AND PROPAGATION IN AN ELASTIC PLATE WITH RANDOMLY DISTRIBUTED HOLES

Sample Preparation

The experimental set-up involved thin perforated sheets made of either an epoxy or an aluminum (2024-T4), each containing 31 randomly distributed non-overlapping circular holes of the same size (volume fraction of holes is 23% in the portion of the specimen away from the edges). The distribution of holes was obtained by generating random numbers to simulate the loci of the holes' centers. We imposed restrictions that the holes did not overlap, they were located at least one diameter away from the edges of the specimen and the distance between the holes was at least 0.1 a, where a was the hole radius. The dimensions of each epoxy plate were 3.5"x9"x0.125" produced in the same manner described for phase 1 of this study. The holes were either 0.25"or 0.3125" in diameter. The holes were introduced in the manner described in task 1. After the preparation of the epoxy samples the photoelasticity method was used to find the stress distributions in these birefringent perforated plates. In order to determine the material fringe value f_σ for the epoxy material used, different levels of loading were applied to either specimens with a hole or to a four-point-loaded beam. It is known from theory of plane elasticity (Michell, 1899; Timoshenko and Goodier, 1956) that, when a material with holes is subjected to tractions and the resultant of forces over each hole boundary vanishes, the stress field is independent of elastic constants. Thus, the stresses obtained from the analysis of fringe

patterns are applicable for both material systems studied, when they are in the elastic range.

Crack propagation

The crack propagation tests were conducted using an Instron testing machine that could apply a constant displacement rate boundary condition. An ASTM standard D2343 requires the use of a cross head speed of 2 mm/min. This recommended cross head speed is used by many other ASTM standards in cases where the stress is distributed uniformly along the tested cross section. In a material with holes the stress is not uniform and thus the stress concentration is more than 1.0. In our experiments we used a cross head speed of 0.1 mm/min. (.04 in/min). To monitor crack propagation and final crack pattern a high speed camera, which could capture 3000 frames/sec., was used. The video camera was connected to an image digitizer and the output was directed either to a super VCR or a thermal printer. The recorded image was then stored in the computer and studied frame by frame to determine a site of crack initiation and crack paths. This experiment was done for a single random configuration of holes only but it was repeated on several epoxy and aluminum specimens.